Effect of Cooling Media and Overlapping Technique on Friction Stir Processed AA2014 and AA6061 Alloys

Submitted in partial fulfilment of the requirements

for the award of the degree of

Doctor of Philosophy

by

Marukurti V N V Satyanarayana

Roll No: 718033

Under the Supervision of

Dr. Adepu Kumar
Professor, MED

Department of Mechanical Engineering
NATIONAL INSTITUTE OF TECHNOLOGY
WARANGAL – 506004
Telangana State, INDIA.
OCTOBER - 2021

THESIS APPROVAL FOR Ph.D.

This thesis entitled **"Effect of Cooling Media and Overlapping Technique on Friction Stir Processed AA2014 and AA6061 Alloys"** by **Mr. Marukurti V N V Satyanarayana** is approved for the degree of Doctor of Philosophy.

Examiner

Dr. Adepu Kumar
Professor, Department of Mechanical Engineering, NIT Warangal
Supervisor

Dr. Adepu Kumar
Head, Department of Mechanical Engineering, NIT Warangal
Chairman

NATIONAL INSTITUTE OF TECHNOLOGY

WARANGAL – 506 004, Telangana State, INDIA

CERTIFICATE

This is to certify the thesis entitled **“Effect of Cooling Media and Overlapping Technique on Friction Stir Processed AA2014 and AA6061 Alloys”** submitted by **Mr. Marukurti V N V Satyanarayana,** Roll No. 718033, to **National Institute of Technology, Warangal** in partial fulfilment of the requirements for the award of the degree of **Doctor of Philosophy in Mechanical Engineering** is a record of bonafide research work carried out by him under our supervision and guidance. This work has not been submitted elsewhere for the award of any degree.

Place: Warangal.
Date:

Dr. Adepu Kumar
Supervisor
Professor,
Department of Mechanical Engineering,
National Institute of Technology,
Warangal, Telangana State.

NATIONAL INSTITUTE OF TECHNOLOGY

WARANGAL – 506 004, Telangana State, INDIA

DECLARATION

This is to certify that the work presented in the thesis entitled **“Effect of Cooling Media and Overlapping Technique on Friction Stir Processed AA2014 and AA6061 Alloys”**, is a bonafide work done by me under the supervision of **Dr. Adepu Kumar**, Professor, Department of Mechanical Engineering, NIT Warangal, India and has not been submitted for the award of any degree to any other University or Institute.

I declare that this written submission represents my ideas in my own words and where ever others ideas or words are included have been adequately cited and referenced with the original sources. I also declare that I have adhered to all principles of academic honesty and integrity and have not misrepresented or fabricated or falsified any idea/data/fact/source in my submission. I understand that any violation of the above will cause for disciplinary action by the institute and can also evoke penal action from the sources which have thus not been properly cited or from whom proper permission has not been taken when needed.

Place: Warangal.
Date:

Marukurti V N V Satyanarayana
Roll No. 718033

ACKNOWLEDGEMENTS

It has been an enjoyable experience while pursuing the doctoral work that provided with the opportunity to come in touch with some of the kindest people with exceptional abilities and fortunate to find phenomenal support and encouragement from them. I sincerely acknowledge all of them for their help and encouragement, without which it would have been an uphill task to overcome the barriers on the way.

The first and foremost person I would like to thank is my research supervisor **Dr. Adepu Kumar**, Professor, for having introduced me to the frontier research area of friction stir processing. I am indebted to him for his inspiring guidance, unstinted support, persistent encouragement, and timely help during my research career. He gave the freedom to work on my way and always had ample time for me whenever I needed it.

I extend my sincere gratitude to **Prof. N. V. Ramana Rao,** Director, National Institute of Technology Warangal, India, for providing the necessary facilities and encouragement throughout my work.

I express sincere thanks to former HODs, **Dr. P. Bangaru Babu**, **Dr N. Selvaraj**, **Dr. R. Narasimha Rao,** and current HOD, **Dr. Adepu Kumar,** for providing all the facilities for the successful completion of the project. I want to thank Doctoral Committee members, **Dr. K.V. Sai Sreenath**, Professor, MED, **Dr. N. Narasaiah**, Professor, MMED, and **Dr. G. Raghavendra**, Assistant Professor, for their constructive criticism and suggestions during the doctoral program.

I would also like to thank **Dr. Mugada Krishna Kishore**, Assistant Professor, SVNIT Surat, **Mr. Kethavath Kranthi Kumar**, Research Scholar, NIT Warangal, **Pokula Narendra Babu**, Research Scholar, NIT Rourkela and **Dr. Kolli Murahari,** Associate Professor, LRBR College of Engineering, Mylavaram, who guided on both professional and personal front and always motivated to do better and with whom I had several fruitful scientific discussions during manuscript preparation.

I sincerely thank **Dr N. Narasaiah,** Professor, and **Dr. Bontha Sreenivasarao**, Assistant Professor, NIT Warangal, for providing access to the Fatigue testing facility. **Dr. Indradev Samajdhar**, Professor, Indian Institute of Technology Bombay, also acknowledged for the use of the National Facility of Texture & OIM for EBSD studies. I also thank to **Dr. Ch. Rajamohan**, Assistant Professor, NIT Warangal, for permitting to access corrosion testing facility.

I was fortunate to have friends who cared for and supported me when I needed it the most. I thank **Mr. Venkatesh Bikkina, Mr. Korra Nagu, Mr. I. Karthikeya Sharma, Mr. Saravanan Sundar,** and **Mr. K Nagendra Prasad** for all the technical discussions I had with them over lunchtime. I also thank **Mr. Raju, Mr. Karthik Gamidi, Mr. Rajkumar, Mr. Venkateswara Reddy, Mr. Babar Pasha, Mr. Shiva Sai, Miss B Sowmya, Mr. Karan Chauhan, and Mr. Praneeth Reddy** for their kind help during my research work. I take immense pleasure in mentioning the names of colleagues and friends who helped during a stay at NIT Warangal viz **Mr. Kattela Siva Prasad, Mr. Chandra Sekhar, Mr. Anjaneyulu and Mr. Pritam Das.**

I am thankful to **Dr. Vikram Kumar S Jain**, IIT Madras, **Dr. Shivraman Thapliyal**, Assistant Professor, NIT Warangal, and other faculty members for their support for material characterization during this period

It is my pleasure to acknowledge my family members, my brother **Babi Marukurthi**, my wife **Mrs. Gowthami Marukurthi,** and my loving daughter, **M.V. Sahasra (Kushi),** for their patience and constant support throughout my research work.

I am indebted to my other family members and friends for their continuous affection and support throughout my research work. I also thank everyone who has supported me in my doctoral work, either directly or indirectly.

Last but not least, "The financial support by Aeronautical Research & Development Board (AR&DB), Defence Research and Development Organization (DRDO), Government of India through a grant CCMT/TM/AR&DB/GIA/16-17/0332 dated 17/01/2017 is duly acknowledged."

M V N V Satyanarayana

ABSTRACT

Aluminium and its alloys are extensively used in various engineering fields such as aerospace applications, automobile sectors, and transport industries due to its superior properties like high strength to weight ratio, toughness, good formability, corrosion, and wear properties. Various manufacturing routes are available for enhancing mechanical properties and corrosion behavior of aluminium alloys, and achieving grain refinement is one such route to enhance the mechanical properties and corrosion behavior. Fine-grained (FG) materials have been finding several applications in industrial sectors over the last two decades owing to unique properties, such as high strength to weight ratio, good thermal stability, enhanced corrosion resistance, and excellent superplasticity. Fine-grained materials are produced through the application of severe plastic deformation (SPD). A wide variety of SPD methods have been used to achieve grain refinement, such as Equal channel angular pressing (ECAP), Accumulative roll bonding (ARB), and High-pressure torsion (HPT). However, these techniques require high strain rates to process the material. And, it is difficult to process the aluminium alloys with these traditional techniques due to the high susceptibility of cold cracking and porosity. Moreover, the techniques mentioned above are not economical, time-consuming, and not eco-friendly due to their lengthy processing time.

To overcome the difficulties associated with the above-mentioned techniques, Friction stir processing (FSP) has been invented and operating for the last decade. FSP emerged as the most promising method for achieving fine-grained structure, especially in aluminium alloys. FSP is a surface engineering methodology invented by R. S. Mishra that adopts the concepts of Friction stir welding (FSW). In FSP, instead of joining plates together, the surface is locally modified and refined for property enhancement. But, during FSP, the frictional heat generated between the work-tool interface causes the grain coarsening of refined grains and results in less grain refinement than expected.

In the present study, different cooling media was utilized during friction stir processing of aluminium alloys (AA2014 and AA6061) to control the grain coarsening. In the initial stages, various trail experiments were carried out on AA2014 and AA6061 with taper cylindrical threaded pin profile to optimize the process parameters such as tool rotational speed and traverse speed based on the defect-free structure and better mechanical properties. The defect-free structure with

better mechanical properties were obtained at 1100 rpm-30 mm/min for AA2014 and 800 rpm-40 mm/min for AA6061.

With the goal to eliminate the grain coarsening during FSP, in the second and third phases of work, a single-pass FSP was conducted in different cooling media (dry ice and water) on AA2014, and AA6061 using above optimized process parameters and taper cylindrical threaded pin profile, and studied the microstructure, mechanical properties, and corrosion behavior. After FSP, the coarse-grained structure present in base metals transformed into recrystallized fine grains. The cooling-assisted FSP successfully eliminated grain coarsening and produced better grain refinement than FSP without cooling media (i.e. air-cooled FSP). In AA2014 FSP, the grain size in the stir zone (SZ) of air-cooled, dry ice-cooled, and water-cooled FSP are 4.9 µm, 3.5 µm, and 0.9 µm, respectively. The ultra-fine grained structure (0.9 µm) was achieved in water-cooled FSP due to uniform heat dissipation from the processing zone to the water. Mechanical properties such as hardness and strength were improved in water-cooled FSP compared to other conditions. The fine precipitates formed in the water-cooled FSP sample were distributed randomly at grain boundaries. Hence, corrosion resistance was improved in the water-cooled sample compared to other conditions. In AA6061, recrystallized fine grains formed in all FSP samples (grain size within a range of 2-6 µm) due to dynamic recovery and recrystallization, while samples processed in cooling-assisted FSP resulted in better grain refinement in the stir zone. Three kinds of precipitates (Fe-based needle-shaped precipitates, Si-based round-shaped precipitates, and chain of small round-shaped Si-based precipitates) were identified in BM and FSP samples. Compared to air-cooled FSP, in cooling assisted-FSP, the hardness and tensile strength increased but remained lower than the base alloy due to the presence of high-density Fe-based needle-shaped precipitates. The ductility after FSP greatly improved due to thermal softening and dissolution of precipitates. The corrosion results demonstrated that the corrosion resistance greatly enhanced after FSP due to the uniform distribution of grain structure and discontinuous chain of small round-shaped Si-based precipitates in SZ. Moreover, cooling assisted-FSP resulted in improved corrosion resistance compared to air-cooled FSP due to the formation of fine precipitates.

In the above studies, the stir region is prepared using single-pass FSP. Generally, the pin diameter varies from 4 to 8 mm, which produces the stir zone of the same diameter with single-pass FSP. Such kind of narrowed SZ is not used for practical applications. To overcome this difficulty, the large-area stir zone of the required size is prepared by several consecutive passes with the pin overlapping. The overlapping FSP aims to prepare larger surface areas to achieve homogenous microstructure and enhanced superplasticity. Similar conditions for each pass are essential to assuring homogeneous properties throughout the processed zone. Initially, trial experiments were conducted in different cooling media with different tool pin profiles (Square pin profile, Hexagonal pin profile, Cylindrical thread pin profile, and Triangle pin profile) to optimize the best tool geometry based on the better mechanical properties. The hexagonal pin geometry resulted in better mechanical properties for AA2014, while the square pin geometry resulted in better mechanical properties for AA6061.

With the goal to create the large-area processing zone and eliminate grain coarsening, in the fourth and fifth phase of work, a multi-pass overlapping FSP was carried out in different cooling media on AA2014 and AA6061 using above optimized process parameters and tool geometry, and studied the microstructure, texture, mechanical properties, work-hardening rate, corrosion, wear and fatigue behavior. The fine equiaxed grains were produced in the large-area stir region of overlapping FSP, and it was identified that the grain size of each overlapping pass is uniform in the large-area stir region. But, the texture components and their intensities varied from one pass to another pass due to variation of heat input and number passes. In AA2014, the ductility increased after FSP by 155% due to the material softening, and dissolution of Al_2Cu precipitates in the stir zone. Kocks-mecking plots of the BM and FSP samples witnessed the stage-III of work-hardening behavior. The wear resistance was significantly improved after FSP, and the wear rate is high at initial sliding distances, reached a steady state at certain sliding distances, and the further increase in sliding distance resulted in a gradual decrease of wear rate. FSP samples sustained a large number of fatigue cycles than BM, and the fractured surface of fatigue samples revealed the presence of ridges and plateaus in Region-I and dimples and striations in Region-II of crack propagation. In AA6061, the difference in wear rate between BM and FSP decreased with an increase in wear load. The fatigue results revealed that the fatigue life improved significantly after FSP and the fatigue crack growth (FCG) rate was lower in cooling assisted FSP due to the grain refinement and precipitation factor. The steady-state propagation region consists of striations marks and secondary cracks, whereas the dimples were identified in the rapid crack propagation region due to ductile failure.

In the final phase of work, a novel relation was established between local strength (i.e. hardness), and bulk mechanical strength (i.e. tensile strength) of friction stir processed aluminium alloys using experimental investigations on selected alloy system together with data reported in literature sources. Initially, the authors generated a linear relation between hardness and strength of friction stir processed aluminium alloys under different cooling conditions. The experimental values of hardness and strength were well fitted with the formulated equations due to the formation of a homogeneous fine-grained structure. Also, two novel linear relations were successfully established between hardness and strength with proportionality constants of 1.9 and 2.7, respectively. On the other hand, it was also concluded that it is not possible to establish a linear relation between hardness and strength of surface composites due to structural inhomogeneity and agglomeration of reinforcement particles.

TABLE OF CONTENTS

CHAPTER 2 LITERATURE SURVEY

CHAPTER 3 EXPERIMENTAL PROCEDURES

CHAPTER 4 **RESULTS AND DISCUSSION**

CHAPTER 5 CONCLUSIONS AND FUTURE SCOPE

LIST OF FIGURES

LIST OF TABLES

LIST OF ABBREVIATIONS

FSW	Friction stir welding
FSP	Friction stir processing
TWI	The Welding Institute
SZ	Stir zone
HAZ	Heat affected zone
TMAZ	Thermo-mechanically affected zone
TSZ	Top stir zone
MSZ	Middle stir zone
BSZ	Bottom stir zone
AS	Advancing side
RS	Retreating side
WNZ	Weld nugget zone
BM	Base metal
ACFSP	Air-cooled FSP
CCFSP	Cryogenic-cooled FSP
UWFSP	Underwater FSP
OM	Optical microscope
SEM	Scanning electron microscope
EDS	Energy dispersion spectroscopy
XRD	X-ray diffraction
EBSD	Electron backscattered diffraction
GS	Grain size
PF	Pole figure
ODF	Orientation distribution functions
DRX	Dynamic recrystallization
C-DRX	Continuous dynamic recrystallization
D-DRX	Discontinuous dynamic recrystallization
G-DRX	Geometric dynamic recrystallization
M-DRX	Meta dynamic recrystallization

DRV	Dynamic recovery
PSN	Particle stimulated nucleation
DE	Dynamic equilibrium
SPD	Severe plastic deformation
IPD	Intense plastic deformation
SD	Shear direction
SPN	Shear plane normal
FCC	Face centered cubic
LABs	Low angle boundaries
HABs	High angle boundaries
IPF	Inverse pole figure
SFE	Stacking fault energy
AGG	Abnormal grain growth
UTM	Universal testing machine
UTS	Ultimate tensile strength
YS	Yield strength
EL	Elongation
NDT	Non-destructive testing
FCGR	Fatigue crack growth rate
COD	Crack opening displacement
CT	Compact tension
OCP	Open circuit potential
EIS	Electrical impedance spectroscopy
PDP	Potentiodynamic polarization
CPE	Constant phase elements
OR	Overlapping ratio
DAQ	Data acquisition system
CNC	Computer numerical control
WHR	Work hardening rate

LIST OF SYMBOLS

V	Linear speed or traverse speed
W	Rotational speed
Q	Activation energy
ϵ	Strain rate
R	Gas constant
T	Temperature
T_{MP}	Melting temperature
f_{HAB}	Fraction of high angle boundaries
HV	Vickers hardness
σ_Y	Yield strength
σ_{UTS}	Ultimate tensile strength
Θ	Work hardening rate
Θ''	Work hardening rate at yield stress
n	Strain hardening index
σ_s	Saturation stress
σ	Stress
E_{COR}	Corrosion potential
I_{COR}	Current density
R_S	Solution resistance
R_{CT}	Charge transfer resistance
C_{DL}	Double-layer capacitance
a	Crack length
K	Stress concentration factor
ΔK	Stress concentration factor range
da/dN	Fatigue crack growth rate
Z	Recrystallization rate

CHAPTER 1

INTRODUCTION

1.1 Background

Grain size is an important microstructural factor that influences the properties of metals and alloys. Grain refined materials have been finding several applications in industrial sectors over the last two decades owing to unique properties, such as high strength to weight ratio, good thermal stability, enhanced corrosion resistance, and excellent superplasticity. Severe plastic deformation (SPD) is the most effective way to fabricate fine-grained metallic materials. The processing of metals to achieve grain refinement via SPD has become essential in materials research over the last two decades. SPD offers the possibility of refining the grains of traditional bulk solids into the sub-micron (less than one micron) or even nano-micron (less than one nanometer) range. Since many of the fundamental properties of materials are determined by grain size, SPD processing can produce materials with unusual and attractive properties. For example, materials with fine grain sizes are expected to have high strength. If these fine grains are relatively stable at elevated temperatures, excellent superplastic forming is possible. While there are many methods for producing SPD in metallic materials, four processing methods stand out as the most common ways to achieve grain refinement; Equal-channel angular pressing (ECAP), Accumulative roll bonding (ARB), High-pressure torsion (HPT), and Friction stir processing (FSP).

1.2 Equal channel angular pressing

Equal channel angular pressing (ECAP) is also known as equal channel angular extrusion (ECAE). It is a SPD technique for achieving grain refinement in a metallic material, invented by Segal in the Soviet Union in 1973. It is an extrusion process that can refine the microstructure of metallic materials and improve strength according to the Hall-Petch relationship. ECAP produces substantial deformation without reducing the cross-sectional area. This is accomplished by pressing the working sample through a die constrained within an internal channel bent abruptly through a sharp angle. For example, a metal bar with a square cross-section is extruded through a 90° angle channel where the channel's cross-section is the same on entry and exit as shown in Fig. 1.1a. It is obvious that the working sample emerges from the die with the same cross-sectional area as in the initial state, implying that repeated pressings can be carried out to impose extremely high strains developed in the working sample that produces the grain refinement [Roberto et al., (2012)].

1.3 High pressure torsion

High-pressure torsion (HPT) is a metal processing technique introduced by Bridgman in 1935. The working principle of HPT involves placing a thin disk between two massive anvils and is subjected to a compressive applied pressure (P) of several magnitudes at room temperature or elevated temperature while also being subjected to a torsional strain exerted by rotation of one of the anvil. As a result, surface frictional forces severely deform the disc by shear, causing it to deform under a quasi-hydrostatic pressure, leading to grain refinement [Alexander et al., (2008)]. The schematic representation of the HPT process is shown in Fig. 1.1b.

1.4 Accumulative roll bonding

Accumulative roll bonding (ARB) is a multi-stage processing technique invented by Tsuji et al. in 1999. In ARB, two or more sheets of similar materials are stacked together, heat-treated (to a temperature below the recrystallization temperature), and passed through the rollers to achieve the SPD. This deformation must be sufficient to trigger solid-state bonding. The bonded sheet is then cut into two halves and stacked through the rollers. The imposed strains by the rollers are sufficient enough to achieve grain refinement in stacked sheets. The process is repeated multiple times until required grain refinement is achieved. Compared to other SPD processes, ARB does not require dedicated equipment and tooling. Conventional rolling mills are enough to apply the SPD [Jalal et al., (2017)]. The schematic representation of ARB is shown in Fig. 1.1c.

Both ECAP and HPT are restricted to manufacture small components and not economical as it requires specialized equipment and tooling, and these processes require relatively large load capacities and dies. In HPT, the strain varies across the disc, with zero strain in the center and maximum strains at the periphery is a possible problem. The limitations of ECAP include limited plastic deformation at room temperature, and the length of the raw billet is restricted by the space available in the equipment. Furthermore, this deformation method does not allow for continuous pressing. That is why there is no industry for this method for obtaining ultrafine-grained (UFG) metal structures. On the other hand, the rolling mechanism in ARB has few drawbacks. One of these concerns is the overall thickness reduction, i.e., the total deformation achieved per pass, which is limited due to tensile deformation and the resultant cracking at the edges. To overcome the difficulties associated with the above-mentioned techniques, friction stir processing (FSP) has been invented and operating for the last two decades.

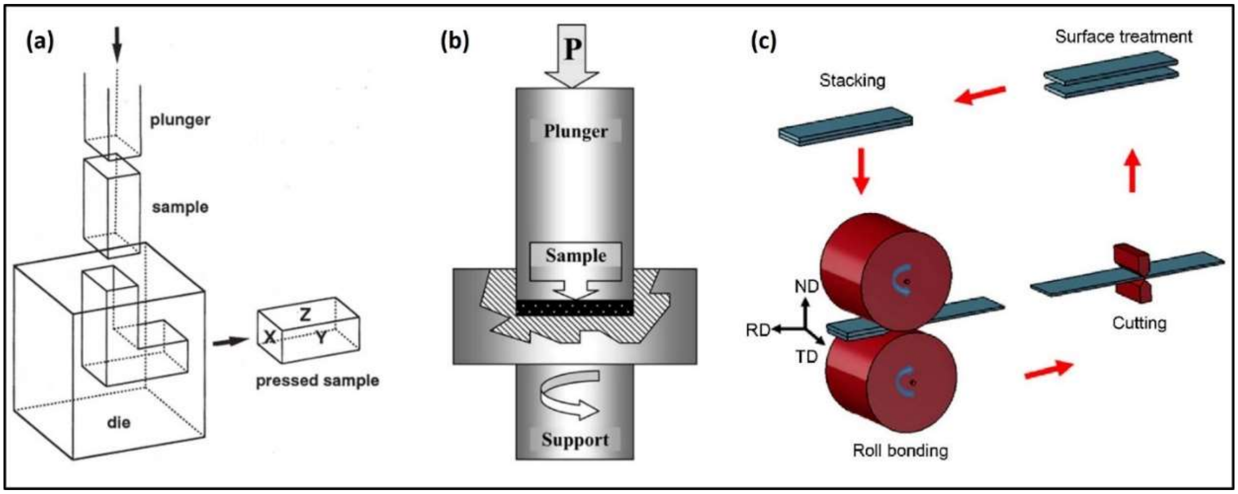

Fig. 1.1. Schematic illustration of (a) Equal channel angular pressing [Roberto et al., (2012)], (b) High-pressure torsion [Alexander et al., (2008)], and (c) Accumulative roll bonding [Jalal et al., (2017)].

1.5 Friction stir welding/processing

Friction stir welding (FSW) is solid-state welding, was invented by Wayne Thomas et al. at the The Welding Institute (TWI), London, UK, for joining of aluminium and its alloys as an alternative for conventional fusion welding techniques [Thomas et al., (1991)]. Later, the application has been extended to joining other metallic materials such as copper, magnesium, titanium, high entropy alloys, and non-metallic materials. FSW is a ‘green’ technology and is considered one of the essential metal joining techniques in the last two decades due to its energy-efficient, environmental friendliness, and versatility [Mishra and Ma (2005)].

Friction stir processing (FSP) is a thermo-mechanical processing technique that has gained remarkable success in achieving grain refinement in metals and alloys. It was invented by R.S Mishra based on the working principles of FSW [Mishra et al., (1999)]. FSP was initially developed to repair the casting defects. Then, the application has been extended to achieve grain refinement, modifying the microstructure of thin surface layers for property enhancement, and preparing surface composites of aluminium and its alloys [Ma et al., (2008)]. The working principle of FSP is remarkably simple and similar to the working principle of FSW. During FSP, a rotating tool constituted by shoulder and pin penetrates the working metal until the shoulder makes little penetration after complete penetration of pin to prevent material from flowing out of pin field. The tool continuously rotates at the same location in the material to achieve desired plastic flow behavior; once the desired plastic flow is reached, the tool starts traveling over the line of action. During the tool travel, the deformed material is moved around the pin from the advancing side (AS) to the retreating side (RS) and deposited behind the tool [Ma et al., (2008)]. The schematic representation of FSP is shown in Fig. 1.2. The tool is typically tilted by 1-3^0 degrees so that the trailing edge of the tool shoulder forges plasticized material downwards and consolidates behind it. FSP is a thermo-mechanical process in which the material undergoes extreme plastic deformation at high temperatures, usually greater than 0.5 T_{MP} (melting point temperature). FSP has been reported to reach temperatures of 0.9 T_{MP}, and since no melting has been observed, it is a solid-state method. FSP does not alter the material's shape and size, and it can be applied locally to a specific part of a component without impacting its overall properties. This method can be used to process even hard to deform HCP metals and low ductility alloys because it deforms the material at a high temperature. Table 1.1 summarizes the major advantages of FSP in terms of technical, metallurgical, energy, and environmental considerations.

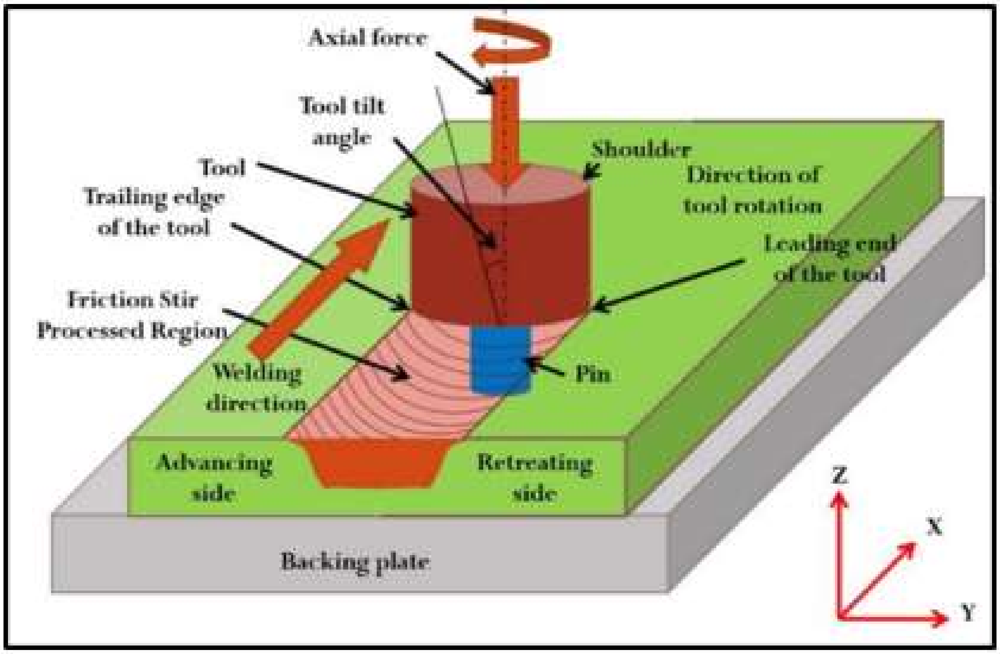

Fig. 1.2. Schematic representation of friction stir processing [Jain et al., (2018)].

Table 1.1 Major advantages of friction stir processing [Ma et al., (2008)].

Technical	• The pin length controls the processing depth. • Single-step technique • Surface cleaning is not required • Excellent dimensional stability • Good repeatability • Scope for automation
Metallurgical	• Solid-state process • Less distortion of working sample • Recrystallized fine grain • Homogenization of processing zone • No cracking in working samples • No chemical affects • Superior metallurgical properties in the processed zone
Energy	• Reduced energy consumption since the frictional heat generated at the work-tool interface is sufficient to achieve plastic deformation. • Enhanced material use (for example, processing different thicknesses) allows weight reduction.
Environmental	• Green technology • High-temperature corrosion (oxidation) is minimized • No shielding gas required • Minimal usage of consumable • No usage of solvents

As like other SPD processes, FSP also has few limitations, which includes; 1) Heavy-duty clamping required to hold the tool, 2) Exit hole defect formed after withdrawing the tool from the processing/weld zone, 3) The thickness of materials to be processed/welded is limited to 50 mm thickness for conventional tools and 100 mm for bobbin tool, and 4) Tool wear is more in case of processing/joining hard materials [Ma et al., (2008)].

1.6 Terminology involved in FSP

Shoulder: Part of the FSP tool that penetrates and deforms the top surface of working plates and acts as a reservoir for material deformed by the pin. Usually, the ratio of shoulder diameter to pin diameter of 2-3 is preferred.

Pin or probe: Part of the FSP tool completely penetrates the working plates to modify the surface.

Tool rotational speed: Rate at which the FSP tool revolute and is usually expressed in rpm

Tool traverse speed: The rate at which the FSP tool travels along the line of action to modify the surface and is usually expressed in mm/min.

Tool tilt angle: Also called spindle head tilt, it is the angle between the axis of the spindle and the normal axis of the working plates.

Advancing side: Side of the working plate where the direction of tool rotation and tool travel is the same.

Retreating side: Side of the working plate where the direction of tool rotation and tool travel is opposite.

Leading edge: Un-processed region of tool front along the line of action.

Trailing edge: Processed region of back to the tool along the line of action.

Plunge depth: The depth up to which the FSP tool shoulder penetrates the working metal.

Start dwell time: The time during which the tool rotates at the same location after complete penetration of the tool to achieve sufficient plastic deformation for processing. Usually, the start dwell time varies from 30 to 120 min depending upon the hardness of the working plate.

End dwell time: The time during which the tool rotates at the same location for easy withdrawal of the tool after processing. Usually, the start dwell time varies from 30 to 45 min.

Axial force: Force applied on the working plate during FSP.

Cavity: The discontinuity in the form of void due to improper selection of process parameters.

Exit hole: The common defect formed in FSW/FSP due to withdrawal of tool.

Flash: Material ejected along the processing region

1.7 Microstructure development in FSW/FSP

The combined action of high temperature and intense mechanical stirring alters the initial microstructure in several ways, resulting in the creation of distinct zones such as stir zone (SZ), thermo-mechanically affected zone (TMAZ) and heat-affected zone (HAZ), as depicted in Fig. 1.3. During FSP/FSW, each zone is subjected to different thermal cycles and temperature combinations and has a different microstructural history.

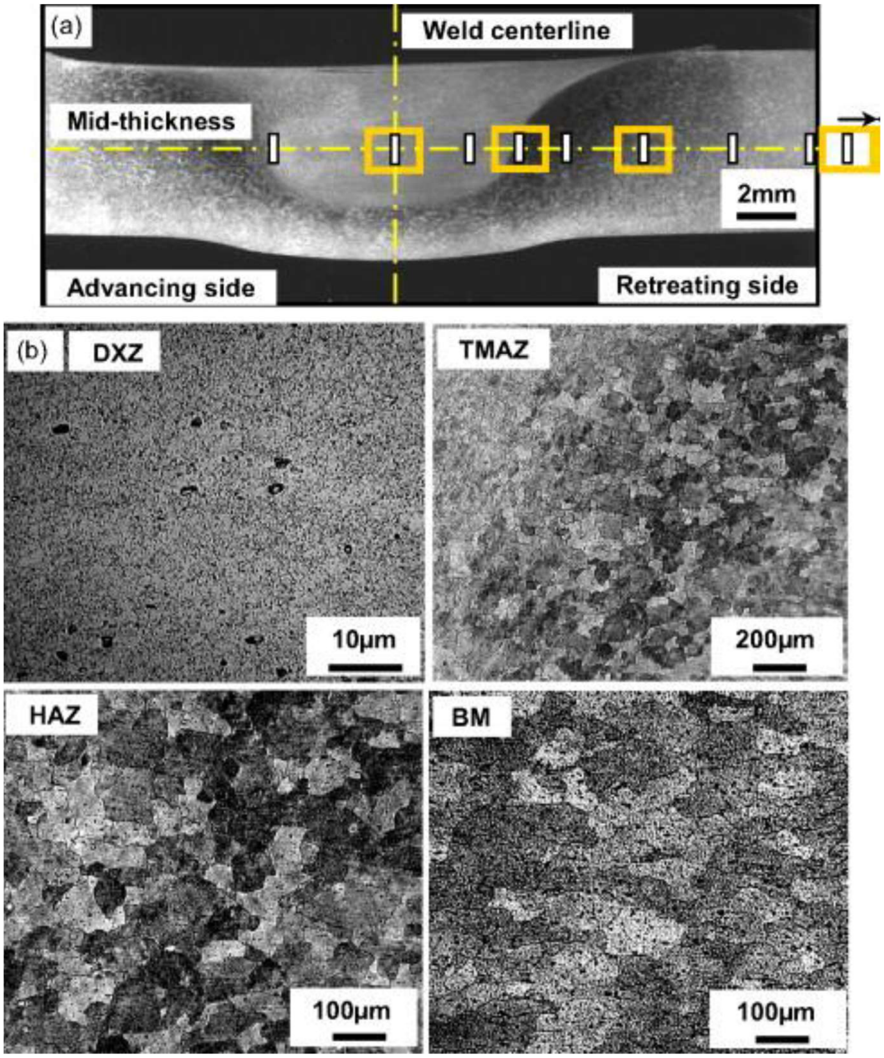

Fig. 1.3. (a) Low-magnification image of the friction stir welded AA6061 alloy, (b) Microstructure of the dynamic recrystallized zone (DXZ) or SZ, TMAZ, HAZ, and initial base metal (BM) captured at yellow square marks displayed in (a) [Woo et al., (2008)].

Stir zone

It is the region where temperature and deformation are maximum, and it is formed by the stirring action of the pin. The stir zone, also called the nugget zone (NZ) or dynamically recrystallized zone (DXZ), where the maximum grain refining occurs due to maximum temperature and deformation. The stir zone volume is determined by tool geometry. The shoulder width usually determines the width of the SZ, and the pin length determines the depth of the SZ. It is also stated that the grain size is not uniform in the volume of the stir zone. Variation occurs not only on the surface but also in the cross-section of the SZ. It is typically due to the strain intensity and temperature gradients during the complex material flow. Mahoney et al. (2001) stated that the average grain size in stir zone varies from 5.3 μm at the top to 3.2 μm at the bottom and from 5.1 μm at the advancing side to 3.5 μm on the retreating side on friction stir processed AA7075 alloy as shown in Fig. 1.4.

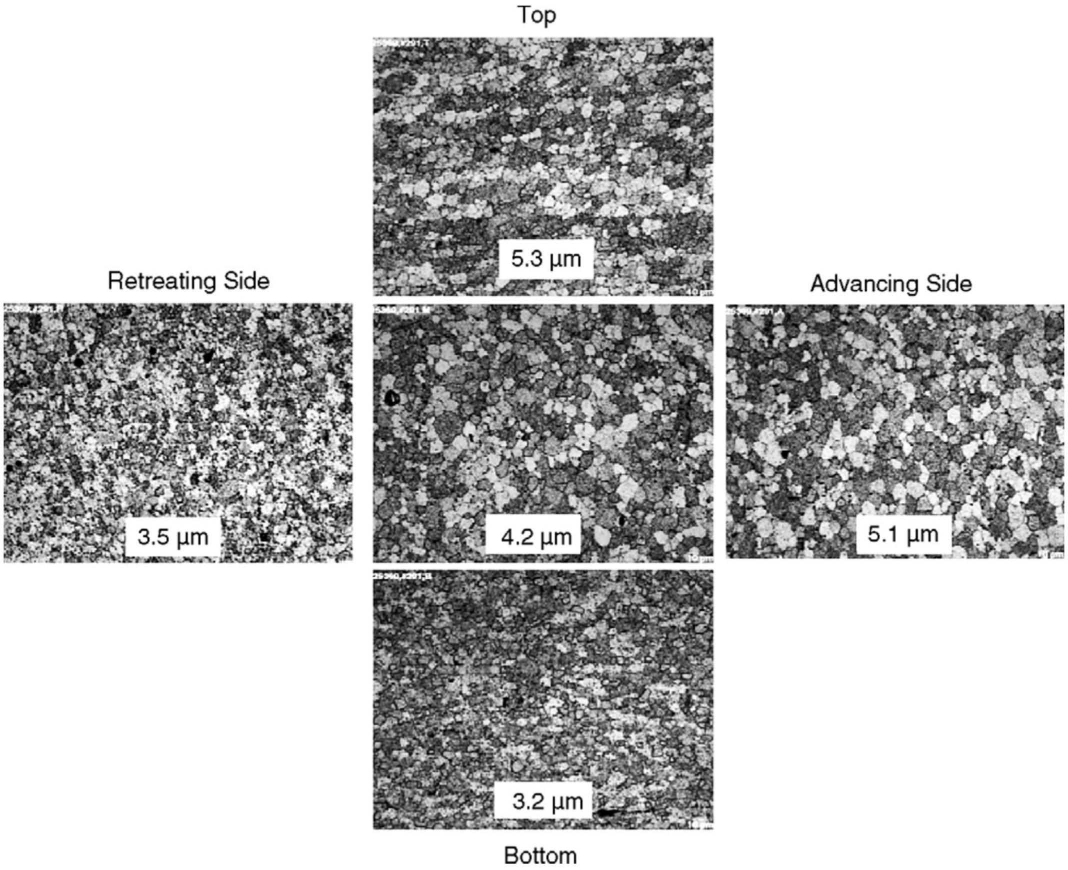

Fig. 1.4. Grain size distribution in various locations of AA7075 stir zone [Mahoney et al., (2001)].

Thermo-mechanically affected zone

Thermo-mechanically affected zone (TMAZ) exists on both sides of the stir zone, and the size of the TMAZ varies from several microns to millimeter. During FSW/FSP, this zone is subjected to high temperature and low strain rate. However, this strain rate is not sufficient to achieve recrystallization and resulted in the formation of elongated coarse columnar grains in the TMAZ. In aluminium alloys, considerable plastic strain can be obtained without recrystallization in the TMAZ, and a distinct boundary separates the stir zone and the deformed zones of the TMAZ.

Heat affected zone

This zone is formed adjacent to both sides of the TMAZ. During FSW/FSP, this zone experiences only thermal cycles. As this zone is far away from the stir zone, no tool plastic deformation effects are transferred to this zone. As a result, heavily deformed coarse grains formed in the HAZ.

Base metal

This zone is adjacent to both sides of the HAZ, and this is the region where no plastic deformation and temperature effects exist during FSW/FSP. As a result, the microstructure and mechanical properties remain unaffected after FSW/FSP, called the unaffected region. The microstructure of base metal is characterized by heavily elongated pancake-shaped grains.

1.8 Understand the basic concept and process parameters

The primary requirements of friction stir processing are to develop a defect-free and quality structure. The quality of friction stir processed structure relies on bond formation for the material flow. The bond formation is interconnected with the contact conditions of the FSP tool, work material, and temperature generation, as displayed in Fig. 1.5.

The process conditions such as tool rotational rate, tool traverse rate, and plunge depth are very important, without which the bond formation in the processed plate does not happen. The rotation of the tool causes the stirring and mixing of material around the tool pin during the tool travel from one end to another end.

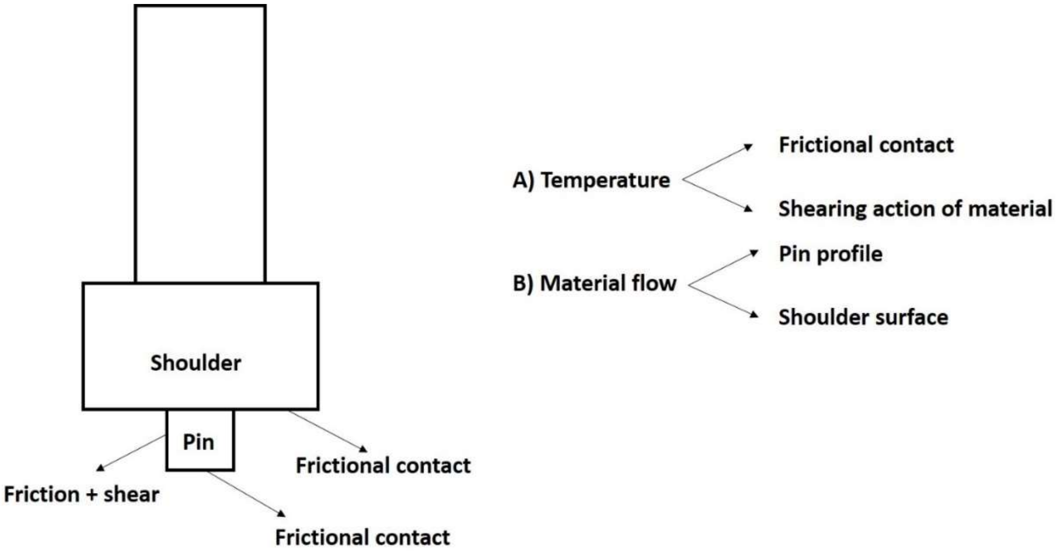

Fig. 1.5. Basic bond formation during friction stir processing.

1.9 Defects formed in FSW/FSP

Improper selection of process parameters and tool geometry leads to the formation of defects in the stir zone. Various kinds of defects observed during FSW/FSP are shown in Fig. 1.6, and the reason for forming those defects is summarized in Table 1.2 [Arbegast et al., (2008)].

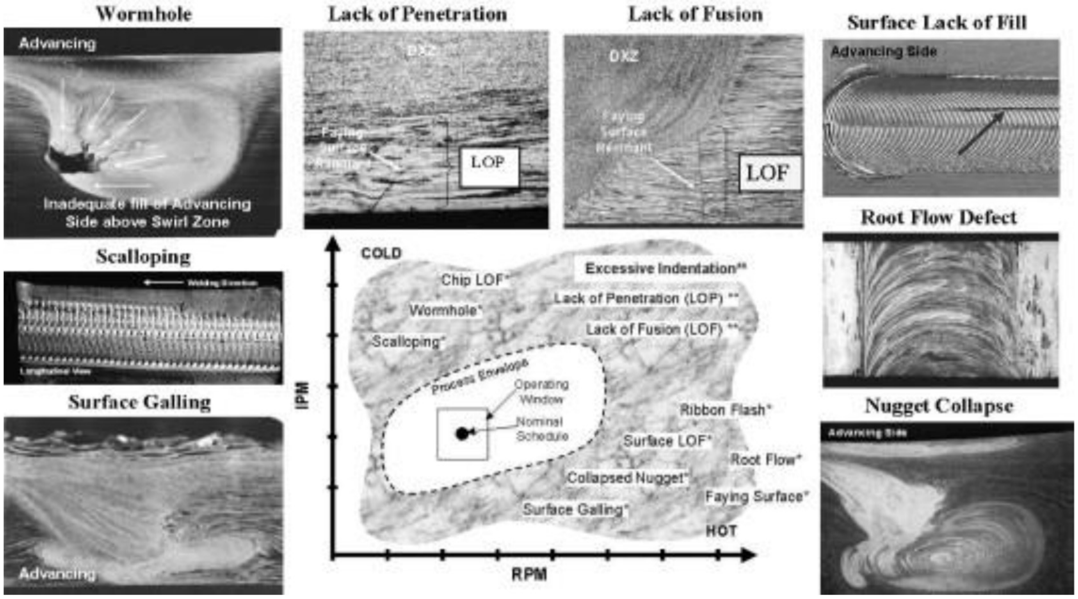

Fig. 1.6. Defects in FSW/FSP [Arbegast et al., (2008)].

Table 1.2 Reasons for the formation of defects in FSW/FSP [Arbegast et al., (2008)].

S. No	**Defect**	**Reason**
1	Wormhole	Generally observed on advancing side • Very high tool travel speeds • Insufficient forging force • Improper work clamping
2	Excessive flash	More material expelled in the form of flash on the surface • Very high tool travel speeds • High forging pressure
3	Nugget collapse	Improper development of nugget shape towards advancing and retreating side • Too hot weld • Very high weld pitch
4	Lack of fusion/penetration	Geometric flaws • Improper selection of tool geometry and placement of the tool • Too high of travel speeds. • Thickness differences in work materials to be joined and the gap between the work materials.
5	Scalloping	Galling and tearing of material on the surface of the stir zone behind the tool pin. • Too hot weld • Very high weld pitch • Sticking of processed metal to tool pin
6	Surface lack of pill	Continuous surface void on advancing side • Insufficient forge pressure • Less plunge depth • Improper work clamping

1.10 Tool material

FSP/FSW is a thermo-mechanical processing route. During FSP/FSW, the temperature of the tool reaches the solidus temperature of the base alloy. Tool material must be appropriately selected to have quality processed or weld zone. Thus, it is undesirable to have a tool that loses dimensional stability and the designed features.

- **Selection of tool materials**

Tool steels, Ni/Co-based steels, Refractory materials, Tungsten-based alloys, Carbides, Inconel alloys, Metal matrix composites, Mo based alloys, Titanium-based alloys, and Poly cubic boron nitride (PCBN) are used as tool materials for FSW/FSP [Collier et al., (2003)]. Refractory metals like tungsten-based alloys and PCBN are used for joining/processing high-strength materials. However, tool steels are used for the joining/processing of aluminium and its alloys.

- **Characteristics of tool material**

Many different material properties could be considered necessary in FSW/FSP, but the ranking of their properties depends on work material, tool life, and other factors. Aside from the physical characteristics of materials, other practical aspects may influence the tool material selection.

- **Elevated temperature strength and stability**

The tool material must be able to sustain compressive loads when it initially contacts the work material and should have sufficient compressive and shear strength at elevated temperatures to prevent tool failure during processing/welding. In addition to having sufficient strength at elevated temperatures, the tool must maintain strength and the dimensional stability during processing/welding.

- **Wear resistance**

Excessive tool wear alters the shape of the tool, thus influencing the weld quality and increasing the risk of defects. Tool wear can be caused by adhesive, abrasive, or chemical actions in FSW/FSP. The interaction between the work and tool materials, the selected tool geometry, and processing parameters determine the exact wear mechanism.

- **Tool reactivity**

Tool material must not react with the work materials or the environment, which will alter the surface characteristics of the tool.

- **Fracture toughness**

The stresses and strains created locally when the tool initially contacts the work surface are sufficient to cause the tool fracture, even when mitigation techniques are employed (a pilot hole, low plunging speed, and preheating of the work material). It is widely accepted that the tool penetration and dwell time produce the most harm to the tool.

- **Coefficient of thermal expansion**

Large variation in the coefficient of thermal expansion between the shoulder and pin materials causes either the shoulder to expand relative to the pin or the pin to expand relative to the shoulder. These circumstances increase the stress between the shoulder and the pin, thus leading to tool fracture.

1.11 Introduction to aluminium and its alloys

The demand for aluminium has been increasing over the last four decades due to its unique combination of properties such as less density (2.7 g/cm^3), soft and highly ductile nature, etc. And, the unique combination of those properties made aluminium is one of the most attractive, versatile, and economical materials for a broad range of applications. Moreover, the aluminium components can be easily manufactured compared to other lightweight metals due to their low melting point temperature (T_{MP} – 660^0 C). Unfortunately, pure aluminium is restricted to use in specialized non-structural applications because of its less mechanical strength. However, the mechanical strength of pure aluminium can be improved by the addition of alloying elements [Davis et al., (2005)].

The most common alloying elements in aluminium include copper, manganese, silicon, magnesium, chromium, and zinc. However, manganese, silicon, and chromium have a high melting point but less solid solubility in aluminium. On the other hand, copper, magnesium, and zinc have significantly high solid solubility in aluminium. The solubility limits of alloying elements are shown in Table 1.3 [Polmear et al., (1995)].

The aluminium alloys are majorly divided into two categories: Wrought alloys and Cast alloys. And, these alloys are further divided based on the processing route for property enhancement. Many cast and wrought alloys respond to heat treatment processes like solution annealing and precipitation or age hardening, which are treated as heat-treatable alloys. Many wrought alloys depend on work hardening through mechanical reduction but with a combination of various heat treatment techniques for property enhancement, and these are referred to as work hardening alloys. On the other hand, some cast alloys cannot be heat-treated, and these are only used in as-cast and thermally modified conditions. These are referred to as non-heat-treatable alloys.

In general, heat treatable alloys show better strength than non-heat-treatable alloys due to the precipitation phenomenon. The precipitates present in the heat-treatable alloys can effectively act as barriers for dislocation movement and improve strength. But, these precipitates are dissolved and coarsened in the processes that involve elevated temperatures, resulting in a change of microstructure and mechanical properties.

Table 1.3 Maximum solubility of commonly used alloying elements in aluminium [Polmear et al., (1995)].

Element	**Temperature (^{O}C)**	**Maximum solubility**	
		at. %	**Wt. %**
Copper	548	2.40	5.65
Chromium	661	0.40	0.77
Manganese	658	0.90	1.82
Magnesium	450	18.50	17.40
Zink	443	28.80	70.00
Silicon	577	1.60	1.65

Aluminium alloys may be fabricated in any form like wrought aluminium sheets or plates, which are extensively used in aerospace and structural applications. The further classification of wrought aluminium alloys is designated by the international designation system adopted by American Association System is shown in Table 1.4 [Callister et al., (2003)].

Table 1.4 International designation system for wrought aluminium alloys [Callister et al., (2003)].

Series	Major alloying elements	Heat treatable
1xxx	Pure Al	
2xxx	Cu (Mg)	Yes
3xxx	Mn (Mg)	No
4xxx	Si	No
5xxx	Mg	No
6xxx	Si & Mg	Yes
7xxx	Mg & Zn (Cu)	Yes
8xxx	Other	
9xxx	Unused	

The wrought alloys are designated using a four-digit system. The first digit is most important as it indicates the primary alloying element (s), and the other digits indicate the purity of alloys or the concentration of other minor alloying elements. In most cases, the alloy system is designated with a four-digit system followed by an alphabet and number to represent the temper conditions. The temper system of wrought aluminium alloys is listed in Table 1.5 [Polmear et al., (1995)].

Table 1.5 Tempering conditions of wrought aluminium alloys [Polmear et al., (1995)].

Condition	Description
T3	Solution annealing and cold working followed by natural aging
T4	Solution annealing followed by natural aging
T5	Cooled from high-temperature shaping followed by artificial aging
T6	Solution annealing followed by artificial aging

T7	Solution annealing followed by artificial over-aging
T8	Solution annealing and cold working followed by artificial aging

The complex geometries of aluminium alloy components are usually fabricated with the casting process into a net shape. The cast aluminium products are widely used in automobile sectors, including engine blocks, connecting rods, piston-cylinder assembly, gearbox and knuckles of car steering, etc. Unlike wrought aluminium alloys, cast aluminium alloys are designated with a three-digit system followed by a decimal value. Like wrought aluminium alloys, the first digit and the next two digits indicate the primary alloying element (s) and purity of alloy or concentration of minor alloying elements. The decimal value in all alloys indicates the casting alloy limits. The classification of cast aluminium alloys is designated by the international designation system adopted by American Association System is shown in Table 1.6 [Callister et al., (2003)]. But, cast aluminium alloys do not have an internationally accepted designation system for tempered conditions. A suffix follows the alloy designation to indicate the tempering condition of the cast alloy as documented in Table 1.7 [Polmear et al., (1995)].

Table 1.6 International designation system for cast aluminium alloys [Callister et al., (2003)].

Series	**Major alloying elements**	**Heat treatable**
1xx	Pure Al	
2xx	Cu	Yes
3xx	Si with Cu and/or Mg	Yes
4xx	Si	No
5xx	Mg	No
6xx	Unused	
7xx	Zn	Yes
8xx	Ti	No
9xx	Other	

Table 1.7 Tempering conditions of cast aluminium alloys [Polmear et al., (1995)].

Condition	**Description**
M	As-cast
TB	Solution annealing and natural ageing
TB7	Solution annealing and stabilizing
TE	Casting followed by artificial aging
TF	Solution annealing and artificial aging
TF7	Solution annealing, artificial aging, and stabilizing
TS	Thermal stress relieving

1.12 2xxx aluminium alloys

In 2xxx series alloys, copper is the primary alloying element, with magnesium as a secondary addition. These alloys must be solution annealed to achieve the best properties; Mechanical properties are comparable to, and often surpass, those of low-carbon steel when solution annealed. In some instances, precipitation heat treatment (aging) is used to boost mechanical properties even further. This treatment improves yield strength at the expense of elongation; however, it has a lesser impact on tensile strength. The 2xxx series alloys do not have as high corrosion resistance as most other alloys of aluminium, and they are susceptible to intergranular corrosion under some conditions. As a result, high-purity aluminium, a magnesium-silicon alloy of the 6xxx series, or an alloy containing 1% Zn are commonly used to clad these alloys in sheet form. The coating, normally between 2 and 5% of the total thickness on each side, protects the core material from corrosion by providing galvanic protection. The 2xxx series alloys are suitable for parts and structures that require a high strength-to-weight ratio and are mostly used to fabricate wheels of trucks and aircraft, truck suspension components, fasteners, and structural components that withstand strength at higher temperatures up to 150^0 C. The relationships between some of the more widely used alloys in the 2xxx series alloys are shown in Fig. 1.7 [Davis et al., (2005)].

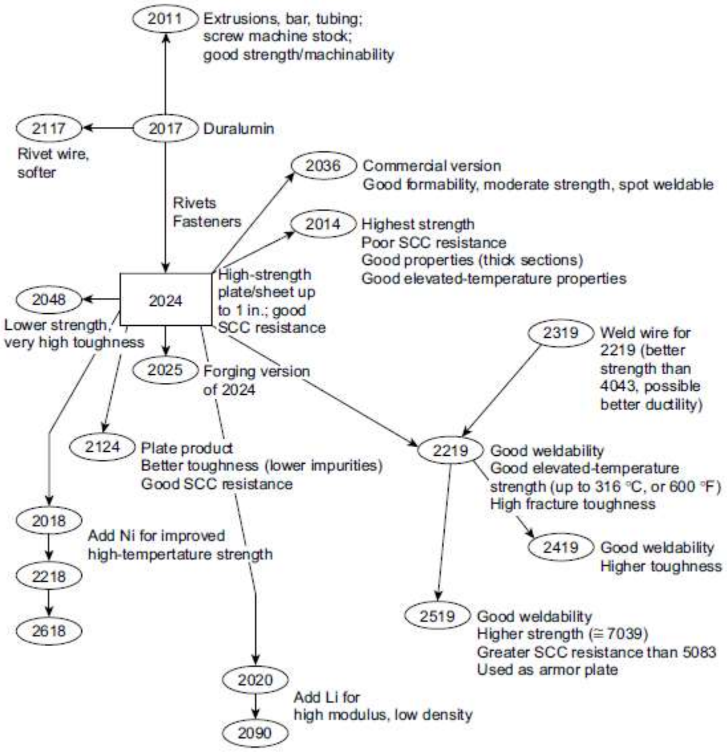

Fig. 1.7. The relationships between some of the more widely used alloys in the 2xxx series alloys [Davis et al., (2005)].

1.13 6xxx aluminium alloys

The 6xxx series alloys contain silicon and magnesium in approximately the proportions needed to form magnesium silicide (Mg_2Si), thus making them respond to heat treatment. Alloys of the 6xxx series have good corrosion resistance, formability, machinability, and weldability but are not as strong as most 2xxx and 7xxx alloys. This heat-treatable group of alloys can be developed in the T4 condition (solution annealed but not precipitation heat-treated) and then strengthened by precipitation heat treatment after forming to full T6 properties. 6xxx series alloys are suitable for the parts and the structures that require good formability and are mainly used to make automotive parts, hospitals, medical equipment, truck components, railroad cars, kitchen equipment, etc. The relationships between some of the more widely used alloys in the 6xxx series alloys are shown in Fig. 1.8 [Davis et al., (2005)].

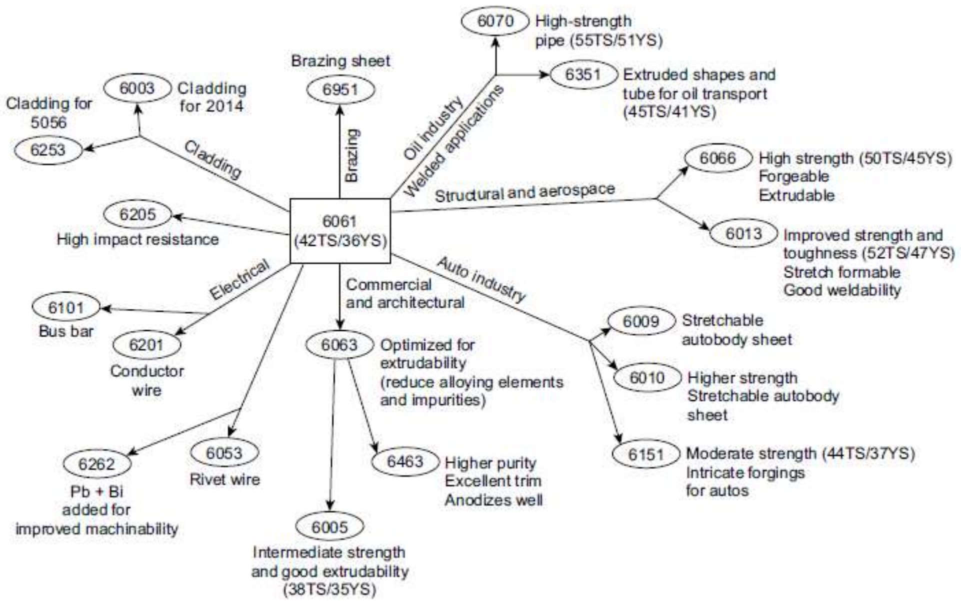

Fig. 1.8. The relationships between some of the more widely used alloys in the 6xxx series alloys [Davis et al., (2005)].

1.14 Definition of the problem

The present industrial and aerospace sectors focus on achieving grain refinement to get superior properties. Various researchers worked on equal channel angular pressing (ECAP), high-pressure torsion (HPT), and accumulative roll bonding (ARB), and friction stir processing (FSP) to produce the grain refined structure. Among those techniques, FSP is one of the best methods for achieving grain refinement in aluminium alloys. However, the frictional heat generated at the work-tool interface during FSP still exists in the plate. It causes the grain coarsening of stirred/refined material resulted in less grain refinement than expected. In the present study, various cooling media were used to eliminate the grain coarsening of already stirred/refined materials. However, the practicality of single-pass does not exist in practical applications because it produces a narrow stir zone of 4-10 mm. In order to make it useful for practical applications, authors conducted multi-pass FSP with pin overlapping to create the large-area stir zone. Very few studies are available on the production of large-area stir zone using FSP with the aid of cooling media. Hence, the present research aimed to produce the large-area stir zone in AA2014 and A6061 alloys using multi-pass overlapping FSP with the addition of cooling media and comparing their properties with single-pass FSP.

1.15 Research objective and approach

The present study explores the possibilities of incorporating various cooling methodologies to achieve the additional grain refinement in narrow stir zone of single-pass FSP and large-area stir zone of multi-pass overlapping FSP in aluminium alloys for various engineering applications. The specific objectives of the present investigation are as follows.

- To select the process parameters and tool geometry during friction stir processing of AA2014 and AA6061 alloys.
- To study the influence of cooling media in achieving grain refinement of AA2014 alloy using friction stir processing.
- To study the effect of microstructure and precipitate formation on mechanical and corrosion behavior of friction stir processed AA6061 alloy using different cooling media.
- To fabricate the large-area stir zone in AA2014 alloy via overlapping friction stir processing using different cooling media and explore the microstructure, texture evolution, mechanical properties, work hardening rate, corrosion, wear, and fatigue behavior processed alloy.
- To study the effect of cooling-assisted overlapping friction stir processing on microstructure, texture evolution, mechanical properties, corrosion, wear, and fatigue behavior AA6061 of alloy.
- To establish a novel relation between local and bulk mechanical strength of friction stir processed aluminium alloys.

1.16 Organization of thesis

The thesis was divided into five chapters: introduction, literature review, experimental procedure, results and discussion, and conclusions.

Chapter-1: This chapter briefly introduces severe plastic deformation techniques, friction stir processing, working principle of friction stir processing, and aluminium alloys and applications.

Chapter-2: This chapter reviews the most cited and recent literature on friction stir processing/welding, mainly focusing on various techniques used to achieve further grain refinement and production of large-area stir zone.

Chapter-3: This chapter presents the experimental methodology followed for conducting the friction stir processing and different characterization techniques to achieve the objective of the present work.

Chapter-4: This chapter contains the explanation of results and discussion of each objective under separate headings.

Chapter-5: This chapter contains the summary of conclusions of present work with possible remarks and future scope.

References

Publications

CHAPTER 2

LITERATURE SURVEY

This chapter summarizes the literature review of various aspects of friction stir processing/welding such as microstructure evolution, heat input influence, production of large-area stir zone, microstructure and texture aspects, corrosion and fatigue behavior, etc. And, the summary of overall literature studies and literature gaps are reported at the end of the chapter.

2.1 Microstructure evolution during FSP

FSP is a thermo-mechanical process that produces fine equiaxed grains in the stir region. Various processes such as localized softening, recovery, recrystallization, grain growth, re-precipitation, precipitate dissolution, and coarsening of precipitates can occur during the process. However, the dynamic recrystallization (DRX) process is thought to be responsible for grain refinement. Different types of dynamic recrystallizations have been suggested as the mechanism of grain refining during FSP of various aluminium alloys, such as continuous dynamic recrystallization (C-DRX), discontinuous dynamic recrystallization (D-DRX), geometric dynamic recrystallization (G-DRX), and dynamic recovery (DRV). In general, the grain refinement is not achieved solely either by dynamic recovery or by discontinuous-DRX. It is believed that grain refinement is achieved in SZ due combined effect of two mechanisms. Other than material properties, the stacking fault energy (SFE) and applied strain affect the restoration phenomenon strongly. When the processing temperature is above 0.6 T_{MP}, low SFE materials with FCC structures like Cu and Ni are restored by D-DRX. Thus, the D-DRX mechanism dominates all FCC materials' restoration mechanism except Al, as it has high SFE. In high SFE materials, DRV is the only restoration mechanism to achieve grain refinement in SZ. Unlike pure Al, Al alloys like AA2014 and AA6061 have alloying additions. These alloying additions try to lower the SFE of Al. In such cases, continuous-DRX (C-DRX) takes place. It was concluded that DRV and C-DRX are dominant restoration mechanisms in Al alloys. The microstructure evolution during FSP of aluminium alloys by DRV and C-DRX are explained as follows;

The DRV quickly happens in high stacking fault energy (SFE) materials such as aluminium under intense plastic deformation, leading to increased flow stress, dislocation density, and interaction. High SFE facilitates dislocation climb and cross slip, which are the primary mechanisms for recovery. The dislocation density increases as the DRV rate increases and these dislocations arrange themselves and convert into sub-grain boundaries (2-5^0). Dynamic equilibrium (DEQ) is achieved when the DRV rate reaches the maximum value. During DEQ, the sub-grains come together by observing more dislocations and convert into LABs (5-15^0). In general, DRV facilitates preferential nuclei sites for recrystallization to happen. It has been established that the formation of sub-grains depends on the Zener-Hollomon parameter and given by:

$$Z = \epsilon \exp(Q/RT) \qquad (2.1)$$

Where Q – activation energy, ϵ- strain rate, R- gas constant, and T- temperature [Humpreys et al., (2004)]. The equation is most commonly used in hot working methods where the strain rate and temperature are known. Later, C-DRX begins when the sub-grain size reaches a critical value. It should be mentioned that the restoration phenomenon during C-DRX is only sub-grains coalescence and rotation. So, further nucleation and grain growth are not occurred in C-DRX like DRV due to lowering the SFE by adding alloying elements. Due to low SFE, the dislocation climb and cross-slip during C-DRX are restricted compared to DRV. This restriction, in turn, causes restoration of energy, and this energy is utilized as a driving force to sub-grains coalescence and rotation, and finally resulted in the formation of fine dislocation-free grains. But at higher strain rates, C-DRX is also dominated when precipitates and/or alloying additions interfere with DRV. These precipitates and alloying additions act as nucleation sites for recrystallization to form a large number of equiaxed fine grains with HABs (beyond 15^0) in SZ of aluminium alloys, and this phenomenon is called particles stimulated nucleation (PSN). Other precipitation aspects affect the final grain size SZ of precipitation-hardened aluminium alloys (such as 2xxx, 6xxx, and 7xxx alloys). In precipitation-hardened aluminium alloys, the precipitates are fragmented into fine precipitates by stirring action of the tool during FSP, distributed uniformly in the matrix, and settled at grain boundaries. The precipitates settled at grain boundaries are pinned to grain boundaries. These fine precipitates can act as an obstacle for grain growth and migration and control the grain size; this effect is known as Zener-Pinning. This effect also shows the occurrence of C-DRX when DRV and D-DRX are restricted or prevented due to the dispersion of fine precipitates. G-DRX is somewhat different from C-DRX and D-DRX in terms of the deformation process. During subgrain boundary formation by G-DRX, the original grains are flattened (compression) or elongated (tension, torsion). Finally, when the grain thickness comes down to around two subgrain sizes, the grain boundaries come together to contact each other locally, allowing the grains to pinch-off and form newly separated grains [McQueen et al., (1998)]. G-DRX can be observed during DRV. When prior boundary separation equals subgrain size, which is connected to Z^{-1}, The boundary separation in the normal direction (d_n) during the hot rolling process is given by; $d_n = d_0 \exp(-\varepsilon)$, d_0 – initial grain size and ε - strain. Low strain rates and stresses result in a low Z value and the appearance of G-DRX. The DRV stage of deformation will last longer at high strain rates and stresses before G-DRX appears. During FSP, the stirring action of the tool causes the processed material to undergo severe plastic strains and stresses [McNelley., (2008) and Su et al., (2005 and 2011)].

Fonda et al., (2003) proposed the DRV as the primary mechanism for achieving grain refinement based on the development of FCC shear texture during friction stir welding of AA2195 Al-Li alloys by the stop-action method. Jata et al., (2000) suggested the C-DRX as a primary mechanism for the formation of refined grain structure due to existing subgrain rotation by dislocation absorption into subgrain boundaries. All of these mechanisms were based on observations of the stir zone microstructure. The path of microstructure evolution during FSP to form fine grains was not obvious. Rhodes et al., (2003) simulated the friction stir welding conditions of AA7075 alloy by tool penetration and extraction method followed by annealing heat treatment. They stated that D-DRX is the primary mechanism for achieving grain refinement of AA7075 alloys. Recently, Su et al., (2005 and 2006) examined the restoration mechanisms during the friction stir processing of aluminium alloys, and they identified grains of various dislocation densities and different degrees of recovery. They proposed that due to heterogeneous plastic flow, the multi-mechanism of DRV, C-DRX, and D-DRX act at different stages of microstructure evolution.

2.2 Heat input influence on grain refinement

It is well known that FSP is one of the best methods for achieving grain refinement in aluminium alloys. During FSP/FSW, the frictional heat is generated between the work-tool interface. The sufficient heat input combined with severe plastic deformation causes the dynamic recrystallization in the processed zone and results in the development of equiaxed fine grains. If the heat input is very less, the desired plastic flow is not achieved, and if the heat input is very high, the desired grain refinement is not achieved. Once the FSW tool left the stirred material during tool traveling, the frictional heat generated at the work-tool interface is still left in the material, and it causes the grain coarsening of refined grains and results in less grain refinement than expected. In order to avoid these difficulties, the heat input must be controlled/minimized during FSP/FSW by selecting optimum process parameters such as tool rotational and travel speed, selection of optimum tool geometry, performing multi-pass experiments, and using different cooling environments.

Sinhmar et al., (2019) conducted friction stir welding on Al-Cu alloy using seven different tool rotational and travel speed combinations to optimize the heat put. Four experiments were carried at constant tool rotational speed (i.e., 931 rpm with 13, 41, 70, 90 mm/min), and another three were carried out at constant travel speeds (i.e., 41 mm/min with 508, 708, 1216 rpm). They measured the peak temperature at all welding conditions and observed higher peak temperatures at higher tool rotational speeds and lower travel speeds. Microstructures of the welded zones were studied using an optical microscope and scanning electron microscope, and mechanical properties were measured using microhardness test and tension test. They found that increased tool rotational speed and decreased tool travel speed resulted in coarsening of refined grains and precipitates in the stir zone. Low rotational speed (i.e., 508 rpm at 41 mm/min) and high travel speeds (i.e., 90 mm/min at 931 rpm) resulted in maximum grain refinement and better mechanical properties due to optimized heat input.

Zhao et al., (2019) performed friction stir processing in AA6063 using eight different processing conditions at constant tool travel speed (i.e., 50 mm/min). The processing conditions includes different tool rotation speeds (i.e., 300, 500, 700,1000, 1200 rpm) and number of FSP passes (i.e., 1, 2). They found that the grain size in the stir zone increased from 300-700 rpm, the grains in the upper stir zones are coarser than that of grains in the bottom stir zones, and two-pass FSP resulted in coarser grain than single-pass FSP. The samples processed at low rotational speeds (i.e., 300-700 rpm) for both single and two-pass resulted in lower tensile strengths than the base alloy. They also detected a tunnel defect at the low rotational speed of 300 rpm. With increased rotational speed from 700 rpm, the increased heat input is sufficient to generate adequate material mixing in the stir zone and result in higher tensile strength than base alloy.

Abrahams et al., (2019) performed friction stir processing on AA5005 and AA7075 alloys. Trail experiments were initially conducted on AA5005 with three different tool geometries at different tool rotational speeds (i.e., 490, 970, 1200 rpm) to optimize the best pin tool design for conducting further experiments. The three different tool geometries include, square base pin with conical head (Tool-1), pyramid shape pin (Tool-2), and taper threaded pin profile (Tool-3), as shown in Fig. 2.1. They found insignificant defects for Tool-1 (at 970 rpm), large tunnel defects for Tool-II (at all rotational speeds), and defects-free structure for Tool-3 (at all rotational speeds). Then, using optimized tool geometry (i.e., Tool-3), they performed FSP on AA7075 at seven different combinations of rotational and travel speeds. After detailed property evolution, they stated that the travel speeds affect the mechanical properties of processed samples more than tool rotational speeds, and mechanical properties are enhanced with an increase in travel speeds.

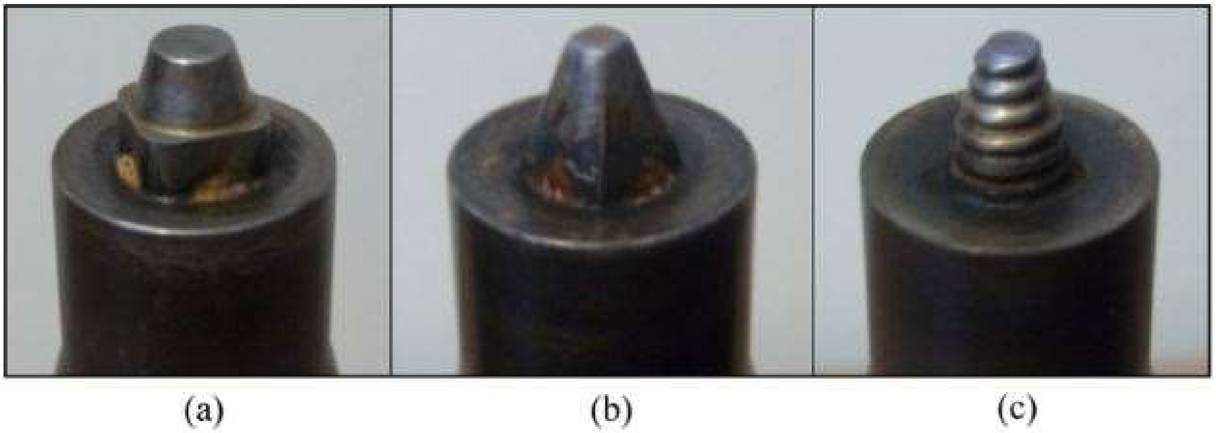

Fig. 2.1. FSP tool profiles (a) Tool-1, (b) Tool-2 and (c) Tool-3 [Abrahams et al., (2019)].

Sharma et al., (2012) performed FSW on AA7039 using three different cooling media, such as compressed air, liquid nitrogen, and water, to minimize the heat input and studied the influence of cooling media on microstructure and mechanical properties. The cooling assisted-FSW reduced the extent of weld joint softening, reduced the width of the stir zone and heat-affected zone, and achieved better grain refinement in the stir zone than normal FSW. In addition, the minimum grain size in cooling-assisted FSW resulted in better mechanical properties than normal FSW. Of all cooling conditions, superior mechanical properties were obtained in water-cooled FSW due to reduced dissolution of magnesium in the stir zone.

Heirani et al., (2017) conducted underwater FSW on AA5083 alloy using four different combinations of tool rotational speed (rpm) and welding speed (mm/min) along with normal FSW, and the processing conditions of each joint are listed in Table 2.1. The results indicated that water cooling caused a rapid cooling rate, depriving the grains of enough time to grow. As a result, the heat-affected zone (HAZ) vanished in the underwater FSW with a rotational speed and welding speed of 600 rpm and 30 mm/min. Furthermore, peak temperature in the weld nugget zone (WNZ) caused changes in the microstructure, resulting in completely different grain and precipitate sizes for each weld. It was observed that the hardness and tensile strength of underwater FSW plates were significantly higher than that of air-cooled welded plates caused by fine grain structure and reduced extent of precipitate dissolution.

Table 2.1 Different processing conditions for conduction of FSW [Heirani et al., (2017)].

Sample condition	Rotational speed (rpm)	Welding speed (mm/min)	Cooling condition
S-1	600	30	Ambient air
S-2	600	30	Underwater
S-3	800	40	Underwater
S-4	1000	50	Underwater
S-5	1250	63	Underwater

Rayes et al., (2012) conducted multi-pass FSP (one to three passes) with 100 percent overlapping at constant tool rotational speed (850 rpm) and three different welding speeds (90, 140, 224 mm/min) on AA6082 alloy. The schematic representation of one to three-pass FSP plate is shown in Fig. 2.2. The article addressed the microstructural features in terms of grain size and precipitate distribution and mechanical characteristics in terms of hardness and tensile behavior of processed samples in relation to the number of passes and welding speeds. FSP induced severe plastic straining and dynamic recrystallization of the stir zone, resulting in equiaxed, fine grains with high angle boundaries that increased with the number of passes. The accumulated heat from multiple passes caused grain coarsening, precipitates dissolution, and second-phase particle fragmentation. Besides, increasing the welding speed had no effect on grain size, but it reduced the size of the second-phase particle and increased their area fraction. The increase in the number of passes caused the softening of the processed zone and lowered the hardness and tensile strength, while the increase in welding speed resulted in increased hardness and tensile strength.

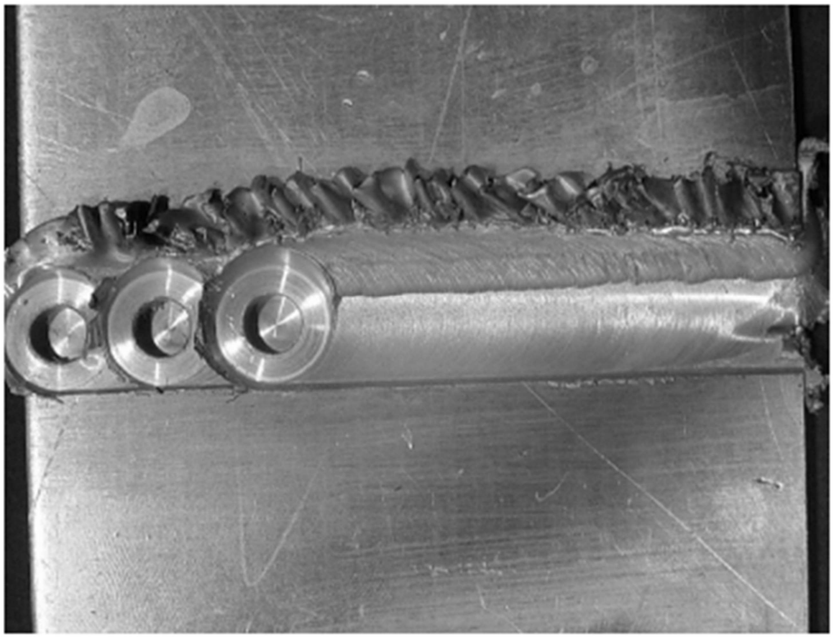

Fig. 2.2. Friction stir processed plate using one to three passes [Rayel et al., (2012)].

Elangovan et al., (2007) made an attempt to investigate the effect of various tool pin geometries (cylindrical, cylindrical threaded, taper cylindrical, square, and triangular pin) on friction stir processed AA2219 alloy at different rotational speeds (1500, 1600, 1700 rpm). The schematic representation of the different pin geometries is shown in Fig. 2.3. They observed that the defect-free structure was obtained at samples processed with square pin profile irrespective of rotational speeds; the samples processed at 1600 rpm yielded better mechanical properties regardless of pin geometries and superior mechanical properties obtained for sample processed at 1600 rpm with square pin profile. They also concluded that square pin geometry is the best tool for processing/joining 2xxx series alloys.

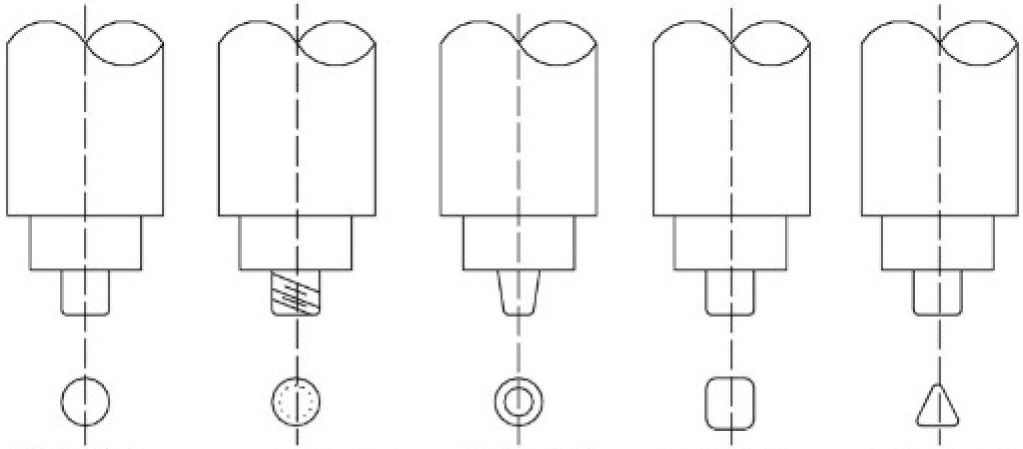
(a) Straight cylindrical (SC)
(b) Threaded cylindrical (TH)
(c) Tapered cylindrical (TC)
(d) Square (SQ)
(e) Triangle (TR)

Fig. 2.3 FSW tools with different pin geometries [Elangovan et al., (2007)].

Zhao et al., (2005) studied the different tool pin profile influence on material mixing and mechanical behavior of friction stir welded AA2014 alloy. They used four different pin profiles: cylindrical pin, cylindrical threaded pin, taper pin, and taper threaded pin, respectively, as shown in Fig. 2.4. The results revealed that defect-free structure, better material mixing, grain refinement, uniform precipitate distribution, and mechanical properties were obtained for taper threaded pin. Muthu et al., (2016) recently conducted friction stir welding on Al-Cu alloy with different pin profiles (taper pin, taper threaded pin, and whorl pin) and optimized taper pin as the best tool geometry for joining Al-Cu alloys based on the defect-free structure and joint properties.

Fig. 2.4. FSW tools with different pin profiles [Zhao et al., (2005)].

Liu et al., (2018) fabricated UFG structure in friction stir welded AA6061 alloy by minimizing the heat input. For reducing the heat input, they conducted FSW in three different conditions which include, 800 rpm with air, 800 rpm with water, and 400 rpm with water. In addition, they selected 400 rpm with water as a low heat input condition as it efficiently controlled the grain coarsening of refined grains, reduced the dissolution of the precipitate, and retained the dislocation density of friction stir welded AA6061 alloy.

Kwon et al., (2003) produced ultrafine-grained structure in AA1050 through FSP. They found that grain coarsening is effectively minimized by controlling maximum temperature and tool rotation rate. Saito et al., (2001) studied the mechanical behavior of ultrafine fine-grained AA1050 and discovered that the strength and hardness increased significantly due to grain refinement produced by FSP. Reza et al., (2016) tried to improve the surface integrity of AA5083 by incorporating ultra-fine grained surface layer and concluded that hardness is increased by 50% due to grain refinement after FSP.

Su et al., (2005) used a mixture of dry ice, water, and ethanol to quench the processing zone immediately after the tool traverse to produce ultrafine-grained structure in AA7075 and stated that sub-micron grains are generated with multi-pass FSP.

Sinhmar et al., (2017) investigated the mechanical and metallurgical behavior in FSW of Al-Cu alloy and reported that fine-grain microstructure with better mechanical properties was obtained by water cooling. They also found that water cooling improves mechanical properties.

Upadhyay et al., (2010) conducted FSW on Al-Zn alloy in water and cryogenic environment to study the influence of quench rate on properties. They reported that strength and elongations improved in water-cooled FSW.

Wang et al., (2020) recently studied the impact of various cooling technologies (air, water, and dry ice) on the FSP of Al-Cu alloy and found that dry ice FSP resulted in better grain refinement and mechanical properties than other media.

Feng et al., (2013) conducted the submerged FSP on AA2219 to evaluate the microstructure. He achieved ultrafine grain structure and observed that the grain size was decreased marginally in the stirred zone due to water cooling.

Chen et al., (2013) performed the three-pass FSP on AA5083 to produce more grain refinement. The results indicated that the rotational speed is responsible for grain size, and the grain size is increased with an increase in rotational speed.

2.3 Production of large-area stir zone using friction stir processing

Although most of the studies focused on single-pass FSP, limited publications are available on multi-pass overlapping FSP. Overlapping ratio, number of passes, and overlapping direction are crucial factors for achieving structural homogeneity in the processed layers.

A 12-pass FSP with 0.5 overlapping ratio was performed on AA5086 by Ramesh et al., (2012). They carried out two methods of FSP, continuous multi-pass FSP (CMP) and intermittent multi-pass FSP (IMP), and concluded that samples processed with IMP showed better properties than samples processed with CMP.

Su et al., (2005) performed 4-pass FSP on AA7075 with one-third pin overlapping, and the results were compared with single-pass FSP. They found that overlapping FSP yielded superior properties than single-pass FSP, and they concluded that this method could be applied to produce any size of the thin sheet with ultra-fine-grained structure.

Johannes et al., (2007) created a large area SZ in AA7075 alloy with 42% pin overlapping between consecutive passes and concluded that multi-pass FSP exhibited slightly lower elongation than single-pass FSP. They also reported that grain boundary sliding is a major strengthening mechanism to achieve super-plasticity behavior in multi-pass FSP.

Gandra et al., (2011) investigated the influence of overlapping direction by retreating side (RS) and advancing side (AS), as shown in Fig. 2.5. They reported that multi-pass overlapping is a promising technique to enhance mechanical properties, and overlapping with AS generates irregular surface finishing with uniform hardness throughout the homogenous SZ.

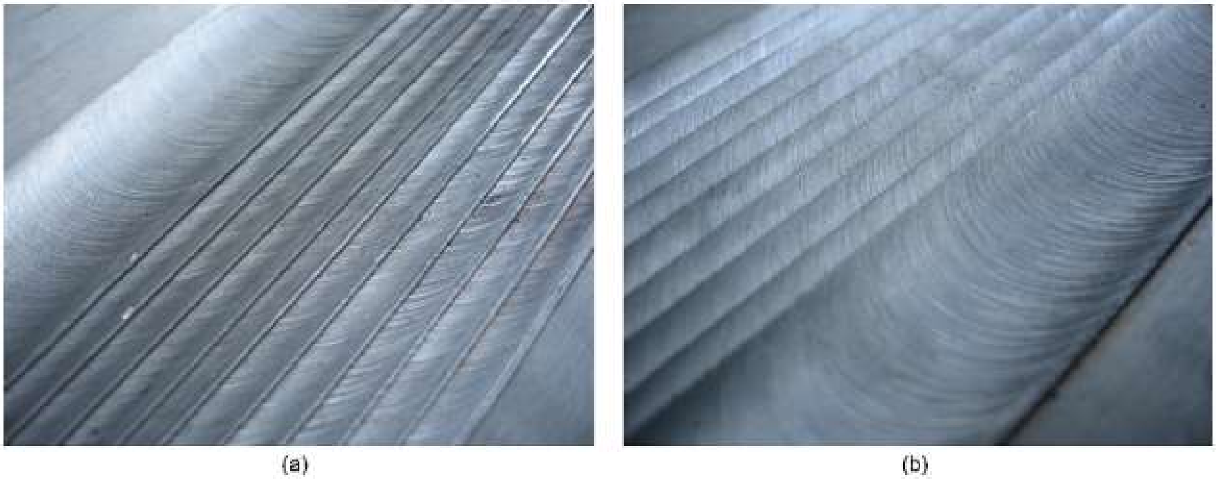
(a)

(b)

Fig. 2.5. Surfaces fabricated by multi-pass overlapping FSP by the (a) advancing side and (b) retreating side [Gandra et al., (2011)].

Khaled et al., (2014) investigated the influence of overlapping ratios, i.e., 0.25, 0.5, and 0.75, on microstructure, texture, and mechanical properties and stated that different overlapping ratios did not affect grain refining in the processing region. However, they also noted that the dissolution of strengthening precipitates caused by the increase of overlap ratio resulted in reduced strength and hardness.

A four-pass overlapping FSP was conducted on 1050 alloy by Kwon et al., (2003) and stated that it was possible to improve the tensile properties due to fine-grained structure development in bulk-area processed zone through FSP.

Similar studies were carried out on other alloys apart from aluminium alloys. Large area fine-grained structure in AZ31B alloy was processed by Venksateswarulu et al., (2013) with different overlapping ratios (OR) of 1, 0.5, and 0, and it was apparent that OR with 1 exhibited better strength and ductility due to better homogenization of alloy. Alavi Nia et al., (2014) performed overlapped FSP in two modes to create a large fine-grained area in AZ31B alloy. In the first mode, the overlapping was done parallel to the primary pass, and in the second mode, the entire overlapped region was overlapped perpendicular to the primary pass. They reported that strength and hardness improved in both modes while ductility improved only in parallel mode vis-a-vis raw material. Xue et al., (2013) fabricated large-area UFG pure copper using five-pass overlapping FSP with additional cooling media. The low magnification image of five-pass overlapping FSP is shown in Fig. 2.6 (where A, B, C, D, and E are overlapping passes). The microstructural analysis reported that overlapping FSP did not affect the grain size and the grain size was approximately uniform in all overlapping passes.

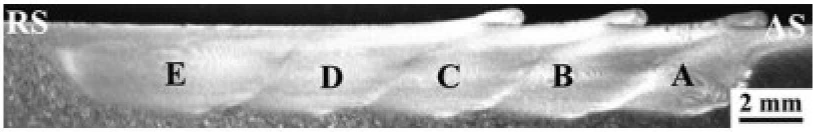

Fig. 2.6. Low-magnification image of 5-pass overlapping FSP [Xue et al., (2013)].

2.4 Microstructure and texture aspects of FSW/FSP

In the published literature, a significant amount of work was carried out on the microstructure and texture evolution of friction stir processed/welded alloys.

Suhuddin et al., (2010) used the stop-action technique to study the grain structure and texture evolution of friction stir welded Al-Mg-Si alloys. The microstructure evolution ahead of the tool probe was noted to be a complicated process involving geometrical strain effects as well as the creation of C-DRX and D-DRX at the same time. The material flow around the circumference of the tool probe was found to be governed by the simple shear plastic flow caused by probe rotation, which resulted in the development of {112}<110> texture component. Beyond the probe, the tool shoulder induced the additional hot deformation in the material, leading to the development of a fine recrystallization grain structure with a Cube texture component in the stir region.

Sarkari et al., (2019) studied the texture variations in friction stir processed AA1050 alloy. They reported that the Cube {001}<100> texture component present in the base AA1050 alloy was transformed into R-Cube {001}<110> texture component in the stir zone due to the shearing action caused by pin as shown Fig. 2.7.

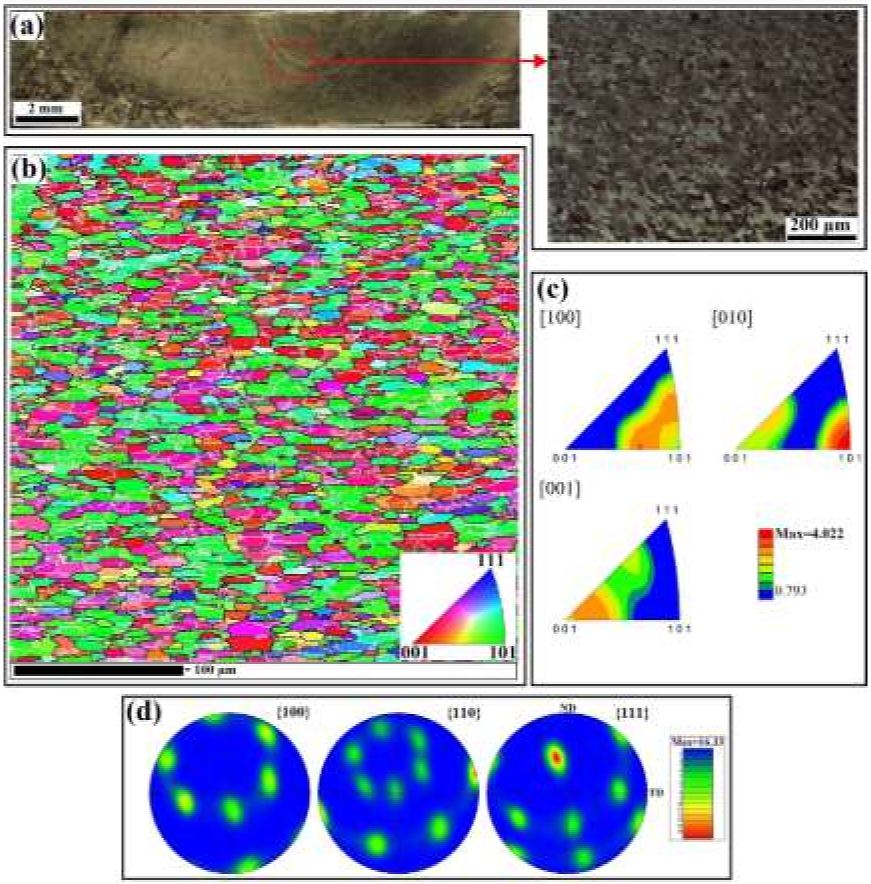

Fig. 2.7. (a) Optical low-magnification image indicating the stir zone, (b) EBSD microstructure, (c) Inverse pole figures, and (d) Pole figures of stir zone [Sarkari et al., (2019)].

Naresh et al., (2018) studied the microtexture and bulk texture evolution of single and multi-pass FSP of AA5086 aluminium alloy. They reported that the strain-induced boundary migration influences the texture evolution in the AA5086 alloy. The microtexture measurements along the stir zone revealed a variation in texture components due to thermal gradient, while the bulk texture measurement in the stir zone revealed the C texture component, and this component is retained after multi-pass FSP.

Khorrami et al., (2019) investigated the influence of cryogenic cooling media on texture evolution of friction stir processed pure aluminium alloy. They reported that abnormal grain growth caused by cooling media along with intense plastic straining resulted in the development of Cube {001}<100> and Goss {110}<001> texture components.

Khaled et al., (2014) performed the single-pass FSP with 100% overlapping on AA6063 alloy and studied the texture variation along processing zone from advancing side to retreating side with an interval of 1.5 mm (Fig. 2.8). The center of the stir zone (Position D) is characterized by strong Brass and Copper texture due to plastic flow and shear stresses induced by the pin. The other positions near Position D (i.e., B, C, E) consist of similar texture components with varied intensities. These results revealed that the texture component at the center and near the center of the stir zone is primarily affected by the pin's stirring action. On the other hand, the positions (A, F, G) near the thermo-mechanically affected zone revealed a Cube component due to additional hot deformation caused by the tool shoulder.

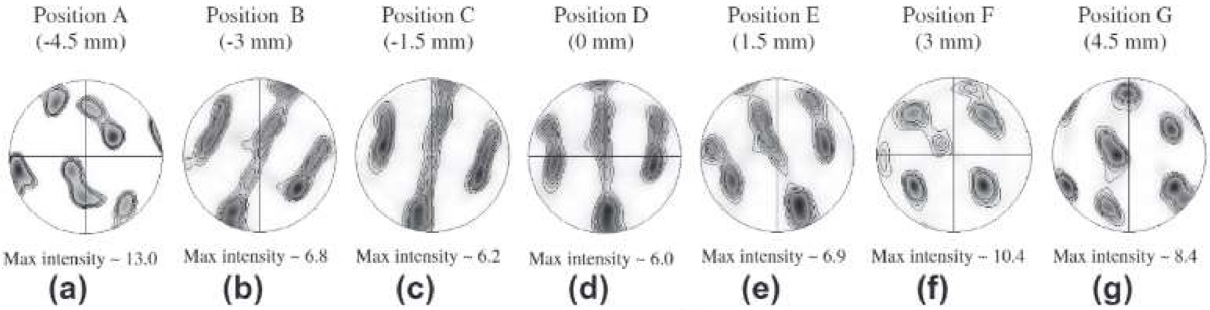

Fig. 2.8. Texture measurement across the processing zone with 1.5 mm interval [Khaled et al., (2014)].

Zhang et al., (2018) conducted friction stir processing on AA6061 alloy using the threaded tool to identify the texture components. They stated that the simple shear deformation caused by intense plastic flow and threaded features on the tool formed a Brass component.

Sato et al., (2001) measured the texture components in friction stir welded Al-Mg-Si alloy, and they reported that the simple shear deformation induced by stirring action of tool resulted in the development of {111}<110> texture component parallel to the tool pin surface of the cylindrical tool and along the welding direction.

Fonda et al., (2007) identified a banded kind of microstructure with different structural features in friction stir welding of AA2195 alloy. They also noticed the existence of Brass and Copper shear texture components in the weld zone.

Fonda et al., (2004) also used a stop-action technique to understand the microstructure and texture evolution during friction stir welding of Al-Li alloys. They stated that the refined structure is developed due to the dynamic recovery and recrystallization process. The texture components of recrystallized grains completely different from the FCC simple shear texture components.

Prangnell et al., (2005) also studied the microstructure evolution during friction stir welding of AA2195 alloy. They noticed that the refined grains were driven by the deformation region formed by the rotation of the tool pin at the outer periphery and the geometrical strain effects.

Ahmed et al., (2008) identified Brass, and Copper shear texture components in friction stir welded AA6082 alloy, and they reported that shearing action created by tool probe dominates the deformation conditions of stir zone.

Wang et al., (2015) used EBSD analysis to study the grain structure, and texture evolution of dissimilar friction stir welded AA5052-AA6061 aluminium alloys. They stated that dynamic recrystallization is the main factor in achieving grain refinement. They also identified that the S-{123}<634> and Cube-{001}<100> deformation texture components present in the base metal are transformed into the shear texture components after welding.

Chen et al., (2014) studied the microtexture development during the friction stir welded Al-Cu alloy. They identified four different texture components: Cube, Goss, Brass, and R-Cube in the weld nugget zone, heat-affected zone, and thermo-mechanically affected zone.

Yadav et al., (2012) carried out friction stir processing on pure Al alloy and studied microstructure and mechanical characteristics. They identified that FSP drastically reduced the grain size of base metal from 84 to 3 µm. Furthermore, the EBSD analysis done on the processed samples revealed dynamic recrystallization and various texture components in the stir zone. Yadav et al., (2011) made another attempt to study the microstructure of processed samples using a transmission electron microscope and EBSD. They identified the development of ultrafine grains with more fraction of high angle boundaries.

2.5 Effect of FSP/FSW on corrosion behavior

As we all know, corrosion affects the environment, industries, and most aspects of human activities. So, understanding the corrosion behavior is the primary step to develop and implement successful mitigation strategies. The microstructural evolution and precipitation phenomenon during FSP significantly affects the corrosion behavior of metal and alloys. Various researchers studied the corrosion behavior of friction stir processed aluminium alloys under different processing conditions.

Navaser et al., (2017) studied the pitting corrosion behavior of friction stir processed Al-Zn alloy at three different rotational speeds (630,1000,1600 rpm). The corrosion behavior was studied using immersion test, intergranular corrosion (IGC) test, open circuit potential (OCP), and Tafel polarization test in 3.5% NaCl solution and reported the following results. The immersion tests and IGC test revealed that the sample processed in all conditions subjected to pitting corrosion as well as intergranular corrosion. OCP test results demonstrated that the potential value of processed samples increased over time due to the formation of passive oxide film on the sample surface. Tafel test results stated that the rotational speed greatly impacted corrosion, and the corrosion attack increased with increasing rotational speed. Interestingly, the IGC attack was decreased with increasing rotational speed, and better less corrosion activity was observed for sample processed with 1600 rpm. The IGC attack of the samples processed at different rotational speeds is shown in Fig. 2.9.

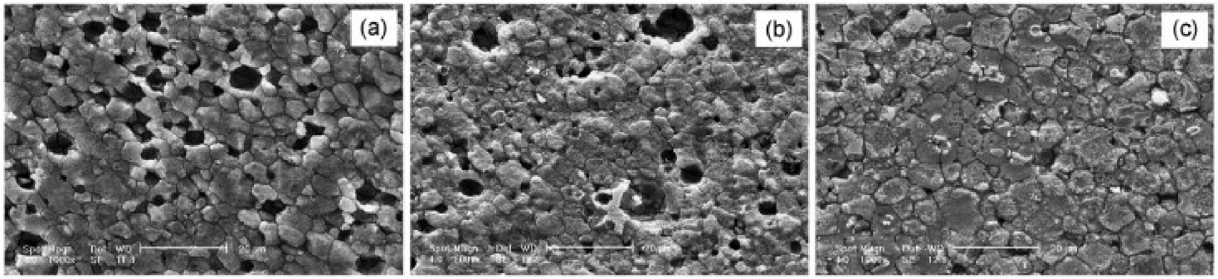

Fig. 2.9. Corroded surface of IGC test of friction stir processed samples at (a) 630 rpm, (b) 1000 rpm, (c) 1600 rpm [Navaser et al., (2017)].

The effect of different weld thermal cycles on electrochemical behavior friction stir welded Al-Cu was investigated by Sinhmar et al., (2019). Different weld thermal cycles were created by increasing tool rotational speed, keeping welding speed constant, and increasing welding speed by keeping the rotational speed constant. The corrosion behavior of all weld samples was investigated by cyclic polarization test and electrical impedance spectroscopy (EIS) test. Fig. 2.10&2.11 show the cyclic polarization and EIS maps of different welded samples in SZ and HAZ. They found that the corrosion resistance enhanced after FSW, and it is further enhanced by lowering the rotational speed and increasing the welding speed.

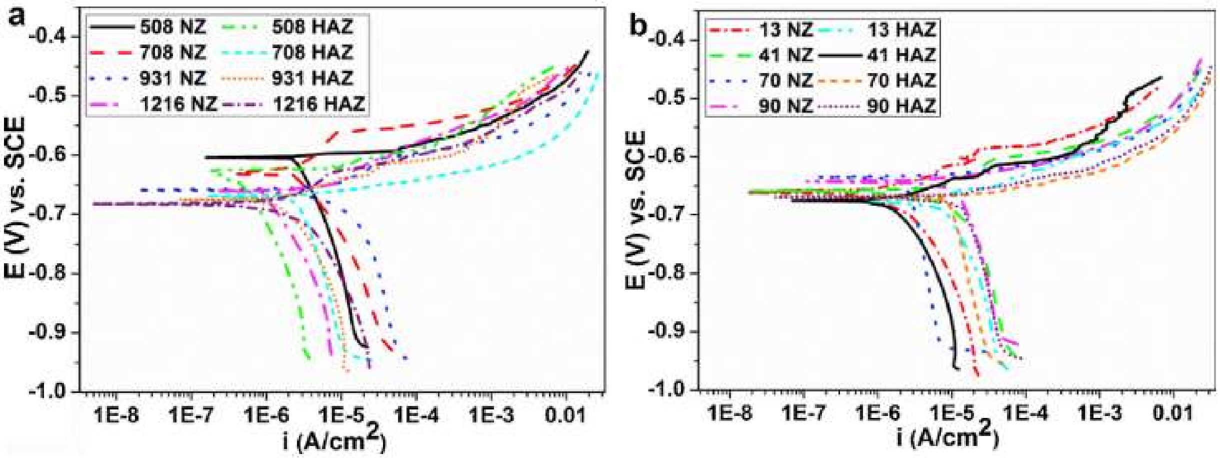

Fig. 2.10. Cyclic polarization curves of samples welded at (a) Constant welding speed and (b) Constant rotational speed [Sinhmar et al., (2019)].

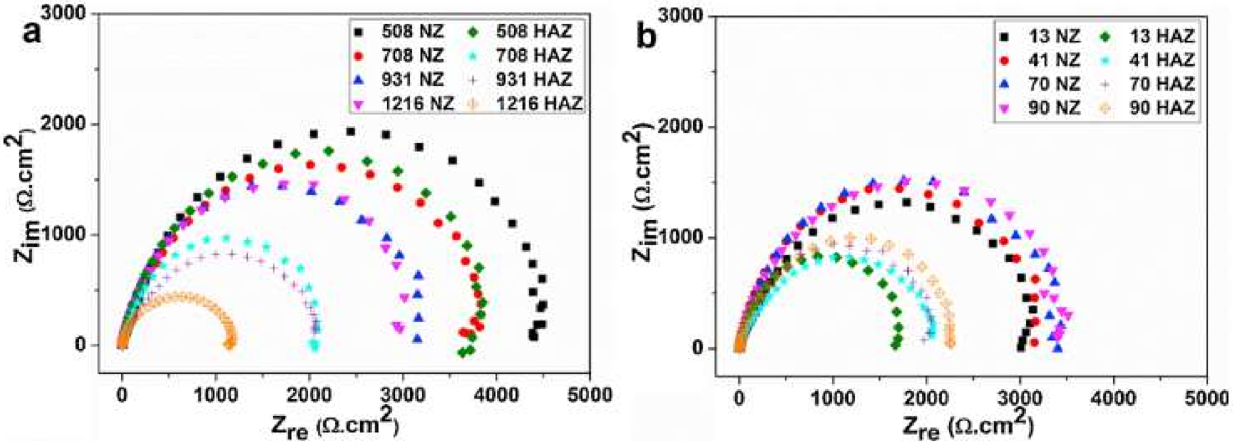

Fig. 2.11. EIS plots of samples welded at (a) Constant welding speed and (b) Constant rotational speed [Sinhmar et al., (2019)].

Xu et al., (2020) studied the influence of air and water cooling on the electrochemical behavior of friction stir welded thick AA2219-T62 joints. They measured the electrochemical behavior top, middle, and bottom cross-section of friction stir welded joint using immersion test, OCP test, and Tafel polarization test in chloride solution. The SEM and TEM were used to study the precipitate evolution during FSW. They reported that the stir zone of weld joints had more positive corrosion potential due to the formation of fine and uniform distribution precipitates and resulted in high corrosion resistance than HAZ and base metal. Compared to air-cooled FSW, the corrosion resistance was improved in water-cooled FSW due to refined grains and precipitates. On the other hand, the corrosion rate decreased from top to bottom of the stir zone due to thermal gradient and grain refinement variation. Finally, the microstructure results showed that the corrosion behavior of the AA2219 alloy depends on the size, shape, and distribution of precipitate particles. The TEM micrographs showing the size, shape, and distribution of precipitation of BM and FSWed joints are displayed in Fig. 2.12.

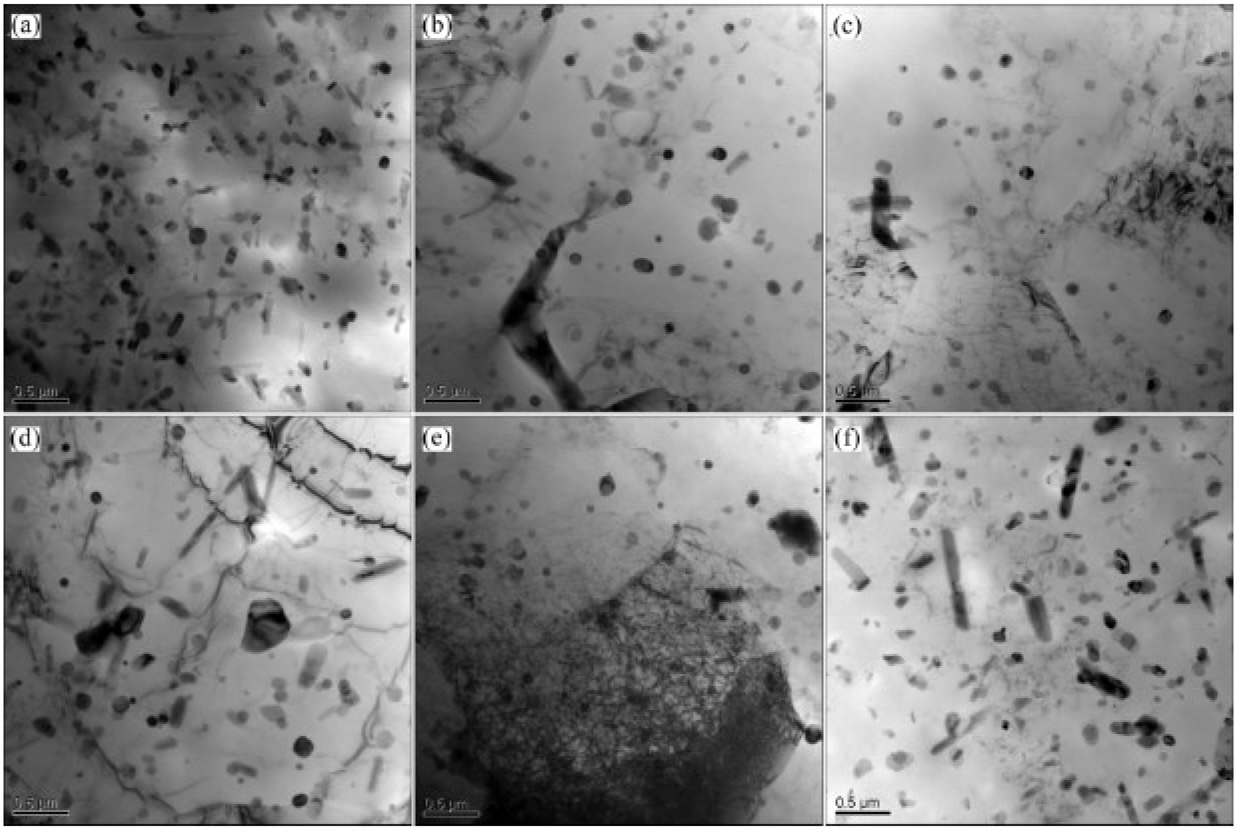

Fig. 2.12. TEM micrographs of (a) BM, (b) Top SZ, (c) Middle SZ, (d) Bottom SZ, (e) TMAZ and (f) HAZ [Xu et al., (2020)].

Qin et al., (2015) studied the corrosion behavior of FSWed AA2014 alloy using immersion test in EXCO solution for 0, 0.5, 1, and 2 hrs. They reported that corrosion attack and precipitate dissolution increased with an increase in immersion time. The corrosion resistance of FSWed alloy improved compared to parent alloy due to intense plastic straining and recrystallization.

The studies of Sinhmar et al., (2017) stated that corrosion resistance of AA2014 alloy significantly improved after FSW due to the presence of refined grains and less potential between Al matrix and the fine precipitates, and further conduction of FSW in cooling media resulted in enhanced corrosion resistance.

Xu et al., (2009) studied the effect of tool rotation rate on the corrosion behavior of friction stir welded 2219 aluminium alloy using Tafel and impedance spectroscopy test and concluded that the increase in tool rotation rate causes the coarsening of Cu intermetallics, leading to poor corrosion resistance.

In addition to these, various studies supported the improvement of corrosion resistance in Al alloys. But, few studies are contradicting the statements regarding corrosion resistance enhancement. These studies reported that fine grain structure formed after FSP consists of more fractions of grain boundaries, and these boundaries are vulnerable to corrosion attacks and result in reduced resistance to corrosion in FSP samples.

The influence of precipitate formation during FSW of AA2016-T8 on corrosion behavior was investigated by Meng et al., (2019). The precipitate evolution on the top surface of the joint was examined by scanning and transmission electron microscopes. In addition, the Tafel polarization test and alternative salt spray methods were employed to study the friction stir welded joints. They stated that the corrosion behavior of the weld joint depends on the precipitation phenomenon. Comparing to HAZ and TMAZ, the corrosion resistance of the nugget zone decreased due to the dissolution of Al_2Cu, Al_3Li, and Al_2CuLi precipitates. However, compared to air-cooled FSW, the corrosion resistance improved in water-cooled FSW due to forming refined grains and precipitates.

Gharavi et al., (2014 and 2016) studied the corrosion behavior of the friction stir welded AA6061 alloy using immersion test and Tafel polarization test in 3.5% NaCl solution at room temperature. Then, the morphology of the corrosion attack was examined by SEM. The corrosion findings revealed that the corrosion rate increased for welded samples due to coarsening of strengthening precipitates.

2.6 Effect of FSP/FSW on fatigue crack growth behavior

Ratnesh et al., (2019) studied the influence of the different cooling environments (air, water, and cryogenic media) and tool travel speed (100, 200, 300, and 400 mm/min) on fatigue crack behavior of friction stir welded AA5052-H32 alloy. With the use of different processing conditions (cooling media and tool travel speed), they designed 12 experiments. The results reported that the combination of cooling media and tool travel speed greatly influenced the heat input, which affected the fatigue crack growth rate. Furthermore, the lower heat input in underwater FSW resulted in reduced fatigue crack growth rate, while the formation of the oxide layer in the stir zone of cryogenic FSW caused a significant increase in fatigue crack growth rate. Along with the above findings, they also concluded that fatigue behavior depends not only on the heat input but other factors like microstructure and mechanical properties also significantly affect it.

Zhang et al., (2020) recently studied the microstructure, mechanical properties, and fatigue crack propagation rate of friction stir welded AA6061. The results indicated that the grain size and hardness, and strength of the weld nugget zone (WNZ) were smaller than that of base metal. The fatigue crack propagation rate was analyzed by plotting crack length (a) vs. number of cycles (N) and crack propagation (da/dN) vs. stress intensity factor range (ΔK). The results revealed that WNZ has better fatigue life than base metal as it experienced more fatigue cycles. From the fatigue fracture surfaces, they observed that striations and secondary cracks are dominant in the stable crack propagation region, while dimples are dominated in the rapid crack propagation region. They reported that fatigue crack propagation behavior also depends on particles present in the aluminium matrix and zonal heterogeneities in processed samples.

The fatigue crack growth response of the friction stir welded Al-Cu alloys was studied by Wedge et al., (2021). They stated that the fatigue crack growth response high toughness materials are influenced by plasticity induced crack closure (PICC). The precipitates present in the BM are dissolved during welding due to high-temperature exposure, leading to high elongation and low mechanical strength in the stir zone. However, the crack propagation is not hindered due to precipitate dissolution. Similarly, the grain refinement factor also influences the fatigue behavior according to the Hall-Petch equation. As the grain size decreases, the grain boundaries will hinder the crack extension. Such fine grains contributed to the high ductility and low strength in the stir zone. This combination provides an opportunity to hinder the crack extension rate due to PICC.

D'Urso et al., (2014) observed that the fatigue crack propagation rate in the stir region with refined grains is always lower than that in the base alloy. Jian et al., (2013) also identified that more refined grains created a high resistance to crack propagation. However, few studies show that fine-grained structure in the stir region deteriorates fatigue behavior and accelerates the crack extension rate. Dai et al., (2013) observed that smaller grains in the stir region have a higher crack extension rate than the base metal. The stir region can absorb high energies due to partial recrystallization, and they noticed the crack extension rate decreased after releasing the observed energy. Jata et al., (2000) advised that the rapid crack extension rate of the stir region was due to the intergranular fatigue fracture mechanism in the stir region.

2.7 Literature related to establishing a relationship between mechanical properties

Most of the studies on FSP/FSW have primarily focused on the enhancement of microstructure, mechanical properties, corrosion resistance, wear resistance, and fatigue behavior. Also, various studies correlated the microstructure of the processed region with mechanical properties, corrosion resistance, wear-resistance, and fatigue behavior to establish a suitable relation. The relation between hardness and strength of friction stir processed alloys has not been reported yet, but it was rarely reported in other processes. Njuke et al., (2019) established empirical relation between Rockwell hardness and tensile strength of medium carbon steel quenched in different cooling media, and they reported that it is possible to predict the tensile strength of quenched steel by using measured hardness values. Zhang et al., (2011) tried to generate a relationship between hardness and strength of three different materials; coarse-grained (CG) materials, ultrafine-grained (UFG) materials, and brittle bulk metallic glasses (BMG), and they concluded that the relation between hardness and strength depends on dislocation pile up and the shear deformation. Pavlina et al., (2008) gathered large data on non-austenitic hypo-eutectoid steels with different microstructures and a wide range of compositions. He successfully developed a linear relationship between hardness and strength using regression analysis over a wide range of data. Lu et al., (2013) also developed an empirical relation between hardness and tensile strength of laser beam welded Ti-6Al-4W joint, and they stated that the linear relations are applicable for prediction of strength in narrow welded and heat-affected zone based on the hardness measurements.

It is well known that the primary objective of FSP is to produce structural homogeneity in processed layers. After FSP, the homogeneous processed zone undergoes mechanical testing and other testing for evaluation of their properties. In mechanical testing, the homogeneous processed zone is tested for both localized and bulk mechanical strength. As reported in many studies, hardness (local strength) and tensile strength (bulk strength) are essential factors in engineering applications. But, the measurements of these two properties require different parameters. Localized mechanical testing includes hardness testing, where the indenter of hardness tester penetrates the material's surface for measuring local strength without fracturing the material. The tensile testing gives bulk strength of the processed region, and it measures the tensile properties such as ultimate tensile strength (UTS) and yield strength (YS) by fracturing a large volume of material. However, both hardness and tensile strength after FSP are decided by the degree of homogeneity and grain refinement. For testing the homogeneity of the processed zone, it is necessary to establish a linear relationship between hardness and tensile strength. In the case of surface composites processed via FSP, the relation between hardness and strength may not be valid as hardness along the processed region is not uniform because it varies drastically due to the presence of secondary particles. For friction stir processed materials without reinforcing, the hardness along the processed zone is approximately uniform, so it is necessary to establish a direct correlation between hardness and tensile strength to test the homogeneity of the processed region, and this relation is expected to be beneficial for practical applications.

2.8 Summary and literature gaps

From the overall literature, it was observed that a considerable amount of work has been done addressing the heat input influence on grain size and grain size influence on mechanical properties, corrosion behavior, and fatigue behavior of the samples processed using single or multi-pass FSP/FSW without overlapping. However, in the aspect of multi-pass FSP with pin overlapping, the work was scare concerned with single and multi-pass FSP without pin overlapping. Along with this, the following literature gaps also have been identified from the overall literature:

1. The literature studies on achieving grain refinement in friction stir processing of AA2014 and AA6061 are scarce.
2. Limited efforts have been made to study the influence of grain refinement on the corrosion behavior of friction stir processed aluminium alloys.
3. Only a few studies focused on the production of large-area stir zone using multi-pass overlapping FSP.

4. The cooling media is not utilized for achieving further grain refinement in overlapping FSP.
5. Systematic studies exploring the influence of overlapping FSP on all possible properties (texture, corrosion, wear, and fatigue) are required.
6. A novel relation should be made between local strength (hardness) and bulk strength (ultimate tensile strength and yield strength) of friction stir processed aluminium alloys.

CHAPTER 3

EXPERIMENTAL PROCEDURES

This chapter includes a detailed explanation of the experimental procedures of the current research work. Initially, FSP process parameters such as tool rotational and traverse speeds were selected from trail experiments based on the defect-free structure and better mechanical properties using the threaded pin profile tool. Then, with the optimized process parameters and cylindrical thread pin profile tool, single-pass FSP was conducted on aluminium alloys to achieve grain refinement in a narrow stir zone. Then, the authors used four different tool geometries for producing a large-area stir zone, including a cylindrical thread pin profile, for optimizing the best tool geometry based on better mechanical properties. The optimized process parameters and tool geometry were then used to investigate the influence of various cooling media for achieving grain refinement in aluminium alloys, which are outlined in Section 3.1. Then, the materials used, FSW machine setup, FSP processing conditions, cooling media description, microstructural examinations, mechanical properties, corrosion behavior, wear behavior, fatigue behavior, and other quantitative analysis have been described in Section 3.7–3.11, respectively.

3.1 Outline of experiments

Initially, feasibility examinations were carried out to produce the defect-free stir zone in AA2014 and AA6061 alloys. The FSP process parameters such a tool rotational speeds (w) were varied from 1000 rpm to 1200 rpm with a step size of 100 rpm, and tool traverse speeds (v) were varied from 25 mm/min to 35 mm/min with a step size of 5 mm/min for AA2014 alloy, respectively, whereas, tool rotational speeds (w) were varied from 700 rpm to 900 rpm with a step size of 100 rpm, and tool traverse speeds (v) were varied from 30 mm/min to 50 mm/min with a step size of 10 mm/min for AA6061 alloy. Besides, other processing conditions and tool geometry (thread pin profile) were kept constant throughout the trial experiments. However, the practicality of single-pass FSP is not found in applications as it produces a narrow stir zone. Therefore, multi-pass FSP with pin overlapping was carried out to create a large-area stir zone using optimized process parameters. For achieving better results, multi-pass FSP was conducted with different tool pin geometries such as threaded pin profile, square pin profile, hexagonal pin profile, and triangle pin profile. Furthermore, single-pass and multi-pass FSP were conducted in different cooling media with optimized process parameters and tool geometry to develop six sets of experimental investigations, summarized in Fig. 3.1.

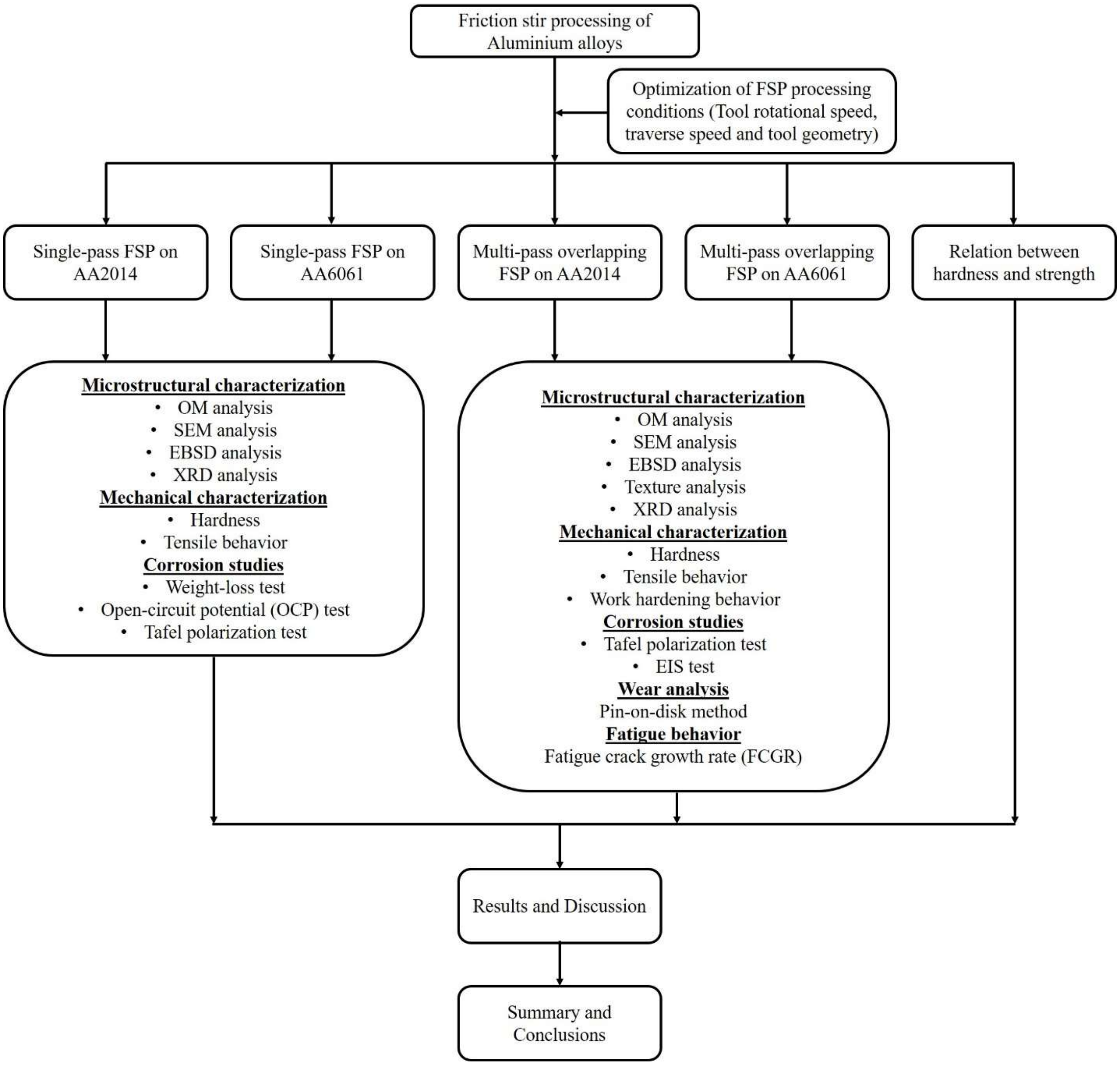

Fig. 3.1 Outline of work plan.

In experimental study 1, trail experiments were carried out to optimize the process parameters such as tool rotational speed, tool traverse speed, and tool geometry based on the defect-free structure and better mechanical properties. In experimental studies 2 and 3, single-pass FSP was conducted to achieve grain refinement on AA2014 and AA6061 alloys using different cooling media and investigated the microstructure, mechanical properties, and corrosion behavior of fine-grained alloys. In experimental studies 4 and 5, multi-pass overlapping FSP was carried out in different cooling media on AA2014 and AA6061 alloys to produce the large-area stir zone. In-depth investigations were carried out for experimental studies 4 and 5, including microstructure evolution, texture evolution, mechanical properties, work-hardening behavior, corrosion behavior, wear behavior, and fatigue behavior. Finally, a novel relation was established between the hardness and strength of friction stir processed aluminium alloys in experimental study 6.

3.2 Selection of base materials and tool materials

Cold-rolled plates of AA2014-T6 and AA6061-T6 aluminium alloys opted as base metals for the present study. Base metals were sectioned into 280x120x4 mm and 280x120x6 mm plates for friction stir processing. The detailed chemical compositions of base metals are documented in Table 3.1&3.2.

H13 tool steel is suitable tool material for joining/processing aluminium alloys, selected from the literature sources [Mishra and Mahoney (2007)] because it has high wear resistance, high fracture toughness, high coefficient of thermal expansion, and can withstand strength at elevated temperatures. The chemical composition of the H13 tool material is listed in Table 3.3.

Table 3.1 Chemical composition (Wt. %) of AA2014-T6 alloy.

Element	Al	Cu	Si	Mg	Mn	Fe	Zn	Cr	Ti
Wt. %	Remainder	4.26	0.69	0.80	0.64	0.23	0.17	0.03	0.02

Table 3.2 Chemical composition (Wt. %) of AA6061-T6 alloy.

Component	Al	Mg	Si	Cr	Cu	Fe	Mn	Ti	Zn	others
Wt. %	Remaining	1.1	0.6	0.18	0.2	0.6	0.1	0.1	0.18	0.15

Table 3.3 Chemical composition (Wt. %) of H13.

Element	Cr	Mo	C	Mn	P	Si	S	V
Wt. %	5.3	1.31	0.38	0.41	0.02	1.06	0.02	1.10

3.3 Friction stir processing machine details

The FSP experiments were conducted on numerically controlled 3-Ton capacity FSW machine developed R.V Machine Tools, Coimbatore, India, shown in Fig. 3.2. The essential components of the FSW machine include spindle motor, servo motor, table with fixture, force and position controller, lubrication system, and data acquisition (DAQ) system. The specifications of the FSW machine are shown in Table 3.4.

Fig. 3.2. Friction stir welding machine.

Table 3.4 Specifications of 3-Ton capacity FSW machine.

S. No	Details	Specifications	S. No	Details	Specifications
1	Z-axis load	50 kN	11	Spindle motor	AC Induction motor 11kW/3-phase/1400RPM/440V

2	Z-axis stroke length	300 mm	12	Tool holder	ISO 40 Arbor
3	Z-axis rate of movement	0-1000 mm/min	13	Mode of control	Position and force control
4	X-axis load	25 kN	14	Spindle head tilt	$\pm 5^0$ (Manual)
5	X-axis stroke length	400 mm	15	Machine size	1350x1750x2290 mm
6	X-axis rate of movement	0-1000 mm/min	16	Table size with thread holes	500x400 mm
7	Y-axis load	Manual	17	Load cell	X and Z-axis
8	Y-axis stroke length	200 mm	18	X-axis drive	Servo with gearbox
9	Lubricating system	Centralized and manual	19	DAQ & Analysis Software	Spindle speed, axis velocity against time, and force
10	Spindle speed	3000 RPM (Max)	20	Spindle torque	75 N-m @ 1400 RPM

3.4 Selection of tool geometry

In this present study, FSP was carried out in two ways on AA2014 and AA6061; 1. FSP using single-pass and 2. FSP using multi-pass overlapping FSP.

3.4.1 FSP using single-pass

Initially, trial experiments were conducted to optimize the process parameters such as tool rotational speed and traverse speed. Then, with the use of optimized processed parameters, single-pass FSP was performed on AA2014 and AA6061. These experiments were performed in order to compare the properties of single-pass FSP with the properties of samples processed with multi-pass overlapping FSP. For this, a taper cylindrical threaded pin profile was used. The tool geometry comprises a 24 mm shoulder with taper cylindrical threaded pin with 3.7 mm length and 8 mm diameter at the top and 6 mm diameter at the bottom. The tool geometry is shown in Fig. 3.3. The schematic representation of single-pass is shown in Fig. 3.4.

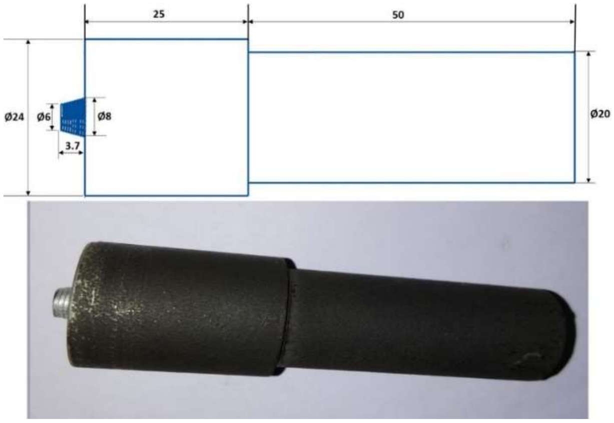

Fig. 3.3. H13 tool with geometry (All dimensions are in mm).

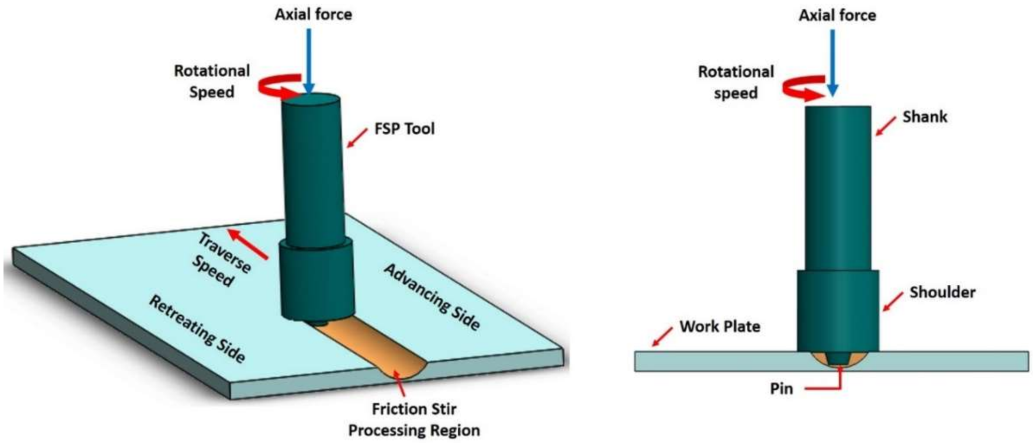

Fig. 3.4. Schematic representation of friction stir processing.

3.4.2 FSP using multi-pass overlapping method

In most of the studies, the stir region (SZ) is prepared using single-pass FSP. Generally, the pin diameter varies from 4 to 8 mm, producing the SZ of the same diameter with single-pass FSP. Such kind of narrowed SZ is not used for practical applications. To overcome this difficulty, the large-area SZ of the required size is prepared by several consecutive passes with the pin overlapping, as shown in Fig. 3.5. The overlapping FSP aims to prepare larger surface areas to achieve homogenous microstructure and enhanced superplasticity. Similar conditions for each pass are essential to assuring homogeneous properties throughout the processed zone.

For overlapping FSP, the overlapping ratio is the primary factor to decide the distance between the successive paths. There are different overlapping ratios from 0-1, which are considered for performing overlapping method, but the frequently used overlapping ratios are 0, 0.25, 0.5, 0.75, and 1. Overlapping FSP with 0 overlapping ratio is not possible practically. In 0.25 overlapping ratio, the final bulk-area processing zone is subjected to 4-pass multi-pass. From the literature source of FSP, it was concluded that multi-pass FSP up to 2-pass enhance the grain refinement and further increase in the number of passes causes grain coarsening. Overlapping with 0.75 overlapping ratio can produce a bulk-area stir zone, but surface homogeneity is not achieved as each region is subjected to different number of passes. Overlapping with 1 overlapping ratio creates a homogeneous single-pass bulk area stir zone. As it creates the bulk area stir zone with single-pass, further grain refinement is not achieved. It is well known that the advancing side is the weakest zone in the FSP sample as it is subjected to more deformation. So, in order to eliminate the advancing side and achieve further grain refinement, FSP with 0.5 overlapping ratio was chosen as suggested by various authors [Ramesh et al., (2012), Gandra et al., (2011), Alavi Ni et al., (2014) and Nascimento et al., (2009)]. An overlapping length between two successive paths (L) was calculated using the overlapping ratio (OR), which is given by [Gandra et al., (2011)].

$$OR = 1 - (L/D) \tag{3.1}$$

D is the diameter of the pin, and L is the distance between the central axis of successive tracks (3 mm). In the above equation, L = 3 mm was used to obtain the uniform large-area SZ uniform material thickness. Next, the 5-pass overlapping FSP was performed by eliminating AS. After successful completion of each pass, the tool was advanced towards AS with an increment of 3 mm, and the processing was performed along the same direction as rolling was done before FSP.

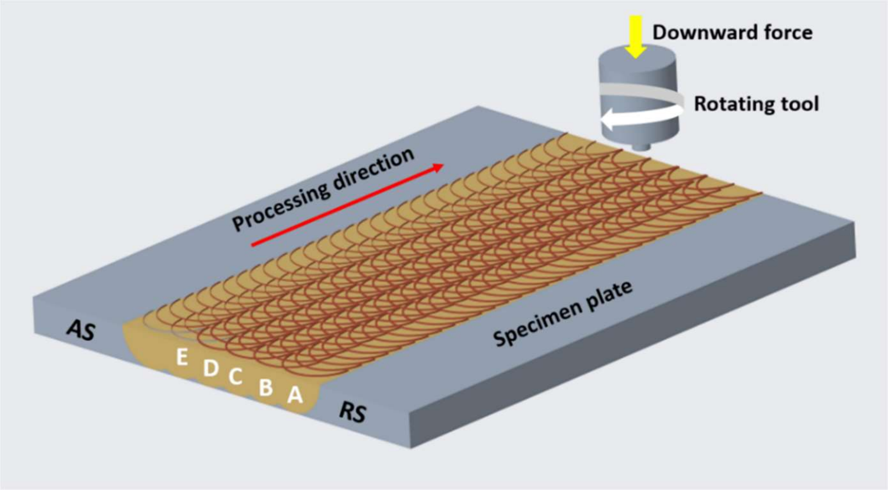

Fig. 3.5. Schematic diagram of 5-pass overlapping FSP.

For overlapping FSP, different tool pin profiles were used to optimize the best tool geometry based on the better mechanical properties. Four different tool pin profiles were selected as suggested by Kishore and Kumar (2018); H13 tool with I. Square pin profile, II. Hexagonal pin profile, III. Cylindrical threaded pin profile and IV. Triangle pin profile. The tool geometry of all tools comprises 18 mm diameter shoulder with 6 mm diagonal/diameter pin profile and 5.5 mm pin length as shown in Fig. 3.6. Detailed optimization of process parameters and tool geometry is given in Chapter 4.1.

Fig. 3.6. Tool profiles with schematic representation.

3.5 FSP in different cooling media

With the use of optimized process conditions, FSP was carried out in two different cooling media (i.e., cryogenic and water cooling). A simple pictorial description of the cooling arrangements is shown in Fig. 3.7. Initially, FSP was carried out under ambient conditions (i.e., without cooling media) to compare with cooling assisted-FSP (Fig. 3.7a). During cryogenic FSP, the processing zone was rapidly cooled by a mixture of dry ice and ethanol by applying them on the processed zone immediately after the tool leaving the stirred material (Fig. 3.7b). Water-cooled FSP was conducted using limited in-house facilities. A water-cooled setup was designed and fabricated according to the table dimensions of the FSW machine. The base of the setup was made of aluminium alloy sheet of thickness of 2 mm, while the sides of the setup were made of transparent fiber sheet, and both of them were attached using silicone gel. To make the joint between the metallic and fiber sheets**,** clay was added near the joint. During water-cooled FSP, the water is circulated manually to maintain the constant temperature throughout the process. Clay was applied at the intersection of the table and aluminium alloy sheet to avoid water leakage, as shown in Fig. 3.7c. For the same set of conditions, FSP in ambient atmosphere, cryogenic media, and water media were denoted as air-cooled FSP (ACFSP), cryogenic-cooled FSP (CCFSP), and underwater FSP (UWFSP), respectively.

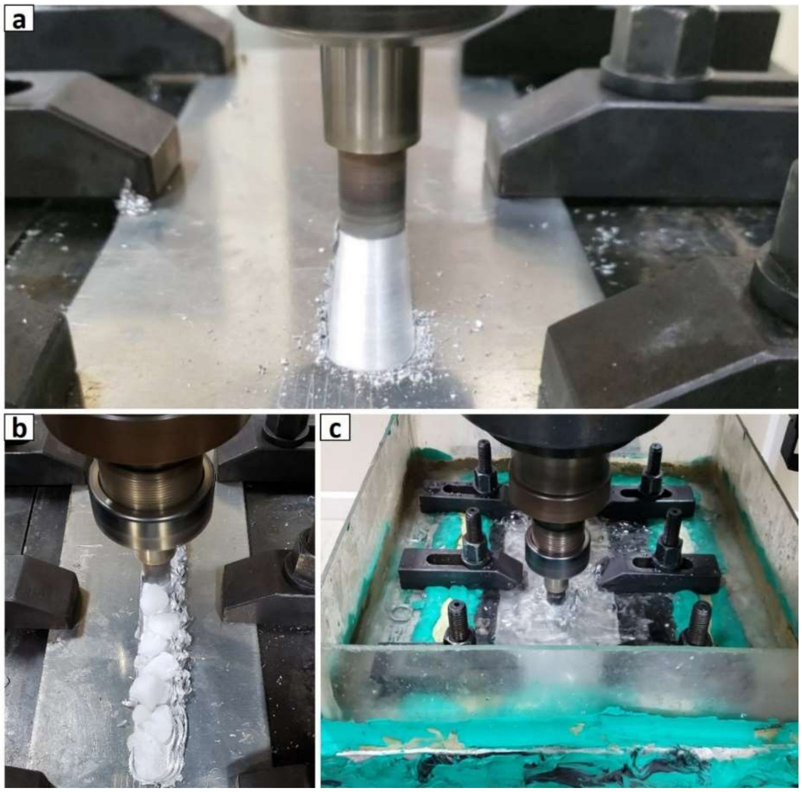

Fig. 3.7. Pictorial view of (a) Air-cooled FSP, (b) Cryogenic-cooled FSP, and (c) Underwater FSP.

3.6 Metallurgical examination

3.6.1 Sample preparation

Samples for microstructure analysis were sectioned transversely to the processing direction with an abrasive diamond saw to the required dimensions. For easy handling, the samples were mounted in a hydraulic mounting press using Bakelite powder. The mounted samples were then ground well with different grades of silicon carbide papers of 80, 120, 220, 400, 600, 800, 1000, 1200, 1500, 2000 grit sizes, followed by disc polishing on velvet cloth using alumina suspension and diamond paste to get the mirror-like surface. After polishing, the samples were washed thoroughly with a water jet to remove the contaminants and dirt present on the polished surface and then dried. The dried samples were then etched in a Keller's solution (190 ml distilled water, 5 ml HCL, 3 ml HNO_3, and 2 ml HF) to reveal the grain morphology. The etching time of 10 s for AA2014 and 150 s for AA6061 optimized after series of trials. After etching, the samples were kept under fully-opened tap water to wash out the etchant presents on the aluminium matrix. The etched samples were then examined under different advanced metallurgical microscopes, including Optical Microscope (OM), Scanning Electron Microscope (SEM), and Electron Backscattered Diffraction (EBSD) along with X-ray diffraction (XRD) to reveal the various metallurgical features of friction stir processed samples.

3.6.2 3D Optical Microscope (OM)

3D Optical Microscope (Model-HRM 300 developed by Huvitz, South Korea) has been employed for macrostructure and microstructure investigations at low to high magnifications, respectively, according to ASTM E407 and E381 standards. The photograph of the 3D optical microscope is shown in Fig. 3.8.

Fig. 3.8. 3D Optical microscope.

3.6.3 Scanning Electron Microscope (SEM)

The studies such as precipitation phenomenon, fracture morphology, and the corroded surface morphology of friction stir processed samples were conducted using VEGA 3 LMU model (developed by Tescon, Czech Republic) high-resolution scanning electron microscope with energy dispersive spectroscopy (EDS) feature to suggest the precipitate phases based on the chemical composition. The photograph of SEM is displayed in Fig. 3.9.

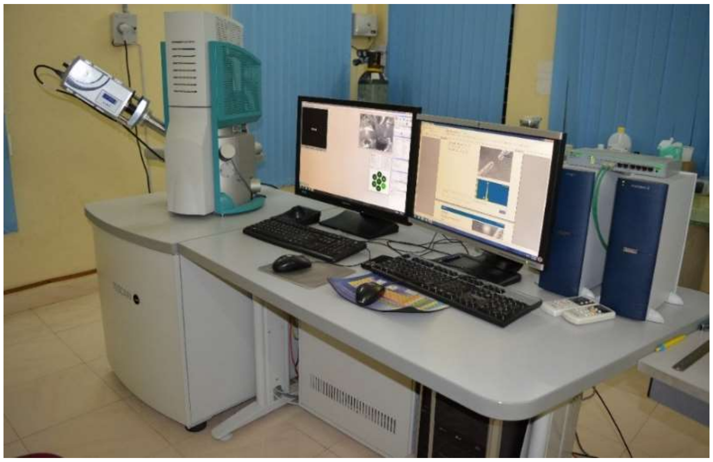

Fig. 3.9. Scanning Electron Microscope.

3.6.4 Electron Backscattered Diffraction

The samples for EBSD analysis were electro-polished in a mixture of perchlorate with acetic anhydride and methanolic solutions of sulfuric acid in Struers Lectropol electropolisher at -10^0 C for 30 s. EBSD was conducted using FEI Quanta 200 HV scanning electron microscope equipped with TSL-OIM software with a step size of 1 μm for base metal and 200-250 mm stir zone of FSP samples. The microstructural features such as grain size distribution, fraction of high angle grain boundaries (HABs) and low angle boundaries (LABs), fraction of recrystallized boundaries, pole figures, and orientation distribution functions (ODF) were extracted using TSL-OIM software.

3.6.5 X-ray diffraction (XRD)

The suggested precipitate phases in SEM analysis were confirmed using 'CuKα radiation-assisted X-ray diffraction. XPERT PRO model (Make: PANalytical, Netherlands) X-ray diffraction was employed to analyze the stir zone of friction stir processed samples. The image of X-ray diffraction is shown in Fig. 3.10. X'Pert High Score software was used to analyze the XRD results.

Fig. 3.10. X-ray Diffraction equipment.

3.7 Mechanical characterization

3.7.1 Hardness test

Vickers microhardness tester (Model – ECONOMET VH-1, Make-Chennai Metco, Chennai) was employed to measure the microhardness using 100 gf load and 15 s dwell time. Hardness was measured across the transverse mid-section of the processing zone with an interval of 0.5 mm. The photograph of the hardness tester is displayed in Fig. 3.11.

Fig. 3.11. Vickers microhardness tester.

3.7.2 Tensile testing

For tensile testing, the samples with 18 mm gauge length, 3.5 mm width, and 3 mm thickness were sectioned in the stir region along the FSP direction using wire-cut EDM according to ASTM-E8 standards as shown in Fig. 3.12. Then, tensile tests were conducted at ambient temperature on a computer-controlled electromechanical universal testing machine (Model: 300 LX Make: INSTRON, USA) with a 0.25 mm/min crosshead speed. The image of the testing machine is shown in Fig. 3.13.

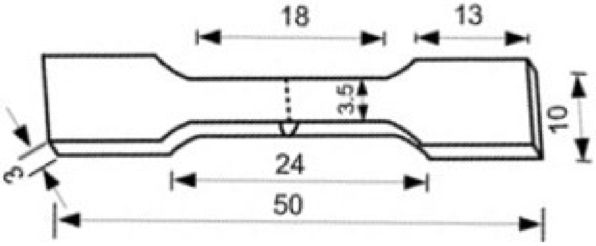

Fig. 3.12. Dimensions of the tensile sample [Sunil et al., (2019)].

Fig. 3.13. Universal testing machine.

3.8 Corrosion behavior

The corrosion behavior of BM and FSP samples was studied in a 3.5% sodium chloride (NaCl) electrolytic solution using weight-loss, Tafel polarization and electrochemical impedance spectroscopy (EIS) test. The corrosion tests were conducted according to ASTM G3 standards.

3.8.1 Weight-loss test

The samples used for the weight-loss test were extracted from the stir zone of processed samples. Before commencement of the weight-loss test, the samples were polished to remove the contaminates and weighed. The samples were immersed in the electrolytic solution for 20 days at ambient temperature. Later, the immersed samples were thoroughly cleaned with distilled water, dried, and re-weighed to measure the corrosion rate. The corrosion rate was measured from the weight-loss method given by CR = 534 (W/DAT). Where, CR – corrosion rate (mpy), W-weight loss (mg/inch^2), A-exposed area, D-density (g/cm^3) and T-immersion time (hours)**.** The samples were then investigated under an optical microscope to assess the rate of corrosion attack.

3.8.2 Tafel polarization test

The Open-circuit potential (OCP) test and Tafel polarization test were conducted using a 3-electrode cell potentiostat (Make: CH Instruments, USA, Model: 604e) as shown in Fig. 3.14. Open circuit potential (OCP) test was initially performed to set the potential range for the Tafel polarization test. Then, the Tafel polarization test was performed on the top region of FSP samples in electrolyte solution. The samples were polished to 1 μm and exposed to electrolytic solution through a hole of 0.15 cm^2 area. A 3-electrode system used platinum electrode as auxiliary electrode, FSP sample as work electrode, and saturated calomel electrode as reference electrode. The open-circuit potential (OCP) test was performed for 600 s before the commencement of the Tafel polarization test. The potential range was kept between -0.5 V to +0.5 V for the OCP test, and the scan rate of 1 mV/s was given for the Tafel polarization test. The OCP and Tafel polarization tests were conducted at ambient temperature. Then, the exposed samples were examined under SEM.

3.8.3 Electrical impedance spectroscopy (EIS) test

EIS is the most promising and accurate non-destructive electrochemical technique to assess corrosion behavior. The information provided by the EIS technique is more comprehensive and in-depth than the information generated by the Tafel polarization technique. EIS test was also performed using a 3-electrode cell potentiostat (Model: PARSTAT 4000). EIS test was performed at frequency range and AC amplitude voltage of 0.01 Hz to 10 kHz and 10 mV, respectively. Gill AC Weld Tester Serial No 1339 software was used to analyze the Tafel and EIS test data.

Fig. 3.14. Electrochemical work-station.

3.9 Wear behavior

The samples for the wear test were extracted from the stir zone of the processed samples. Dry sliding wear test was employed on the pin on disk tribometer as per ASTM-G99 standards. The process parameters such as load, sliding velocity, and siding distance were kept at 20-40 N, 1 m/s, and 250-1000 m, respectively. To assess the progress of wear, wear experiments were interrupted at precise intervals (i.e., at 250 m). At each interval, samples were washed in acetone and weighed to an accuracy of 0.1 mg. A hardened steel disk (HRC58) of 160 mm diameter was used as the counter-face material. The surface roughness of the disk was kept between 0.5 and 1 m. The image of the wear testing machine is shown in Fig. 3.15.

Fig. 3.14. Wear testing equipment.

3.10 Fatigue behavior

Compact tension (CT) specimens were prepared and tested to measure fatigue crack growth rate (FCGR) of processed samples as per ASTM-E647 standard are shown in Fig. 3.16a. Since the surface asperities such as weld flash, tool marks, and other surface irregularities created during the FSP process could affect fatigue crack initiation at the notch, the surface of the CT specimen was ground with emery papers to assure a clean and flat surface. The photograph of the prepared CT specimen is depicted in Fig. 3.16b. FCGR test was conducted under constant force amplitude at ambient temperature on fatigue testing machine (Model: UT-04-0100 MEDIAN 100, Make: BISS, Bangalore, India, frequency range – 15 Hz, capacity-100 kN) with a stress ratio (R) of 0.1 at a frequency of 10 Hz. The photograph of the fatigue testing machine is shown in Fig. 3.17. Crack propagation was continuously measured by the compliance method with a COD (crack opening displacement) gauge. The fractured CT specimens were then investigated under SEM.

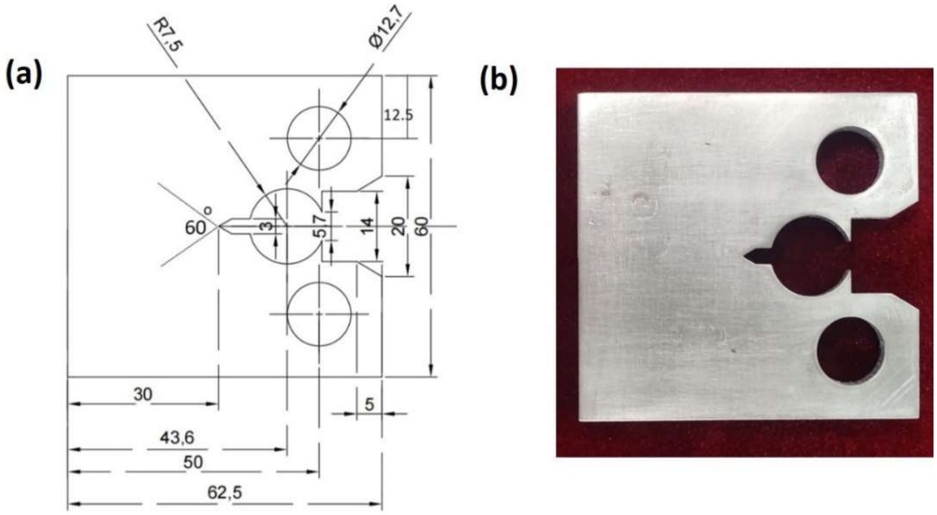

Fig. 3.16. (a) Dimensions of fatigue sample and (b) Photograph of fatigue testing specimen.

Fig. 3.17. Fatigue testing machine.

CHAPTER 4

RESULTS AND DISCUSSION

4.1 Selection of process parameters and tool geometry during friction stir processing of AA2014 and AA6061 alloys

The tool rotational speed, traverse speed, and tool geometry are the two key influencing parameters determining the quantity of heat generated in the processed sample. However, other processing parameters such as plunge depth and tool tilt angle have a minor impact on the formation of the stir zone, but they were held constant in most of the studies. A sufficient quantity of heat input is needed to achieve a defect-free stir zone. The heat generated by the pin of the FSP tool controls the material flow in the stir zone, directly impacting the microstructure development and mechanical properties.

4.1.1 Selection of process parameters

The primary objective of this section is to optimize the process parameters such as tool rotational speed and traverse speed based on the defect-free structure and better mechanical properties. A tapered cylindrical threaded pin profile was used for initial trial experiments, and the detailed tool dimensions are displayed in Fig. 3.3. For trail experiments, different combinations of tool rotational speeds and traverse speeds were selected from the literature works of AA2014 and AA6061, as shown in Table 4.1&4.2. Other process conditions, such as tool tilt angle and penetration depth of 2^0 and 0.2 mm, respectively, were held constant throughout the process.

For AA2014, nine different combinations of tool rotational speeds and traverse speeds were selected to conduct the trial experiments. The FSP process parameters such a tool rotational speed(w) was varied from 1000 rpm to 1200 rpm with a step size of 100 rpm, and tool traverse speed (v) was varied from 25 mm/min to 35 mm/min with a step size of 5 mm/min for AA2014 alloy, respectively as shown in Table 4.1. A big void was formed during FSP with 1200 rpm-35 mm/min, so this condition was not considered for further mechanical testing. Moreover, the samples processed at 35 mm/min with different rotational speeds yielded poor results due to high traverse speed. The rotational speed of 1000 rpm with varying traverse speeds resulted in minor defects in the stir zone due to insufficient stirring action. Of all parameters, the samples processed with 1100 rpm-25 mm/min and 1100 rpm-30 mm/min produced a defect-free structure, and better mechanical properties were obtained with 1100 rpm-30 mm/min. So, these parameters (1100 rpm-30 mm/min) were selected for further experimentation.

Table 4.1 Results of trial experiments (AA2014)

Process parameters	Macrostructure, key observations, and mechanical properties
1000 rpm - 25 mm/min	 Defects - Small defects were detected in stir zone Hardness (HV) - 119.7 UTS (MPa) - 199 EL (%) - 12.8
1100 rpm - 25 mm/min	 Defects – No defects Hardness (HV) - 113.7 UTS (MPa) - 198 EL (%) – 13.6
1200 rpm - 25 mm/min	 Defects - Small defects were detected in stir zone Hardness (HV) - 101.7 UTS (MPa) - 197 EL (%) – 11.5
1000 rpm - 30 mm/min	 Defects - Very small defects were detected in stir zone Hardness (HV) – 120.3

	UTS (MPa) - 233 EL (%) - 15.6
1100 rpm - 30 mm/min	 Defects – No defects Hardness (HV) - 119.1 UTS (MPa) - 247 EL (%) - 12.9
1200 rpm - 30 mm/min	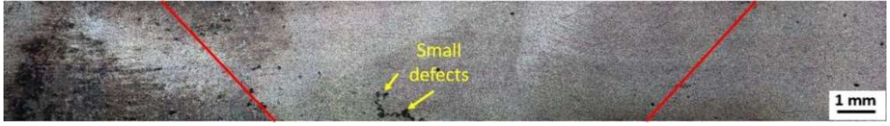 Defects - Small defects were detected in stir zone Hardness (HV) - 118.4 UTS (MPa) - 229 EL (%) - 15.4
1000 rpm - 35 mm/min	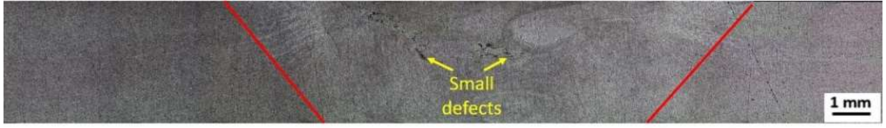 Defects - Small defects were detected in stir zone Hardness (HV) - 113.1 UTS (MPa) - 202 EL (%) - 11.7
1100 rpm - 35 mm/min	 Defects - Small defects were detected in the stir zone. Hardness (HV) – 108.3 UTS (MPa) - 181 EL (%) - 10.9

1200 rpm - 35 mm/min	 Defects - Big void was detected in stir zone Hardness (HV) - NA UTS (MPa) - NA EL (%) - NA

Similarly, nine different combinations of tool rotational speed and traverse speed were selected for AA6061. The tool rotational speeds (w) were varied from 700 rpm to 900 rpm with a step size of 100 rpm, and tool traverse speeds (v) were varied from 30 mm/min to 50 mm/min with a step size of 10 mm/min for AA6061 as shown in Table 4.2. A big void was formed during FSP with 50 mm/min at different rotational speeds and yielded poor results due to high traverse speed. The traverse speed of 30 mm/min with different rotational speeds resulted in minor defects in the stir zone due to insufficient stirring action. Moreover, the sample processed at 700 rpm-30 mm/min resulted in extensive crack formation due to low rotational speeds. Of all parameters, the samples processed with 40 mm/min with different rotational speeds produced a defect-free structure, and better material flow was obtained at 40 mm/min with 700 rpm & 800 rpm. Compared to 700 rpm-40 mm/min, 800 rpm-40 mm/min yielded better mechanical properties. So, these parameters (800 rpm-40 mm/min) were selected for further experimentation.

Table 4.2 Results of trial experiments (AA6061)

Process parameters	Macrostructure, Key observations, and mechanical properties
700 rpm - 30 mm/min	 Defects – Big crack was detected in stir zone Hardness (HV) - 60.3 UTS (MPa) – 94.1 EL (%) – 10.4

800 rpm - 30 mm/min	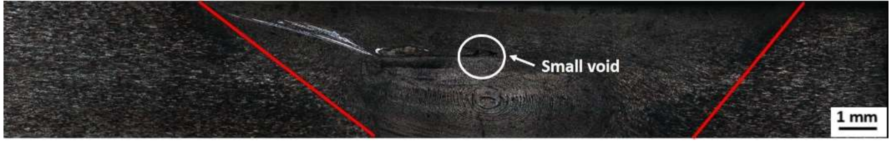 Defects – Small defects were observed in the stir zone Hardness (HV) - 59.1 UTS (MPa) – 95.9 EL (%) – 11.1
900 rpm - 30 mm/min	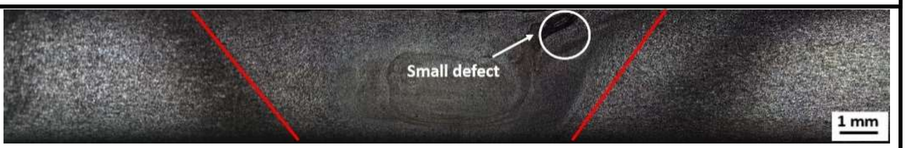 Defects - Small defect was detected in stir zone Hardness (HV) - 62.7 UTS (MPa) – 98.2 EL (%) – 11.5
700 rpm - 40 mm/min	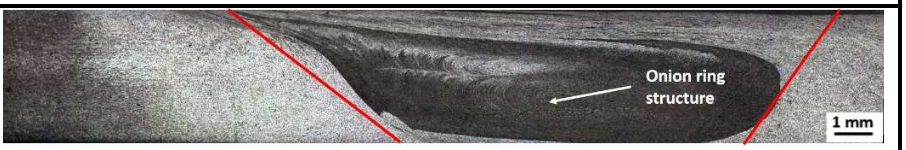 Defects – No defects Hardness (HV) – 63.4 UTS (MPa) – 103.2 EL (%) – 12.85
800 rpm - 40 mm/min	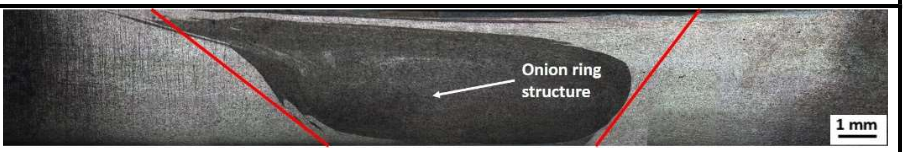 Defects – No defects Hardness (HV) – 65.5 UTS (MPa) – 105.0 EL (%) – 13.98
900 rpm - 40 mm/min	

	Defects – No defects Hardness (HV) - 62.9 UTS (MPa) – 104.2 EL (%) – 13.12
700 rpm - 50 mm/min	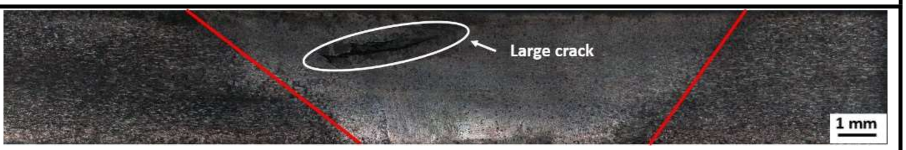 Defects – Big crack was detected in stir zone Hardness (HV) - 59.1 UTS (MPa) – 96.4 EL (%) – 8.5
800 rpm - 50 mm/min	 Defects - Bid void was detected in stir zone. Hardness (HV) – 58.9 UTS (MPa) – 96.9 EL (%) – 8.3
900 rpm - 50 mm/min	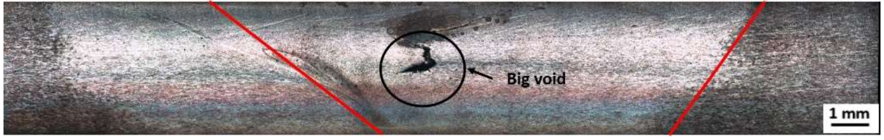 Defects - Big void was detected in stir zone Hardness (HV) – 55.1 UTS (MPa) – 95.5 EL (%) – 7.9

Using the above optimized processed parameters and threaded pin profile, single-pass FSP was performed on AA2014 and AA6061 alloys using different cooling media such as air, dry ice, and water.

4.1.2 Selection of tool geometry

Along with the process parameters, the tool geometry also plays a significant role in determining the heating and plastic flow of the processed metal. For multi-pass overlapping FSP, different tool pin profiles were used to optimize the best tool geometry based on the better mechanical properties. For trail experiments, four different tool pin profiles (including threaded pin profile) were selected as suggested by Kishore and Kumar (2018), such as I. Square pin profile, II. Hexagonal pin profile, III. Cylindrical threaded pin profile and IV. Triangle pin profile.

Using the optimized process parameters (800 rpm-40 mm/min), FSP was conducted in three different cooling media such as air, dry ice, and underwater with four tool geometries; for the same set of parameters, FSP in air, underwater and dry ice is denoted as ACFSP (air-cooled FSP), UWFSP (underwater FSP) and CCFSP (cryogenic-cooled FSP), respectively. After successful completion of overlapping FSP in AA6061, mechanical properties such as average hardness in stir zone, tensile properties (ultimate tensile strength (UTS), yield strength (YS), and elongation (El)) in transverse direction for each tool in different media are summarized in Table 4.3-4.5.

Table 4.3 Mechanical properties of ACFSP samples (AA6061)

Tool profile	UTS (MPa)	YS (MPa)	El (%)
Tool-I	156±5	105±4	21.48±1.2
Tool-II	141±4	83±1	25.02±1.3
Tool-III	148±4	95±2	20.06±1.5
Tool-IV	135±3	100±3	26.26±1.6

Table 4.4 Mechanical properties of CCFSP samples (AA6061)

Tool profile	UTS (MPa)	YS (MPa)	El (%)
Tool-I	158±4	106±3	21.13±1.9
Tool-II	139±3	103±2	25.94±2.1
Tool-III	156±3	106±3	19.84±1.8
Tool-IV	140±2	101±2	24.64±2.2

Table 4.5 Mechanical properties of UWFSP samples (AA6061)

Tool profile	**UTS (MPa)**	**YS (MPa)**	**El (%)**
Tool-I	162±3	114±2	20.90±2.1
Tool-II	156±2	110±1	20.65±2.3
Tool-III	164±3	109±1	21.20±1.9
Tool-IV	163±3	110±1	21.30±2.4

From the summary of mechanical properties, it was identified that the samples processed with square pin profiles and hexagonal pin profiles achieved better mechanical properties than other tool pin profiles. Among the two tools, a square pin profile resulted in better mechanical properties. Hence, overlapping FSP in AA6061 was performed with a square pin profile.

It was also identified that the triangle pin profile in all conditions resulted in poor mechanical properties. Three sharp edges of triangle pin profiles resulted in insufficient plastic flow and leading to poor mechanical properties. So, Tool-IV was not used for optimizing tool geometry in AA2014. With optimized processed parameters (1100 rpm-30 mm/min), overlapping FSP in AA2014 was performed with three tool geometries in different media. After successful completion of overlapping FSP in AA2014, mechanical properties such as average hardness in stir zone, tensile properties along the welding direction for each tool in different media are documented in Table 4.6-4.8.

Table 4.6 Mechanical properties of ACFSP samples

Tool profile	**UTS (MPa)**	**YS (MPa)**	**El (%)**
Tool-I	384±3	223±2	45.7±3.5
Tool-II	390±2	225±3	46.4±3.1
Tool-III	342±4	273±4	35.4±2.8

Table 4.7 Mechanical properties of CCFSP samples

Tool profile	UTS (MPa)	YS (MPa)	El (%)
Tool-I	398±5	229±2	45.9±4.1
Tool-II	401±6	236±3	42.3±2.7
Tool-III	381±4	220±1	42.3±3.4

Table 4.8 Mechanical properties of UWFSP samples

Tool profile	UTS (MPa)	YS (MPa)	El (%)
Tool-I	384±6	289±4	37.6±3.7
Tool-II	410±5	316±5	42.0±3.4
Tool-III	272±3	179±4	39.5±3.6

From the summary of mechanical properties, it was identified that the samples processed with hexagonal pin profiles achieved better mechanical properties than square pin profiles. The samples processed with Tool-III resulted in poor properties compared to other tools. Hence, overlapping FSP in AA2014 was performed with a hexagonal pin profile.

4.2 Influence of cooling media in achieving grain refinement of AA2014 alloy using friction stir processing

From section 4.1, it was identified that the defect-free structure with better mechanical properties was obtained in the AA2014 plates processed with tool rotational speed and traverse speed of 1100 rpm and 30 mm/min. Using optimized process parameters and a simple threaded pin profile, a single-pass FSP was carried out on a 4mm-thick AA2014 plate using different cooling media (water and cryogenic media). The influence of different cooling media on microstructure, mechanical, and corrosion behavior of friction stir processing of AA2014 were studied in the following sections.

4.2.1 Microstructural characterization

4.2.1.1 Optical microscopy

The optical micrograph of BM is depicted in Fig. 4.1. The microstructure of BM includes highly deformed and elongated grains of aluminium matrix along with some strengthening precipitates marked with yellow arrows. The macrostructures of FSP specimens with the microstructures of various zones in different environments are shown in Fig. 4.2-4.4. The microstructure revealed no defects for all FSP samples. The results are attributed to the proper selection of process parameters. The microstructures of the stir zone (SZ) exhibit fine equiaxed grains with no defects like porosity or tunnels, etc., after FSP, as depicted in Fig. 4.2a-c, 4.3a-c and 4.4a-c. The area of the stir zone in ACFSP, CCFSP, and UWFSP samples are ~7.3 mm^2, ~5.9 mm^2, and ~3.9 mm^2, respectively. The presence of cooling media reduces the area of SZ due to rapid heat dissipation in the CCFSP sample. Additionally, the width of SZ is further decreased in the UWFSP sample due to the complete submergence of the processing zone in water, leading to faster heat transfer.

During FSP, the working metal undergoes severe plastic deformation (SPD) and dynamic recrystallization (DRX). The microstructures in SZ of all FSP samples (Fig. 4.2a-c, 4.3a-c, and 4.4a-c) showed fine equiaxed grains of the Al matrix. Within the SZ, grain refinement is not uniform, and it increased from bottom to top of the SZ due to variation of thermal exposure [Xu et al., (2009)]. The top portion of SZ (TSZ) exhibited grain coarsening compared to the middle (MSZ) and bottom SZ (BSZ) owing to more frictional heat generation by the stirring action of the shoulder (Fig. 4.2a, 4.3a, and 4.4a). As compared to pin, high linear velocity was obtained by tool shoulder as per V = W.R (V - linear velocity, W – tool rotation rate, and R – radius of pin or shoulder), which can generate more frictional heat at TSZ [Chen et al., (2016)]. In MSZ (Fig. 4.2b, 4.3b, and 4.4b), the stirring action of the pin causes less linear velocity, which produces less frictional heat, resulting in better grain refinement than TSZ. At BSZ, the linear velocity is similar to MSZ, but swirling action is more at the end of the pin [Zhao et al., (2014)]. Therefore, more grain refinement was achieved in BSZ (Fig. 4.2c, 4.3c, and 4.4c). Fig. 4.2d&f, Fig. 4.3d&f, and Fig. 4.4d&f represent elongated grains on either side of SZ, i.e., advancing side (AS) and retreating side (RS). This zone experiences longer thermal cycles and insufficient plastic deformation, resulting in forming a new zone called thermo-mechanically affected zone (TMAZ). As the deformation and temperature generation are more in AS, coarse grains were produced in SZ near

AS-TMAZ than SZ near RS-TMAZ. Un-recrystallized coarse grains were seen in the heat-affected zone (HAZ), and it was due to the absence of pin action and a longer stay at elevated temperatures in HAZ (Fig. 4.2e, 4.3e, and 4.4e).

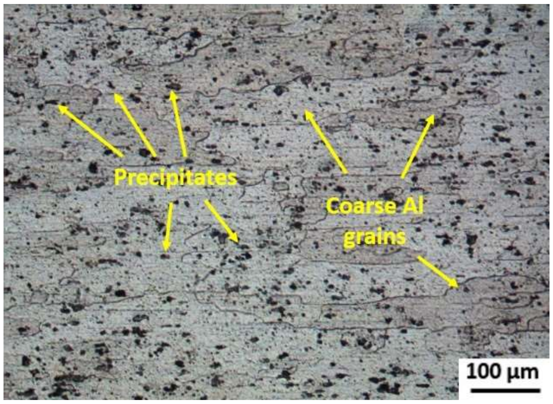

Fig. 4.1. Optical micrograph of base metal.

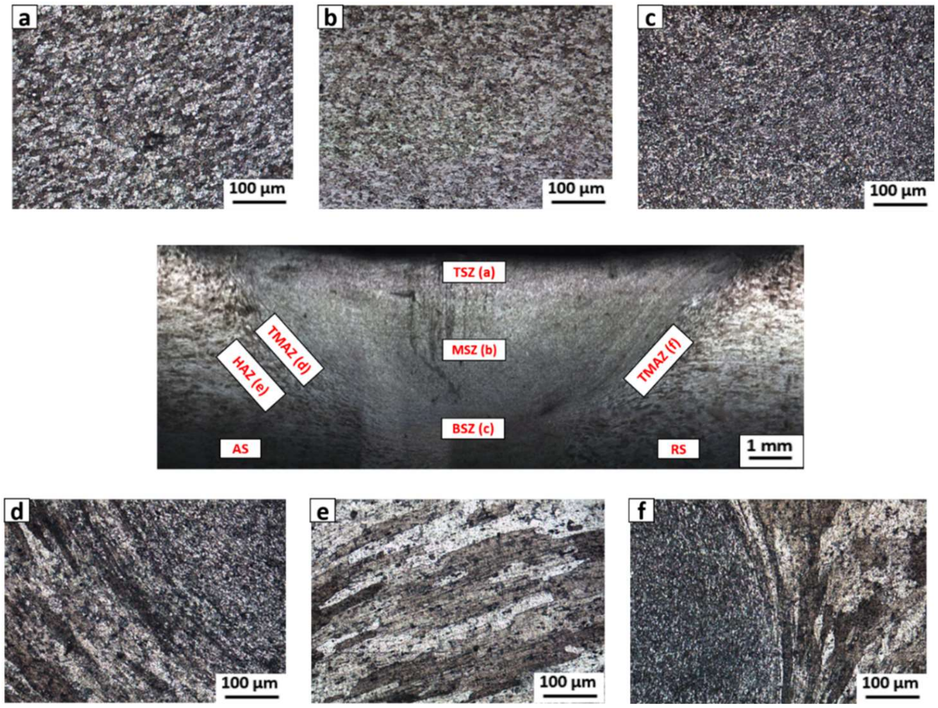

Fig. 4.2. Microstructures of (a) TSZ, (b) MSZ, (c) BSZ, (d) AS-TMAZ, (e) HAZ, and (f) RS-TMAZ of ACFSP specimen along with macrostructure.

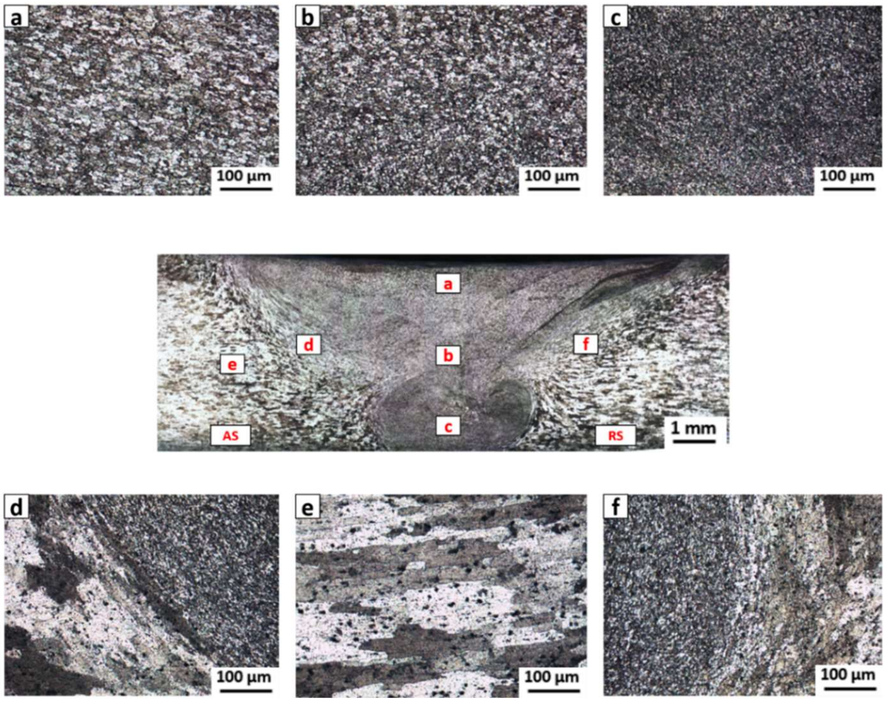

Fig. 4.3 Microstructures of (a) TSZ, (b) MSZ, (c) BSZ, (d) AS-TMAZ, (e) HAZ, and (f) RS-TMAZ of CCFSP specimen along with macrostructure.

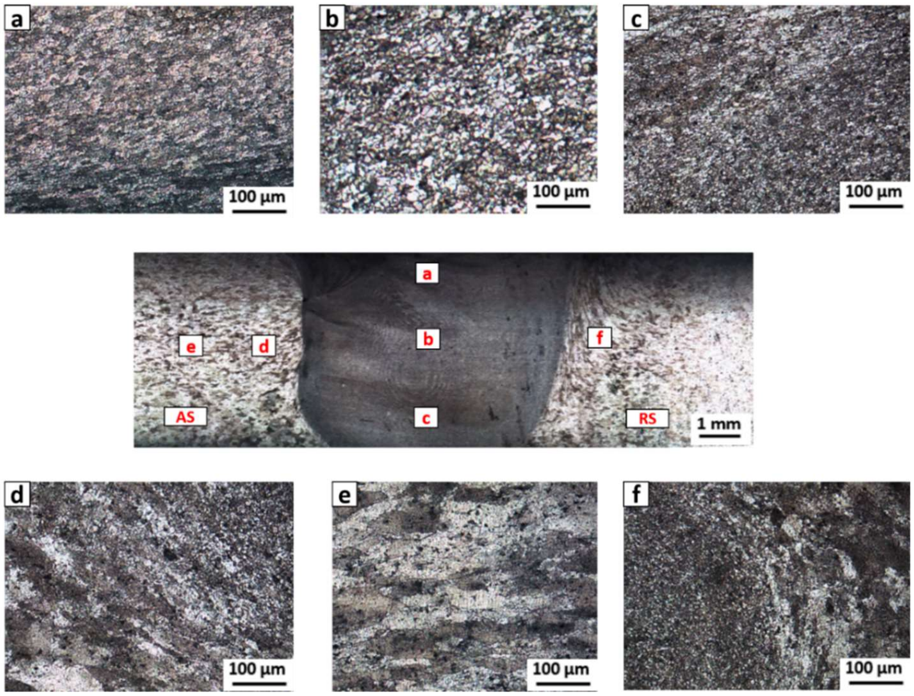

Fig. 4.4. Microstructures of (a) TSZ, (b) MSZ, (c) BSZ, (d) AS-TMAZ, (e) HAZ, and (f) RS-TMAZ of UWFSP specimen along with macrostructure.

4.2.1.2 EBSD analysis

EBSD microstructure (IPF + grain boundary) along with grain size distribution map of the BM are depicted in Fig. 4.5. The microstructure of BM is characterized by highly deformed grains with an average grain size of 80.5±50.5 µm, as illustrated in Fig. 4.5a. After FSP, the micrographs of all samples show fine-equiaxed gain structure (Fig. 4.6a-c), which corroborates optical microstructure results. The EBSD results such as grain size, the fraction of high angle grain boundaries (HABs), and low angle grain boundaries (LABs) of BM and FSP samples are documented in Table 4.9. Fig. 4.7 displays the EBSD map of the UWFSP sample highlighted with LABs and HABs. LABs are indicated by a green line with a misorientation angle 2^0-$15^{0,}$ whereas HABs are indicated by a blue line with a misorientation angle beyond 15^0. The fraction of HABs and LABs in BM is 96.9% and 3.1%, respectively. After FSP, the fraction of HABs increased compared to BM. The increase in HABs was due to dynamic recovery (DRV) and continuous DRX (C-DRX) [Zhao et al., (2019)]. The metals with high stacking fault energy like aluminium quickly undergo DRV, leading to increased flow stress. The increase in flow stress during the earlier stage of deformation resulted in dislocations grow and interact. However, the DRV rate rises with an increase in dislocation density, and these dislocations begin to rearrange themselves to form subgrains with LABs (2^0-5^0). Finally, dynamic equilibrium (DE) is achieved as flow stress reaches a threshold limit due to dislocation growth and rearrangement, leading to steady-state deformation. During steady-state deformation, sub-grains come together and transform into equiaxed subgrains with LABs (5^0-15^0) by absorbing dislocations. The steady-state deformation is continued until sub-grain size reaches a critical value, leading to the beginning of C-DRX. Then, C-DRX increases the misorientation of sub-grains by slow rotation and transforming them into HABs (beyond 15^0) [Su et al., (2005)].

The grain size distribution of FSP samples obtained from EBSD is depicted in Fig. 4.8. The average grain size in SZ of ACFCP, CCFSP, and UWFSP samples is 4.9±3.5 µm, 3.5±2.9 µm, and 0.9±0.5 µm, respectively. The minimum grain size in UWFSP is attributed to uniform heat dissipation from the processing zone by the principle of convection heat transfers due to complete submergence in the cooling medium. However, in CCFSP, dry ice was affecting the processed zone only while the heat from surrounding areas of the plate transferred to the processing region, leading to little grain coarsening compared to UWFSP. As expected, the maximum grain size was obtained in ACFSP as the grain refinement was only due to SPD and DRX.

Table 4.9 EBSD results

Sample condition	Grain size (µm)	Fraction of grain boundaries (%)	
		LABs	HABs
BM	80.5±50.5	96.9	3.1
ACFSP	4.9±3.5	77.0	23.0
CCFSP	3.5±2.9	37.6	62.4
UWFSP	0.9±0.7	26.7	73.3

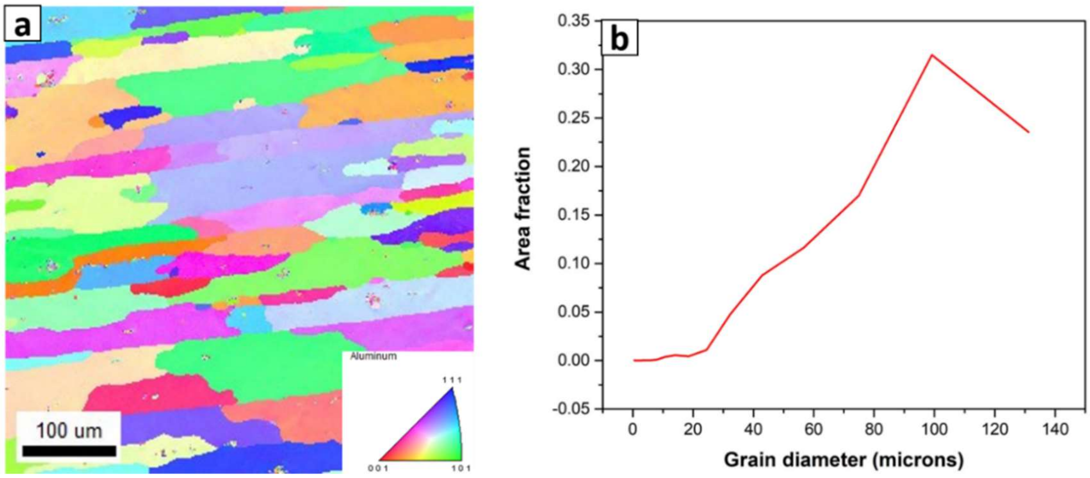

Fig. 4.5. (a) EBSD microstructure (IPF + grain boundary), and (b) Grain size distribution map of BM.

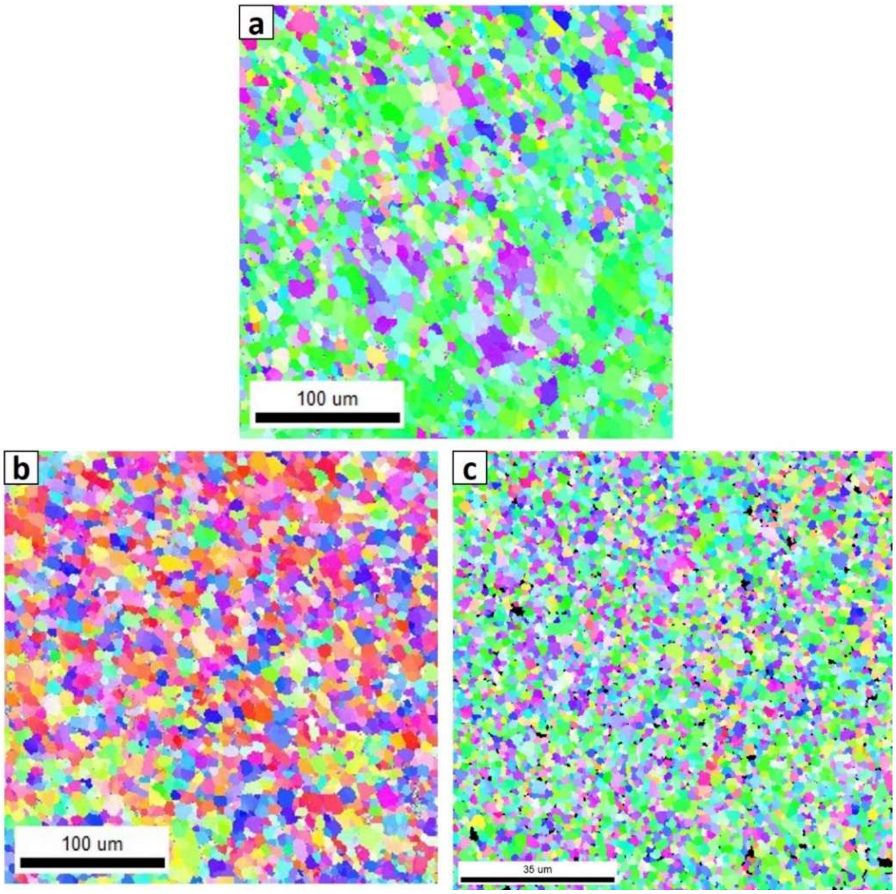

Fig. 4.6. EBSD microstructure (IPF + grain boundary) of (a) ACFSP, (b) CCFSP, and (c) UWFSP samples.

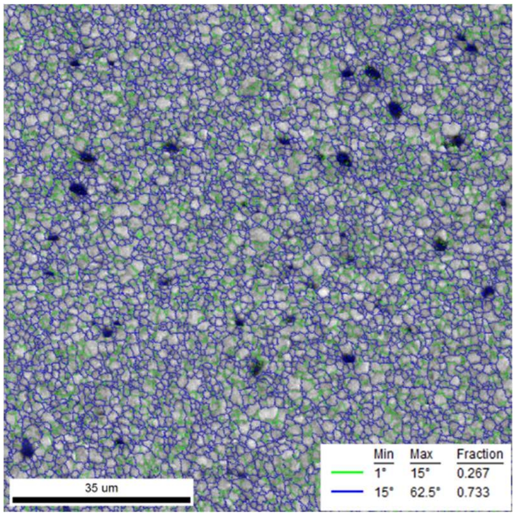

Fig. 4.7. EBSD grain boundary map of UWFSP sample highlighting high and low angle grain boundaries.

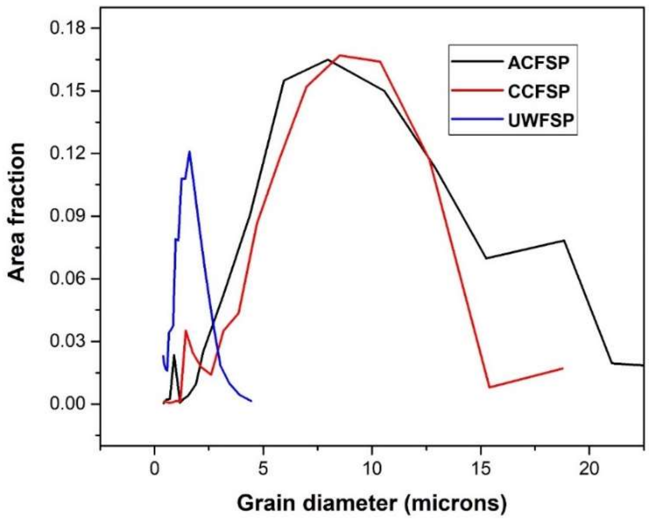

Fig. 4.8. Grain size distribution maps of FSP samples.

4.2.1.3 SEM analysis

SEM micrographs of BM and SZ of ACFSP, UWFSP, and CCFSP specimens are shown in Fig. 4.9. The EDS analysis was used to measure the composition of precipitates, shown in the inset of Fig. 4.9. As in optical microscopy, the profile of BM has un-recrystallized coarse grains of Al matrix along with Al_2Cu precipitates (The presence of Al_2Cu was confirmed by XRD maps as shown in Fig. 4.10) as shown in Fig. 4.9a. The precipitation behavior was examined in each sample to obtain a clear picture of the effect of different cooling media on the FSP of AA2014. The average size of precipitates near the grain boundaries in BM, SZ of ACFSP, CCFSP, and UWFSP samples are ~1.94 µm, ~0.43 µm, ~0.34 µm, and ~0.29 µm, respectively. The coarser precipitates in BM were fragmented into fine particles and uniformly distributed along the grain boundaries due to the stirring action of the FSP tool (Fig. 4.9a). In CCFSP and UWFSP samples (Fig. 4.9b&c), the fine precipitates are randomly distributed along the grain boundary. Similar results were observed in the literature studies of Sinhmar et al. (2017). The heat generation and cooling media are essential factors for the size of precipitates. So, the heat generated during FSP provides sufficient time for precipitate coarsening. On account of this, coarser precipitates were observed in the ACFSP sample. Additional cooling in UWFSP and CCFSP prevents precipitation growth and dissolution, which results in fine precipitates. According to Sinhmar et al. (2017), the finer precipitates pinned to the grain boundaries have a strong ability to hinder grain boundary migration and improve mechanical properties. Similar results were achieved in the UWFSP sample, where finer precipitates were settled at grain boundary (Fig. 4.9d). The more precipitates-free areas (PFA) near grain boundaries were observed in Fig. 4.9a. Moreover, the inter-distance between the precipitates is more in BM as compared to FSP samples. The regions of PFA in BM are severely attacked during the corrosion process, and the coarser precipitates and inter-distance between the precipitates in BM will have a deleterious influence on the corrosion process [Sinhmar et al., (2018) and Navaser et al., (2017)].

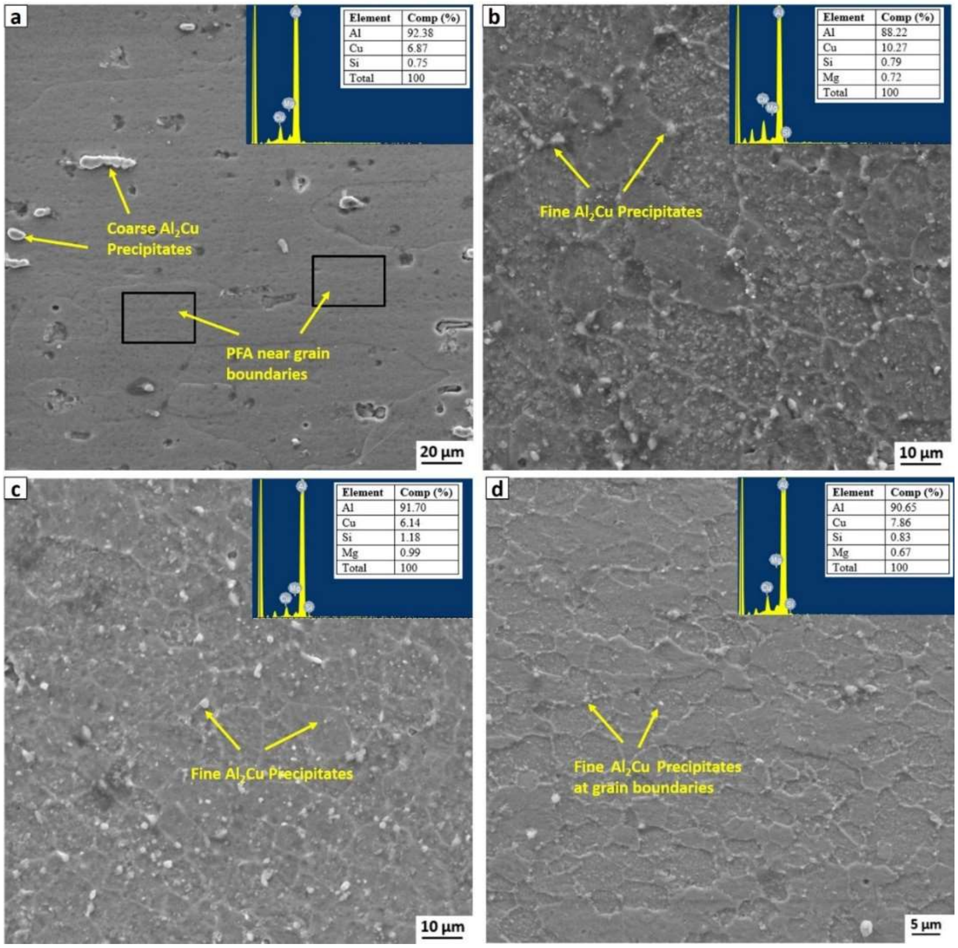

Fig. 4.9. SEM micrographs of (a) BM, (b) ACFSP, (c) CCFSP, and (d) UWFSP samples with EDS maps.

4.2.1.4 XRD analysis

XRD analysis of BM along with FSP samples is shown in Fig. 4.10. EDS analysis gives the composition of precipitate phases, but the existence of those phases needed to be confirmed by XRD analysis. The high intense peaks of Al and less intense peaks of Al_2Cu precipitates were detected in XRD graphs. The presence of Al_2Cu peaks in BM confirms the intermetallic formation. The severe plastic straining of FSP causes fragmentation of Al_2Cu precipitates into fine particles. Hence, the intensity of these precipitates decreased after FSP, as shown in Fig. 4.10. And the peaks of Al_2Cu broadened slightly owing to the refinement and straining of grains [Balakrishnan et al., (2019)]. The intensity of Al_2Cu precipitates in the ACFSP sample was slightly higher than that of CCFSP and UWFSP samples. These results could be attributed to coarser precipitates in ACFSP samples due to frictional heat generated in the SZ. The minimum peak intensity of precipitates in UWFSP suggests minimum precipitate size, which is in line with SEM results. The existence of Al_2Cu was detected in all samples in XRD analysis, and these were therefore categorized as major strengthening precipitates in AA 2014. Additionally, the existence of Mg_2Si peaks with very low intensity was detected in all samples. Moreover, the presence of the Al_2CuSi compound was also detected in ACFSP samples. Other possible phases of AlCu, Al_3Cu, Al_4Cu, and $AlCu_2$ were not detected in XRD patterns. The non-existence of other phases suggests that Al_2Cu precipitates remain stable during FSP, and they did not decompose into another compound by the transformation.

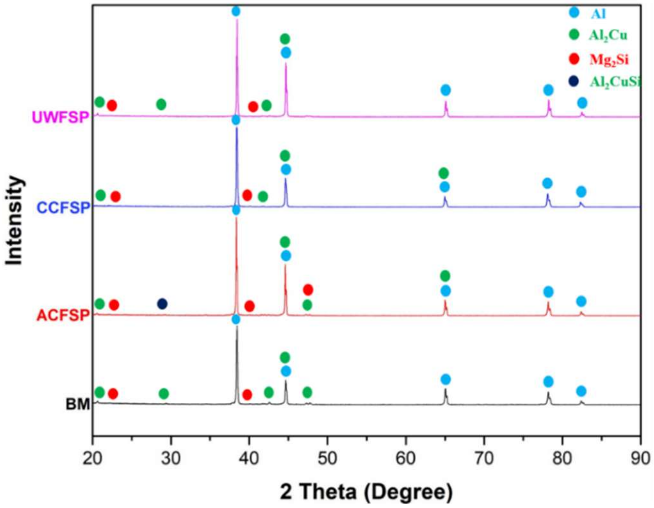

Fig. 4.10 XRD results of BM and FSP samples.

4.2.2 Mechanical characterization

4.2.2.1 Hardness

Initially, microhardness was measured within the SZ of all FSP samples, and the results were compared with BM. It was seen that the hardness in the SZ of the FSP sample was lower than BM

(151 HV) owing to thermal softening during FSP [Chen et al., (2016)]. The high temperature encountered during FSP results in softening of SZ, which is in line with previously published literature. The average hardness in SZ of ACFSP, CCFSP, and UWFSP samples is 119 HV, 124 HV, and 134 HV, respectively. The presence of cooling media reduces the softening effect by reducing peak temperature, which increases hardness compared to FSP without cooling media. These findings corroborate the reports of microstructural studies. The microhardness distribution across processed zones of all conditions is shown in Fig. 4.11. The hardness distribution across FSP samples in different regions was nearly symmetrical about the weld center. The hardness profile was sectioned into three distinct zones, SZ, TMAZ, and HAZ. The hardness was very high in SZ compared to other zones. In SZ, the stirring action causes intense plastic deformation, which helps grain refinement and uniform distribution of precipitates, leading to increased hardness compared to TMAZ and HAZ. Little effect of stirring action and long thermal cycles in TMAZ led to low hardness compared to SZ. HAZ exhibits minimum hardness as it did not deform mechanically.

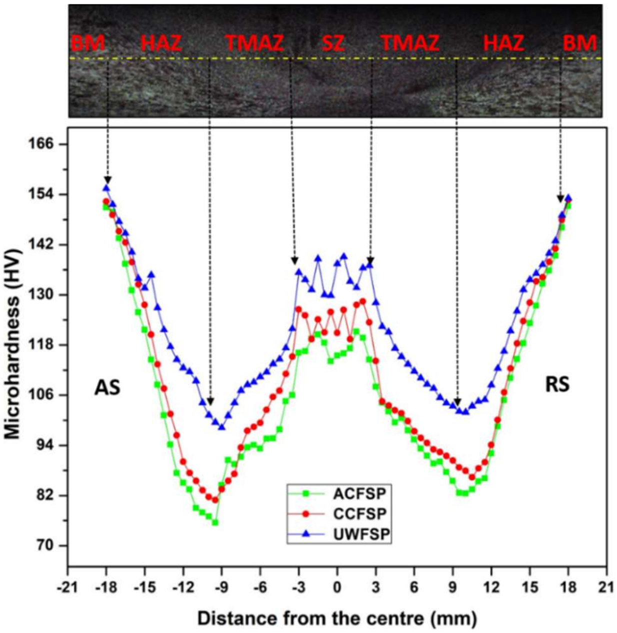

Fig. 4.11. Hardness profile of FSP samples.

4.2.2.2 Tensile properties

The tensile test results of BM and FSP samples are shown by stress-strain curves (Fig. 4.12) and Table 4.10. The results show that strength was reduced in all FSP conditions compared to BM, and these findings are consistent with hardness studies. The reduction in strength is attributed to the thermal softening of FSP samples, as discussed in previous sections. The ultimate tensile strength (UTS) of the ACFSP specimen was 276 MPa, which is 57.74% of the BM. The effect of UWFSP and CCFSP cooling is shown in Fig. 4.12. CCFSP specimen shows a reasonable increment of 23.91% in UTS compared to ACFSP specimen. Compared to all FSP conditions, the sample processed in water offers a marginal increment in UTS due to rapid grain refinement in SZ. UTS of UWFSP specimen was 36.23% more than ACFSP specimen, which is equivalent to 78.49% of BM. Compared to BM, the elongation was elevated in FSP samples due to the homogenization of fine equiaxed grains. The highest elongation was obtained in ACFSP samples. Cooling media lowers the thermal softening effects and reduced elongation in CCFSP and UWFSP samples compared to the ACFSP sample. Additionally, the presence of finer precipitates in grain boundary hinders grain boundary sliding, which improves UTS.

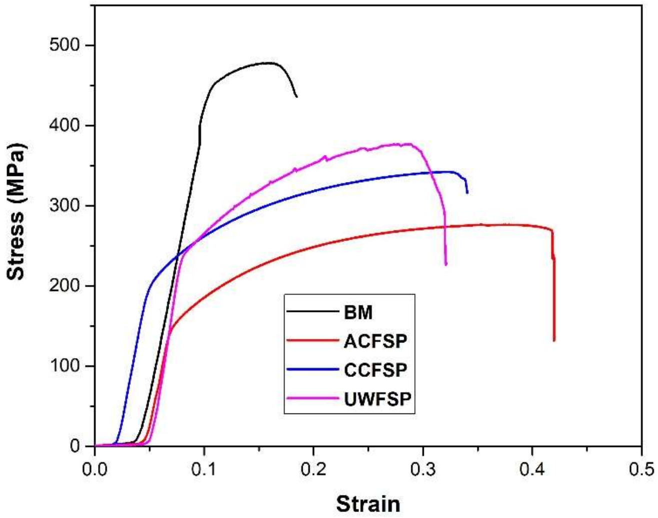

Fig. 4.12. Stress-strain curves of BM and FSP samples.

Table 4.10 Tensile properties of BM and FSP specimens.

Condition	YS (MPa)	UTS (MPa)	EL (%)
BM	409±6	478±6	18.44±1.1
ACFSP	146±3	276±3	41.98±2.9
CCFSP	198±4	342±4	34.05±2.5
UWFSP	240±4	376±5	32.10±1.9

The fracture features of BM and other FSP specimens are shown in Fig. 4.13. All the fracture surfaces consist of dimples with varying sizes and shapes, confirming that failure is due to ductile shear fracture. BM exhibits large and deep dimples (~10 µm) owing to significant plastic deformation during testing (Fig. 4.13a). Compared with BM, the size of dimples was reduced in FSP samples due to fine-grained structure and material flow during FSP. The fracture feature of the ACFSP sample (Fig. 4.13b) includes the high density of small dimples (~6 µm) interposed with the flat surface, and this also can be categorized as a pure ductile failure. The fracture surface of the UWFSP specimen shows a low density of fine dimples (~5 µm) with few flat surfaces, which generally indicates a combination of ductile and brittle fracture (Fig. 4.13d). It is believed that the rapid cooling of the UWFSP specimen is responsible for the earlier failure of tensile samples with less deformation than other FSP samples. And in a few locations, time was not enough to grow the dimples; instead, it formed a flat surface. The fracture features of the CCFSP reveals a similar trend as UWFSP but with coarse dimples (~5.5 µm) than UWFSP, as represented in Fig. 4.13c.

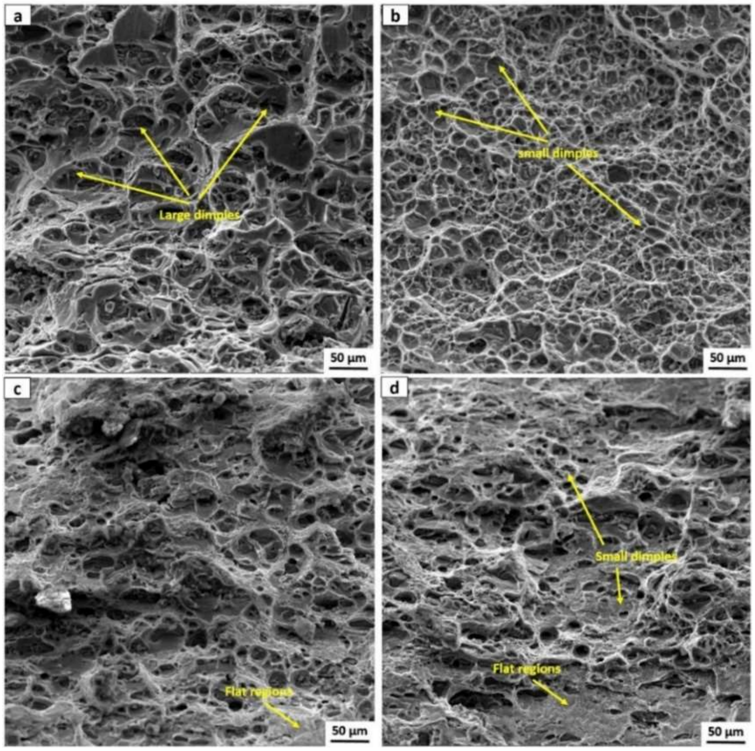

Fig. 4.13. Fracture features of (a) BM, (b) ACFSP, (c) CCFSP, and (d) UWFSP specimens.

4.2.3 Corrosion studies

4.2.3.1 Weight-loss test

The results of the weight-loss test of BM and FSP samples after 20-days of immersion in 3.5% NaCl electrolytic solution are documented in Table 4.11. The corrosion rate was measured from the weight-loss method, which is given by, CR = 534 (W/DT) where CR – corrosion rate (mpy), W – weight loss (mg/inch^2), D – density (g/cm^3), and T – immersion time (hours). From the results, it was identified that the weight loss and corrosion rate of BM were more than FSP samples. Grain refinement by FSP causes an increase in grain boundaries, and these grain boundaries are more passive to surface attack. Moreover, the defects and inhomogeneous microstructure present in BM are eliminated during FSP and resulted in homogeneous microstructure, enhancing corrosion resistance [Mahdi et al., (2019)]. Further, the incorporation of the cooling media during FSP (CCFSP and UWFSP samples) contributes to additional grain refinement by controlling grain coarsening, which resulted in low weight loss and improved corrosion resistance.

Table 4.11 Weight loss test results.

Sample condition	Wight loss (mg/cm^2)	Corrosion rate (mpy)
BM	0.00141	0.0036
ACFSP	0.00039	0.0010
CCFSP	0.00025	0.0006
UWFSP	0.00019	0.0005

4.2.3.2 Open-circuit potential test

The open-circuit potential (OCP) test was initially performed at ambient temperature in a 3.5% NaCl solution to ensure the potential range for the Tafel polarization test. The OCP trends of BM and FSP samples are illustrated in Fig. 4.14. From the OCP trend, it has been observed that the OCP (V_{OCP}) trend of BM and ACFSP samples is maintained constant throughout the process, and it is evident that corrosion attack is uniform. The initial V_{OCP} of the UWFSP sample was -679 mV, increased to -644 mV after 13 s, and then it followed a decreasing trend over the entire process and reached a final value of -840 mV after 600 s, whereas, the initial V_{OCP} of the CCFSP sample was -720 mV, decreasing to -834 mV after 89 s and then maintained constant potential with little fluctuations and reached a final value of -598 mV after 600 s. The increasing trend of V_{OCP} in the earlier stages could be attributed to the formation of the protective oxide layer by electrolytic solution on the attacking region of the working sample, and the decreasing trend of V_{OCP} may be due to the dissolution of the protective oxide layer by the continuous attack of electrolytic solution on the sample surface [Samar et al., (2011)]. From the results, it was observed that the corrosion resistance enhanced after FSP as the final V_{OCP} of FSP samples is more than the BM. The BM undergoes SPD and DRX during FSP and has resulted in the uniform fine-grained microstructure. The uniform microstructure strictly prevents the possibility of galvanic coupling and has resulted in enhanced corrosion resistance [Qin et al., (2015)].

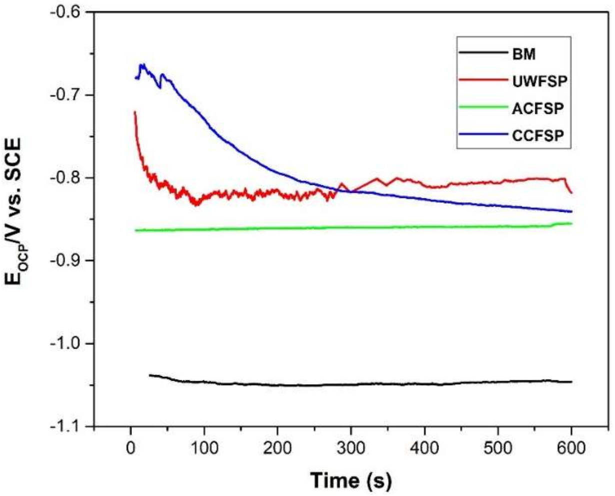

Fig. 4.14. OCP trends of BM and FSP samples.

4.2.3.3 Tafel polarization test

Tafel polarization test was performed on BM and FSP samples processed in different environments. The corrosion potential (E_{COR}) of each sample was extracted from Tafel curves (Fig. 4.15), and the results are shown in Table 4.12. The situation of low E_{COR} (highest negative value) indicates poor corrosion resistance. In this study, BM has a more negative E_{COR} than FSP samples, and it was concluded that corrosion resistance was improved after FSP. During FSP, the working metal was severely deformed and dynamically recrystallized and leading to a homogeneous microstructure. The homogenous microstructure strictly controls the possible formation of galvanic coupling [Qin et al., (2015)]. So that corrosion resistance is improved in FSP samples.

Within the FSP, the sample processed in underwater has more corrosion resistance than other samples.

In AA2014, The E_{COR} of precipitates is nobler (acts as a cathode) compared to the Al matrix (acts as anode). So that the Al matrix around the precipitates is dissolved during the corrosion process leading to the formation of pits (shown in Fig. 4.16). The larger potential difference between Al matrix and precipitate causes corrosion of the matrix around the precipitate by forming galvanic coupling between them. Generally, the metals are corroded because of the galvanic cell formation between the Al matrix and precipitates due to the potential difference between them. The less potential difference leads to more resistance to corrosion. In comparison with fine precipitates, the coarse precipitates are more susceptible to form the galvanic coupling with the Al matrix. So that, coarse precipitates contained by BM are more prone to corrosion attack than FSP samples [Navaser et al., (2017)]. According to Sinhmar et al. (2018), the finer grains produced in FSP/FSW samples facilitate more fraction of grain boundary area and provide more passivation to corrosion attack than BM, improving corrosion resistance. Fine-grained structure achieved after FSP has more ability to form the oxide layer than coarse-grained structure due to large grain boundary area. Corrosion resistance greatly improved after FSP due to oxide layer formation in aluminium alloys. These results indicate that grain refinement is an important factor that lowers corrosion activity by enhancing passivation. More grain refinement, discontinues fine precipitates at grain boundaries and other factors in the UWFSP sample provided better corrosion resistance than other FSP samples.

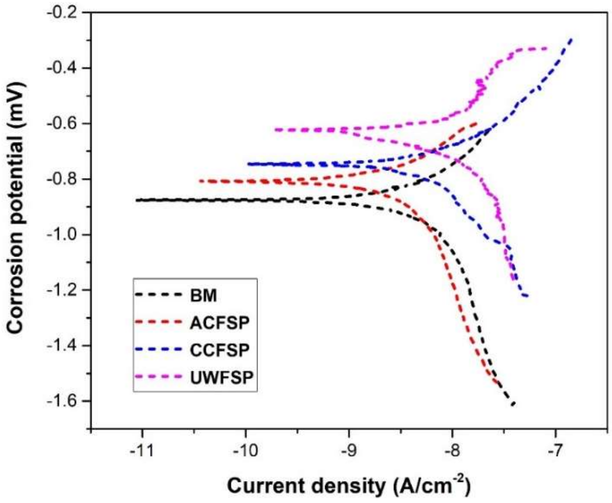

Fig. 4.15. Tafel curves of BM and FSP samples.

Table 4.12 Corrosion potentials.

Sample condition	BM	ACFSP	CCFSP	UWFSP
E_{COR} (mV)	-854	-796	-710	-628

After the Tafel polarization test, the corroded surfaces of BM and FSP samples were examined under SEM (Fig. 4.16). Trenches and pits were identified in corroded samples. Generally, trenches are formed by the dissolution of material particles during corrosion activity. Continuous corrosion activity causes the growth of trenches, and finally, these trenches result in the formation of pits [Sinhmar et al., (2019)]. Severe pitting corrosion (large and shallow pits) was seen in BM (Fig. 4.16a). In contrast, less pitting corrosion activity was observed in the UWFSP sample (Fig. 4.16d). These results are attributed to the high and low corrosion resistance of BM and UWFSP samples, as discussed in the previous section.

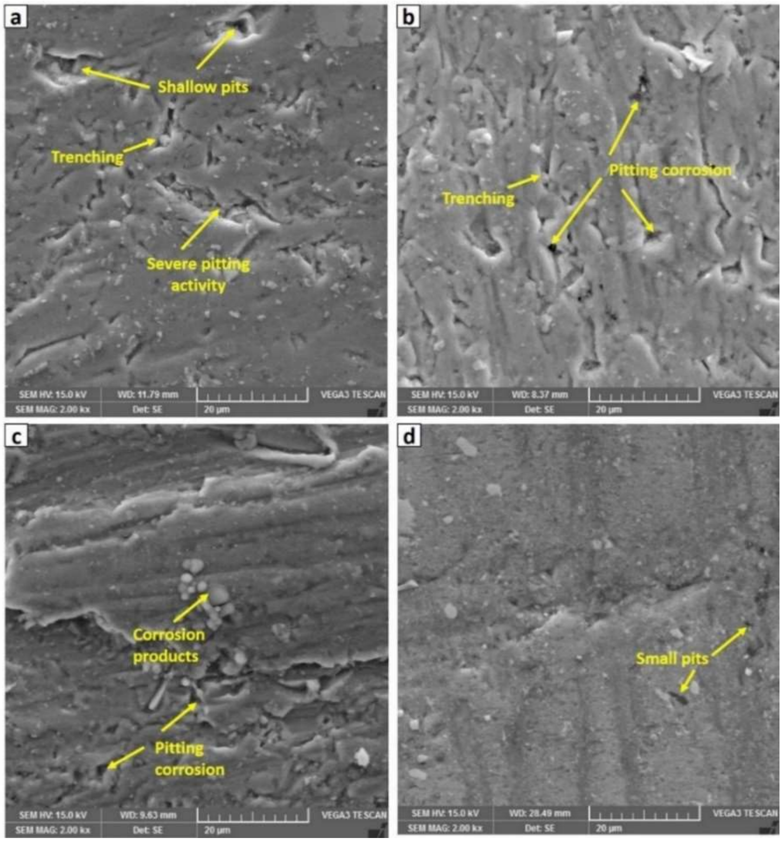

Fig. 4.16. Corroded surface of Tafel test samples of a) BM, b) ACFSP, c) CCFSP, and d) UWFSP samples.

4.3 Effect of microstructure and precipitate formation on mechanical and corrosion behavior of friction stir processed AA6061 alloy using different cooling media

The present section studies the effect of microstructure and precipitate formation on mechanical and corrosion characteristics of friction stir processed AA6061 alloy using different cooling technologies. For this study, a single-pass FSP was carried out in three different environments (such as air, dry ice, and water) on 4-mm thick AA6061 plate using a simple threaded pin profile. The process variables for FSP, such as tool revolution and traverse rate, were kept at 800 rpm and 40 mm/min, respectively, as optimized in Section 4.1.

4.3.1 Microstructure

4.3.1.1 Grain structure evolution during FSP

The EBSD maps of BM and FSP samples and grain size distribution maps are shown in Fig. 4.17-4.19. The microstructure of BM consists of heavily deformed α-Al grains with a mean grain size of 88.4 μm (Fig. 4.17a). From the grain size distribution map of BM (Fig. 4.17b), it was observed that the distribution of grain size was non-uniform and varied between 22-126 μm. However, most of the grain size was in the range of 75-126 μm. The non-uniform grain size distribution could be attributed to nonhomogeneous deformation during cold-working conditions, i.e., as received condition of BM. After FSP, the microstructure of BM transformed completely into a newly essential structure, as shown in Fig. 4.18. The BM underwent intense plastic straining and high-temperature exposure during FSP, resulting in homogeneous fine recrystallized grains with a high fraction of high angle boundaries (HABs) in the SZ of all FSP samples. Besides, the grain refinement and distribution of grain size were homogeneous throughout the SZ of FSP samples. The mechanical and microstructural phenomena involved in achieving fine grains during FSP are explained as follows.

During FSP, the frictional heat produced in the SZ due to the tool stirring action went into deforming the working material. The tool revolution rate caused the deformed material to move around the tool, while the tool traverse rate caused it to travel along the line of action. Due to the combined action of tool revolution and traverse rate, the deformed material was allowed to flow in all directions and finally forged behind the tool. The complex plastic flow induced by the tool fragmented the elongated coarse grains in BM into fine recrystallized grains in FSP samples in SZ, while the tool rotation and traverse motion enabled the grains to re-distribute themselves homogeneously [Balakrishnan et al., (2019)].

During FSP, due to high-temperature exposure, the material underwent thermal softening, also known as thermal annealing. The dynamic recovery occurred quickly during the initial stages of annealing following increased flow stress induced by thermal effects. The point defects, i.e., vacancies created during cold-working, were removed during this process. In general, dynamic recovery caused the dislocation to be annihilated by the dislocation climb, and the dislocation climb, in turn, led to a reduction in vacancies. During the dynamic recovery, dislocations of the opposite sign came together and annihilated themselves, while for dislocations of the same sign, annihilations probably did not occur; instead, the dislocations re-arranged themselves and created low-angle grain boundaries (LABs). The high dislocation density left in the grains after the dynamic recovery acted as the driving force for recrystallization. High dislocation density grains were transformed into strain-free recrystallized grains of low dislocation density. The recrystallization rate (Z) depends exponentially on temperature and is given by $Z = A \exp(Q/RT)$, Where Q is the activation energy for recrystallization, A is strain rate, R is gas constant, and T is temperature [Su et al., (2005)]. After recrystallization, i.e., after the tool leaves the stirred material, grain coarsening occurs due to the high temperature in the processing zone. In order to eliminate the coarsening of grains, FSP was conducted with the aid of cooling media. The grain size distribution maps of FSP samples are depicted in Fig. 4.19. The mean grain size of ACFSP, CCFSP, and UWFSP samples was 4.8 µm, 3.9 µm, and 2.8 µm, respectively, and it was observed that, compared to the ACFSP sample (Fig. 4.18a), the samples processed using cooling-assisted FSP (Fig. 4.18b&c) showed more refined grains, where the cooling media took away the frictional heat generated during FSP. Within cooling-assisted FSP, the sample processed in UWFSP resulted in very fine grains due to the rapid cooling effect provided by submerged conditions. Though dry ice produces more rapid cooling than submerged water, in dry ice FSP, most of the cooling effect results from extraction of the heat from the surroundings rather than the processing zone. Fig. 20 depicts the angle misorientation of BM and FSP samples. Compared to BM, the fraction of high angle boundaries (%HABs) increased after FSP could be attributed to recovery and recrystallization. In FSP samples, the fraction of HABs increased with a decrease in grain size and an increase in cooling rate. Hence, the UWFSP sample resulted in a higher fraction of HABs.

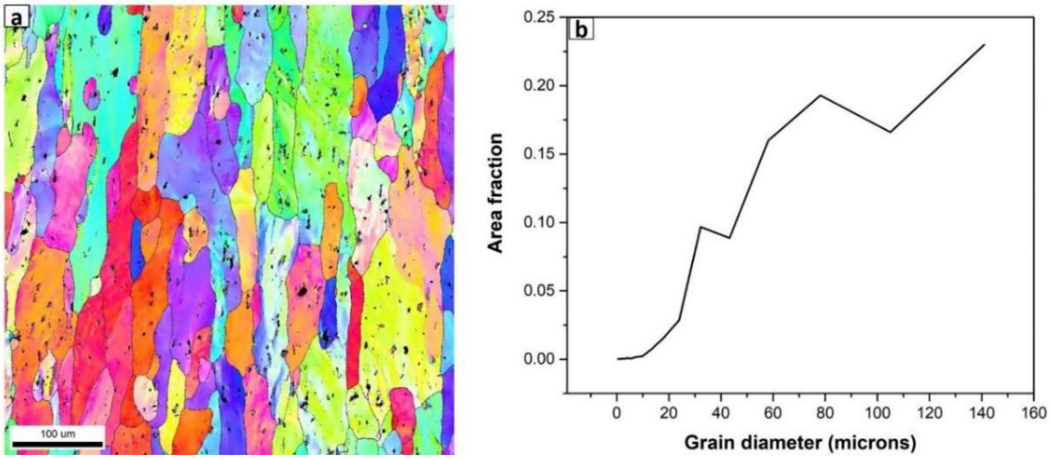

Fig. 4.17. (a) EBSD map and (b) Grain size distribution of base metal.

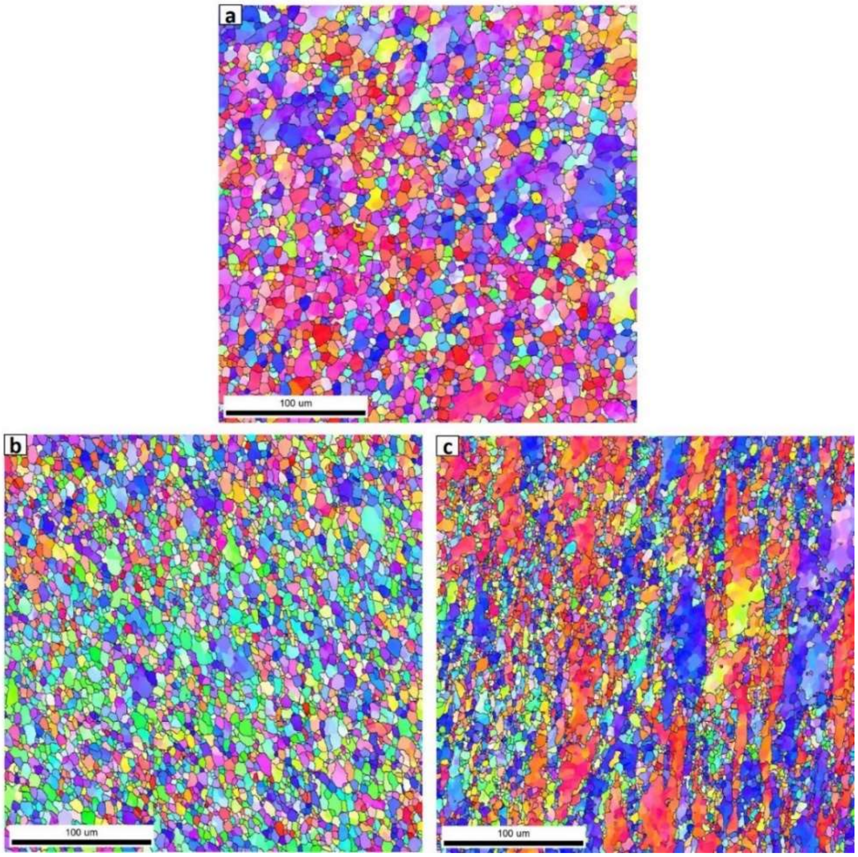

Fig. 4.18. EBSD maps of (a) Air-cooled FSP, (b) Cryogenic FSP, and (c) Underwater FSP samples.

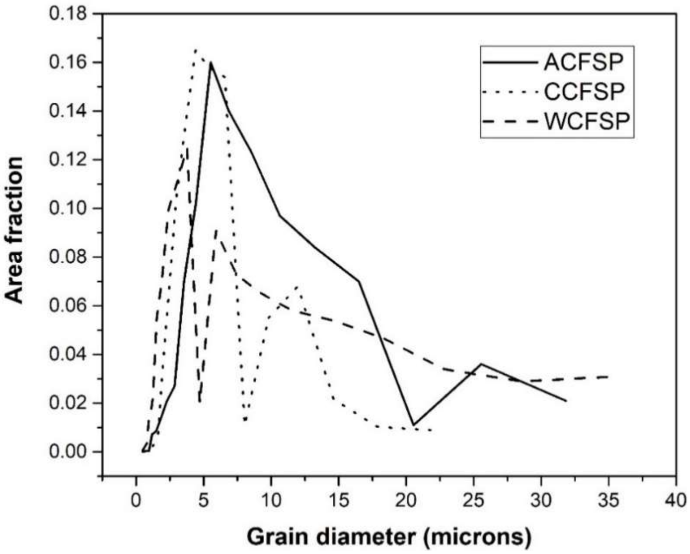

Fig. 4.19. Grain size distribution of FSP samples.

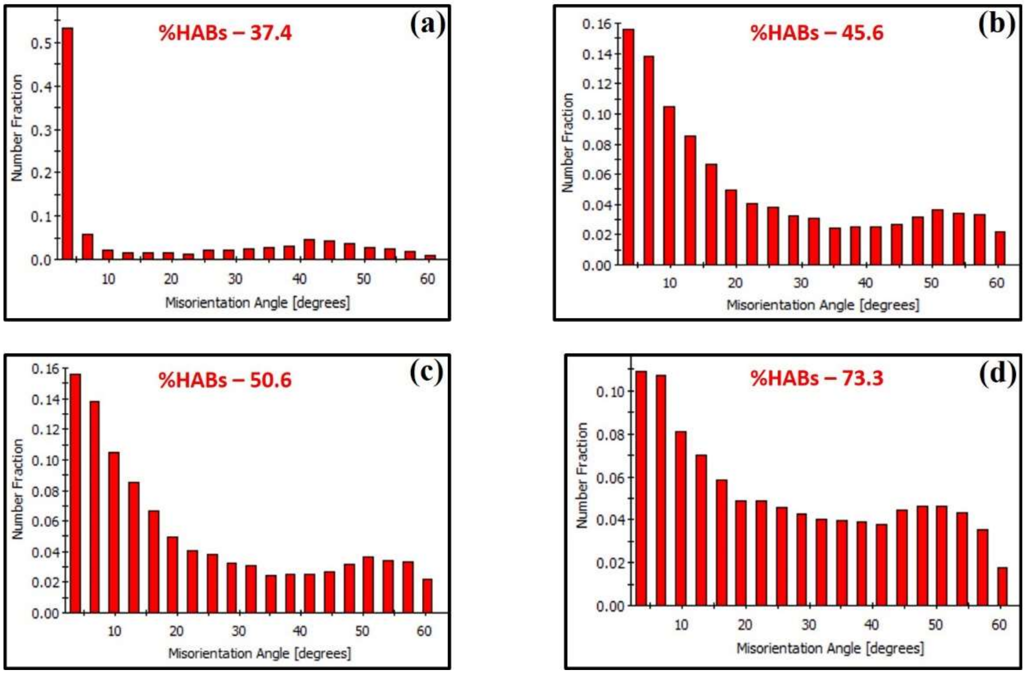

Fig. 4.20. Angle misorientation maps of (a) Base metal, (b) Air-cooled FSP, (c) Cryogenic FSP, and (d) Underwater FSP samples.

4.3.1.2 Effect of precipitate formation

SEM analysis was used to study the precipitation phenomenon in BM and FSP samples. Fig. 4.21-4.24 display the BSE-SEM images of BM and FSP samples along with EDS results. The micrograph of BM contains a dark region of Al matrix surrounded by high density of precipitates, and the average precipitate size was ~1.5 µm, as shown in Fig. 4.21. These precipitates were broken down into fine particles during FSP and distributed homogeneously in the matrix, and some of the precipitates settled at the grain boundaries. The average size of the precipitates in ACFSP, CCFSP, and UWFSP samples is ~1.2 µm, ~1.1 µm, and ~1 µm, respectively. In general, FSP induces precipitate coarsening and dissolution due to long periods of thermal exposure. Most of the precipitates in the ACFSP sample are dissolved in the matrix instead of being coarsened, and thus the precipitate density in the ACFSP sample decreased. Because of the additional cooling provided in CCFSP and UWFSP samples, precipitate dissolution was minimized, and the stirring action of the tool fragmented the precipitates into small precipitates. From Fig. 4.21-4.24, it was discovered that the BM and FSP samples consist of two different shapes of precipitates, i.e., needle and round-shaped precipitates. In BM, the needle-shaped precipitates are coarser than precipitates in the round shape. And, the density of needle-shaped precipitates was considerably reduced after FSP, possibly due to intense plastic straining during FSP [Zhao et al., (2019)].

EDS analysis was conducted on the precipitates of BM and FSP samples. In each sample, three different precipitate regions were marked and analyzed. EDS analysis revealed that the BM contains needle-shaped precipitates identified as Fe-based precipitates (Point A) and round-shaped precipitates, identified as Si-based precipitates (Point B). This might be attributed to the initial alloy composition and as-received condition (T6 condition-solution annealed and artificially aged) of raw material. Additionally, the BM also contains a continuous chain of very fine round-shaped precipitates along the grain boundaries (highlighted in white ellipse), and these were also identified as Si-based precipitates (Point C). In particular, this kind of fine precipitates that stick to the grain boundaries can impede the grain boundary sliding and enhance the strength. Moreover, these precipitates significantly affect corrosion behavior.

The EDS results of FSP samples are shown in Fig. 4.22-4.24. As with BM, all FSP samples consist of needle-shaped Fe-based precipitates (Point D, G, and J) and round-shaped Si-based precipitates (Point E, H, and K). However, unlike BM, FSP samples contain a discontinuous network of small round-shaped Si-based precipitates along the grain boundary (Point F, I, and L). This is because, during FSP, the continuous network present in BM is destroyed by tool stirring action, resulting in a discontinuous network of precipitates in FSP samples.

As discussed above, the precipitates present in the alloy greatly influence the mechanical and corrosion behavior. The BM consists of high density of needle-shaped precipitates compared to FSP samples. At the time of tensile deformation, the needle-shaped particles serve as stress concentration sites, resulting in a sudden failure of BM. Thus, compared to FSP samples, the elongation is reduced in BM. At the same time, the needle-shaped particles also act as a barrier for grain boundary migration during tensile and local deformation (local deformation is caused by indentation during hardness test) [Polmear., (2006)]. So, a high concentration of needle-shaped precipitates in BM results in improved hardness and strength than FSP samples. Such compositional analysis of precipitates also influences corrosion behavior. The study by Sinhmar et al., (2017 and 2019) indicated that base alloy corrosion resistance decreased due to a continuous chain of precipitates along the grain boundaries. Compared to discontinuous precipitates present in the FSP sample, the continuous network of precipitates present in BM can quickly form galvanic coupling with the Al matrix. According to Gharavi et al., (2014), in AA6061, the galvanic coupling is made between Fe-based precipitates (needle-shaped precipitates) and Al matrix. In this study, the BM contains more Fe-based precipitates (needle-shaped precipitates) compared to FSP samples, resulting in more galvanic cells being formed in BM. Hence, these results show that BM corrodes more than FSP samples.

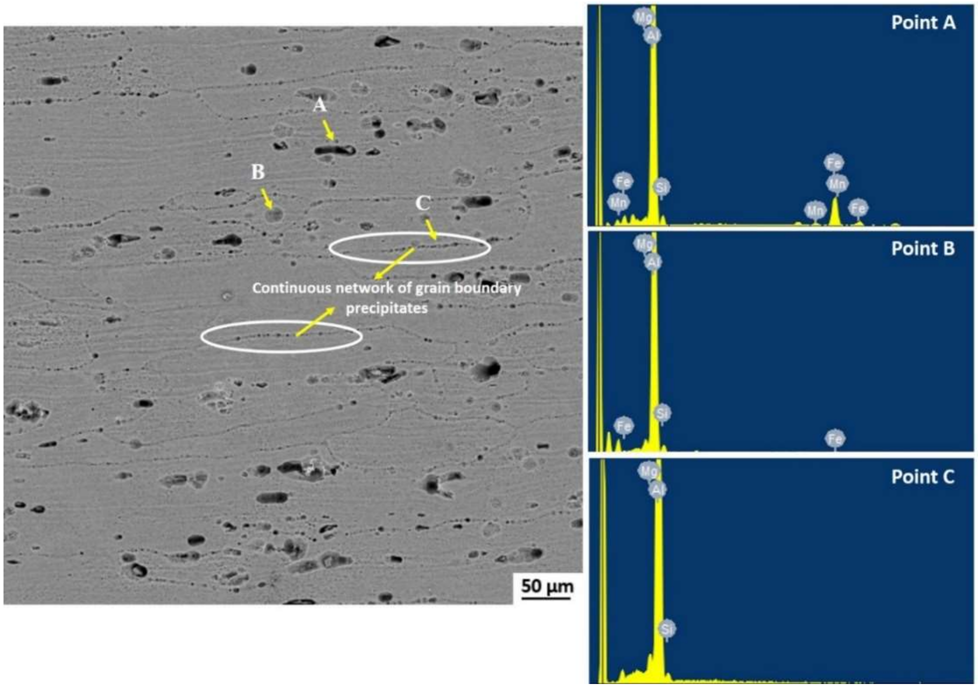

Fig. 4.21. SEM micrograph of base metal along with EDS maps.

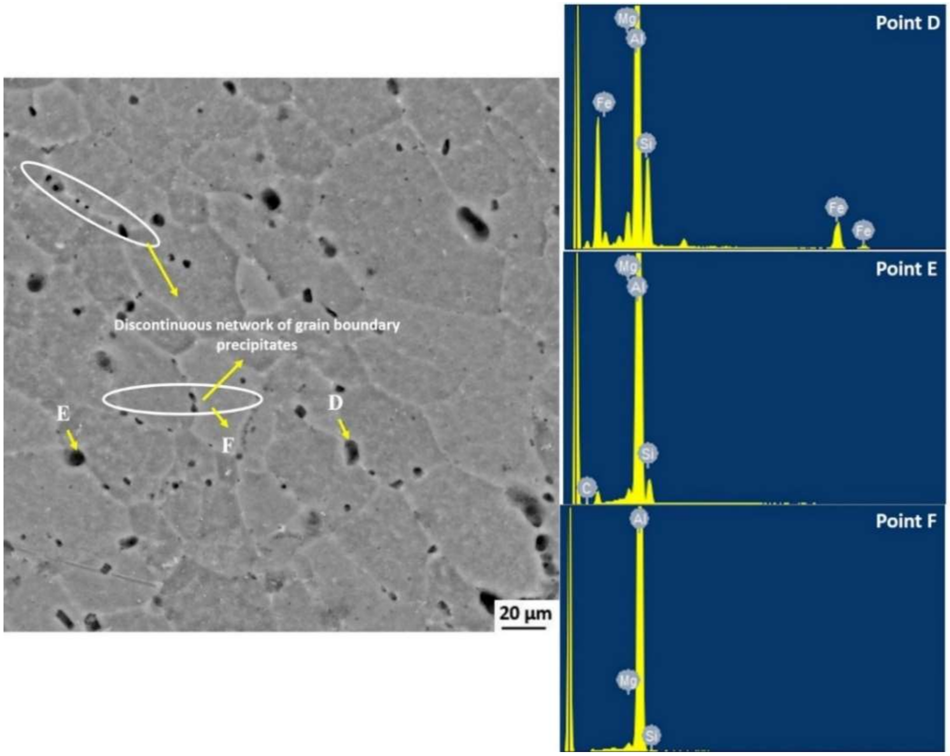

Fig. 4.22. SEM micrograph of air-cooled FSP sample along with EDS maps.

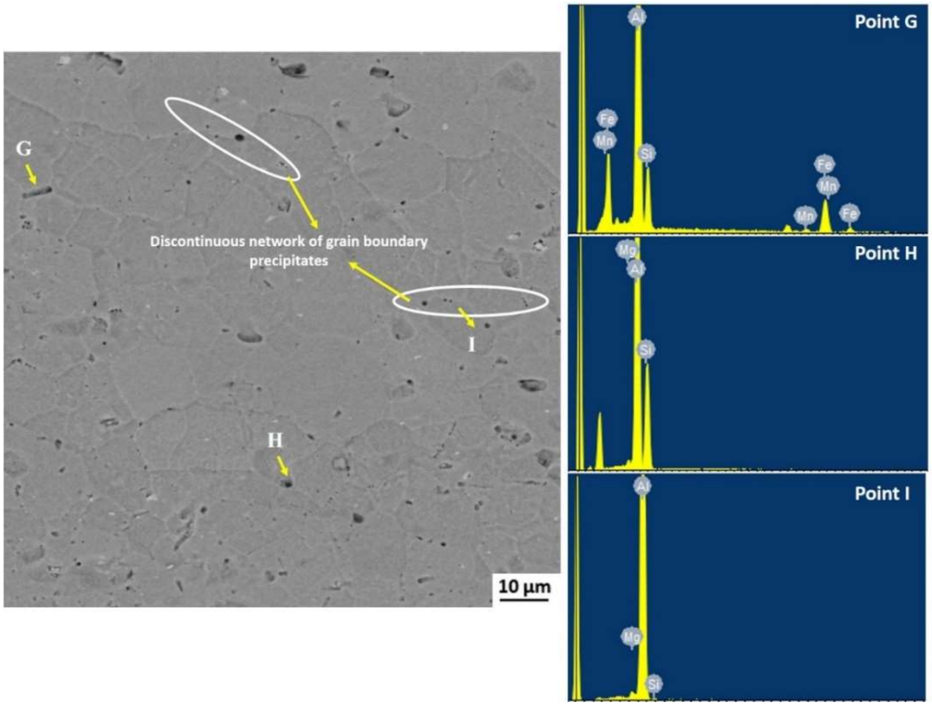

Fig. 4.23. SEM micrograph of cryogenic FSP sample along with EDS maps.

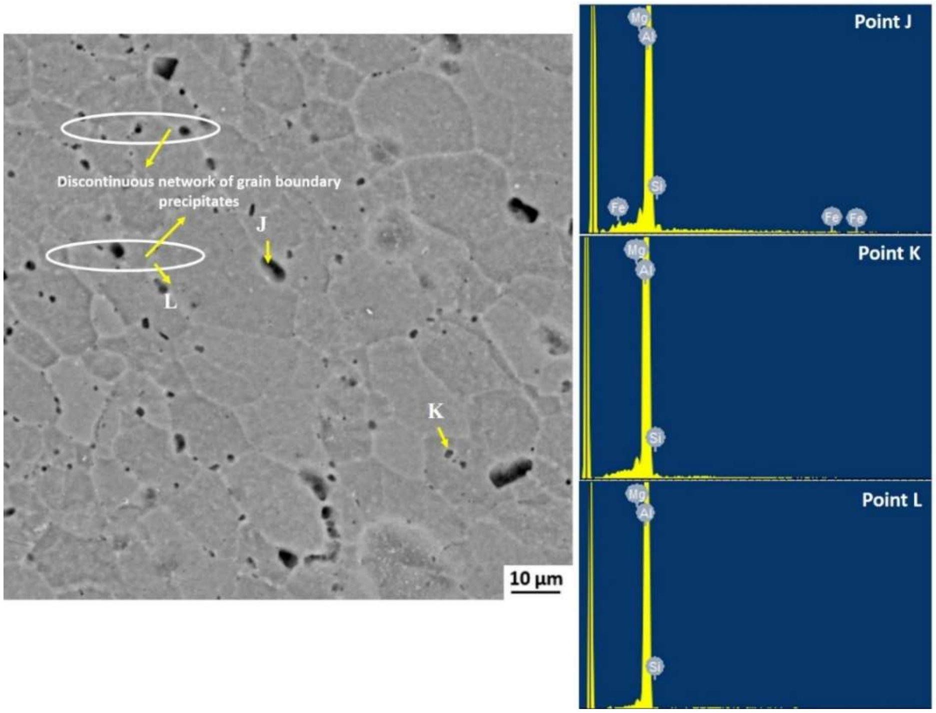

Fig. 4.24. SEM micrograph of underwater FSP sample along with EDS maps.

4.3.2 Mechanical properties

4.3.2.1 Hardness

Initially, the average hardness was measured with an interval of 0.5 mm across the SZ of each FSP sample. The average hardness of BM, ACFSP, CCFSP, and UWFSP samples was 91 HV, 65 HV, 78 HV, and 85 HV, respectively. The average hardness in the SZ of FSP samples decreased compared to BM. The decrease in hardness of SZ in FSP samples is attributed to thermal annealing and softening. AA6061 alloy is well known to be a precipitation hardening alloy, with the precipitation factor in these alloys influencing mechanical properties of the FSP sample rather than the grain refinement factor. The precipitates dissolve and coarsen due to more prolonged thermal exposure at elevated temperatures (0.6-0.7 T_{MP}, where T_{MP} is melting point temperature of BM) during FSP [Chen et al., (2016)]. So, in FSP samples, the hardness was found to decrease compared to BM. In FSP samples, the highest hardness was attained in cooling-assisted FSP samples due to increased grain refining, fine precipitates, and decreased precipitate dissolution. As discussed in the microstructural section, the rapid cooling effect induced by water resulted in more grain refinement and higher hardness among FSP samples. These findings coincide well with the results reported in microstructure analysis.

The hardness distribution map of FSP samples along the processing zone is shown in Fig. 4.25. The hardness profile followed the 'W' trend. This trend is attributed to the grain refining and precipitation behavior in each zone of FSP samples. This trend is symmetrical about the center of the processing zone. The hardness in each zone is in the order SZ>TMAZ>HAZ; the highest and lowest hardness in the SZ and HAZ are related to grain size as per the Hall-Petch equation. According to this relation, fine grains in SZ resulted in high hardness, while coarse grains in HAZ resulted in low hardness. The features of TMAZ are always found between SZ and HAZ, as that zone experiences little mechanical stirring action along with a longer thermal cycle.

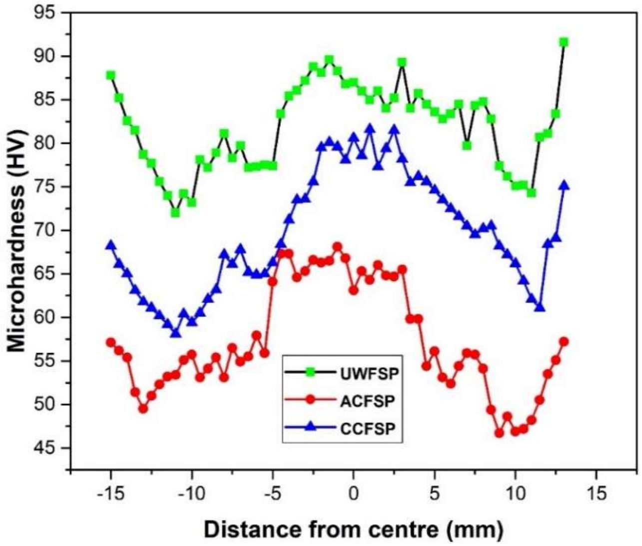

Fig. 4.25. Hardness profile of FSP samples.

4.3.2.2 Tensile properties

The stress-strain trends of the BM and FSP samples are shown in Fig. 4.26. As a whole, the trends of BM and FSP samples show ductile nature. The tensile properties were extracted from the stress-strain curve and reported in Table 4.13. The tensile test results corroborate the hardness results. The ultimate tensile strength (UTS) of FSP samples was lower than that of BM due to thermal softening, as stated in hardness analysis. In contrast, the ductility of the FSP sample was found to be improved compared to BM due to recrystallized fine grains in SZ. Khaled et al., (2014) reported that the drop in strength of FSP samples was due to the dissolution of second phase particles and restriction of re-precipitation during processing. Chen et al., (2016) also obtained similar tensile results and stated that improvements in ductility were due to homogeneous recrystallized fine-grained structure and low dislocation density in SZ. The fine precipitates formed in UWFSP samples can be effectively pinned to the grain boundaries and impede the grain boundary sliding, resulting in high strength among all FSP samples. In contrast to strength, in cooling-assisted FSP, the lowest elongation was found as rapid cooling introduces brittle nature in the samples.

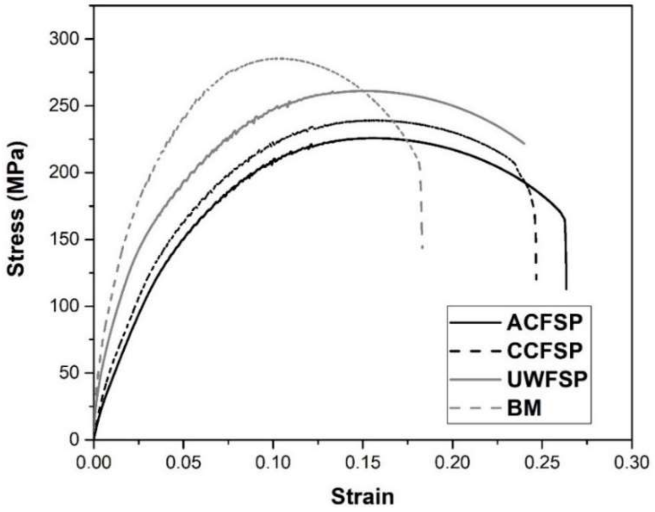

Fig. 4.26. Stress-strain curves of BM and FSP samples.

Table 4.13 Tensile properties.

S. No.	Condition	UTS (MPa)	YS (MPa)	EL (%)
1	BM	285±3	192±3	18.3±2.5
2	ACFSP	224±2	105±3	26.2±3.4
3	CCFSP	240±2	101±2	24.6±3.7
4	UWFSP	261±3	105±3	24.0±3.2

The morphology of the tensile fractured specimens is shown in Fig. 4.27. AA6061 base alloy is known to be a purely ductile material. So, BM contains high volume large and shallow dimples, as shown in Fig. 4.27a. And these are accounted under the category of pure ductile failure. On the other hand, the FSP samples revealed small dimples compared to BM, and the depth of the dimples decreased in FSP samples (Fig. 4.27b-d). These results could be ascribed to the presence of homogeneous refined grains and material flow during FSP. Therefore, the fracture features of the ACFSP sample consist of a large volume of fine dimples and are considered a ductile failure (Fig. 4.27b). In contrast, the fracture features of the cooling-assisted FSP sample comprise a high volume of fine dimples and a low volume of flat regions (Fig. 4.27c&d). Therefore, these failures are classified under a combination of brittle and ductile failure.

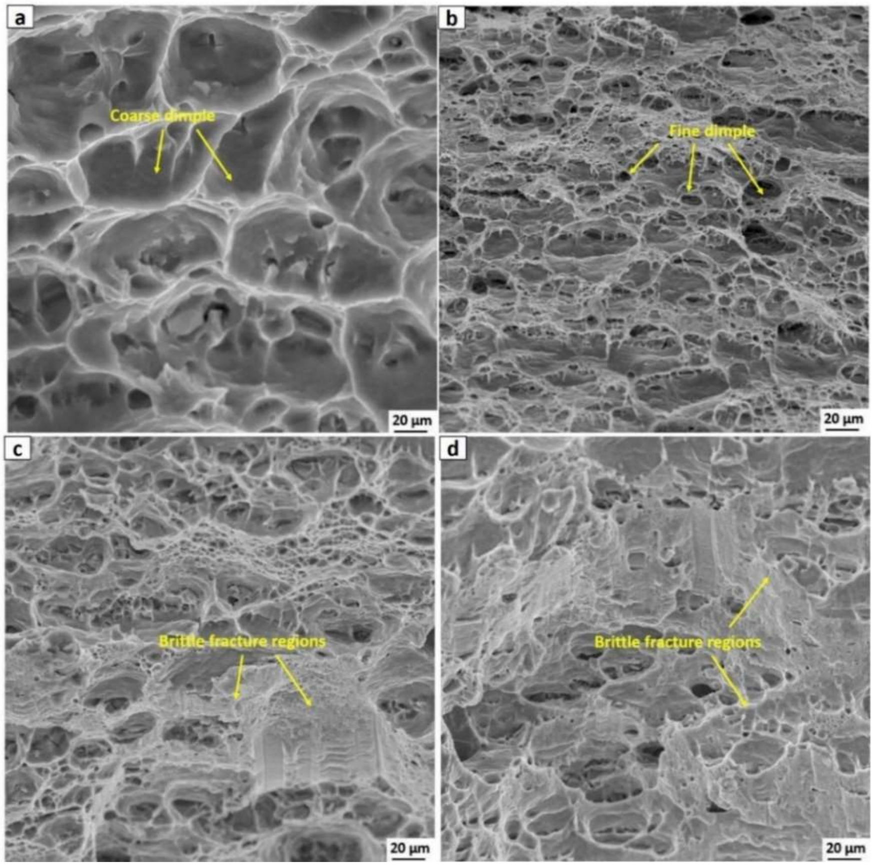

Fig. 4.27. Fracture images of (a) Base metal, (b) Air-cooled FSP, (c) Cryogenic FSP, and (d) Underwater FSP samples.

4.3.3 Corrosion

4.3.3.1 Open-circuit potential

The open-circuit potential (OCP) test was initially performed at ambient temperature in a 3.5% NaCl solution to ensure the potential range for the Tafel polarization test. The OCP trends of BM and FSP samples are illustrated in Fig. 4.28. From the OCP trend, it was observed that the potential of OCP trend (V_{OCP}) of the UWFSP sample was maintained constant throughout the process, and it is evident that the corrosion attack is uniform. The initial V_{OCP} of BM and ACFSP samples was -810 mV and -788 mV, respectively, and it increased gradually with time to a maximum value of -785 mV and -776 mV, respectively after 600 s. Whereas the initial V_{OCP} of CCFSP samples is -604 mV which decreased gradually to -642 mV after 229 s and immediately increased to -633 mV after 233 s; the voltage was stable up to 486 s and gradually decreased to the final value of -648 mV s after 600 s. The increasing trend of V_{OCP} in the earlier stages could be attributed to the formation of a protective oxide layer on the attacking region of the working sample, and the decreasing trend of V_{OCP} might be on account of the dissolution of that protective oxide layer by the continuous attack of electrolytic solution on the sample surface [Samar et al., (2011)]. The final V_{OCP} values of BM and FSP sample are shown in Table 4.14. The results showed that the corrosion resistance improved after FSP as the final V_{OCP} of FSP samples is more than that of BM. This is because the BM undergoes intense plastic straining and dynamic recrystallization during FSP, resulting in the homogeneous fine-grained microstructure. The homogeneous microstructure strictly prevents the possibility of galvanic coupling and results in improved corrosion resistance [Mahdi et al., (2019)].

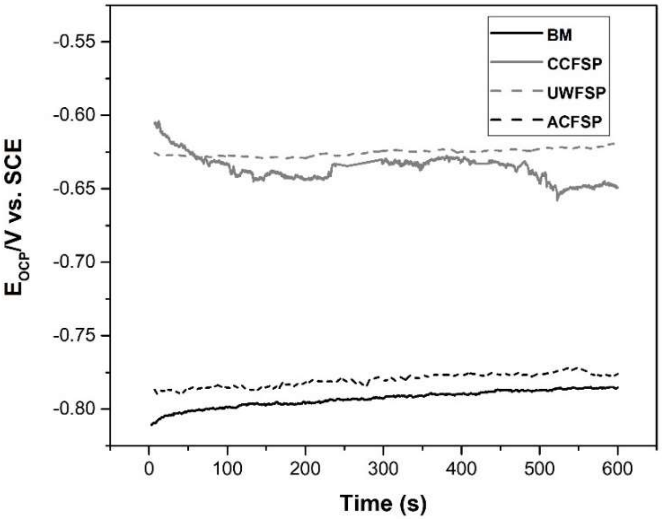

Fig. 4.28. OCP trends of BM and FSP samples.

Table 4.14 Open-circuit potentials.

Sample condition	BM	ACFSP	CCFSP	UWFSP
V_{OPC} (mV)	-785	-777	-620	-648

4.3.3.2 Tafel polarization test

Tafel curves obtained from the electrochemical polarization experiments, shown in Fig. 4.29, and corrosion potentials (E_{COR}) of BM and FSP samples were extracted from the Tafel curves are documented in Table 4.15. It is well known that the highest negative E_{COR} represents low resistance to corrosion attack and vice versa. It was identified from Tafel curves that the E_{COR} of BM showed more negative value than the E_{COR} of FSP samples, which made it evident that corrosion resistance significantly improved after FSP.

In general, corrosion occurs due to potential difference between cathode and anode, and less potential difference implies better corrosion resistance. During corrosion, the anode (more negative E_{COR}) is a more vulnerable element to corrosion attack where oxidation reaction occurs, whereas cathode (less negative E_{COR}) is a less vulnerable element to corrosion attack where reduction reaction occurs. The basic corrosion reactions of Al in aerated solutions are given below [Xu et al., (2009)].

Anode or oxidation reaction:

$$Al - 3e \rightarrow Al^{3^{+}} \qquad (1)$$

Cathode or reduction reaction:

$$3H + 3e \rightarrow 3/2\ H_2 \qquad (2)$$

During the Tafel polarization test, the reduction reaction induces the evolution of hydrogen identified on the surface of the cathode. The reduction reaction results in Al surface dissolution, as it serves as anode relative to adjacent precipitates. In the present analysis, the Al matrix functions as anode while the precipitates near and along the grain boundaries function as cathode. As discussed, the E_{COR} of the cathode is more than that of the anode, and so it dissolves and corrodes the Al matrix surrounded by precipitates. The galvanic cells are made between the Al matrix and precipitate along the grain boundaries due to the potential difference between them. In Fig. 4.21-4.24 (SEM images along with EDS maps), it was mentioned that the BM consists of high density and continuous chain of precipitates along the grain boundaries. In contrast, the FSP samples consist of low density and discontinuous precipitates along the grain boundaries, respectively. The galvanic coupling was made between the coarse precipitates and the Al matrix in BM, resulting in more potential difference than in the galvanic coupling between the fine precipitates and Al matrix [Navaser et al., (2017)]. Factors like discontinuous precipitate along the grain boundaries and a large potential difference in the BM result in the samples becoming more susceptible to corrosion attack. Besides, the fine-grained structure present in FSP samples has an excellent capacity to develop passive (oxide) film than the coarse-grained structure present in BM, and the passive film acts as a proactive layer and prevents corrosion attack [Sinhmar et al., (2018)]. Hence, FSP samples are more resistant to corrosion than BM. Due to the presence of fine-grained structure, the samples processed in cooling-assisted FSP resulted in more corrosion-resistant samples within FSP samples. The findings of the polarization test are in line with OCP and SEM results.

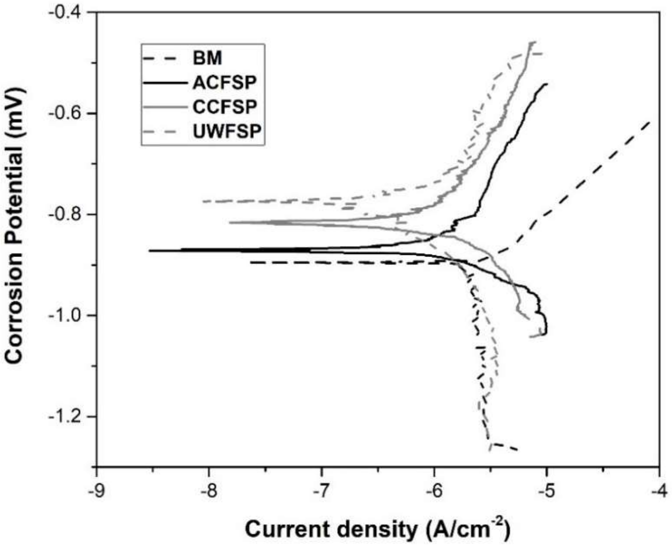

Fig. 4.29. Tafel curves of BM and FSP samples.

Table 4.15 Corrosion potentials.

Sample condition	BM	ACFSP	CCFSP	UWFSP
E_{COR} (mV)	-909	-880	-785	-767

4.3.3.3 Weight-loss test

Findings of weight-loss tests such as weight loss and corrosion rate of BM and FSP samples after 20-days immersion in 3.5% NaCl solution are listed in Table 4.16. From Table 4.16, it was observed that the rate of corrosion in the FSP sample reduced compared to BM because of the presence of a homogeneous microstructure in the SZ. Compared to non-homogeneous microstructure in BM, the homogeneous microstructure in FSP samples strictly prevents the formation of galvanic cells, resulting in improved resistance to corrosion. As already mentioned, AA6061 cold-rolled plates were chosen as BM. However, more defects were produced during cold-rolling, such as point defects, vacancies, and dislocations; cold-rolling also causes the growth of casting defects already present in it. These defects (other than dislocations) lead to galvanic coupling with Al-matrix during the immersion test and corrode the samples [Mahdi et al., (2019)]. Hence, the homogeneous microstructure and minimization of defects in FSP samples result in greater corrosion resistance than BM.

Table 4.16 Weight loss test results

Sample condition	**Weight loss (mg/cm^2)**	**Corrosion rate (mpy)**
BM	0.00123	0.0031
ACFSP	0.00068	0.0017
CCFSP	0.00045	0.0011
UWFSP	0.00026	0.0006

In BM, the severe corrosion attack was seen in the form of large pits (Fig. 4.17a&b). On the other hand, the less severe corrosion attack was seen in the FSP samples (Fig. 4.17c-h), and these findings comply with weight loss test results. The corrosion attack in FSP samples is almost uniform, and small pits were identified over the surface. The corrosion attack on precipitates and grain boundaries are depicted in Fig. 4.17d, 4.17f, and 4.30h. Of all FSP samples, the minimum amount of corrosion attack was seen in the UWFSP sample, and the findings agree with the results of the weight loss test.

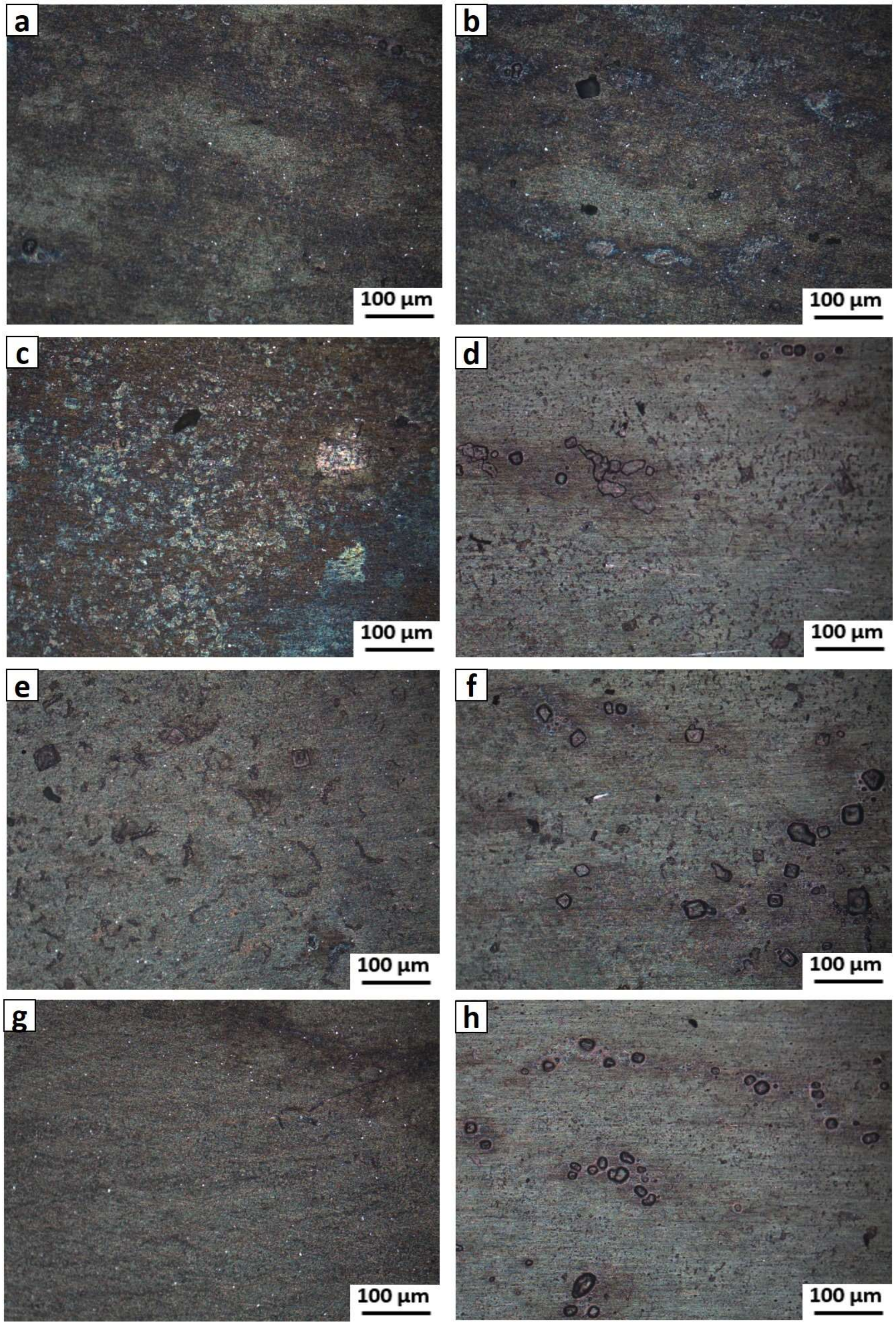

Fig. 4.30. Corroded images of (a&b) Base metal, (c&d) Air-cooled FSP, (e&f) Cryogenic FSP and (g&h) Underwater FSP samples.

4.4 Fabrication of large-area stir zone in AA2014 alloy via overlapping friction stir processing using different cooling media

As discussed in previous chapters, the stir zone prepared using single-pass FSP is not used for practical applications. To overcome this difficulty, the large-area SZ of the required size is prepared by several consecutive passes with the pin overlapping, as shown in Fig. 3.5. For overlapping FSP, the overlapping ratio is the primary factor to decide the distance between the successive paths. There are different overlapping ratios from 0-1, which are considered for performing overlapping FSP, but the frequently used overlapping ratios are 0, 0.25, 0.5, 0.75, and 1. Researchers have suggested that FSP with 50% pin overlapping (i.e., 50% overlapping ratio) produces a large-area SZ with homogeneous microstructure in all FSP passes [Ramesh et al., (2012), Gandra et al., (2011), Alavi Nia et al., (2014) and Xue et al., (2013)]. From Section 4.1, it was observed that the defect-free structure with better mechanical properties was obtained at tool rotational speed of 1100 rpm and traverse speed of 30 mm/min. The hexagonal pin tool produces better mechanical properties than other tools at the same processing conditions (i.e., 1100 rpm-30 mm/min) in overlapping FSP of AA2014 alloy. With optimized process parameters and tool geometry, a 5-pass overlapping with 50% pin overlapping was performed in different cooling environments to produce the large-area stir zone in AA2014. The findings of large-area stir zone such as microstructure, texture, precipitation behavior, mechanical properties, corrosion, wear, fatigue behavior were discussed in the following sections.

4.4.1 Optical microscopy

The optical low-magnification representations of the overlapping FSP samples identified with distinct regions are displayed in Fig. 4.31. Proper selection of process parameters and overlapping ratio resulted in quality structure, faultless macrostructure, and homogeneous processed region through the entire thickness in the large-area SZ. The multi-pass overlapping FSP sample contains four different regions, large-area SZ, thermo-mechanically affected zone (TMAZ), heat-affected zone (HAZ), and unaffected region, or BM, as reported by Fadhalah et al., (2014) and Ramesh et al., (2012). The present study also showed similar features on AA2014 alloy, as shown in Fig. 4.31, where the left side of SZ was the advancing side (AS), and the right side of SZ was the retreating side (RS). A sharp transition boundary was identified on AS, while the diminished transition boundary was identified on RS, and the transition boundary disappeared. On AS, the tool travel and the tool rotation were in opposite directions, leaving a sharp boundary as a sign of opposite nature. In contrast, the same direction of tool rotation and tool travel on RS left a light boundary. As already mentioned, the large-area SZ was generated by five-pass FSP, and these passes were marked 1, 2, 3, 4, and 5 in large-area SZ, as shown in Fig. 4.31. Swirl patterns formed near AS symbolizing material flow due to the stirring action of the tool. The swirl patterns were supposed to be identified throughout the large-area SZ. As the overlapping was done in the direction of AS, it eliminated the swirl patterns and sharp boundary formation on AS after each pass. Sato et al., (2005) identified oxide clusters and defects due to increased heat input at the work-tool interface, causing degradation of mechanical properties. Due to optimized process parameters and the provision of cooling media, which reduce heat generation, no such oxide layers or defects were identified in the present study. As the overlapping was done towards the advancing side, it removed the flashes and irregularities produced in the advancing side, resulting in a uniform flow of material in the SZ [Gandra et al., (2011)].

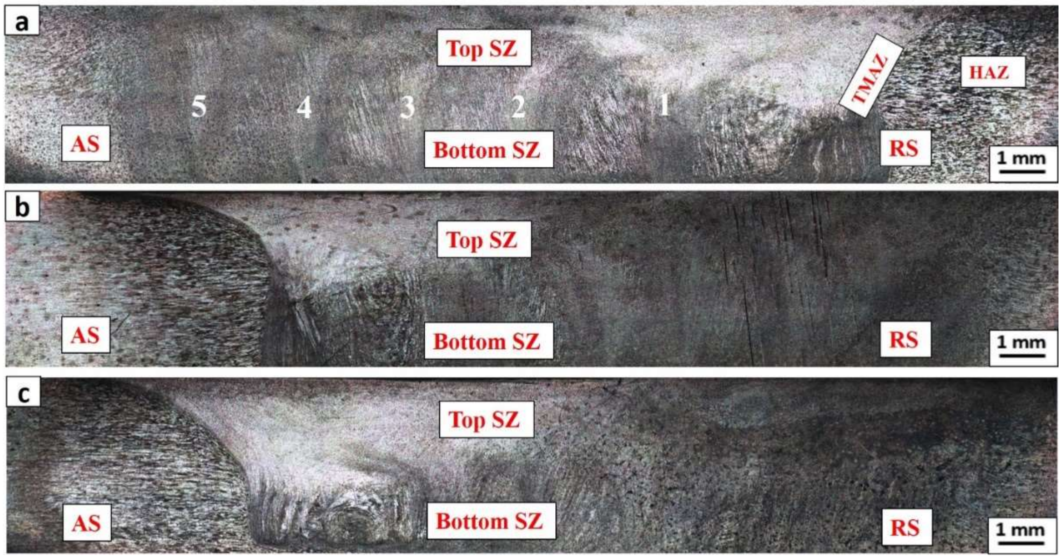

Fig. 4.31. Low-magnification optical images of overlapping (a) Air-cooled, (b) Dry ice, and (c) Underwater FSP samples indicated with distinct regions.

The optical micrographs of the FSP sample in SZ of each overlapping pass (labeled as 1 to 5) are shown in Fig. 4.32-4.34**,** indicated with grain size (GS). After FSP, the microstructure was refined entirely in the SZ. As a whole, the microstructure in SZ comprises equiaxed refined grains of α-aluminium matrix, which are evidence of severe plastic deformation (SPD) and high-temperature exposure during processing. As illustrated in Fig. 4.32-4.34, further overlapping FSP did not influence the difference in grain size in the upper and lower SZ areas. The average grain size in large area SZ of air-cooled, dry ice-cooled, and underwater FSP samples was measured 4.6±3.2 µm, 4.1±2.8 µm, and 0.9±0.6 µm. Within the SZ, the grain size is little varied from top to bottom. The ratio of the coarse to average grain size (C) varied from 1.9-2.4. The term C is used to forecast the abnormal grain growth (AGG), and AGG is the reason for grain size variation in the top and bottom regions SZ [Chen et al., (2016)]. The grains in the upper regions of SZ are coarser than those in the lower regions of SZ. At the upper zone, the refinement was due to the stirring action of both shoulder and pin (mainly due to shoulder). As the size of the shoulder is more than the pin, this resulted in high linear velocity at the upper zones as per equation V = W.R (V- linear speed, W- rotational speed of the tool, and R- radius of the tool at pin or shoulder), producing more heat (more than 75%) at upper region [Chen et al., (2016)]. Xu et al., (2009) showed that the upper zones of SZ were exposed to high temperature for a longer duration so that upper zones of stir regions have slightly coarser grains compared to regions below them (Fig. 4.32-4.34a). At the bottom of SZ, the refinement was only due to the stirring of the pin, which experiences shorter thermal cycles due to the lower linear velocity of the tool at the pin region. Moreover, the stirring action at the end of the pin causes more swirling action [Zhao et al., (2014)]. As a result, more refined grains are formed at the bottom of the SZ (Fig. 4.32-4.34b).

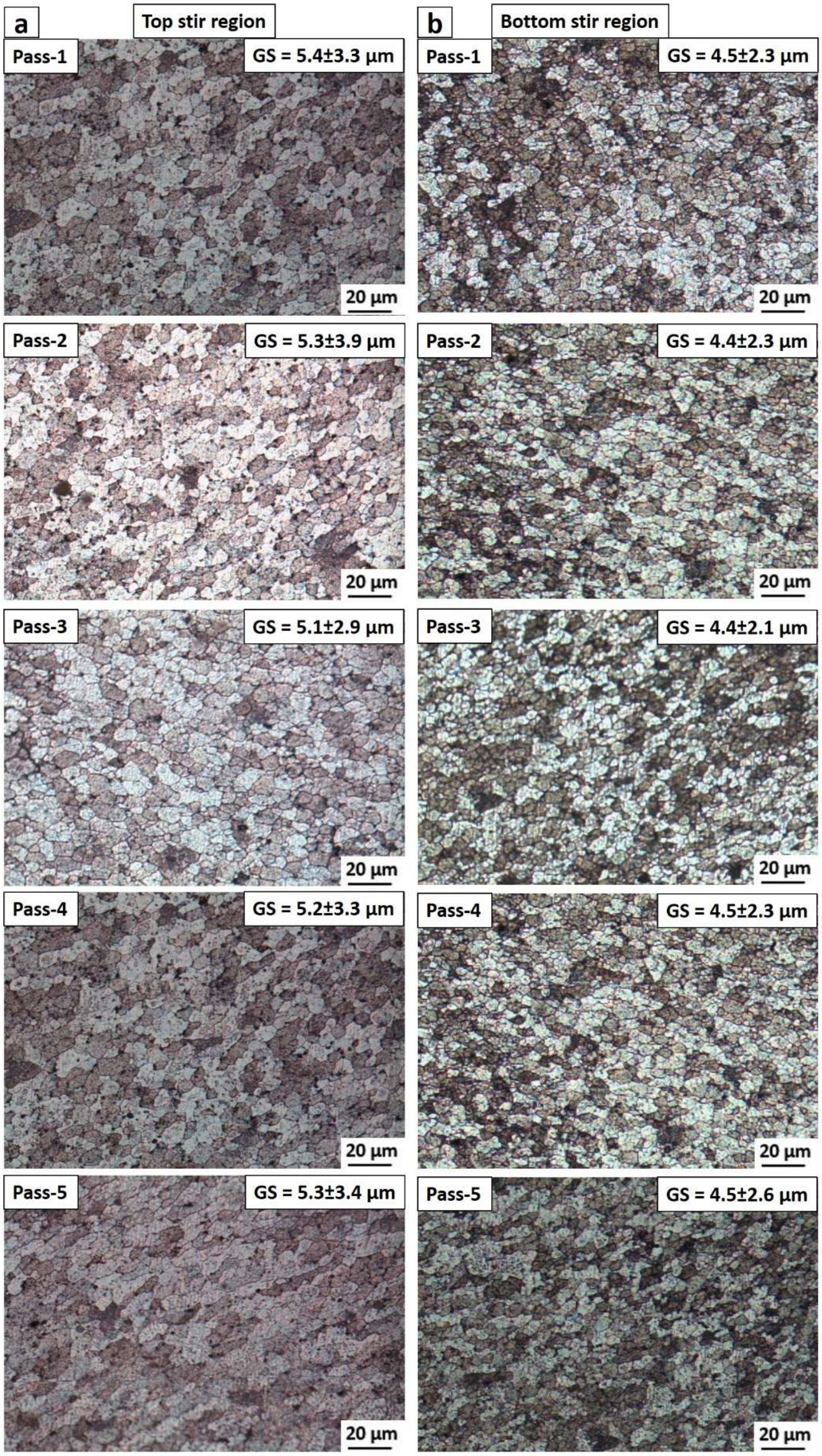

Fig. 4.32. Optical micrographs of (a) Top and (b) Bottom stir zones of air-cooled FSP sample.

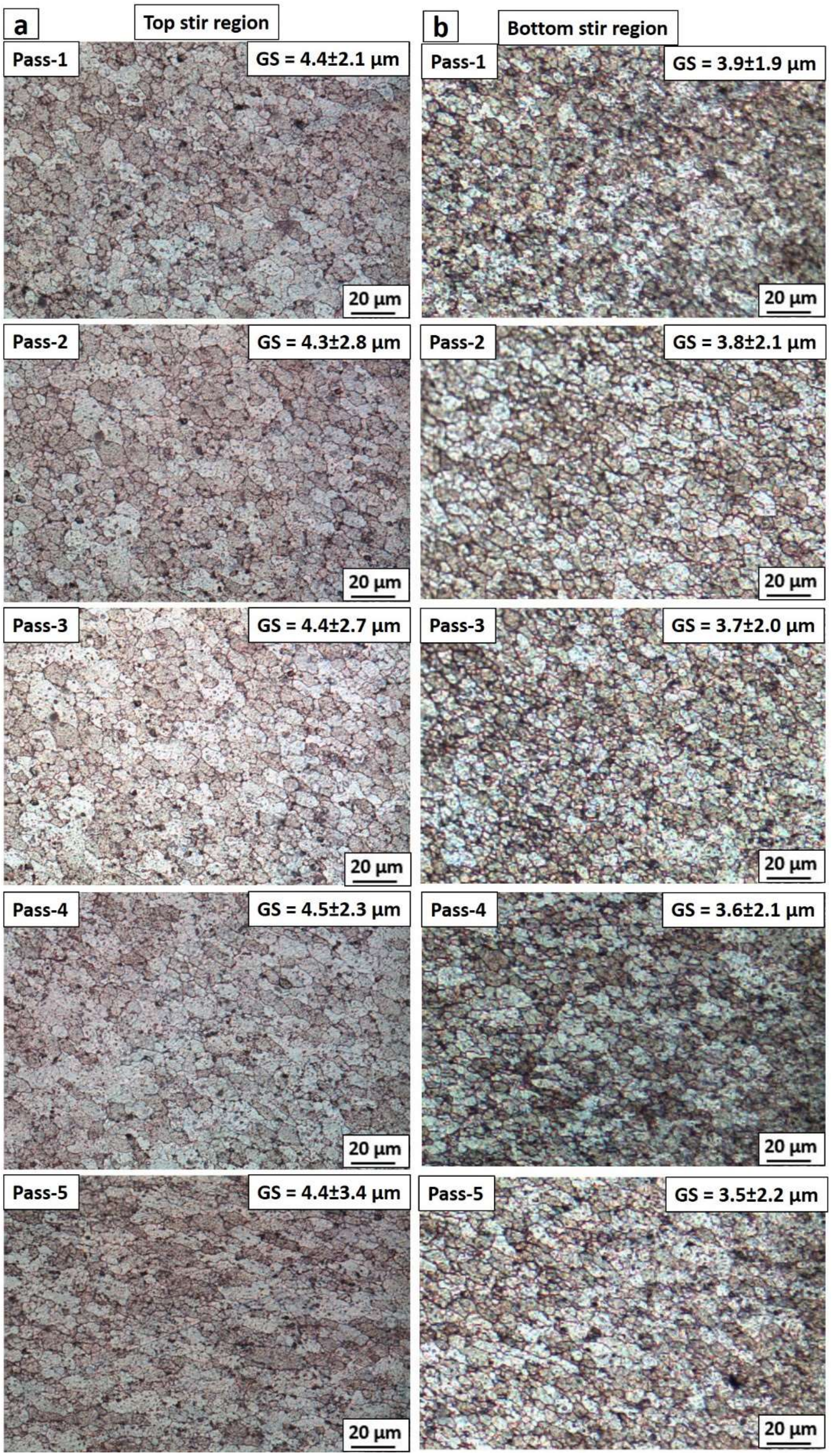

Fig. 4.33 Optical micrographs of (a) Top and (b) Bottom stir zones of dry ice FSP sample.

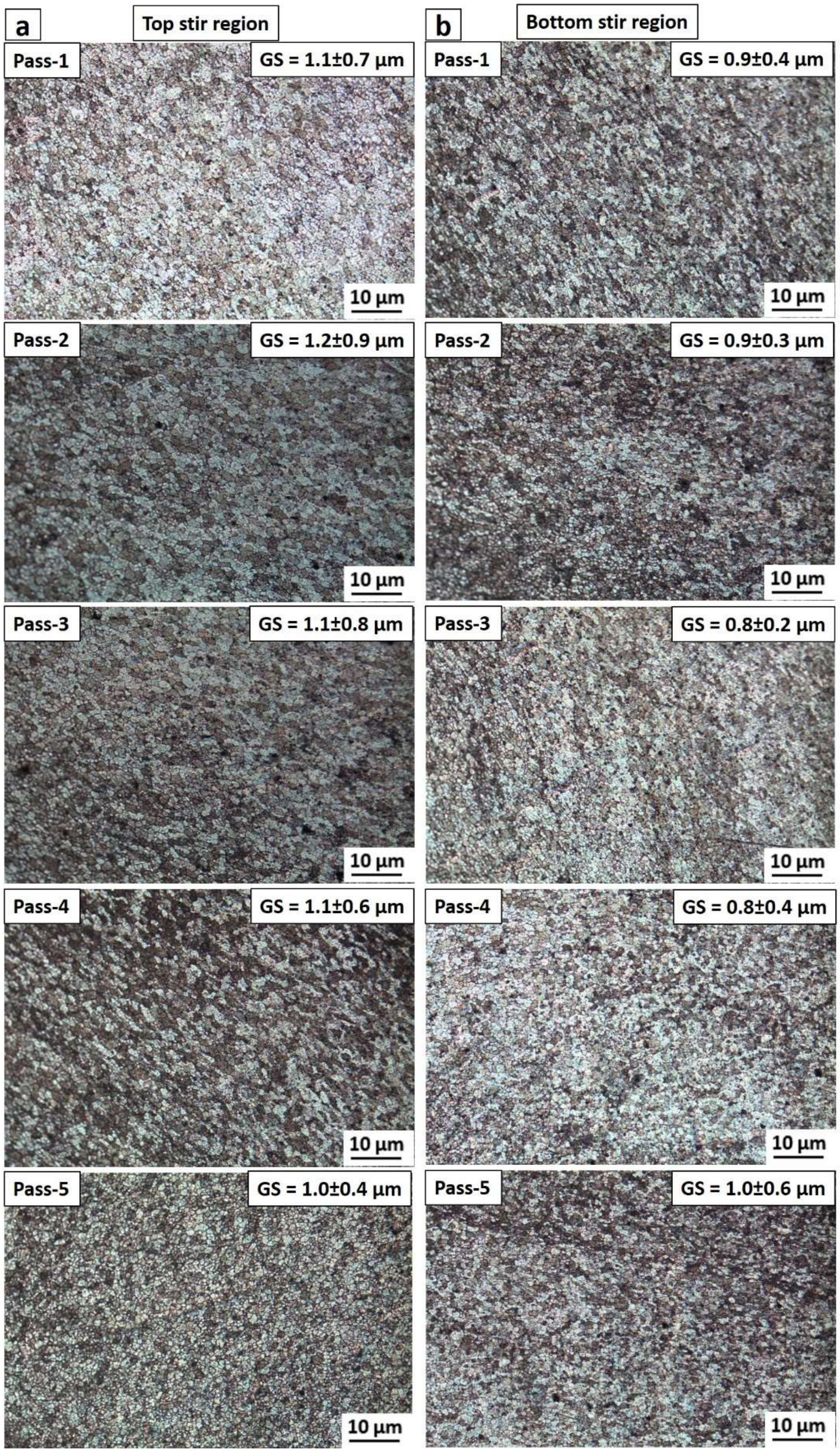

Fig. 4.34. Optical micrographs of (a) Top and (b) Bottom stir zones of underwater FSP sample.

4.4.2 EBSD analysis

The microstructure of the FSP sample was further discussed in detail using EBSD. Initially, EBSD analysis was made at the center of the large-area stir zone for all FSP samples. And, to better understand the microstructure and texture evolution in each overlapping pass, EBSD analysis was then made on each pass of the large-area stir zone in air-cooled FSP.

4.4.2.1 Microstructure evolution during FSP

The EBSD maps of BM and the center of the large-area stir zone of FSP samples are shown in Fig. 4.35. After FSP, the coarse grain structure in BM transformed to recrystallized fine grains in SZ of all FSP samples. The average grain size in the base metal and center of the large-area SZ of air-cooled, dry ice-cooled, and underwater FSP samples are 80.5±50.5 µm, 4.6±3.2 µm, 4.1±2.8 µm, and 0.89±0.6 µm. As discussed, the underwater FSP resulted in the production of the UFG structure due to the rapid cooling effect, which controlled the grain coarsening during FSP.

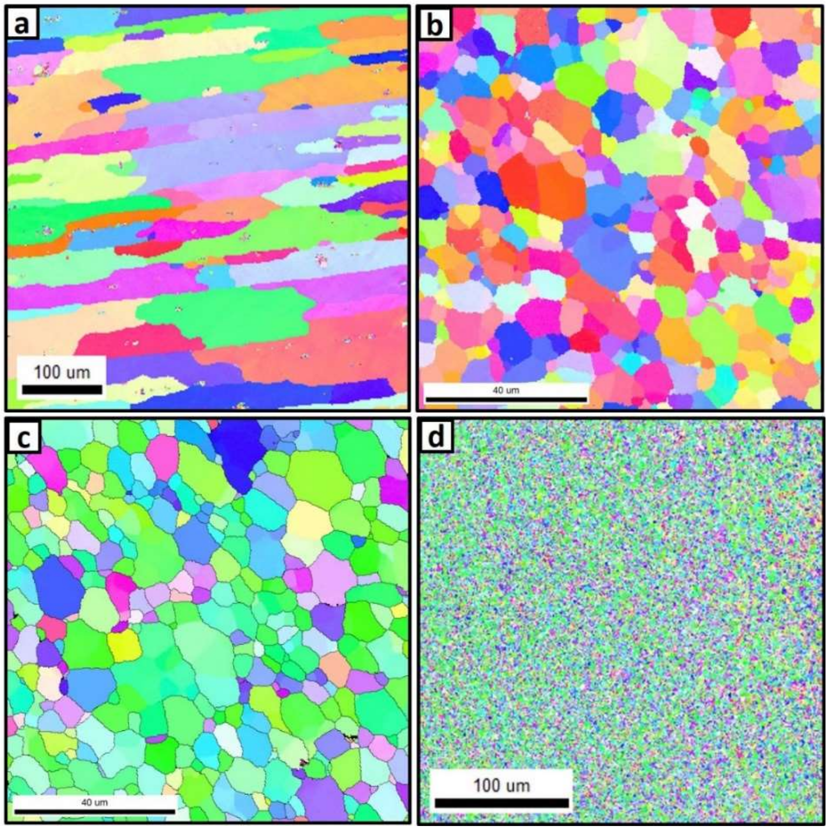

Fig. 4.35. EBSD microstructures (IPF + grain boundary) of (a) ACFSP, (b) CCFSP, and (c) UWFSP samples.

Fig. 4.36 displays the EBSD maps, EBSD recrystallization maps of each pass of the air-cooled FSP sample. The statistical data obtained from the EBSD study, such as grain size and boundary misorientation, are recorded in Table 4.17. After FSP, the microstructure was wholly refined. Likewise, the fraction of high angle boundaries (HABS) increased due to intense plastic straining. Moreover, each overlapping pass's grain size is approximately uniform (see Fig. 4.36a-e and Table 4.17). Hence, the results of EBSD have confirmed the grain size results of optical microscopy. Histograms of various kinds of grain distribution are displayed in Fig. 4.36k-o, and it represents the fraction of deformed, recrystallized, and substructure grain boundaries along with boundary misorientations. From Fig. 4.36k-o**,** it was noticed that the fraction of recrystallized grains increased with an increase in overlapping passes due to increased heat input and plastic deformation [Khodabakhshi et al., (2018)].

Various mechanisms such as dynamic recovery (DRV), geometric DRX (G-DRX), discontinuous DRX (D-DRX), and continuous DRX (C-DRX) are involved in grain refinement and angle misorientation during FSP [Zhao et al., (2019)]. During FSP, the materials undergo SPD with high strain rates at high temperatures. Metals with high stacking fault energy (SFE) such as aluminium are restored by DRV at high temperatures when subjected to SPD than those with low SFE such as Mg and Cu **[**McNelley et al., (2008)**]**. During earlier stages of SPD, the flow stress increases, leading to increased dislocation density and interaction. The dislocation density and interaction continue to increase as the DRV rate rises, and these dislocations begin to rearrange themselves to form sub-grain LABS with a 2°-5° angle of misorientation. Subsequently, the flow stress exceeded the threshold limit as increased dislocation density due to dislocation rearrangement and finally, leading to dynamic equilibrium. The dynamic equilibrium induces steady-state deformation at constant flow stress. Upon steady-state deformation, the subgrain LABS coalescence starts and forms into LABS (2°-5°). Moreover, the C-DRX starts when the size of the subgrains reaches a critical value, and this C-DRX causes subgrains to migrate and rotate. New strain-free grains are formed during the migration mechanism and grow within the deformed zone, i.e., in the SZ, whereas the rotational mechanism causes the increase in angel misorientation of subgrains into HABS (> 15^0) formation. It has been established that the formation of sub-grains depends on the Zener-Hollomon parameter and given by [Su et al., (2005)]:

$$Z = \epsilon \exp(Q/RT) \qquad (4.1)$$

Where Q – activation energy, ϵ- strain rate, R- gas constant, and T- temperature. The D-DRX usually occurred in metals with low SFE, while G-DRX involves the formation of serrated boundaries so that in the present study, the presence of D-DRX and G-DRX is not shown. Along with the above restoration mechanisms, the incorporation of reinforcements also serves as nucleation sites for grain refinement, and this process is called particle stimulated nucleation (PSN). Furthermore, incorporated reinforcements can impede the grain boundary sliding by pinning them as per the Zener-Holloman mechanism. The authors did not use any reinforcement particles, and therefore the occurrence of PSN and Zener-Holloman mechanisms are not found in the present study. Hence, it has been identified that the DRV and C-DRX mechanisms are dominant restoration mechanisms in the FSP of AA2014.

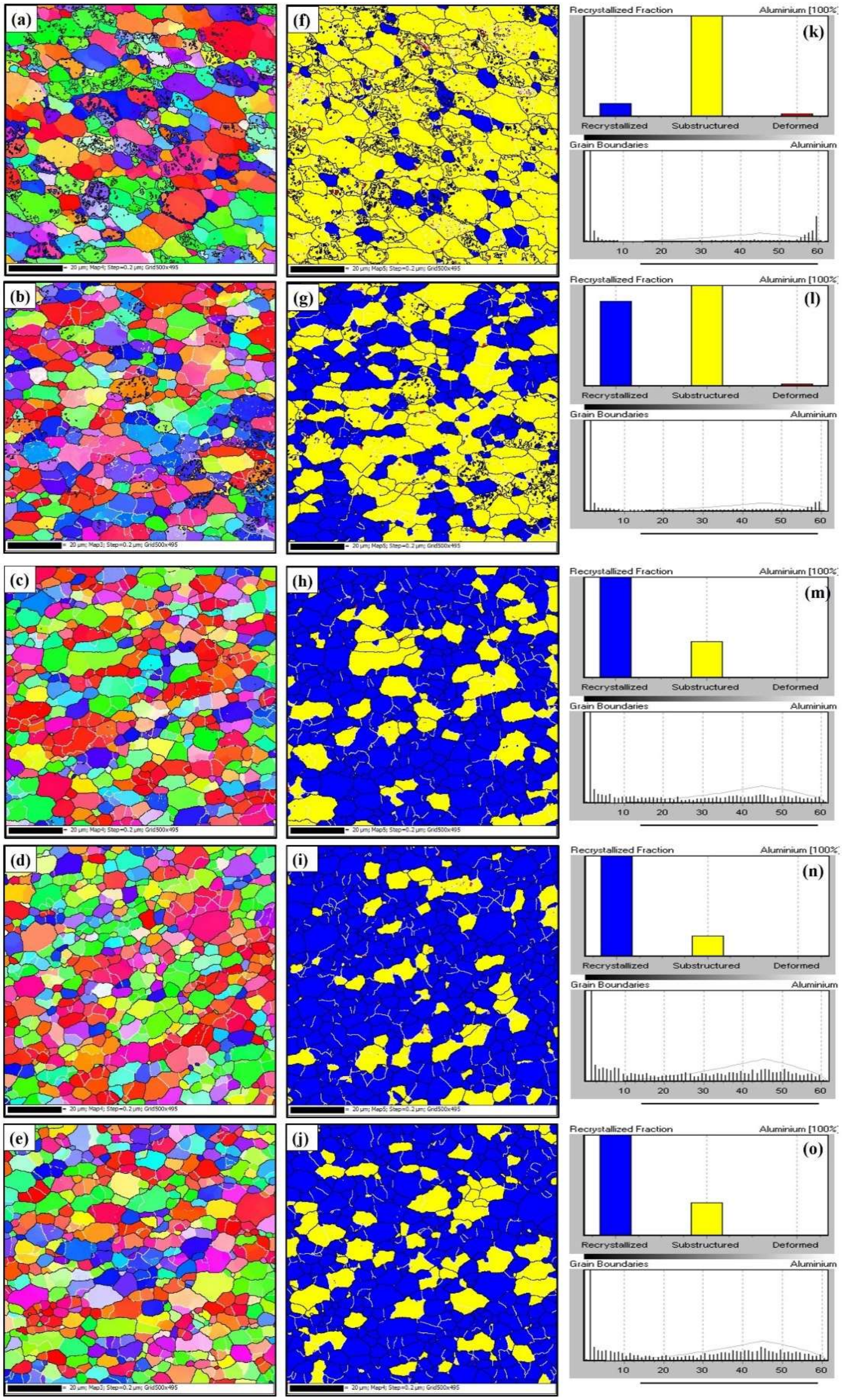

Fig. 4.36. (a-e) EBSD microstructures, (f-j) EBSD recrystallized maps and (k-o) Fraction of grain boundaries of ACFSP sample from 1 to 5th pass.

Table 4.17 Statistical data of EBSD analysis (ACFSP sample).

Overlapping Passes	Average grain size (µm)	Standard deviation (µm)	Fraction of LABS (%)		Fraction of HABS (%)
			2°-5°	5°-15°	15°-180°
Pass-1	4.79	2.54	16.0	18.5	65.5
Pass-2	4.53	2.48	16.1	18.9	65.0
Pass-3	4.49	2.80	14.3	18.5	67.1
Pass-4	4.59	2.27	15.3	9.20	75.5
Pass-5	4.80	2.16	13.8	2.6	83.6

4.4.2.2 Texture evolution during FSP

Texture formation is related to the deformation mechanism during friction stir processing. In general, SPD grain refinement is accomplished by throwing the different sheared parts of the original grains into different texture components, and those texture components are described in this section. During FSP, the material flows in a complicated nature. However, the deformation in FSP/FSW is well known to be a simple shear texture. Fig. 4.37 shows ideal shear deformation texture components of FCC metals in {111} pole figure (PF), and the main ideal orientations are also indicated [Suhuddin et al., (2010)]. To compare ideal shear texture with experimental texture, the texture measurement was made at the center of the large-area stir zone of each FSP sample. Fig. 4.38 displays {111} and {100} pole figures of base metal and FSP samples. The experimental texture components slightly deviated from the ideal texture components due to 2^0 tilt angle and little vibration during FSP [Fonda et al., (2008)]. The as-received BM having a strong rolling texture and is characterized by dominant S-{123}<634> component and minor presence of Cube-{001}<100> and Goss-{110}<100> component with a maximum texture intensity of 2.1 (as shown in Fig. 4.38a). The pole figures of the air-cooled FSP sample are characterized by dominant Copper-{112}<111> component and Brass-{110}<112> component with maximum texture intensity of 3.2 (Fig. 4.38b), the pole figures of dry ice FSP sample include the dominant A-{110}<111> component and minor presence of the Copper-{112}<111 > component with a peak intensity of 2.5 (Fig. 4.38c) and the pole figures of underwater FSP sample shows dominant Copper-{112}<111 > and A-{110}<111> components with a peak intensity of 1.3 (Fig. 4.38d).

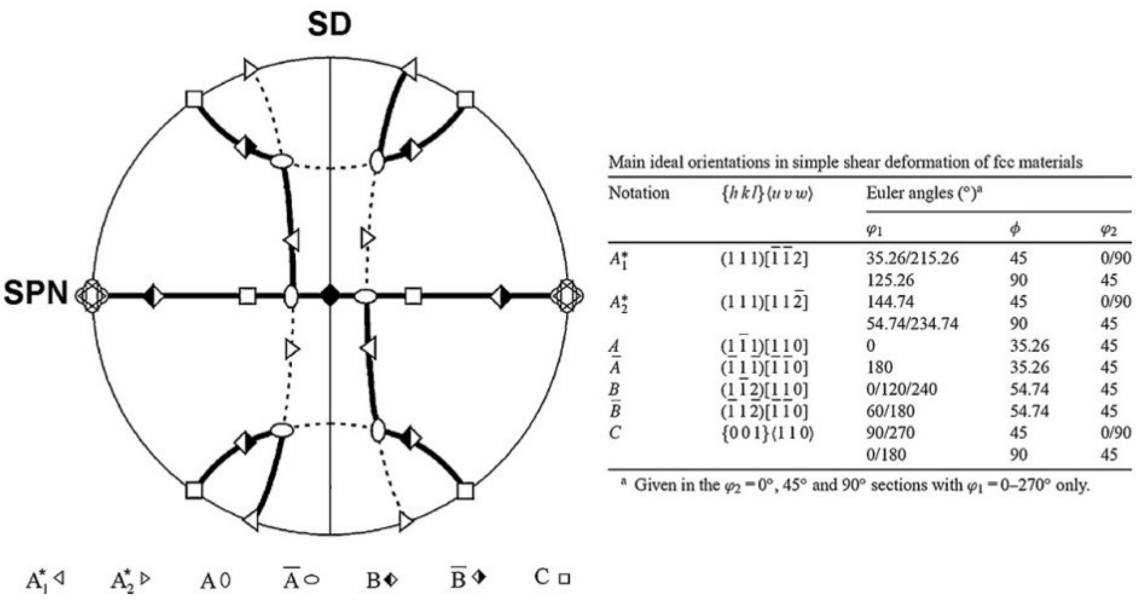

Main ideal orientations in simple shear deformation of fcc materials

Notation	$\{h\,k\,l\}\langle u\,v\,w\rangle$	Euler angles (°)[a]		
		φ_1	ϕ	φ_2
A_1^*	$(1\,1\,1)[\bar{1}\,\bar{1}\,2]$	35.26/215.26	45	0/90
		125.26	90	45
A_2^*	$(1\,1\,1)[1\,1\,\bar{2}]$	144.74	45	0/90
		54.74/234.74	90	45
A	$(1\,\bar{1}\,1)[1\,1\,0]$	0	35.26	45
$\bar{A}$	$(\bar{1}\,1\,\bar{1})[\bar{1}\,\bar{1}\,0]$	180	35.26	45
B	$(1\,\bar{1}\,2)[1\,1\,0]$	0/120/240	54.74	45
$\bar{B}$	$(\bar{1}\,1\,\bar{2})[\bar{1}\,\bar{1}\,0]$	60/180	54.74	45
C	$\{0\,0\,1\}\langle 1\,1\,0\rangle$	90/270	45	0/90
		0/180	90	45

[a] Given in the $\varphi_2 = 0°$, 45° and 90° sections with $\varphi_1 = 0–270°$ only.

Fig. 4.37. Ideal texture orientation of FCC metal under simple shear in the {1 1 1} pole figure, where SD and SPN are shear directions and shear plane normal [Shahuddin et al., (2010)].

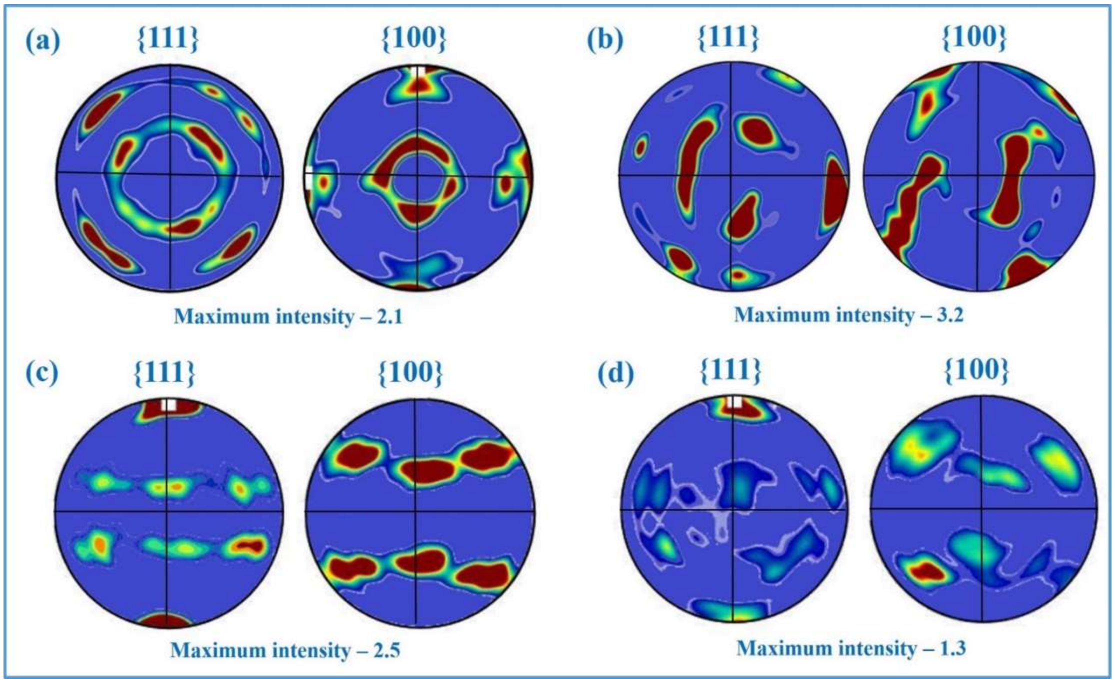

Fig. 4.38. {1 1 1} and {1 0 0} pole figures labelled with measured texture orientations in (a) BM, (b) Air-cooled, (c) Dry ice, and (d) Underwater FSP sample.

To better understand the influence of overlapping FSP, texture components were extracted from each pass of the large-area stir zone in the air-cooled FSP sample. The measured {100}, {110}, and {111} pole figures of each overlapping pass of the FSP sample are displayed in Fig. 4.39 and compared with ideal shear deformation texture components of FCC metals [Suhuddin et al., (2010)]. Also, to compare with the ideal shear texture, orientation distribution functions (ODFs) in the Euler angles space of $\text{Ø}_2 = 45^0$, $65^{0,}$ and 90^0 were measured for FSP samples and presented in Fig. 4.40. The recrystallized SZ of the first pass of the FSP sample contains dominant Brass-{110}<112> component and A-{110}<111> component due to shear deformation and material flow around the pin induced by stirring action of tool (as shown Fig. 4.39a&4.40a). Unlike first pass, the second pass, presents dominant Copper-{112}<111> component and Cube-{001}<100> component (as shown Fig. 4.39b&4.40b). As like the second pass, third, fourth, and fifth passes also contains Copper-{112}<111> and Cube-{001}<100> components, but instead of Copper-{112}<111> component, Cube-{001}<100> is dominated in the third pass. And, the intensity of Copper-{112}<111> component is further decreased in the fourth pass, and it completely disappeared in the fifth pass, while the intensity of Cube-{001}<100> component is increased with several overlapping passes (as shown Fig. 4.39c-e&4.40c-e). The grain refinement in all FSP passes is uniform, as shown in EBSD maps (Fig. 4.36), the further conduction of overlapping FSP causes the shoulder to participate multiple times on each overlapping stir zone (because the pin's size is small compared to the shoulder), leading to an increase in the heat input. On the other side, the conduction of multi-pass overlapping passes leads to increase plastic deformation. So, the increase in heat input and deformation resulted in variation of texture components and their intensity. The overall texture intensity increased after FSP could be attributed to the homogenous distribution of fine recrystallized grains in SZ. Within the FSP sample, the variation in texture intensity could be due to variation of heat input and plastic deformation because the processing condition for all passes is the same. Fonda et al., (2008) reported that the Copper component is dominated at lower strains, the Goss component replaces as the strain value rises and stabilizes at strain values 3-5, and further rises in strain allows the Brass component to dominate. The studies of Shahuddin et al., (2010) stated that the formation of Brass texture is due to shear deformation and material flow around the pin. So, the Brass texture is dominant in the SZ of FSP/FSWed materials.

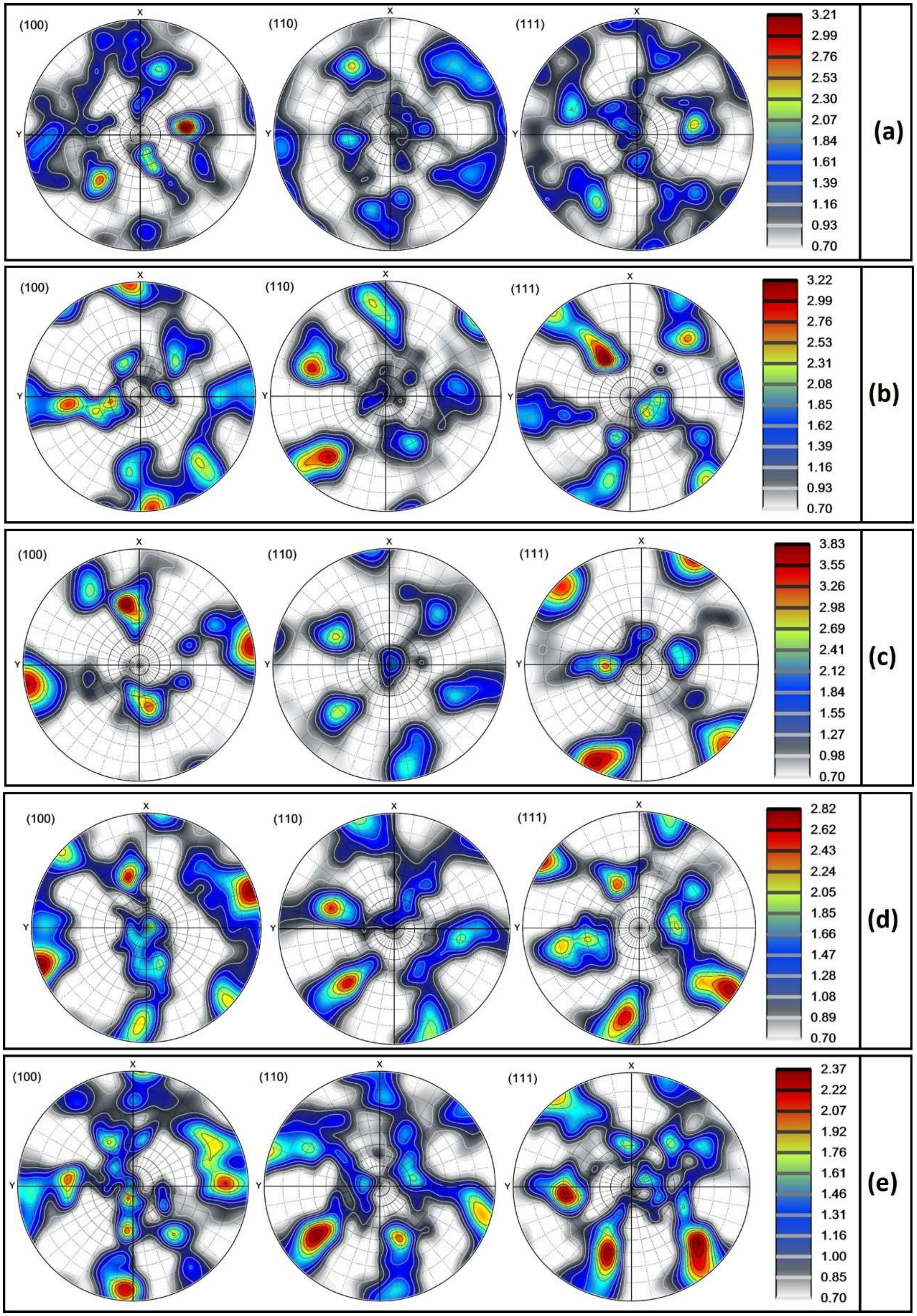

Fig. 4.39. {100}, {110}, and {111} pole figures of SZ of (a) First (b) Second, (c) Third, (d) Fourth, and (e) Fifth pass of ACFSP sample.

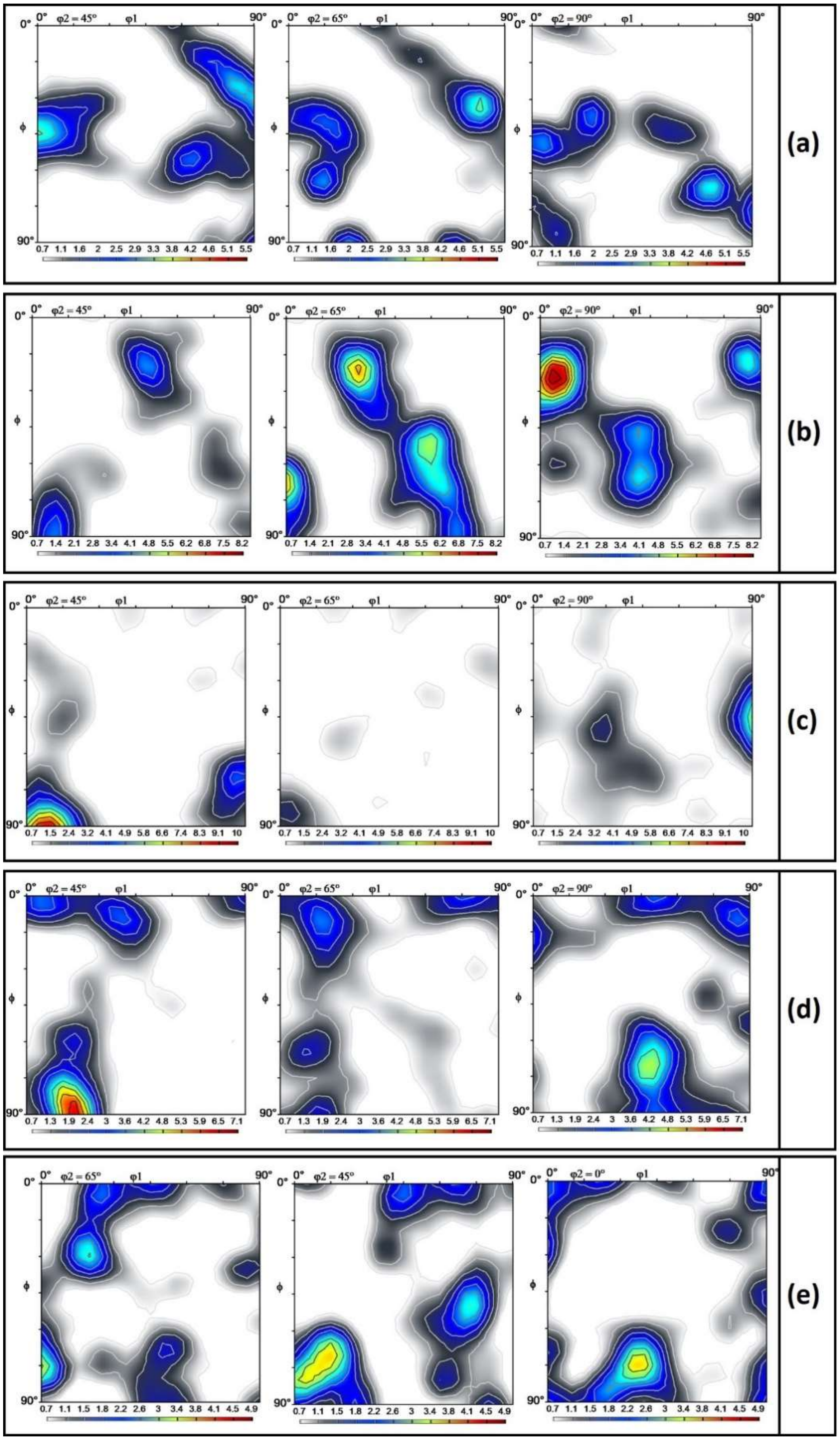

Fig. 4.40. ODFs of SZ of (a) First (b) Second, (c) Third, (d) Fourth, and (e) Fifth pass of ACFSP sample.

4.4.3 Scanning electron microscope

SEM micrographs of BM, SZ of each overlapping pass of air-cooled FSP sample and center of the large-area SZ of dry ice and underwater FSP samples are shown in **Fig. 4.41** along with EDS maps. SEM image of BM consists of uniformly distributed strengthening precipitates in the matrix, and the average precipitate size was estimated as ~1.94 µm (**Fig. 4.41a**). These precipitates were fragmented into fine precipitates (~0.92 µm) after FSP and distributed uniformly in the SZ (**Fig. 4.41b-f**). Furthermore, the precipitate distribution in all stir zones is the same. But, the density of precipitates decreased with increasing overlapping passes, and very less density of precipitates observed in the fifth overlapping pass due to increased heat put by multiple overlapping passes resulted in the dissolution of strengthening precipitates. EDS study was performed to suggest precipitates in BM and overlapping FSP sample (first and fourth pass) based on the compositional analysis. Targeting points for the EDS analysis have been labeled with yellow arrows, and EDS spectra are shown in the inset of **Fig. 4.41** along with the elemental compositions (inset). The EDS spectra of targeted points present high intensity of Al, less intensity of Cu, and notable existence of Mg and Si. This phase was suggested as Al_2Cu precipitates based on the literature and expanded information on AA2014. The provision of cooling media during FSP further reduced the size of the precipitates. The average precipitate size in dry ice and underwater FSP are ~0.8 µm and ~0.7 µm. Within FSP samples, fine precipitates were detected in underwater FSP sample. These fine precipitates can have more ability to pin to the grain boundaries and impede the grain boundary sliding.

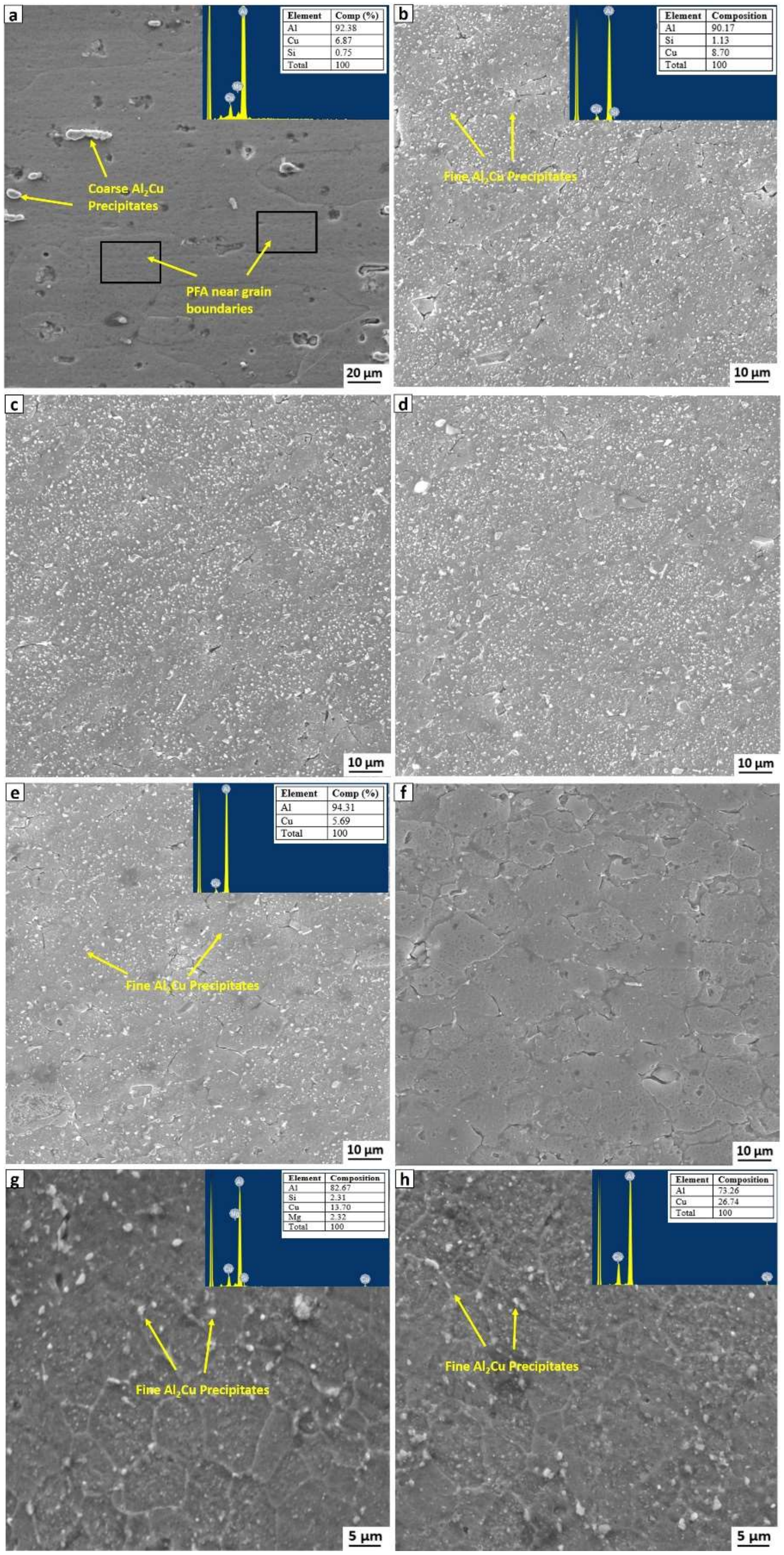

Element	Comp (%)
Al	92.38
Cu	6.87
Si	0.75
Total	100

Element	Composition
Al	90.17
Si	1.13
Cu	8.70
Total	100

Element	Comp (%)
Al	94.31
Cu	5.69
Total	100

Element	Composition
Al	82.67
Si	2.31
Cu	13.70
Mg	2.32
Total	100

Element	Composition
Al	73.26
Cu	26.74
Total	100

Fig. 4.41. SEM micrographs of (a) BM, (d-e) SZ of ACFSP sample from 1st to 5th pass, (g) CCFSP, and (h) UWFSP samples.

4.4.4 Mechanical properties

4.4.4.1 Hardness

The hardness profile across the mid-section of the overlapping FSP samples is displayed in Fig. 4.42. Similar hardness was achieved in SZ of each overlapping pass, and a uniform hardness of 119±5 HV, 122±6, and 133±8 HV was achieved in large-area SZ of air-cooled, dry ice, and underwater FSP samples. The presence of UFG structure in underwater FSP sample resulted in the highest hardness compared to other FSP samples. It was identified that the overlapping FSP samples showed reduced hardness in SZ as compared to BM (151±10 HV). As received, BM in cold-rolled conditions undergoes strain hardening effects which contribute to improved hardness. The SZ experiences peak temperatures of up to 0.6-0.9 T_{MP}, softening the material and reducing hardness in the SZ [Chen et al., (2016)].

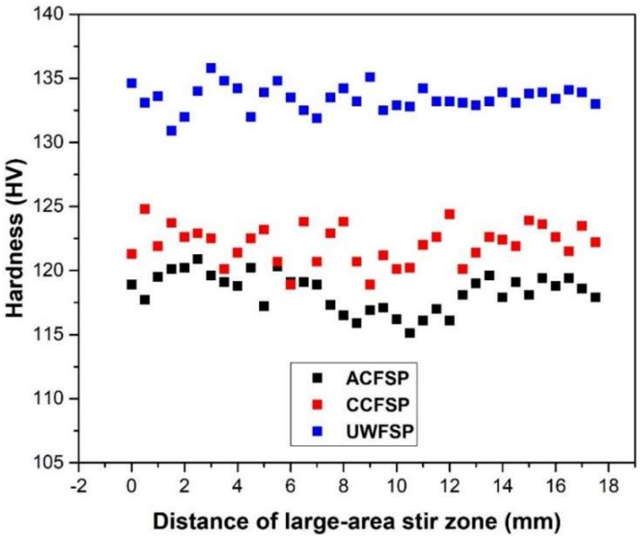

Fig. 4.42. Hardness profile of FSP specimens.

4.4.4.2 Tensile behavior

To investigate the effect of overlapping FSP, tensile properties like yield strength (YS), ultimate tensile strength (UTS), and elongation (EL) were compared with BM. Table 4.18 shows the tensile properties of BM and FSP samples extracted from the stress-strain curve (Fig. 4.43). The tensile properties clearly showed that the strength of overlapping FSP samples was lower than the BM due to thermal softening during FSP, as discussed in hardness analysis. According to Khaled et al., (2014), the reduction in strength and hardness in the FSP sample due to dissolution of strengthening precipitates and limited re-precipitation. But overlapping FSP led to an increased elongation of about 155% of BM. The increase in EL may be attributed to strain homogenization, allowing deformation to be uniform in a longitudinal tensile specimen extracted from the stir zone. According to Chen et al., (2016), the improvement in FSP elongation is attributed to recrystallized fine grains and the low dislocation density of the processed sample. Like in the previous analysis, the highest strength and lowest elongation were achieved in the underwater sample due to UFG structure and fine precipitates. In most of the steel industries and aerospace applications, the product of strength (UTS) and elongation (EL) is measured to assess the combined effect of strength and elongation [Chen et al., (2016)]. As documented in Table 4.18, the highest product of strength and elongation was obtained for FSP samples, which will be more useful in practical applications.

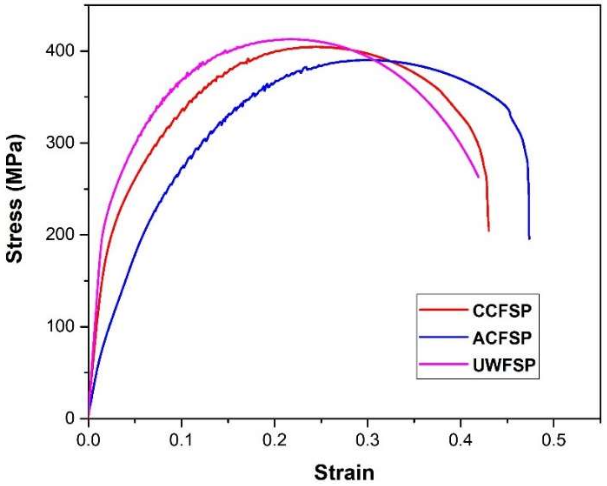

Fig. 4.43. Stress-strain curves of FSP specimens.

Table 4.18 Tensile properties

Condition	UTS (MPa)	YS (MPa)	EL (%)	UTS X EL (MPa%)	Ɵ″ (MPa)	n
BM	478±6	409±5	18±1.1	8640	~4500	0.37
ACFSP	390±2	201±2	46±2.1	17940	~4000	0.54
CCFSP	402±3	223±3	43±2.0	17286	~4100	0.55
UWFSP	410±4	225±2	42±1.9	17220	~4100	0.62

4.4.4.3 Work hardening behavior

The work-hardening nature of metals and alloys is expressed using various stages of the Kocks-mecking plot [Kocks et al., (1970 and 2003)]. Stage-I hardening relies heavily on crystal orientations. It is not found in the present study, whereas stage-II hardening occurs primarily due to the interaction of dislocations in the primary slip system with dislocations intersecting slip system [Kocks et al., (1976]. Rollett et al., (1993) stated that stage-III hardening is denoted by work hardening rate, which increases as flow stress decreases. Generally, none of the metals and alloys shows Stage-I and Stage-II work-hardening behavior. The work hardening behavior in all FCC polycrystalline is similar to Stage-III linear work hardening behavior [Kocks et al., (2003)]. The stage-III work hardening behavior is expressed by using the equation proposed in the form of net flow stresses given by:

$$\Theta = \Theta''\left(1 - \frac{\sigma-\sigma_Y}{\sigma_S}\right) \qquad (4.2)$$

Where Θ is work hardening rate, Θ'' is work hardening rate at stress equals to yield stress, σ_s is saturation stress where $\Theta = 0$. Kocks-mecking work hardening plots of BM and FSP samples are presented in Fig. 4.44, where work hardening rate ($\Theta = d\sigma/d\epsilon$) is taken abscissa, and net flow stress (σ-σ_y) is taken at ordinate. The work-hardening rate values were obtained from the Fig.4.44 are documented in Table 4.18. The work-hardening trend reveals that the base metal exhibited better work-hardening behavior than the FSP samples. The high work hardening rate in the BM could be attributed to the strain hardening effects induced during cold working. The work hardening is improved in cooling-assisted FSP compared to FSP without cooling media due to better grain refinement and strength [Yadav et al., (2017)].

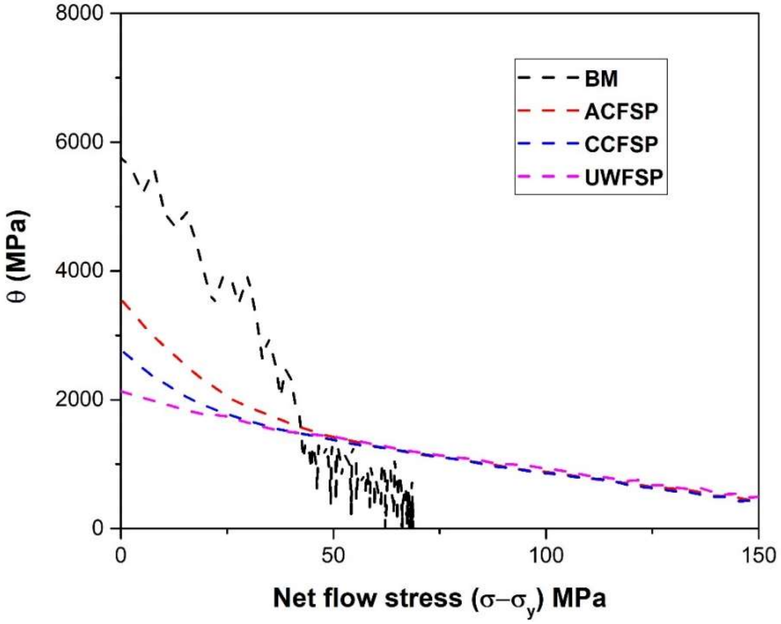

Fig. 4.44. Kocks-mecking plots for BM and FSP samples.

The strain hardening rate (SHR) accounts for the restoration effects during the plastic deformation process [Kocks et al., (2003)]. It is evident that the flow stress changes linearly with plastic strain during tensile deformation of elastic-plastic materials, and it is expressed using the Hollomon equation. Hollomon equation establishes the relation between double logarithmic true stress and logarithmic true strain. The Hollomon equation for measuring strain hardening exponent is given by Eq. (4.3) [Nutor et al., (2017)];

$$\sigma = K\epsilon^{n} \qquad (4.3)$$

Where n is the strain-hardening exponent and K is material constant. For the n value determination, a plot was constructed between true logarithmic strain on the ordinate and true logarithmic stress on the abscissa, as depicted in Fig. 4.45. The Hollomon equation is re-written in the form y = mx + c to calculate the n value, as given eq. (4.4);

$$\log\sigma = n\log\epsilon + \log K \qquad (4.4)$$

where n is the value corresponding to slope m is obtained by linear curve fitting (shown in dashed lines of Fig. 4.45) of logarithmic true strain at x-axis and logarithmic true stress at y-axis data. It is well known, the n value denotes the elastoplastic nature of materials, and it varies from 0-1, where 0 denotes 100% plastic nature, 1 denotes 100% elasticity nature, and the value of 0.5

indicates perfect elastoplastic nature [McLean et al., (1963)]. The n values of the present study are documented in Table 4.18. Shivasankaran et al., (2017) studies stated that the n value should vary from 0.2-0.6 for metallic materials. From n values of the present study, it was identified that the BM has plastic nature due to strain hardening effects induced during cold-working. The SPD and long thermal exposure during FSP resulted in the elastic nature of the FSP sample. The elastic nature of the was further improved with increasing the cooling rate.

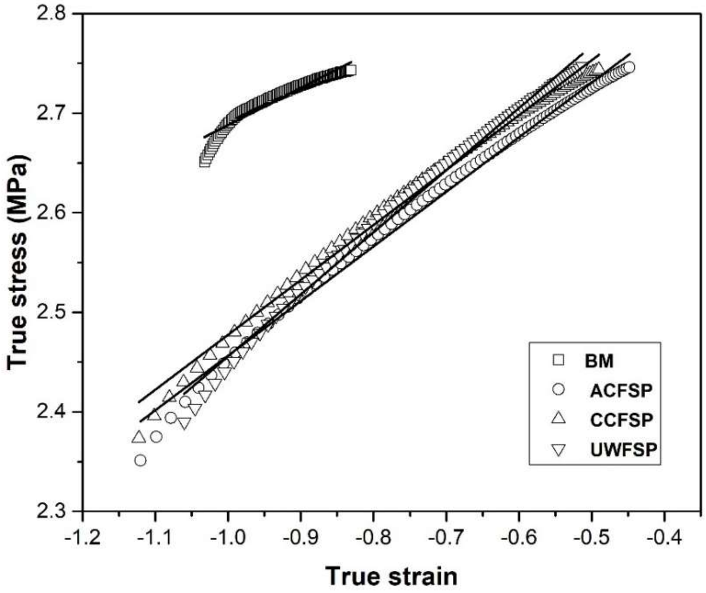

Fig. 4.45. True stress-strain plots for BM and FSP samples.

4.4.5 Corrosion analysis

4.4.5.1 Tafel polarization test

The Tafel plots obtained from the Tafel polarization test in 3.5% NaCl solution are shown in Fig. 4.46. The corrosion potentials (E_{COR}) and corrosion current densities (I_{COR}) were extracted from the Tafel plots and listed in Table 4.19. Generally, E_{COR} values signify the corrosion tendency or corrosion resistance of the sample, whereas I_{COR} values quantify corrosion rate [Alishavandi et al., (2020)]. The high negative E_{COR} value usually indicates low corrosion resistance. From Table 4.19, it was identified that the lower negative corrosion potential in the FSP samples led to higher corrosion resistance. It was clear that corrosion resistance improved after FSP. Unlike corrosion potential, the highest negative current density value indicates a lower corrosion rate. From Table

4.19, it was observed that the corrosion rate decreased after FSP as the FSP samples had higher negative current density value than BM.

The corrosion occurs due to galvanic cells forming between anode and cathode due to potential differences between them. The higher potential difference leads to an increased corrosion rate. In the present study, the electrolytic solution containing water and sodium chloride acts as a cathode where cathodic reaction or reduction happens. Working samples act as anode where anodic reaction or oxidation occurs. The cathode is usually a more passive element in corrosion than anode so that the working sample leaves electrons in the electrolytic solution and rusts, and the corrosion reactions are as follows [Xu et al., (2009)];

Anode or oxidation reaction:

$Al - 3e \rightarrow Al^{3+}$ (1)

Cathode or reduction reaction

$3H + 3e \rightarrow \frac{3}{2}H_2$ (2)

Within the electrolytic solution, Cl releases electrons into the water, and oxidation happens. The reactions are as follows:

Anode or oxidation reaction:

$Cl^- - e \rightarrow Cl_2$ (3)

Cathode or reduction reaction

$2\mathrm{H_2O} + 2\mathrm{e} \rightarrow \mathrm{H_2} + 2OH$ (4)

In AA2014 alloy, precipitates act as a cathode (passive), while Al-matrix acts as an anode (active), and more potential difference leads to more corrosion. As discussed in SEM analysis, precipitates are coarser in BM and fragmented into fine precipitates after FSP. Compared to finer precipitates in the FSP sample, the coarse precipitates in BM can easily make galvanic coupling with Al-matrix due to the large potential difference between them [Navaser et al., (2017)]. Navaser et al., (2017) and Sinhmar et al., (2017) reported that the inter-distance between precipitates also affects corrosion. The more the inter-distance between the precipitates, the more the corrosion, since it creates a large potential difference. The inter-distance between the precipitates is more in BM than in the FSP sample. Furthermore, the fine equiaxed grains present in FSP samples can quickly form a protective oxide layer compared to coarse grains in BM [Sinhmar et al., (2018)]. This protective oxide film prevents corrosion attack. Thus, factors such as low potential difference, small inter-distance between precipitates have made FSP samples more corrosion resistant than BM. More grain refinement and discontinues fine precipitates at grain boundaries and other factors in underwater FSP sample provided better corrosion resistance compared to other FSP samples.

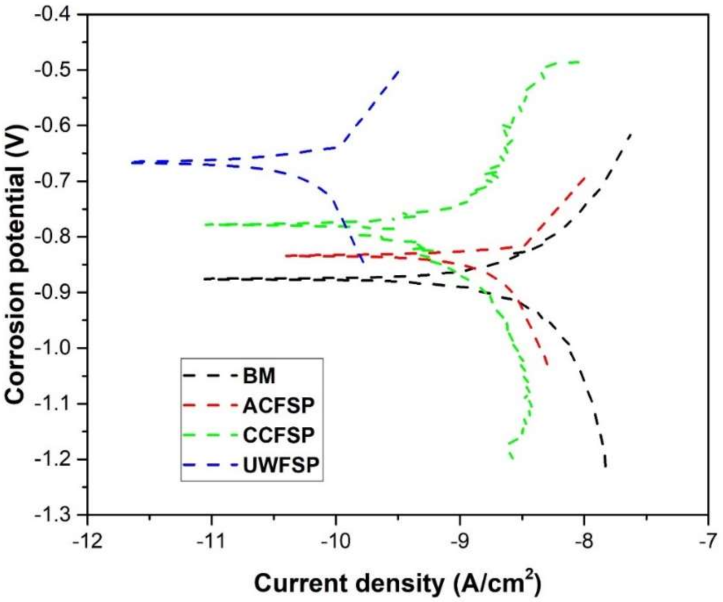

Fig. 4.46. Tafel curves of BM and FSP samples.

Table 4.19 Tafel test results.

Sample condition	**Corrosion potential (mV)**	**Current density (A/cm^2)**
BM	-862	-8.2
ACFSP	-851	-8.6
CCFSP	-786	-9.5
UWFSP	-685	-10.1

4.4.5.2 Electrochemical impedance spectroscopy (EIS) test

EIS is one of the most reliable methods for studying corrosion behavior. The EIS methodology reveals more information than the Tafel polarization test [Tedan et al., (2006)]. This method measures average corrosion behavior over the entire attacked region, and it provides the corrosion behavior based on the capacitive performance of the attacked region of the sample surface. Loops generated in the Nyquist plots are categorized based on the frequency range, and the number of loops formed denotes the number of time constants. High-frequency loops, also known as capacitive loops, are generated by forming a protective oxide layer on the sample's surface. The presence of intermediate frequency loops, also known as an inductive loop, is associated with the relaxing process into the oxide film. The low-frequency loops, also known as the second capacitive loops, can be attributed to the dissolution of the material. Low-frequency loops are generally formed in aggressive electrolytic solutions. The EIS results of BM and FSP samples are shown in Fig. 4.47. The Nyquist plot shows real impedance on the x-axis and imaginary impedance on the y-axis as shown in Fig. 4.47a, and the loops formed were found to be high-frequency single time constant capacitive loops. The real impedance value indicates the corrosion resistance of the material. A high impedance value indicates a higher corrosion resistance. As compared to BM, the FSP sample resulted in higher impedance, leading to improved corrosion resistance. The sample processed using underwater showed high impedance value than other FSP samples. Thus, the corrosion resistance of the UWFSP sample is higher than the other samples. The Bode plot (Fig. 4.47b) shows the impedance of material with respect to frequency. The impedance was steady at low frequencies, but it decreased at high frequencies. The data obtained from the EIS plots were fit in the equivalent circuit as shown in Fig. 4.48. The equivalent circuit model uses the constant phase elements (CPE) because the frequency dispersion shown at the electrode/electrolyte interface is not well described by simple elements like capacitor, inductor, or resister. This frequency dispersion is associated with capacitive dispersion, which is expressed by the CPE. The CPE response is related to the inhomogeneity, roughness, and porosity of the exposed sample surface [Jorcin et al., (2006)]. The data extracted from the equivalent circuit, such as solution resistance (R_S), capacitor resistance (R_{CT}), and double-layer capacitance (C_{DL}), are shown in Table 4.20. The solution resistance nearly the same for all the samples because the fresh electrolytic solution was used for each sample. A high R_{CT} value indicates more corrosion resistance. From Table 4.20, it was observed that the UWFSP sample has a high R_{CT} value and resulted in high corrosion than other samples. Finally, the results of EIS confirmed the results obtained from the Tafel test.

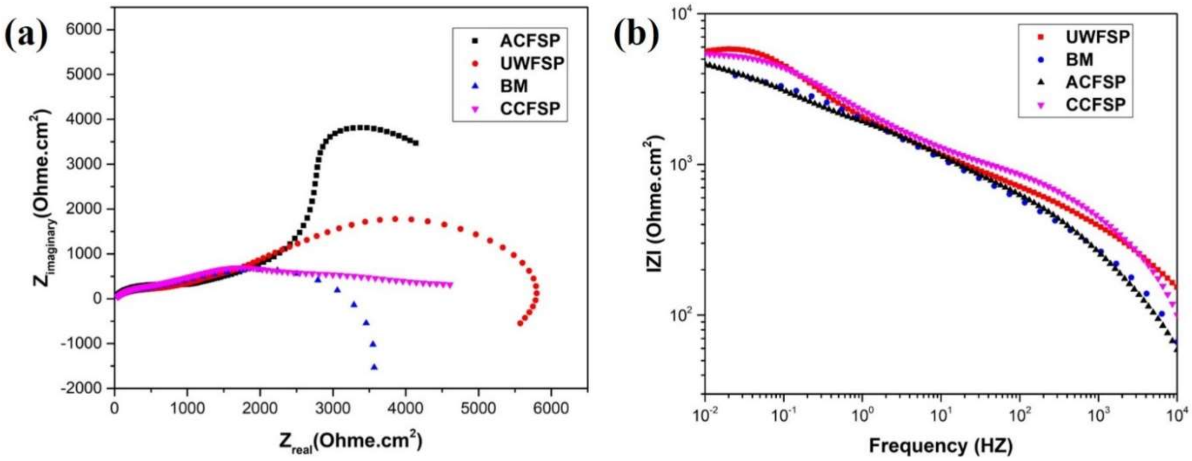

Fig. 4.47. EIS test results of BM and FSP samples (a) Nyquist plot and (b) Bode plot.

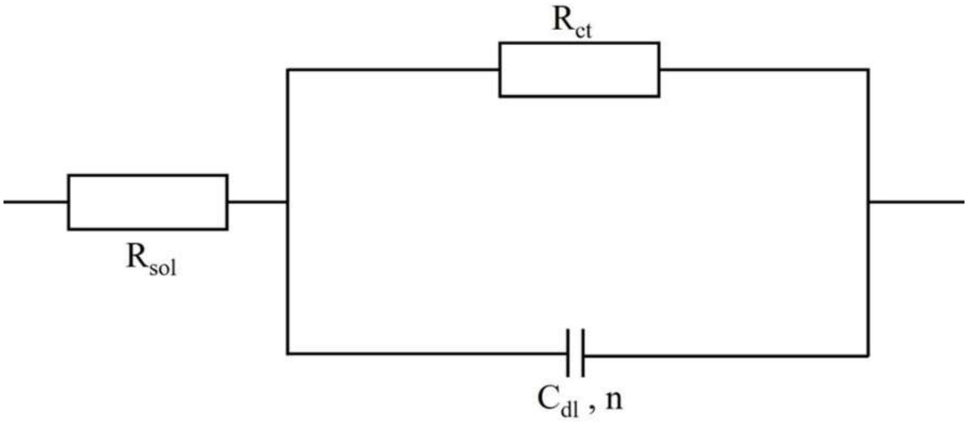

Fig. 4.48. Equivalent circuit for fitting the EIS data.

Table 4.20 EIS data extracted from equivalent circuit.

Condition	RS (Ohm.cm^2)	RCT (Ohm.cm^2)	CDL (F)	n
BM	2.4x10^3	2.9x10^3	7.8x10^{-5}	0.55
ACFSP	2.2x10^3	3.5x10^3	3.5x10^{-4}	0.98
CCFSP	2.9x10^3	3.9x10^3	1.3x10^{-4}	0.94
UWFSP	2.5x10^3	5.6x10^3	1.7x10^{-4}	0.93

4.4.6 Wear analysis

The wear test results such as weight loss (mg) and wear rate (mg/m) are listed in Table 4.21. The variation of the weight loss with respect to the sliding distance is represented in Fig. 4.49. From Fig. 4.49a, it was observed that the weight loss of BM and FSP samples increased with increasing the sliding distance. Compared to BM, the weight loss in the FSP sample is less due to the development of fine-grained structure and uniform distribution of strengthening precipitates [Mahdi et al., (2019)]. Compared to the coarse-grained structure in BM, the fine-grained structure in the FSP sample shows the high resistance to wear due to the high fraction of grain boundary area. On the other hand, the weight loss of both FSP samples followed a similar trend in weight loss due to the homogeneous grain refinement of the large-area stir zone. But, the weight loss of the cooling-assisted FSP is less than air-cooled FSP could be attributed to the formation of ultrafine-grained structure.

The variation of the wear rate with respect to sliding distance is shown in Fig. 4.49b. From 0-500 m, the wear rate of all samples increased drastically with an increase in sliding distance, and from 500-1000m, the wear rate of all samples decreased gradually with an increase in sliding distance. At initial distances, the friction between the counter surface and sample is higher, resulting in increased wear rate and reaching a steady state at certain sliding distances. And, the further increase in sliding distance causes the formation of protective oxide layer on the samples and decreases the contact surfaces, and resulted in a gradual decrease in wear rate. The wear rate of the FSP samples drastically reduced due to less weight loss. The deviation of wear rate between the BM and FSP sample is more due to large variation in grain size, and this deviation is increased with sliding distance from 0-500 and decreased with siding distance from 500-1000. On the other hand, the wear rate of FSP samples followed a similar trend up to 500 m sliding distance, but the wear rate of cooling-assisted samples is slightly less than the air-cooled FSP sample. The wear rate of FSP samples maintained approximately the same wear rate from 750-1000.

Table 4.21 Wear test results.

Sample condition	Weight-loss with respect to sliding distance (mg)				Wear rate with respect to sliding distance (mg/m)			
	250 m	500 m	750 m	1000 m	250 m	500 m	750 m	1000 m
BM	1.04	5.18	7.08	8.27	0.00416	0.01036	0.00944	0.00827
ACFSP	0.68	3.08	4.67	6.13	0.00272	0.00616	0.00622	0.00613
UWFSP	0.62	2.82	4.63	6.11	0.00248	0.00564	0.00617	0.00611

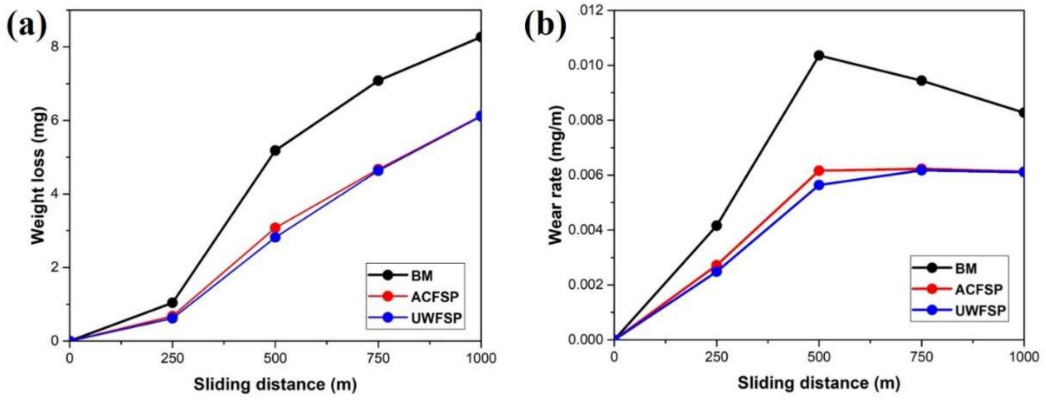

Fig. 4.49. Variation of (a) Weight loss and (b) Wear rate with sliding distance.

4.4.7 Fatigue behavior

Initially, a graph was plotted between fatigue crack length (a) and number of cycles (N) to know the fatigue life of the samples, as shown in Fig. 4.50a. From Fig. 4.50a, it was observed that the FSP samples sustained for a large number of cycles as compared to the base metal, indicating that the stir zone in the FSP sample prevented the fatigue crack propagation. It was concluded that fatigue life was improved after FSP. The fatigue life was enhanced further with the provision of cooling-assisted FSP.

The fatigue behavior was further studied by plotting a graph between fatigue crack propagation (da/dN) and stress-intensity factor range (ΔK), as shown in Fig. 4.50b. The variation in fatigue behavior of BM and FSP samples is clearly evident in Fig. 4.50b. Paris constants (m and c) were extracted from the steady-state propagate region (i.e., Region-II) of the curve and listed in Table.

4.22. From Table 3, it was observed that processing conditions of samples affect the Paris constants and thus influence the fatigue crack propagation behavior by controlling metallurgical behavior in the BM and FSP samples. It is also evident from Fig. 4.50b that the FCG rate of BM and FSP samples is accelerated with an increase of fatigue cycles. Initially, the FCG rate of BM is higher than FSP samples up to the ΔK value of 7.4 MPa.m$^{1/2}$, while the FCG rate UWFSP sample is minimum. The crack propagation rate of FSP samples is minimum at the initial stages due to the domination of internal stresses [Zhang et al., (2020)]. As the crack propagates, the FCG rate of both FSP samples became maximum, while the FCG rate of BM is minimum up to ΔK value of 10.9 MPa.m$^{1/2}$. After that, the FCG rate of BM became maximum and fractured earlier than the other samples. It is worth noting that the fatigue life of BM is shorter than in the FSP samples. On the other hand, the initial FCG rate of the UWFSP sample is higher than the ACFSP sample up to ΔK values of 8.2 MPa.m$^{-1/2}$, after that, the FCG rate of both samples are having almost the same FCG rate up to stress intensity factor range of 10.2 MPa.m$^{-1/2}$, and after this value, the FCG rate of ACFSP sample increased. However, the final FCG rate of the UWFSP sample is less than the ACFSP samples. It is evident from the microstructural analysis that the drastic change of the grain size from BM to FSP samples could be the reason for the variation of FCG behavior. The fine-grained structure developed in FSP samples have more grain boundary area, which can hinder crack propagation. Jata et al. [2009] also achieved similar results, and they stated that fine-grained structure formed by dynamic recrystallization during FSP in the stir zone influenced the FCG rate by contributing to the crack closure behavior. Along with the grain size factor, the precipitation behavior and residual stresses also affect the FCG behavior. As explained in SEM analysis, the less density (i.e. in number) of coarse precipitates in the BM are fragmented into high-density fine precipitates after FSP and distributed uniformly in the matrix. Compared to coarse precipitates, the fine precipitates can act as obstacles for crack propagation, thus reducing the FCG rate in FSP samples. Zhang et al. [2020] stated the tensile residual stresses developed along the rolling direction in the base metal and compressive residual stresses are produced in the stir zone of the FSP sample. It is well known that the compressive residual stresses present in the material can hinder the FCG behavior. Compared to FSP/FSW without cooling media, the intensity of compressive residual stresses increases in FSP/FSW with cooling media. Hence, the presence of UFG structure and very fine precipitates in the UWFSP sample resulted in better fatigue life than other samples.

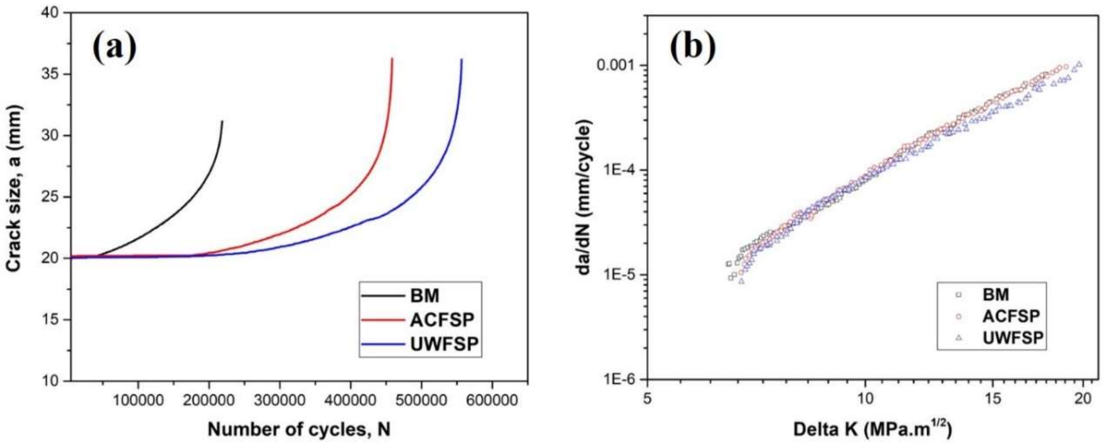

Fig. 4.50. (a) Crack length vs. Number of cycle curve, (b) FCG rate vs. ΔK curve.

Table 4.22 Paris constants

Sample	C	m	Correlative coefficient
BM	2.08E-09	4.43	0.9947
ACFSP	1.30E-08	4.30	0.9935
UWFSP	2.32E-08	3.88	0.9928

The fracture analysis was carried out to analyze the deformation behavior in the fatigue samples. The fatigue fracture features of the base metal are shown in Fig. 4.51. The low-magnification image of fatigue fractured base metal is shown in Fig. 4.51a. The macroscopic image mainly consists of three different regions. A high-magnification view of Region-I is shown in Fig. 4.51b. Region-I is Stage-I crack propagation, mainly characterized by the presence of ridges and plateaus. In this stage, crack mostly propagates along the crystallographic directions [Shukla., (2018)]. Region-II is also called stage-II crack propagation, is characterized by fatigue striations (i.e., crack arrest marks) on the fractured sample surface. Such fatigue striations generally indicate crack front position during the Stage-II crack propagation. Region-III is Stage-III crack propagation, mainly characterized by the presence of dimples and voids. Fig. 4.51c shows the presence of striation marks, secondary cracks, and dimples, and it is often represented as Stage-II and Stage-III fatigue failure. The magnified view of Fig. 4.51c is shown in Fig. 4.51d. The fatigue striation marks developed perpendicular to the crack propagation. The striations formed in Stage-II are not continuous, and many striations steps are created due to grain boundary misorientation. The grain boundary misorientations act as obstacles for fatigue crack propagation. On the other hand, secondary cracks also retard the FCG rate. The fracture features of different regions of the ACFSP sample, along with the macroscopic view, are shown in Fig. 4.52. The fracture features of the different regions of the FSP sample are similar to the base metal. But, the size of the dimples in FSP samples is smaller than the dimples in the base metal due to the presence of fine-grained structure. Fig. 4.53 shows the enlarged view of fatigue striations in the Region-II of BM and FSP samples. In FSP samples, the striation marks are continuous, and the distance between the striations is less. In BM, the striation marks are discontinuous, and the distance between the striations is more than the FSP sample. Williams et al., (2011) stated that the distance between the striations is equivalent to the FCG rate (i.e., da/dN). Therefore, more distance in BM has a high FCG rate than the FSP sample. On the other hand, continuous striation marks denote the steady-state propagation with better fatigue life. Hence, the fracture features of the fatigue samples corroborate the results of measured fatigue results.

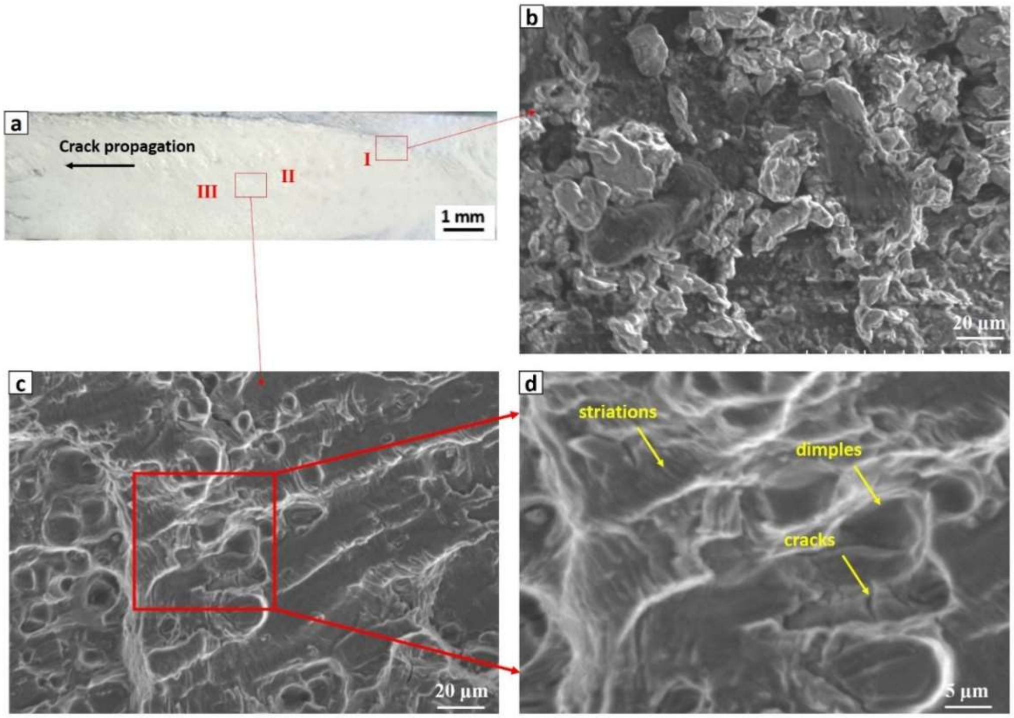

Fig. 4.51. SEM fatigue fracture features of base metal (a) Low-magnification view showing different fracture regions, (b) Stable crack growth region (Region-1), (c) Final fracture region, (d) High-magnification view of final fracture region showing striations and dimple.

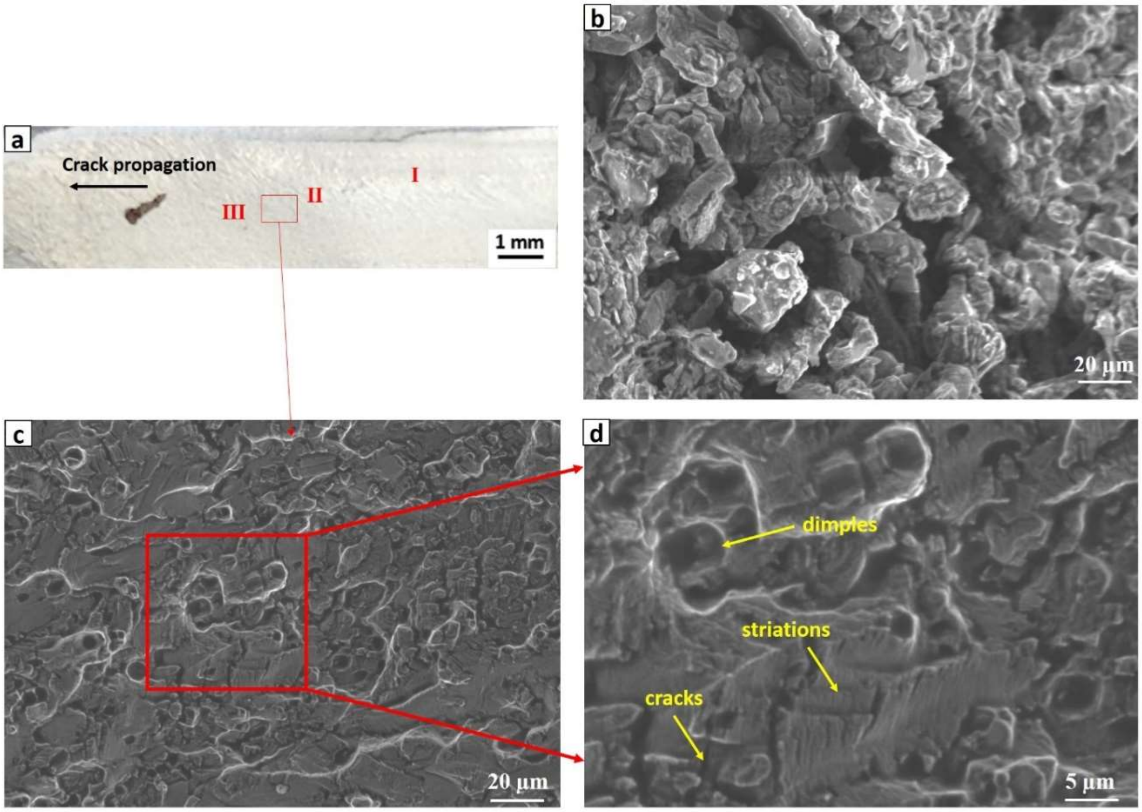

Fig. 4.52. SEM fatigue fracture features of ACFSP sample (a) Low-magnification view showing different fracture regions, (b) Stable crack growth region (Region-1), (c) Final fracture region, (d) High-magnification view of final fracture region showing striations and dimple.

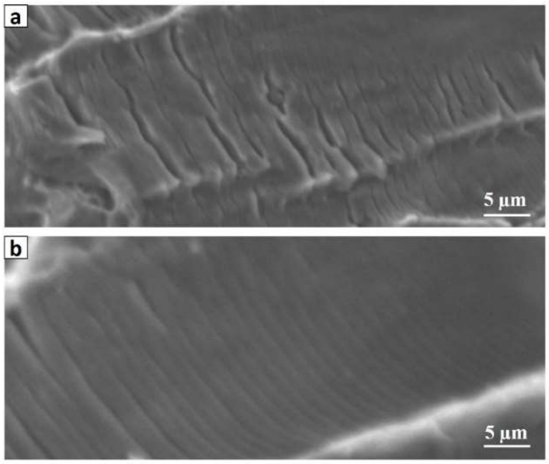

Fig. 4.53. Enlarged view of fatigue striations of (a) BM and (b) ACFSP sample.

4.5 Effect of cooling-assisted overlapping friction stir processing on microstructure, texture evolution, mechanical properties, corrosion, wear, and fatigue behavior of AA6061 alloy

From Section 4.1, it was identified that the square pin tool geometry yielded better mechanical properties in AA6061 alloy. In this section, a large-area stir zone was prepared using 5-pass overlapping FSP with 50% pin overlapping in different cooling environments using optimized process parameters (800 rpm-40 mm/min) and square pin tool; the results were discussed in the following sections.

4.5.1 Microstructure analysis

4.5.1.1 Macrostructure

The low-magnification optical micrographs of 5-pass overlapping FSP specimens are depicted in Fig. 4.54. Each region of overlapping SZ from the first to the fifth pass is labeled A to E, respectively, as illustrated in Fig. 4.54. The selected processing conditions resulted in better surface quality, defect-free structure, a uniform layer thickness of processed zone, and wavelike finish to the surface in bulk area processed zone. The process overlaps with AS, which tried to eliminate irregularities with flashes forming in the AS direction and providing uniform material flow in the processed region. Additionally, dark bend regions were identified in Fig. 4.54, known as swirl patterns. The swirl pattern indicates the material flow due to the shoulder as well as the tool pin profile. Here, only three swirl patterns are visible because the processing zone moved from RS to AS side. However, very light patterns of the dark region can be observed on the RS side, which shows the diminishing of the swirl pattern due to shifting of the processed zone.

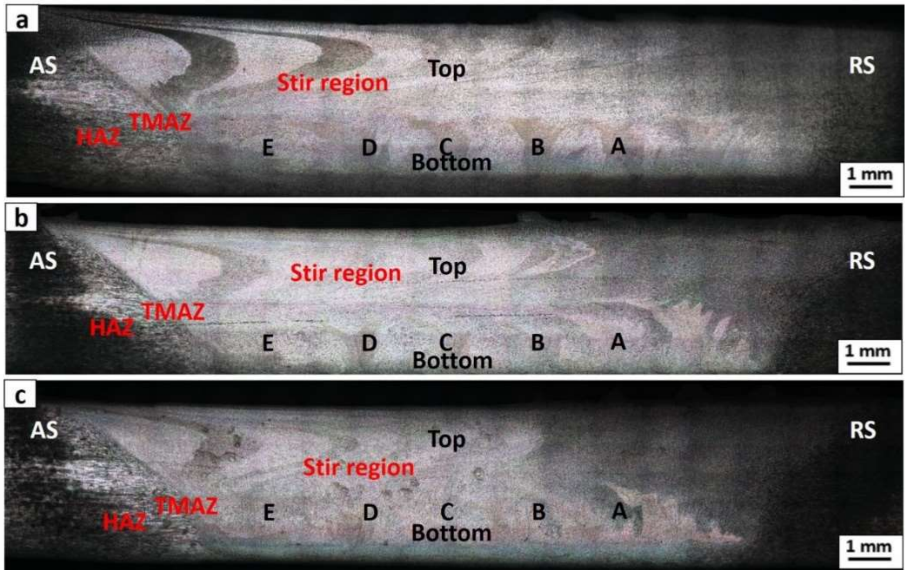

Fig. 4.54. Low magnification optical image of overlapping (a) ACFSP, (b) CCFSP and (c) UWFSP samples.

4.5.1.2 Grain structure evolution

Initially, EBSD analysis was done at the center of the large-area stir zone. EBSD micrographs of BM and FSP samples are depicted in Fig. 4.55. The statistical data of the EBSD analysis are presented in Table 4.23. A complete transformation of the BM micrograph into a newly wanted structure is seen. After FSP, the structure of BM has undergone severe plastic deformation and dynamic recrystallization (DRX) and transformed into fine equiaxed α-aluminium grains with high angle boundaries. The mechanism involved in the total transformation of BM into a fine equiaxed grain structure is demonstrated as follows. The heat generated at the tool-work interface plasticizes the BM structure. At the same time, tool rotation makes the plasticized material move around it, and tool traverse makes it flow along the processing direction. Due to the combined action of rotation and traversing of the tool, the plasticized material was forced to move in a complicated manner, flowing in all directions and finally forged behind the tool. The severe plastic flow caused by the tool breaks the coarse aluminium grains into fine grains while the tool movement allows the grains to disperse themselves uniformly. From Table 4.23, it was observed that the grain size was further reduced in cooling-assisted FSP, and the better grain was achieved in underwater FSP. On the other hand, the fraction of HABs increased with the increase in cooling rate.

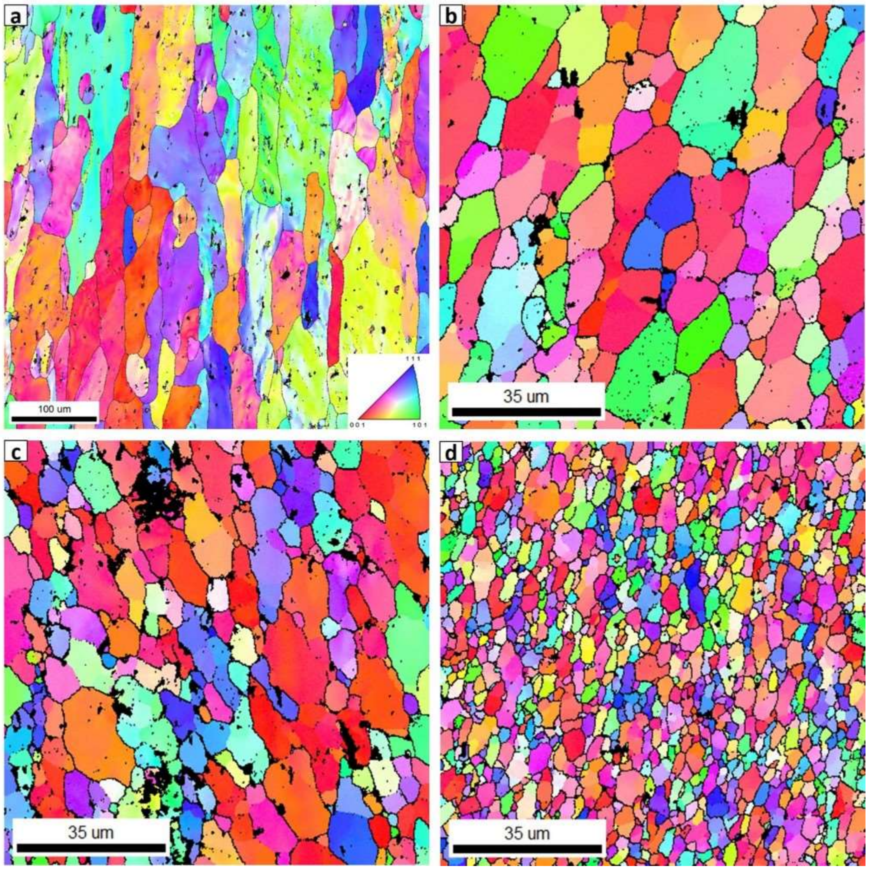

Fig. 4.55. EBSD maps of (a) BM, (b) ACFSP, (c) CCFSP and (d) UWFSP samples.

Table 4.23 Statistical data of EBSD analysis.

Sample condition	Grain size (µm)	Fraction of grain boundaries (%)	
		LABs	HABs
BM	88.4±43.2	62.5	37.5
ACFSP	4.7±3.5	62.1	37.9
CCFSP	3.8±2.5	54.4	45.8
UWFSP	2.5±1.2	26.7	67.2

For better understanding of the grain refinement across the large-area stir zone, EBSD analysis was done at each overlapping pass of air-cooled FSP. The EBSD micrographs of SZ in each overlapping pass (labeled as A to E) of air-cooled FSP samples are depicted in Fig. 4.56, and it was identified that the grain size of each pass is uniform in stir regions. So, it was concluded that the execution of successive overlapping paths did not affect grain size in the large-area SZ.

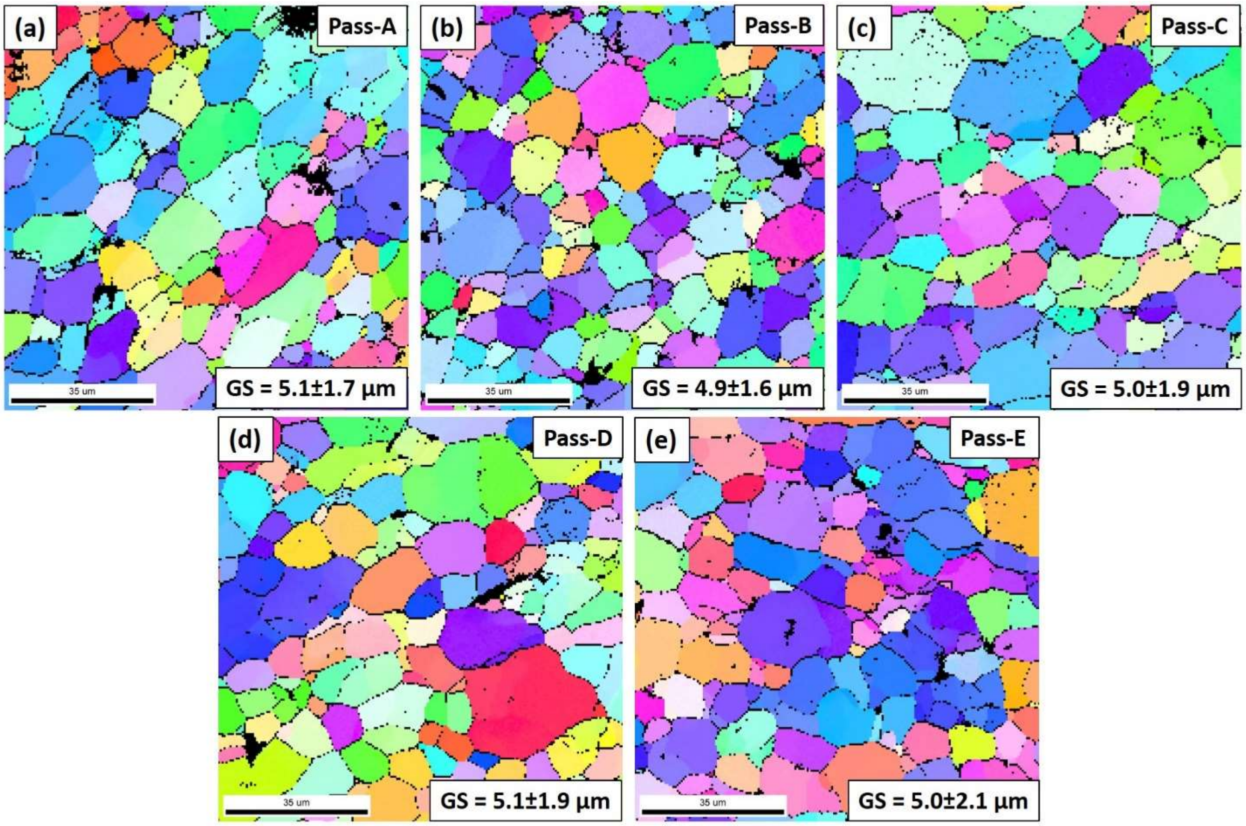

Fig. 4.56. EBSD microstructures of (a) First, (b) Second, (c) Third, (d) Fourth, and (e) Fifth pass of large-area stir zone of ACFSP samples indicating grain size (GS).

4.5.1.3 Identification and effect of second-phase particles

The backscattered electron SEM images of BM and SZ of overlapping FSP samples are displayed in Fig. 4.57-4.60. The SEM image of BM consists of a dark region of α-aluminium matrix surrounded by second-phase particles with an average size of ~1.53 µm (Fig. 4.57). However, the tool movement during FSP causes the fragmentation of second-phase particles into homogeneous fine particles (~1.1 µm, ~1 µm, and ~0.9 µm), as shown in Fig. 4.58-4.60. The secondary phase particles in the BM and FSP samples come in two shapes: lath and rod. In BM, the size of the lath particles is larger than rod shape particles, While, in the FSP sample, the lath particles are smaller than rod shape precipitates. Moreover, the density of lath particles decreases after FSP. This remarkable change in the microstructure of FSP could be on account of severe plastic straining during FSP.

EDS analysis was carried out on those second-phase particles of BM (Fig. 4.57). The second-phase particles in lath shape (point A) contained iron-based particles, whereas second-phase particles in rod shape (point B) contained silicon-based particles. This can be ascribed to the elemental weight composition and received condition (i.e., solution annealing followed by artificial ageing-T6) of parent alloy. Additionally, a continuous network of small round-shaped particles was identified along the grain boundaries in BM, and these grain boundary precipitates were detected as silicon-based particles from EDS analysis (point C). It is well known that the precipitates along the grain boundaries act as obstacles for grain boundary migration, leading to an increase in strength. These strengthening precipitates can influence the corrosion behavior of BM in corrosive environments.

The backscattered electron SEM image along with EDS maps of the FSP sample are shown in Fig. 4.58-4.60. Like in BM, the FSP samples contain iron-based particles (point D, G, and J) and silicon-based particles (point E, H, and K). Unlike BM, a discontinuous network of small precipitates was observed along the grain boundaries, and these were detected as silicon-based precipitates (point F, I, and L). As compared to BM, the number of second-phase particles are less in the FSP sample. The peak temperature generated during FSP caused the dissolution of second-phase particles and resulted in fewer precipitates. The intensity of silicon increased after FSP. After FSP, the precipitates were fragmented and a small amount of silicon accumulated on existing precipitates due to the stirring action of the tool in the stir zone.

It is a fact that the second-phase particles control the mechanical properties and corrosion behavior in BM and FSP samples. First, compared to FSP samples, the BM had a high density of lath particles, and these particles act as stress concentration sites at the time of tensile loading, leading to sudden failure and lower elongation compared to FSP samples. And, the lath particles have more ability to hinder the grain boundary sliding during tensile deformation and local deformation (the indentation in hardness testing causes the local deformation) [Polmear et al., (2006)]. Hence, the high density of lath particles in BM resulted in better strength and hardness than the FSP sample. Second, the elemental compositional analysis of second-phase particles affects corrosion behavior. The continuous network of grain boundary precipitates present in the BM can quickly form the galvanic coupling with Al matrix and then discontinuous grain boundary precipitates in FSP.

According to Gharavi et al., (2014), the galvanic cells are formed between the iron-based particles (lath-shaped particle) and Al matrix. In the present study, the density of lath-shaped precipitates (iron-based particles) is more in BM compared to FSP samples, resulting in the formation of more galvanic cells in BM. This envies that, FSP sample will have better corrosion resistance than BM.

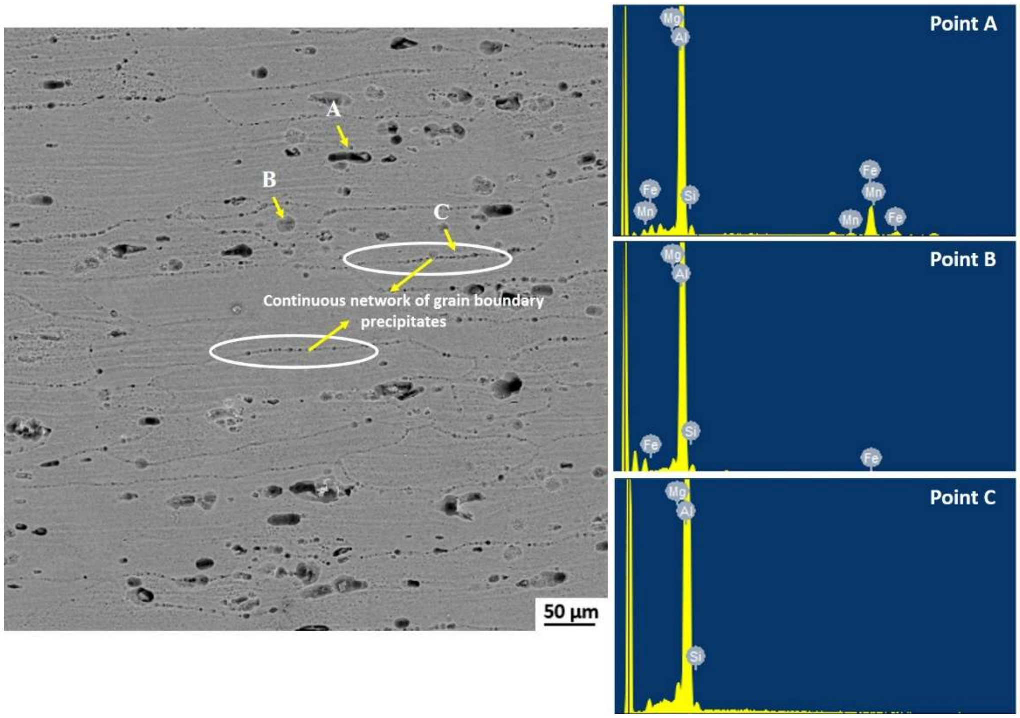

Fig. 4.57. SEM image of BM along with EDS results.

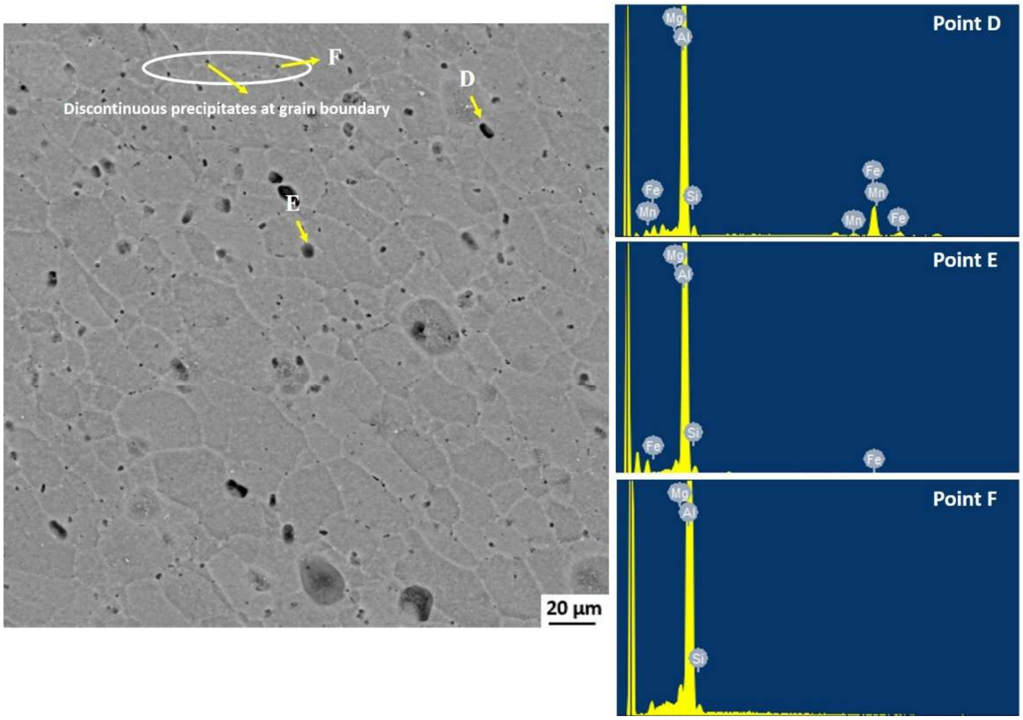

Fig. 4.58. SEM image of ACFSP sample along with EDS results.

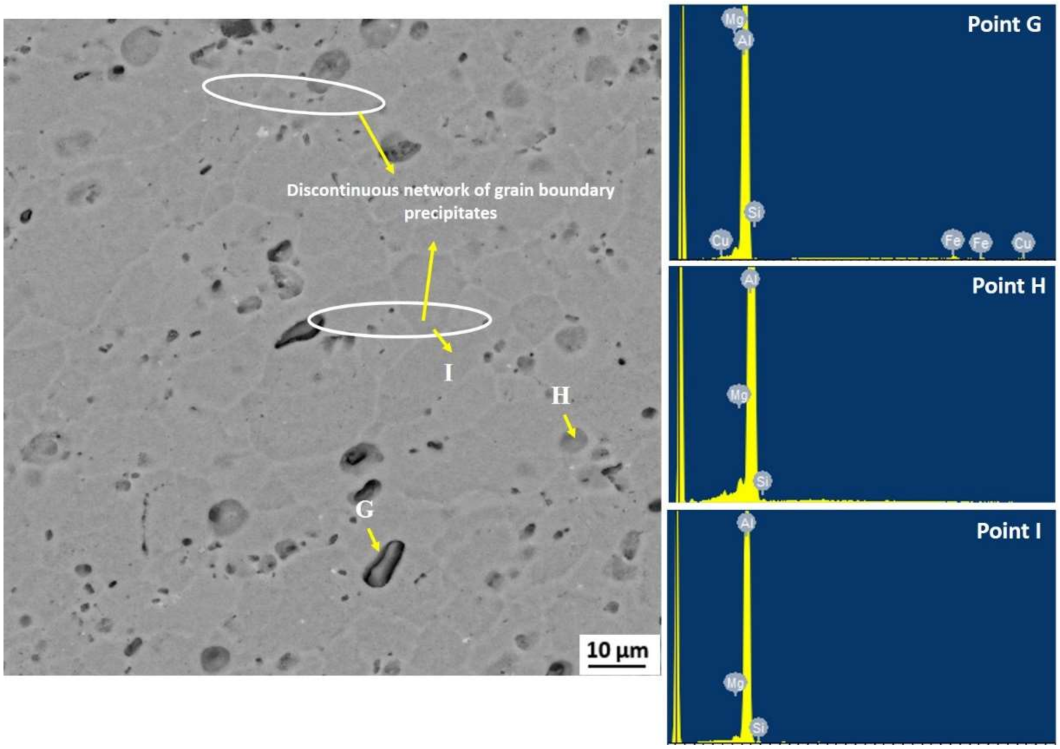

Fig. 4.59. SEM image of CCFSP sample along with EDS results.

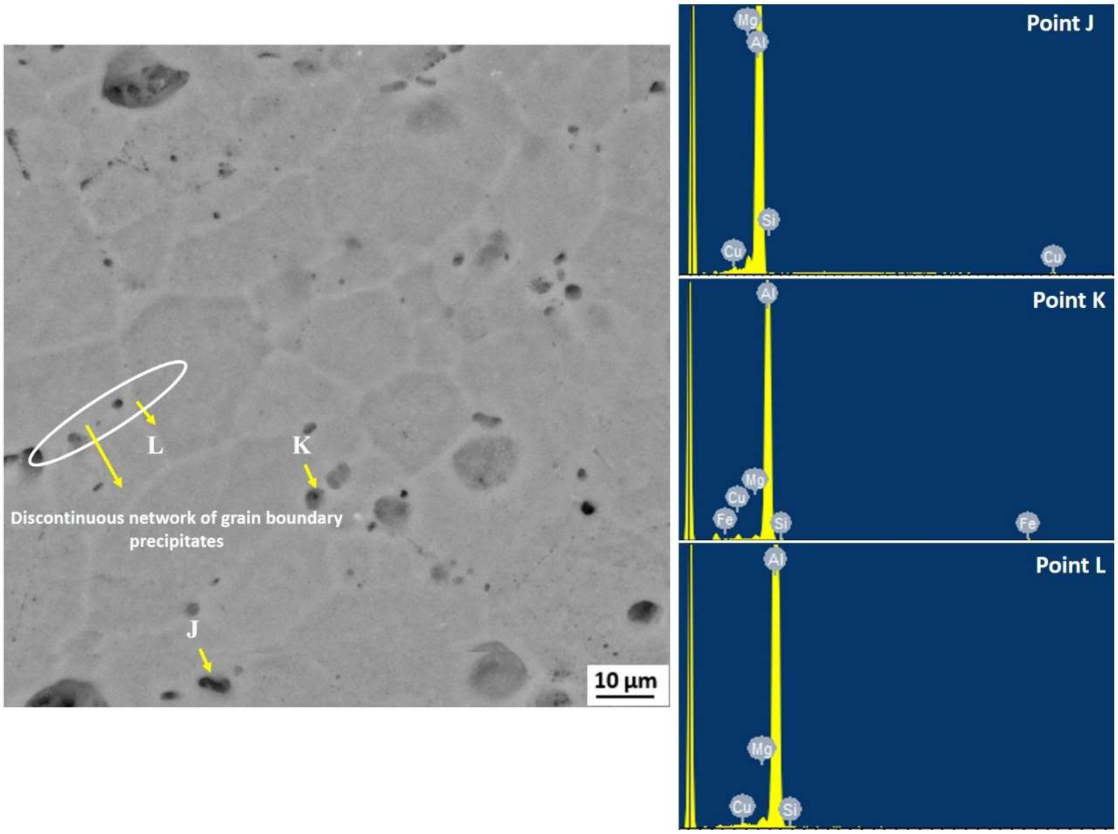

Fig. 4.60. SEM image of UWFSP sample along with EDS results.

4.5.1.4 Texture analysis

Initially, the texture analysis was made at the center of the large-area stir zone of all FSP samples. Generally, high stacking fault energy (SFE) materials having FCC crystal structure such as aluminium and its alloys strongly impact the dynamic restoration mechanism such as dynamic recovery (DRV) and dynamic recrystallization (DRX) and control the resulting deformation texture components. The measured {100} and {111} EBSD pole figures of BM and FSP samples are presented in Fig. 4.61. The pole figures of the BM consist of strong rolling texture, and it is characterized by dominant S-{123}<634> component with a maximum texture intensity of 4.7 (Fig. 4.61a), While the recrystallized ACFSP sample exhibits strong A$_1$-{111}(112) component and Goss-{110}(100) component with a peak intensity of 7.4 (Fig. 4.61b), the pole figures of the CCFSP sample presents strong A-{111}(110) component with maximum texture intensity of 10.7 (Fig. 4.61c) and the pole figures of the UWFSP sample exhibited a strong A$_1$-{111}(112) component with a peak intensity of 5.4 (Fig. 4.61d). The texture intensity after FSP increased could be attributed to the formation of recrystallized fine-grained structure. Moreover, the texture intensity was drastically reduced for the UWFSP sample due to the high cooling rate that led to limited flow stress resulted in lower texture intensity.

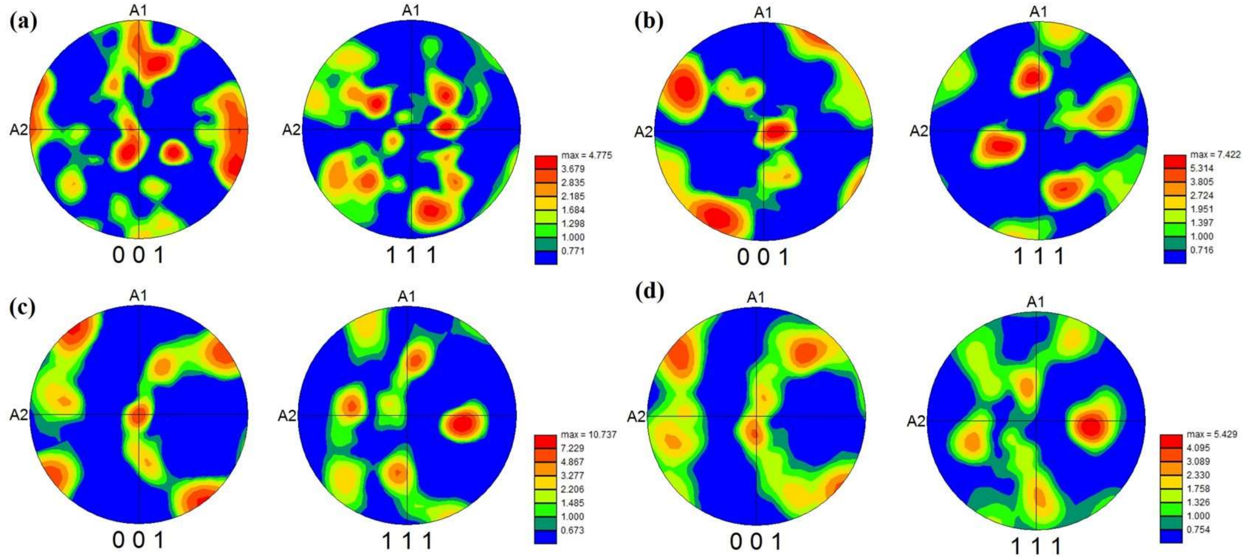

Fig. 4.61. {1 1 1} and {1 0 0} pole figures labelled with measured texture orientations in (a) BM, (b) ACFSP, (c) CCFSP and (d) UWFSP samples.

To better understand the influence of overlapping FSP on the texture analysis, EBSD analysis was made on each pass of the large-area stir zone of the ACFSP sample, and texture components were measured. The measured {100}, {110} and {111} pole figures of each pass of 5-pass overlapping ACFSP sample are presented in the Fig. 4.62. The recrystallized first pass of the FSP sample contains dominant A-{111}(110) component and less intensity of Brass-{110}(112) component with a maximum intensity of 6.62 (Fig. 4.62a), while the recrystallized second-pass of FSP sample presents strong Cube-{100}(001) component and Brass-{110}(112) component with a texture intensity of 5.12 (Fig. 4.62b). As compared to the first-pass, the texture intensity of Brass-{110}(112) increased due to the increase of heat input, and the Cube-{100}(001) component is formed due to the material flow around the pin by stirring action of the tool. The recrystallized third pass of the FSP sample is dominated by a strong Brass-{110}(112) component with a texture intensity of 7.25 (Fig. 4.62c). The intensity of the Brass-{110}(112) component increased further, and the Cube-{100}(001) component is disappeared almost after the third pass. The recrystallized fourth pass FSP sample present completely different texture components of dominant A-{111}(110) and A_1-{111}(112) with a maximum intensity of 5.73, and it also contains minor intensity of Brass-{110}(112) component (Fig. 4.62d). The recrystallized fifth-pass of the FSP sample is characterized by dominant Brass-{110}(112) component with a texture intensity of 8.81 (Fig. 4.62e). The variation of texture components and texture intensity from one pass to another pass could be attributed to increased heat input as each pass of overlapping FSP is affected by the multiple shoulder interactions. Finally, it was concluded that in AA6061, the overlapping FSP did not affect the grain size but, it influenced the grain orientations from one pass to another pass.

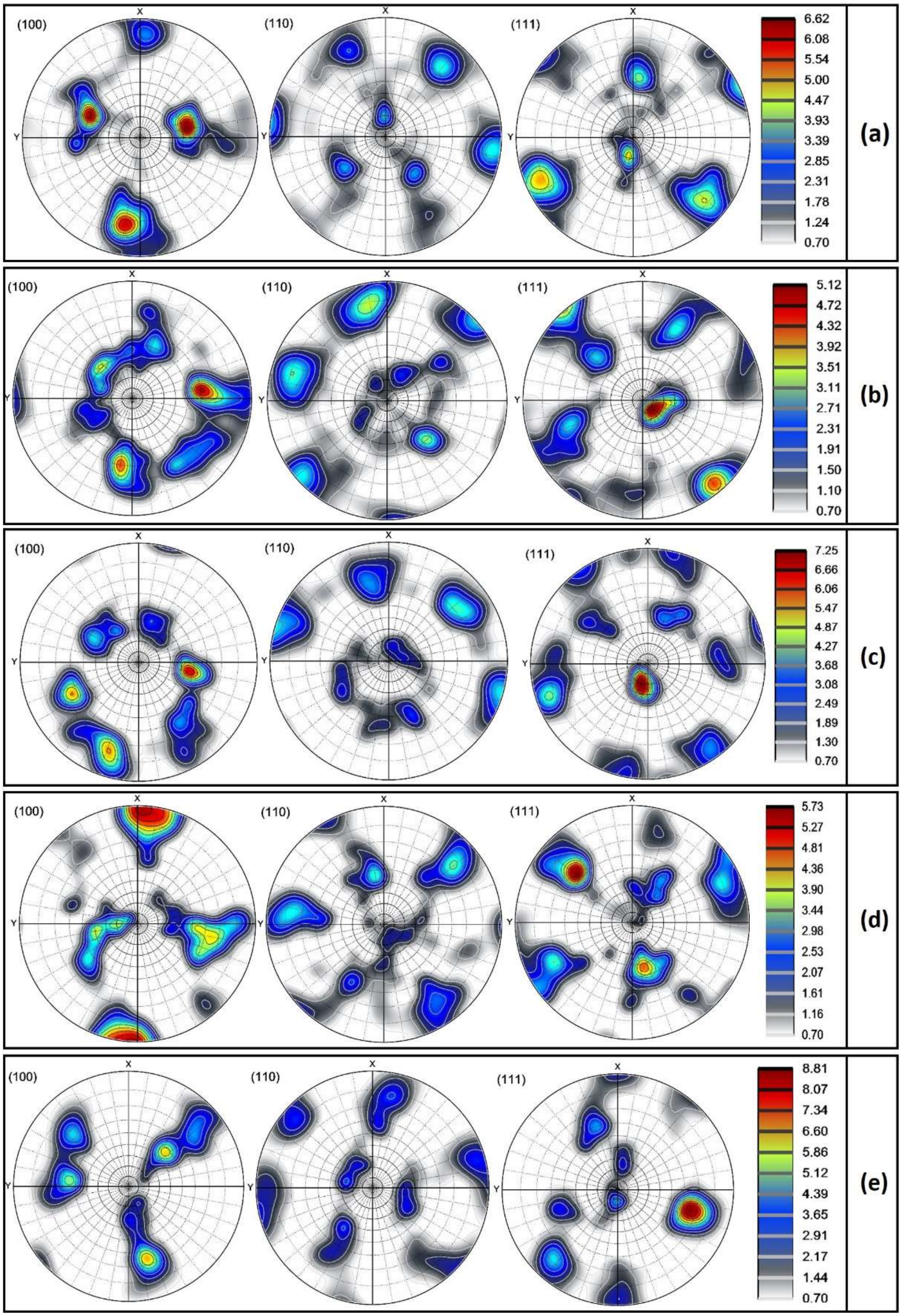

Fig. 4.62. {100}, {110}, and {111} pole figures of SZ of (a) first (b) second, (c) third, (d) fourth, and (e) fifth pass of ACFSP sample.

4.5.2 Mechanical Properties

4.5.2.1 Hardness

The hardness profiles of overlapping FSP specimens across the processed zone are represented in Fig. 4.63. Compared to TMAZ and HAZ, the average hardness in SZ reached a maximum value of 68.7 HV after FSP. Thermal cycle variation, precipitation behavior, and grain refinement were responsible for hardness variation in each zone [Sinhmar et al., (2017)]. As discussed in the microstructural analysis, more grain refinement in SZ provides high hardness as per the Hall-Petch statement [Dua et al., (2015)]. The hardness distribution in the large-area SZ was uniform and 24.50% lower than the average hardness of BM (91 HV). During FSP, the region processed by pin underwent thermal softening due to thermal exposure at maximum temperature up to 0.6-0.9 T_{MP} (melting temperature of alloy), leading to less hardness compared to BM [Chen et al., (2016)]. According to Zhao et al., (2019), the decrease in density of lath-shaped particles presented in the stir region of the AA6063 FSPed sample resulted in a considerable drop in hardness compared to BM. Liu et al., (2018) conducted FSP of AA6061 at 800 rpm and achieved a hardness of 52 HV in the SZ and reported that the tool rotational speed, which causes heat generation in the processed zone, is the reason for the decrease of hardness in SZ compared to cold rolled BM. The present study findings corroborate the results of Zhao et al., (2019) and Liu et al., (2018). The average hardness in the SZ of CCFSP and UWFSP samples is 80.2 HV and 85.1 HV. Within FSP samples, the sample processed in underwater attained the highest hardness due to the presence of refined grains.

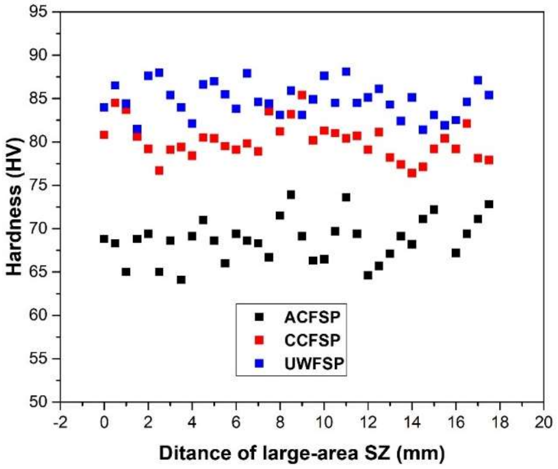

Fig. 4.63. Hardness profiles of overlapping FSP samples.

4.5.2.2 Tensile properties

The tensile properties of BM and FSP samples are documented in Table 4.24, were extracted from the stress-strain curves (Fig. 4.64). The ultimate tensile strength (UTS) and yield strength (YS) were inferior to BM. These are consistent with hardness results. This phenomenon is mainly due to thermal softening and the presence of less density of needle-shaped precipitates, as discussed in the previous analysis. But the elongation (EL) of the FSP sample improved compared to BM, attributed to uniform fine equiaxed grain structure in SZ. Chen et al., (2016) arrived at similar results, and they stated that elongation elevation is due to homogeneity of grain structure and low dislocation density in the processed zone, while the drop in UTS and YS is attributed to annealing softening. The analysis of Khaled et al., (2014) concluded that the reduction in UTS and hardness was due to the dissolution of intermetallics and limited re-precipitation during FSP. In order to balance the mechanical properties in steels, the term product of UTS and EL has been used in industries [Chen et al., (2016)]. As presented in Table 4.24, the FSP samples exhibit a higher product of UTS and EL compared to BM. The fine precipitates present in underwater FSP sample can impede the grain boundary sliding and result in the highest strength among all FSP samples. While the heat treatment after FSP did not affect the strength much, it led to a drop in elongation. The results of mechanical properties are in line with the precipitation behavior as discussed in the SEM analysis.

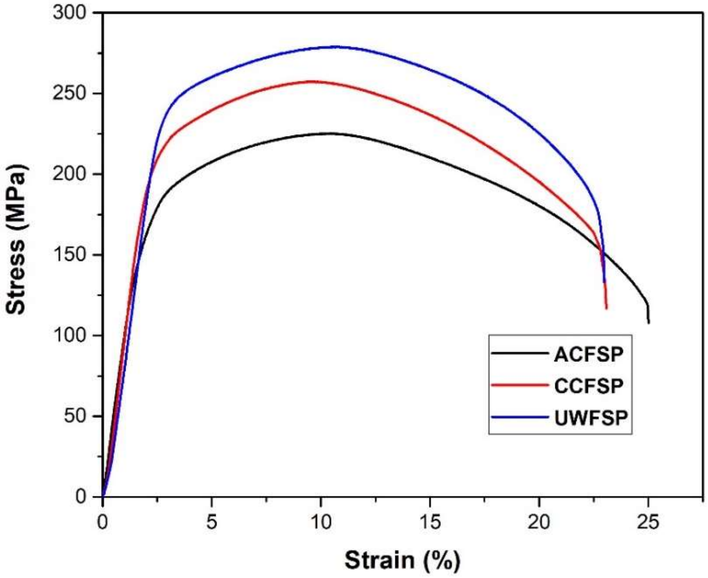

Fig. 4.64. Stress-strain curves of BM and FSP samples.

Table 4.24 Tensile properties

Condition	UTS (MPa)	YS (MPa)	EL (%)	UTS X EL (MPa%)
BM	285±3	192±3	18±2	5130
ACFSP	224±2	134±2	25±1	5600
CCFSP	258±2	214±2	23±2	5934
UWFSP	272±2	224±2	23±1	6256

4.5.3 Corrosion

4.5.3.1 Tafel polarization test

The potential-dynamic polarization (PDP) curves of BM and FSP samples in 3.5% NaCl solution are depicted in Fig. 4.65. The corrosion potentials (E_{COR}) of the BM and FSP samples were extracted from PDP curves are documented in Table 4.25. And, it is showing that the E_{COR} value of BM is more negative than the FSP samples, indicating better corrosion resistance of the FSP sample over BM. During FSP, the working metal undergoes intense plastic straining and DRX, leading to a homogenous microstructure. The homogenous microstructure reduces the possibility of corrosion attack and enhances corrosion resistance [Li et al., (2005)]. In general, the corrosion occurred due to potential difference between second-phase particles and aluminium matrix. During corrosion attack, the second-phase particles act as a cathode, which is more noble, while the aluminium matrix plays the role of an anode and is subjected to anodic dissolution. Thus, localized corrosion attacks happened between coarser second-phase particles, aluminium matrix, and precipitate free area [Sinhmar et al., (2019)]. Therefore, the BM, which includes coarser second-phase particles (as mentioned in the previous analysis) and heterogeneous microstructure, becomes more prone to corrosion attack. Within FSP samples, the underwater FSP sample attained the highest corrosion resistance due to the presence of very fine precipitates, leading to a less potential difference. These findings are in line with the effect of precipitates on corrosion behavior as discussed in SEM analysis.

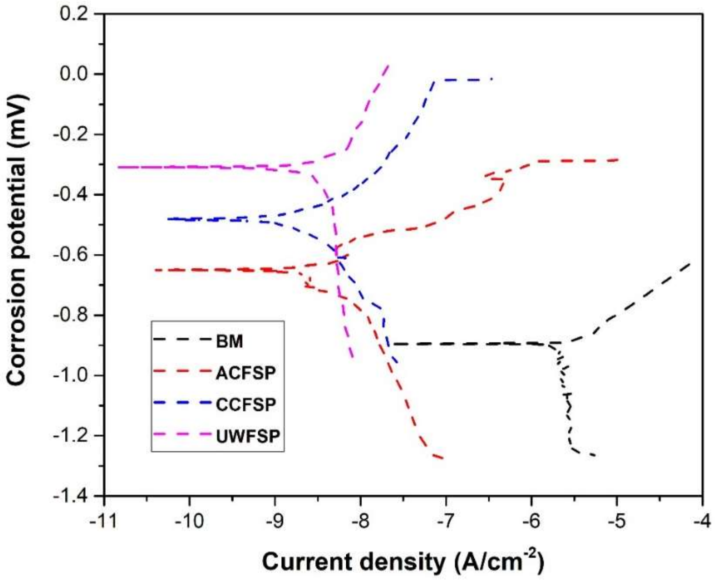

Fig. 4.65. PDP Curves of BM and FSP samples.

Table 4.25 Tafel test results.

Sample condition	**Corrosion potential (mV)**	**Current density (A/cm^2)**
BM	-909	-5.5
ACFSP	-639	-7.9
CCFSP	-527	-8.4
UWFSP	-357	-8.3

4.5.3.2 Electrochemical impedance spectroscopy (EIS) test

Electrochemical impedance spectroscopy was carried out on BM and the top surface of the FSP samples. The Nyquist plots of BM and FSP samples developed in EIS tests are displayed in Fig. 4.66. The Nyquist plot presents the real impedance on the x-axis and imaginary impedance on the y-axis, and single-time high-frequency capacitive loops were formed for all samples. The semi-circle or capacitive loop diameter indicates the corrosion behavior, and the large diameter indicates high corrosion resistance. As compared to FSP samples, the BM showed smaller diameter capacitive loops indicate less corrosion resistance. On the other hand, sample processed in underwater showed larger diameter capacitive loops than other FSP samples and resulted in better corrosion resistance. The data such as real impedance, imaginary impedance, and frequency extracted from the EIS test were fitted in the equivalent circuit as shown in Fig. 4.67. The equivalent circuit provides information in terms of solution resistance (R_S), capacitor resistance (R_{CT}), double layer capacitance (C_{DL}), and n. The data extracted from the equivalent circuit is shown in Table 4.26. From Table 4.26, it was identified that the solution resistance of all samples is comparatively small compared to capacitor resistance. The capacitor resistance increased after FSP, and it is increased with the increase of cooling effect. In the present study, the n value is less than 1, called frequency dependence capacitor. The n value of BM is lower than the FSP samples due to inhomogeneity present in the material [Liu et al., (2018)]. Hence, the findings of EIS tests are in line with Tafel results.

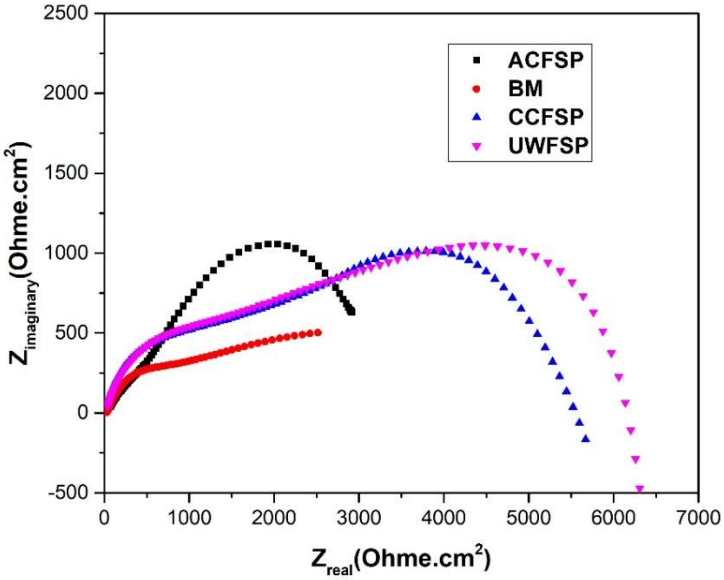

Fig. 4.66. EIS test results BM and FSP samples (a) Nyquist plot and (b) Bode plot.

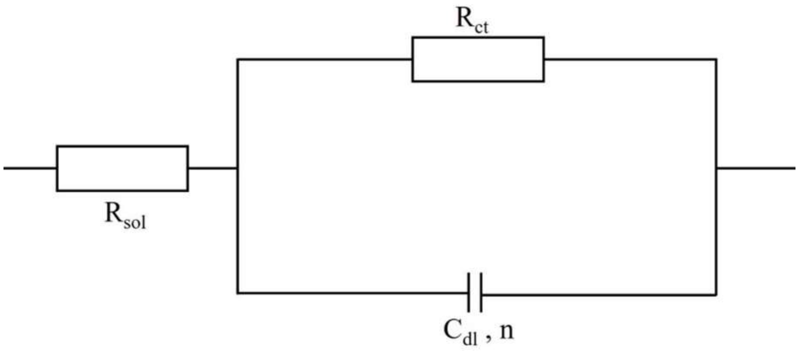

Fig. 4.67. Equivalent circuit for fitting the EIS data.

Table 4.26 EIS data extracted from equivalent circuit

Sample	R_S (Ohm.cm^2)	R_{CT} (Ohm.cm^2)	C_{DL} (F)	n
BM	4.6x10^2	2.8x10^3	3.0x10-^{5}	0.76
ACFSP	5.6x10^2	5.4x10^3	4.3x10^{-4}	0.82
CCFSP	2.7x10^2	5.7x10^3	6.2x10^{-5}	0.85
UWFSP	5.4x10^2	5.8x10^3	8.7x10^{-5}	0.77

4.5.4 Wear analysis

The wear test results such as weight loss (mg) and wear rate (mg/m) tested at 20 N and 40 N for 1000 m of sliding distance are listed in Table 4.27. From Table 4.27, it was observed that the wear rate after FSP was decreased by 28% at 20 N could be attributed to the high toughness and grain refinement of the FSP sample. The high toughness of the FSP sample decreases the detachment of the metal from the wear surface, while the high fraction grain boundaries in grain refined FSP sample resist the frictional force between the contacting surfaces and controls the formation of wear debris, and resulted in high wear resistance [Mahdi et al., (2019)]. Table 4.27 also represents a further reduction of wear rate in cooling-assisted FSP. The wear rate of the UWFSP sample is decreased by 34% and 8% as compared to BM and ACFSP samples. The increase in wear resistance of the UWFSP sample with respect to the ACFSP sample is attributed to the better grain refinement and fine strengthening precipitates. By comparing results**,** the samples tested at 40 N resulted in a high wear rate due to an increase of frictional force between the counterpart and sample surfaces. But, at 40 N, the difference of wear rate between the BM and FSP samples is 11%, and the wear rate of both FSP samples is almost the same. It indicates that the wear rate difference between BM and FSP sample is decreased with the increase of wear load.

Table 4.27 Wear test results.

Sample condition	Weight-loss with respect to load (mg)		Wear rate with respect to load (mg/m)	
	20 N	**40 N**	**20 N**	**40 N**
BM	9.96	15.87	0.0099	0.0159
ACFSP	7.16	14.12	0.0072	0.0141
UWFSP	6.58	14.09	0.0066	0.0140

4.5.5 Fatigue

4.5.5.1 FCG behavior

The fatigue crack length (a) vs. number fatigue cycle (N) graph is plotted initially to estimate the fatigue life of samples as displayed in Fig. 4.68. It was identified from the graph that the fatigue life of FSP samples is greater than the BM, and with the increase of fatigue cycles, the FCG rate also accelerated. It proves that FSP samples stopped the fatigue crack from further expanding. In addition, it can be observed from the graph that the a-N curve of FSP samples consists of fluctuations, while it was smooth for the base metal. The smooth curve in the BM represents rapid crack propagation without any obstacles. In FSP samples, various factors such as fine-grained structure, a high fraction of grain boundaries, precipitation factor, etc., act as obstacles for fatigue crack propagation and stop the crack from further expanding.

The log-log curve of the da/dN vs. ΔK is displayed in Fig. 4.69. Three distinct regions can be identified in the sigmoidal curve as represented in Fig. 4.69a. Region-I (R-I) is the crack initiation stage. In this region, when the value of da/dN approaches zero as ΔK reaches a threshold value (ΔK_{th}) below which crack would not propagate [Su et al., (2020)]. It was identified from Fig. 4.69a that the sample with a smaller grain size has more ΔK_{th}, and the UWFSP sample has higher the ΔK_{th} as the grain size of the sample is smaller than the other samples. The smaller grain size in the UWFSP sample has more volume fraction of grain boundaries, which can act as obstacles for crack propagation. Region-II (R-II), called the steady-state crack propagation stage, and the FCG rate is linear in this region. The FCG rate deviated from linearity at the low and high ΔK values. The log-

log curve of the da/dN vs. ΔK of Region-II is shown in Fig. 4.69b for calculation of Paris constants by liner fitting. The logarithmic curve of the linear region is described by the Paris model given by;

$$\frac{da}{dN} = C(\Delta K)^m \qquad (4.5)$$

Where C and m are constants [Beden et al., (2009)]. The equation indicates that the da/dN depends only on ΔK irrespective of the value of the stress ratio. A linear relationship can be made between log(ΔK) and log(da/dN), and the equation gives it;

$$\log\left(\frac{da}{dN}\right) = \log C + m\log(\Delta K) \qquad (4.6)$$

The estimated values of the Paris constant, such as slope (m) and the intercept (C), are given in Table 4.28. Greater the value of slope implies greater the value of m, which indicates that the da/dN is more sensitive to change in ΔK. In Region-II, the fitting results exhibited linear relation with a correlation coefficient of 0.996 or more, as shown in Table 4.28. At the initial stages of crack propagation, the crack growth rate of BM is faster than ACFSP samples at the same ΔK value, and da/dN of UWFSP is minimum. As the crack propagates, the crack growth rate UWFSP samples attained maximum value after the ΔK value of 11.97 MPa·m$^{1/2}$. Region-III (R-III), called a rapid or unstable crack propagation region. At high ΔK in this region, the microstructural defects can drastically accelerate the crack growth rate compared to the base metal.

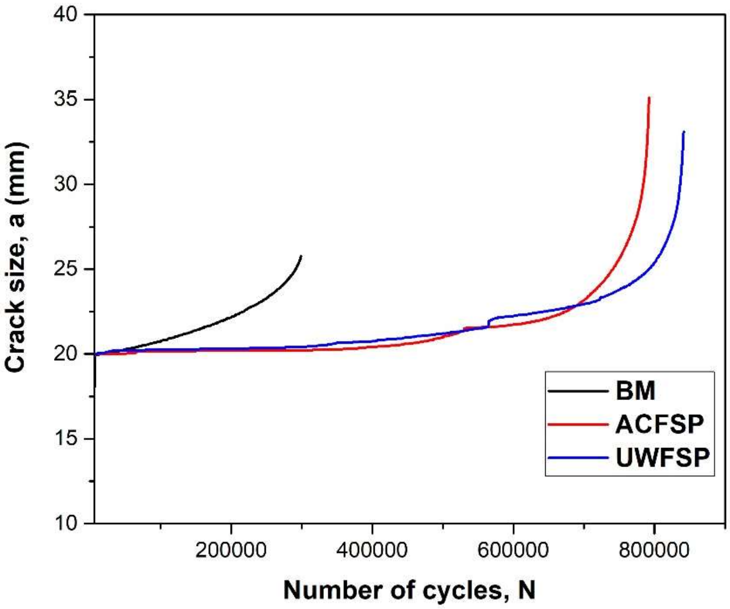

Fig. 4.68. Crack size (a) vs. Number of cycles (N) curve.

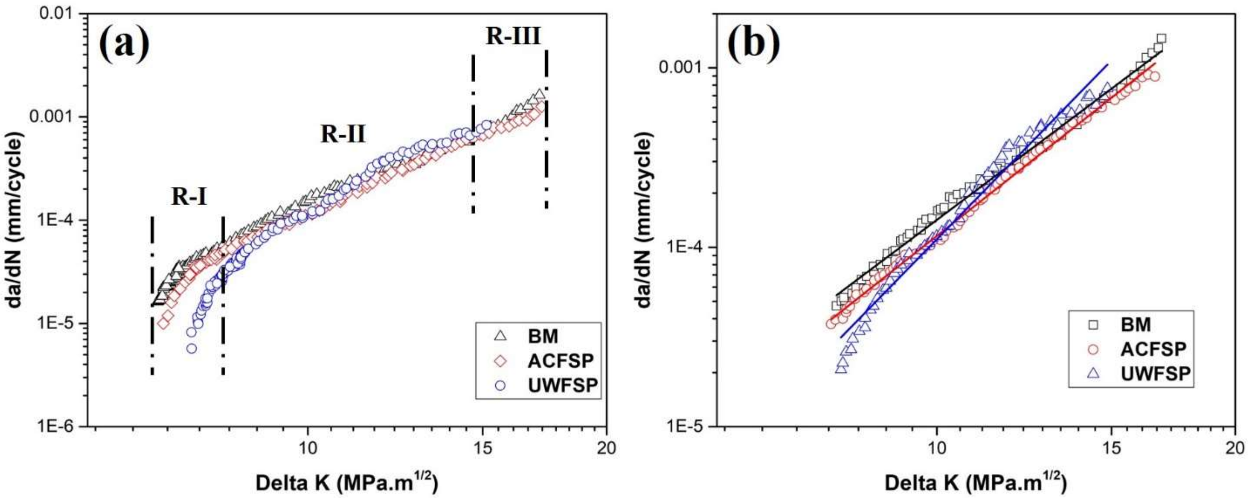

Fig. 4.69. (a) log-log plot of da/dN vs. ΔK graph showing three different regions of crack propagation and (b) log-log plot of da/dN vs. ΔK graph or Paris curve showing Region-II for evaluating Paris constants.

Table 4.28 Paris constants.

Sample	C	m	Correlative coefficient
BM	1.05E-08	4.128	0.995
ACFSP	5.09E-09	4.355	0.998
UWFSP	2.43E-10	5.658	0.987

4.5.5.2 Fracture analysis

Fig. 4.70 displays the low-magnification fracture images of BM and UWFSP samples showing three different regions of fracture. Different fracture regions of the BM are not clearly evident as they did not sustain for a large number of fatigue cycles (Fig. 4.70a), whereas the different fracture regions in UWFSP are clearly evident (Fig. 4.70b). The different fatigue fracture features such as striations, dimples, and cracks are not visible at the low-magnification view. The high magnification SEM fracture images of BM and ACFSP samples are shown in Fig. 4.71. Fig. 4.71a-c presents the fracture features of BM and FSP samples in Region-1 or crack initiation stage. The fractured image of BM shows the ridges and plateaus interposed with a flat surface (Fig. 4.71a), whereas the FSP samples witnessed peak and valley type of fracture surface, which contains striations marks and secondary cracks, as shown in Fig 4.71b-c. Due to the instability of crack propagation during the initial stages, the peak and valley type of fracture features are formed on the fracture surface.

The energy at the crack tip can be reduced by the presence of these secondary cracks, which retards the crack growth. As witnessed in Fig. 4.68 and Fig. 4.69a, the crack propagation is almost rapid throughout BM, resulting in less fatigue life with a flat fracture surface. Fig 4.71d-e shows the second stage (R-II) fracture features or steady-state crack propagation of BM and FSP samples. All samples show striations, often called fatigue striations, which are general indications of second-stage fracture region. Along with striation marks, the dimples are present in the BM (Fig. 4.71d), and it was regarded as a mix-mode of fracture (i.e., the fracture surface contains both Region-II and Region-III fracture features). The dimples present in the fracture surface of BM indicated the rapid crack propagation in the second stage and resulted in an earlier fracture. Compared to FSP samples, many striation steps are formed in BM. Most of the striation marks formed are discontinuous, indicating accelerated crack propagation [Zhang et al., (2020)]. The FCG rate can also be estimated by the striations spacing [D'Urso et al., (2014)]. As compared to the ACFSP sample, the striation space is less in the UWFSP sample. The spacing between the striations is proportional to the crack propagation rate. The precipitation factor has a significant influence on the striations and fatigue crack growth. Striations slightly bend when it encounters the precipitate particles as it acts as a barrier for crack propagation. But in some cases, these particles have a poor interface with the aluminium matrix, act as stress concentration regions and accelerate fatigue growth. The crack growth can even break the precipitate particles. Compared to coarse grains, finer grains have more grain boundary area, hindering crack growth and increasing fatigue life. Along with the above factor, the high angle boundaries also act as barriers for crack propagation. As seen in microstructural analysis, the fraction of high angle boundaries is more in the UWFSP sample. From the above factors, it was observed that the fatigue life improved significantly after UWFSP, and it was improved further with the addition of cooling media. Hence, it was concluded that the cooling media has a significant impact on fatigue life. The fracture features of Region-III or the unstable crack propagation region of FSP samples show the dimples and striation marks depicted in Fig. 4.71(f-g). The fracture morphology is similar for the two samples.

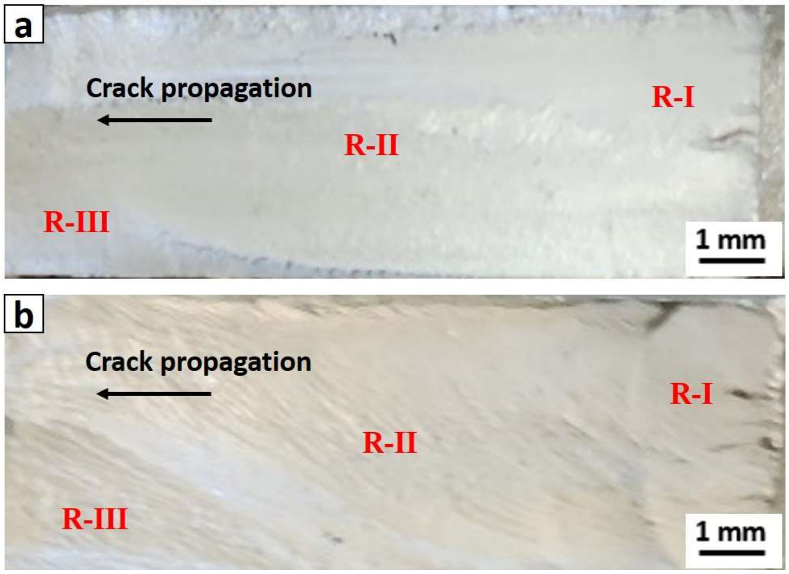

Fig. 4.70. Low-magnification fracture images of (a) BM and (b) UWFSP sample.

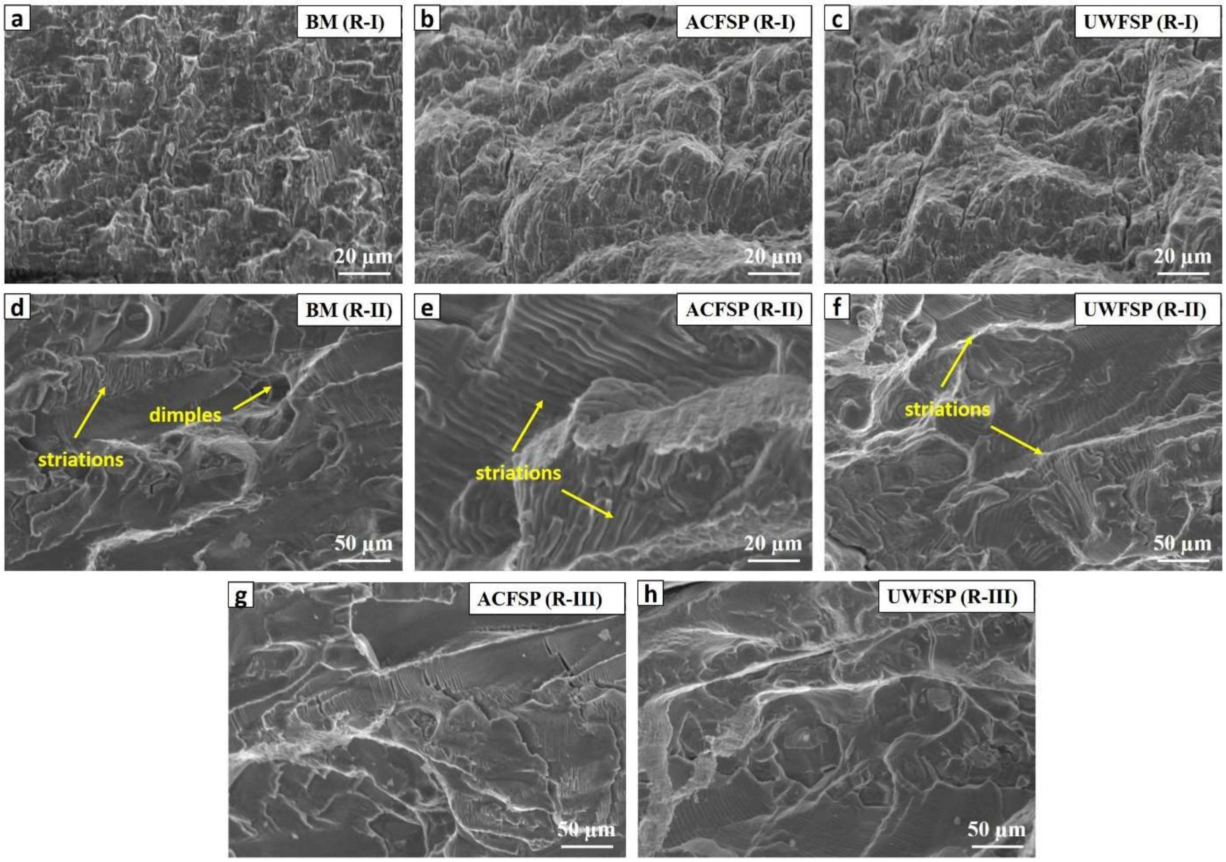

Fig. 4.71. Fracture features in (a-c) Region-I of BM, FSP, and UWFSP samples, (d-f) Region-II of BM, FSP, and UWFSP samples, and (g-h) Region-III of FSP and UWFSP samples.

4.6 Establishing a novel relation between local and bulk mechanical strength of friction stir processed aluminium alloys

In this context, the primary objective is to establish a linear relationship between local strength (i.e., hardness) and bulk mechanical strength (i.e., tensile strength) of friction stir processed aluminium alloys using experimental investigations on selected alloy systems together with data reported in literature sources.

It is well known that the primary objective of FSP is to produce structural homogeneity in processed layers. After FSP, the homogeneous processed zone undergoes mechanical testing and other testing for evaluation of their properties. In mechanical testing, the homogeneous processed zone is tested for both localized and bulk mechanical strength. As reported in many studies, hardness (local strength) and tensile strength (bulk strength) are essential factors in engineering applications. But, the measurements of these two properties require different parameters. Localized mechanical testing includes hardness testing, where the indenter of hardness tester penetrates the material's surface for measuring local strength without fracturing the material. The tensile testing gives bulk strength of the processed region, and it measures the tensile properties such as ultimate tensile strength (UTS) and yield strength (YS) by fracturing a large volume of material. However, both hardness and tensile strength after FSP are decided by the degree of homogeneity and grain refinement. For testing the homogeneity of the processed zone, it is necessary to establish a linear relationship between hardness and tensile strength. In the case of surface composites processed via FSP, the relation between hardness and strength may not be valid as hardness along the processed region is not uniform because it varies drastically due to the presence of secondary particles. On the other hand, for friction stir processed materials without reinforcing, the hardness along the processed zone is approximately uniform [Gandra et al., (2011)]. So it is necessary to establish a direct correlation between hardness and tensile strength to test the homogeneity of the processed region, and this relation is expected to be beneficial for practical applications.

Grain refinement is one of the primary factors to determine hardness and strength. Grain refinement during FSP is controlled by various factors such as varying process parameters, conducting multi-pass experiments, and using different cooling media. Moreover, for establishing a correlation between hardness and strength, a detailed case study is required. So, for analysis, a case study on FSP of AA2014 with single (data Section 4.2) and two-pass FSP using different cooling media was performed initially. The author also took the data of single and multi-pass overlapping FSP on AA6061 using various cooling media from Section 4.3&4.5 and gathered the reported data from literature sources on surface composites of friction stir processed aluminium alloys in order to validate the relationship between strength and hardness.

4.6.1 Grain size and mechanical properties data required for establishing a correlation between hardness and strength

The EBSD maps of BM and single-pass FSP samples and optical images of 2-pass FSP samples of AA2014 are presented in Fig. 4.72. The grain size data of BM and FSP samples are documented in Table 4.29. In FSP samples, the assistance of cooling media (water and dry ice) further reduced the grain size. Within cooling-assisted FSP, the sample processed using water media produced a more refined structure than the sample processed in dry ice media, as shown in Fig. 4.72d&g. From Table 4.29, it was observed that, as compared to single-pass FSP, better grain refinement was achieved in 2-pass FSP owing to further plastic deformation and dynamic recrystallization.

The hardness profile of FSP samples measured in SZ is shown in Fig. 4.73a, and the average hardness was calculated and reported in Table. 4.29. On the other hand, the tensile properties of SZ were extracted from stress-strain curves (Fig. 4.73b), also documented in Table. 4.29. Despite grain size, there was a decrease in hardness and strength of the FSP sample compared to that of BM. The reduction in hardness and strength is due to the dissolution of fine strengthening precipitates. This is especially true for AA2014 precipitation hardening alloy, which relies heavily on the distribution and intensity of precipitates rather than grain size [Fadhalah et al., (2014)]. It was concluded that, in precipitation-hardened alloys, the Hall-Petch equation is not valid for grain refinement between the BM and FSP sample [Fadhalah et al., (2014)]. But, within the FSP samples, a consistent relation was identified between the grain size and mechanical properties (i.e., hardness and yield strength), where the finer grain size resulted in improved hardness and strength. In other words, by achieving further grain refinement in the FSP sample using different cooling media and multi-pass experiments, the hardness and strength simultaneously improved as per the Hall-Petch equation. Finally, more grain refinement in water cooling with 2-pass FSP resulted in high hardness and strength. Compared with hardness and strength, ductility in the FSP sample significantly improved compared to BM due to thermal softening during FSP. Unlike hardness and strength, the ductility within the FSP sample maintained an inverse linear relationship with grain size. Therefore, the ductility tendency decreased on further refining grain size in FSP samples.

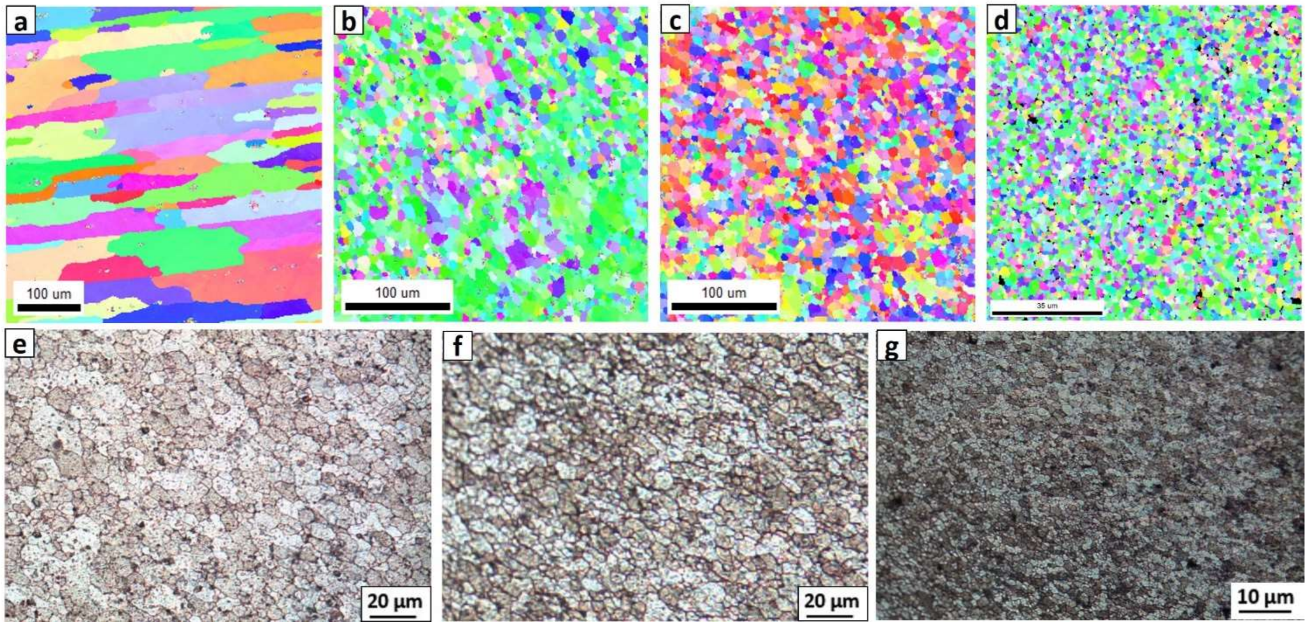

Fig. 4.72. EBSD maps of (a) BM, first-pass (b) ACFSP, (c) CCFSP and (d) UWFSP samples, and optical images of second-pass (e) ACFSP, (f) CCFSP and (g) UWFSP samples of AA2014.

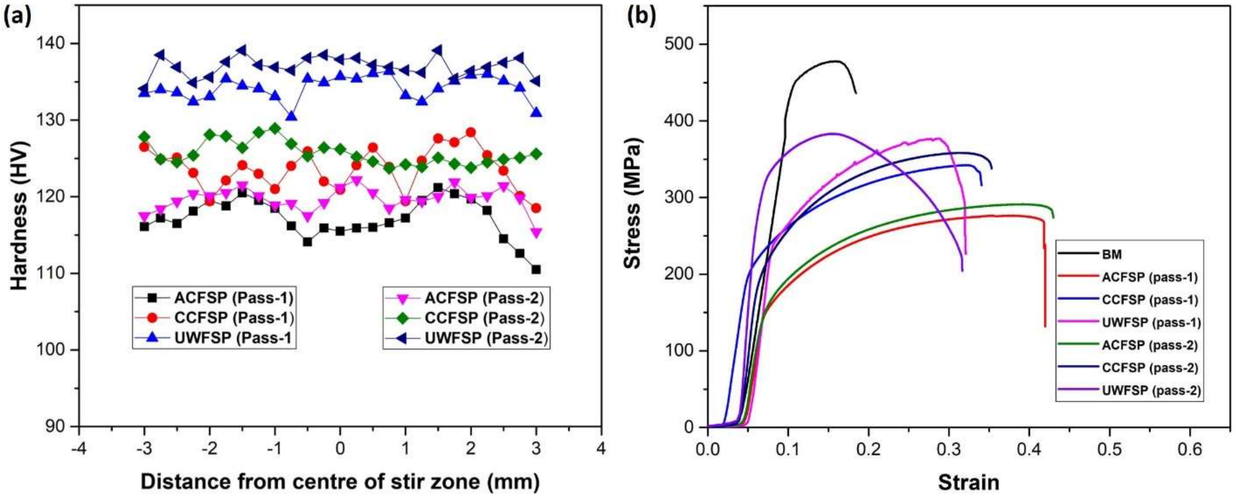

Fig. 4.73. (a) Hardness profile of friction stir processed AA2014 samples, and (b) Stress-strain curves of BM and FSP samples of AA2014.

Table 4.29 Statistical data of friction stir processed AA2014.

Sample condition	Grain size (µm)	Mechanical properties			
		Hardness (HV)	YS (MPa)	UTS (MPa)	Elongation (%)
BM	80.5±50.5	151±12	409±6	478±6	18.40±1.1
ACFSP (1st Pass)	4.9±3.5	116±6	146±3	276±3	41.90±2.9
CCFSP (1st Pass)	3.5±2.9	123±5	198±4	342±4	34.00±2.5
UWFSP (1st Pass)	0.9±0.4	134±3	240±4	376±5	32.00±1.9
ACFSP (2nd Pass)	4.6±3.8	119±4	157±5	291±6	43.00±2.7
CCFSP (2nd Pass)	3.4±3.1	126±2	194±2	356±3	35.00±1.7
UWFSP (2nd Pass)	0.9±0.7	137±3	285±3	381±3	31.00±2.6

4.6.2 Relation between hardness and strength

As discussed earlier, the grain refinement produced in SZ after FSP using different processing conditions controls mechanical properties. It means that in precipitation-hardened alloys, the Hall-Petch equation is valid within the FSP samples using different processing conditions. The Hall-Petch equation can be written in two ways; the first way establishes the relation between grain size and hardness is given by equation [Du et al., (2015)];

$$H = H_O + K_1 D^{-1/2} \qquad (4.7)$$

H is hardness, H_O is the hardness for infinitely large grain size or, to be more precise, the average hardness of a single crystal, D is the mean grain size, and K_1 is the constant for a particular material. The second way establishes the relation between grain size and yield strength is given by equation [Sato et al., (2003)];

$$\sigma_Y = \sigma_O + K_2 D^{-1/2} \qquad (4.8)$$

Where σ_Y is the yield strength, σ_O is the yield stress for infinitely large grain size, or it can be termed as average yield stress of a single crystal, D is the mean grain size, and K_2 is the constant for a particular material. The results obtained after FSP, such as mean grain size, hardness, and yield strength, were plotted to arrive at connections between variables, where the grain size was taken at ordinate, and hardness and yield strength were taken at abscissa (Fig. 4.74a). And, the Hall-Petch equation for hardness and yield strength were fitted across the relations to find the constants. The trend showed that the experimental values of hardness and yield strength fitted well with theoretical estimations. And it is also noted that, compared to hardness values, the yield strength values deviated a little. Thus, hardness and yield strength with grain size are not the same, and the relating constants are different, as shown in Fig. 4.74a. It is well known that grain size, hardness, and strength depend on each other. So, considering the dependency on each other, it is necessary to establish a relation between hardness and strength of friction stir processed alloys.

It is apparent that during tensile deformation of elastic-plastic materials, the flow stress varies linearly with plastic strain, and it is expressed using Hollomon's equation. Hollomon's equation gives the relationship between logarithmic stress and logarithmic strain. The Hollomon's equation for calculation of work-hardening exponent is given by [Nutor et al., (2017)];

$$\sigma = K\epsilon^{n} \qquad (4.9)$$

Where n is the work-hardening exponent and K is the constant for particular materials. For calculation of work-hardening exponent (n), a plot was drawn between logarithmic true stress (at ordinate) and logarithmic true strain (at abscissa) as shown in Fig. 4.74b and Hollomon's equation re-written in the form y = mx + c is given by;

$$\log\sigma = n\log\epsilon + \log K \qquad (4.10)$$

where n is the value corresponding to slope m is obtained by linear curve fitting (shown by dotted lines Fig. 4.74b) of logarithmic true stress (at ordinate) and logarithmic true strain (at abscissa) data.

By considering the n value, Cahoon et al., (1971) formulated empirical equations for elastic-plastic materials. The equations (4.11&4.12) show that the hardness varies linearly with strength and is given by:

$$\frac{\sigma_Y}{HV} = \frac{(0.1)^n}{3} \qquad (4.11)$$

As shown in Fig. 4.74c, by considering n values, the above relation fitted well with experimental values of friction stir processed alloys and gave a proportionality constant of 1.9 by linear curve fitting.

$$\frac{\sigma_{UTS}}{HV} = \frac{1}{2.9}\left[\frac{n}{0.217}\right]^2 \tag{4.12}$$

As with the previous case, this expression also matched experimental values of friction stir processed alloys and gave a proportionality constant of 2.7 by linear curve fitting as shown in Fig. 4.74c.

Finally, the curve fitting of both the equations is in good agreement with experimental results due to the homogenization of the SZ. However, compared to σ_{UTS} vs. H values, σ_Y vs. H experimental values show a slight deviation from the curve fitting, which might be due to the highly plastic nature of processed alloys.

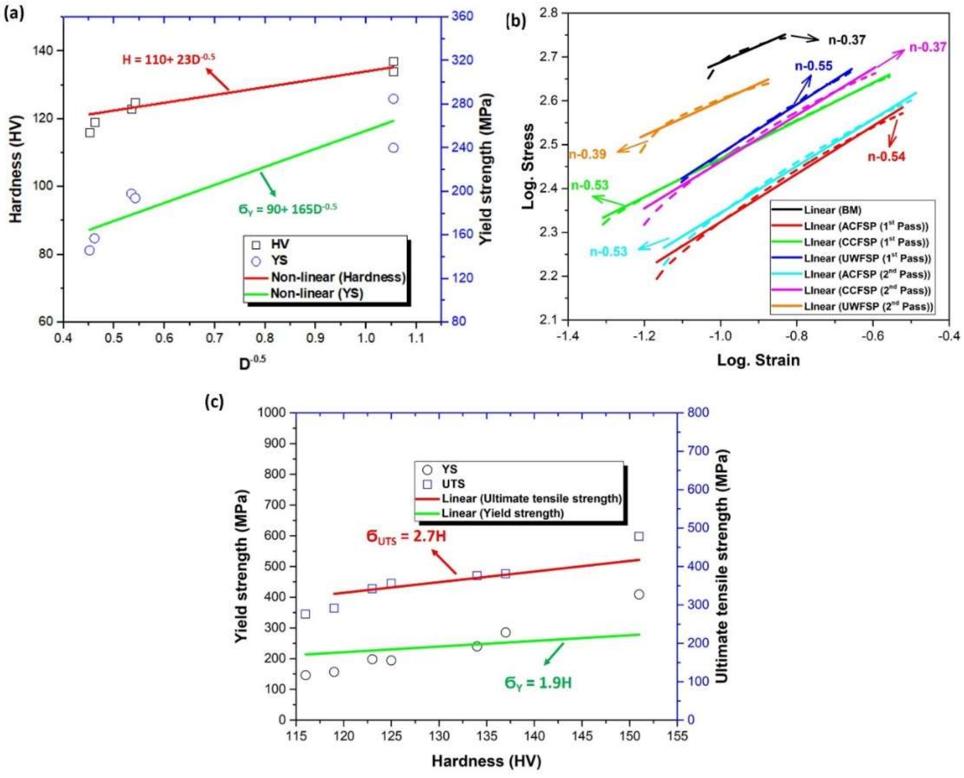

Fig. 4.74. (a) Non-linear curve fitting of variation of hardness and strength in relation to grain size, (b) Extraction of n values using linear curve fitting, and (c) Extraction of the relation between hardness and strength using linear curve fitting of AA2014.

In order to validate the equation for aluminium alloys, the authors also considered the data of Chapters 4.3 and 4.5, i.e., the influence of single-pass and multi-pass with 50% overlapping data of FSP on AA6061 alloy using different cooling media. The results obtained from friction stir processed AA6061 alloy such as EBSD maps, hardness profile, and stress-strain curves are shown in Fig. 4.75&4.76, and the statistical data exacted from those data such as grain size, hardness, and tensile properties are documented in Table 4.30. Like friction stir processed AA2014, similar results were obtained in friction stir processed AA6061 alloys, i.e., the grain refinement, hardness, and tensile strength increased with an increase in cooling rate and two-pass FSP.

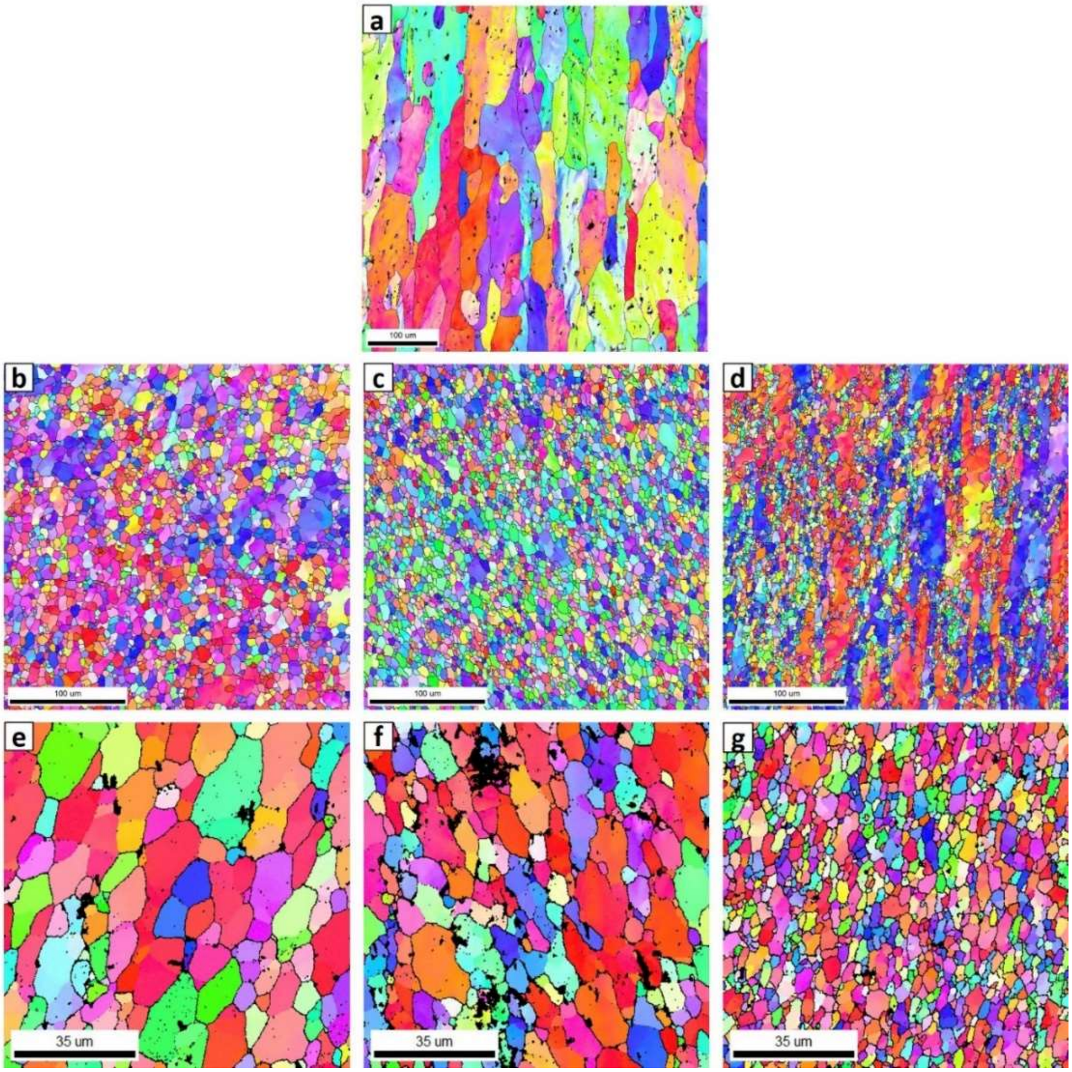

Fig. 4.75. EBSD maps of (a) BM, single-pass (b) ACFSP, (c) CCFSP and (d) UWFSP samples and multi-pass (e) ACFSP, (f) CCFSP and (g) UWFSP samples of AA6061.

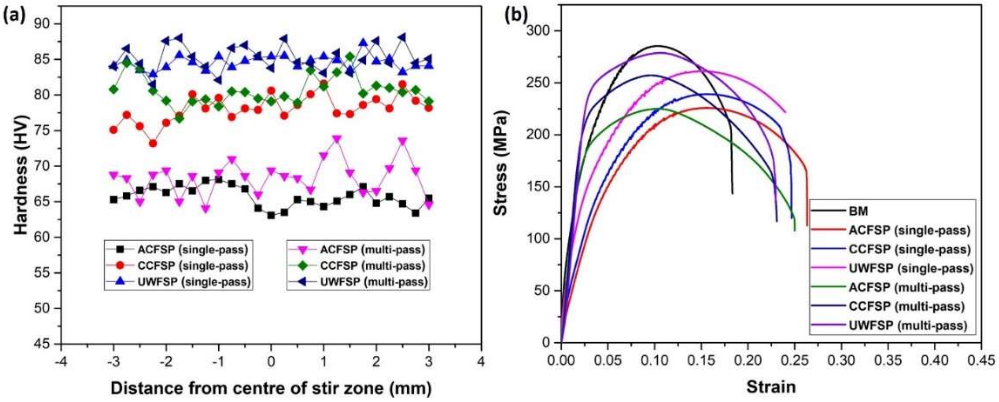

Fig. 4.76. (a) Hardness profiles of FSP samples and (b) Stress-strain curves of BM and FSP samples of AA6061.

Table 4.30 Statistical data of friction stir processed AA6061.

Sample condition	Grain size (µm)	Mechanical properties			
		Hardness (HV)	YS (MPa)	UTS (MPa)	Elongation (%)
BM	88.4±43.8	90±11	192±5	285±3	18.3±2.5
ACFSP (single-pass)	4.8±3.2	65±3	105±3	224±2	26.2±3.4
CCFSP (single-pass)	3.8±2.1	78±4	101±2	240±2	24.6±3.7
UWFSP (single-pass)	2.8±1.1	84±3	105±3	261±3	24.0±3.2
ACFSP (multi-pass)	4.7±3.5	68±3	134±2	224±2	25.0±1
CCFSP (multi-pass)	3.8±2.5	80±4	214±2	258±2	23.0±2
UWFSP (multi-pass)	2.5±1.2	85±2	224±2	272±2	23.0±1

In Fig. 4.77a, the Hall-Petch relations were established between the grain size and strength (i.e., local and bulk strength) for friction stir processed AA6061 alloys under different processing conditions based on the Eq. (4.7) and (4.8), respectively. Unlike AA2014 alloy, the established relations did not fit well with the experimental values, especially in the yield strength case, the experimental data deviated in a wide range. As discussed earlier, in precipitation-hardened aluminium alloy, the strength and hardness are decided by precipitation factor rather than grain refinement factor. As in the previous case, the strain hardening exponents were measured for friction stir processed AA6061 alloys using linear curve fitting as shown in Fig. 4.77b. Based on the calculated n values, the relations between hardness and strength (yield strength and ultimate tensile strength) were established using Eq. (4.11 and 4.12) to find the novel constants. The proportional constants measured using experimental investigations, as shown in Fig. 4.77c. Similar to the AA2014 case, the Eq. (4.11 and 4.12) fitted well with experimental values of friction stir processed AA6061 samples and left a proportionality constant of 2.1 for σ_Y vs. H relation and 3.2 for σ_{UTS} vs. H relation by linear fitting. Finally, the curve fitting of both equations is in good agreement with the experimental results of friction stir processed AA2014 and AA6061 alloys due to the homogeneous processed zone.

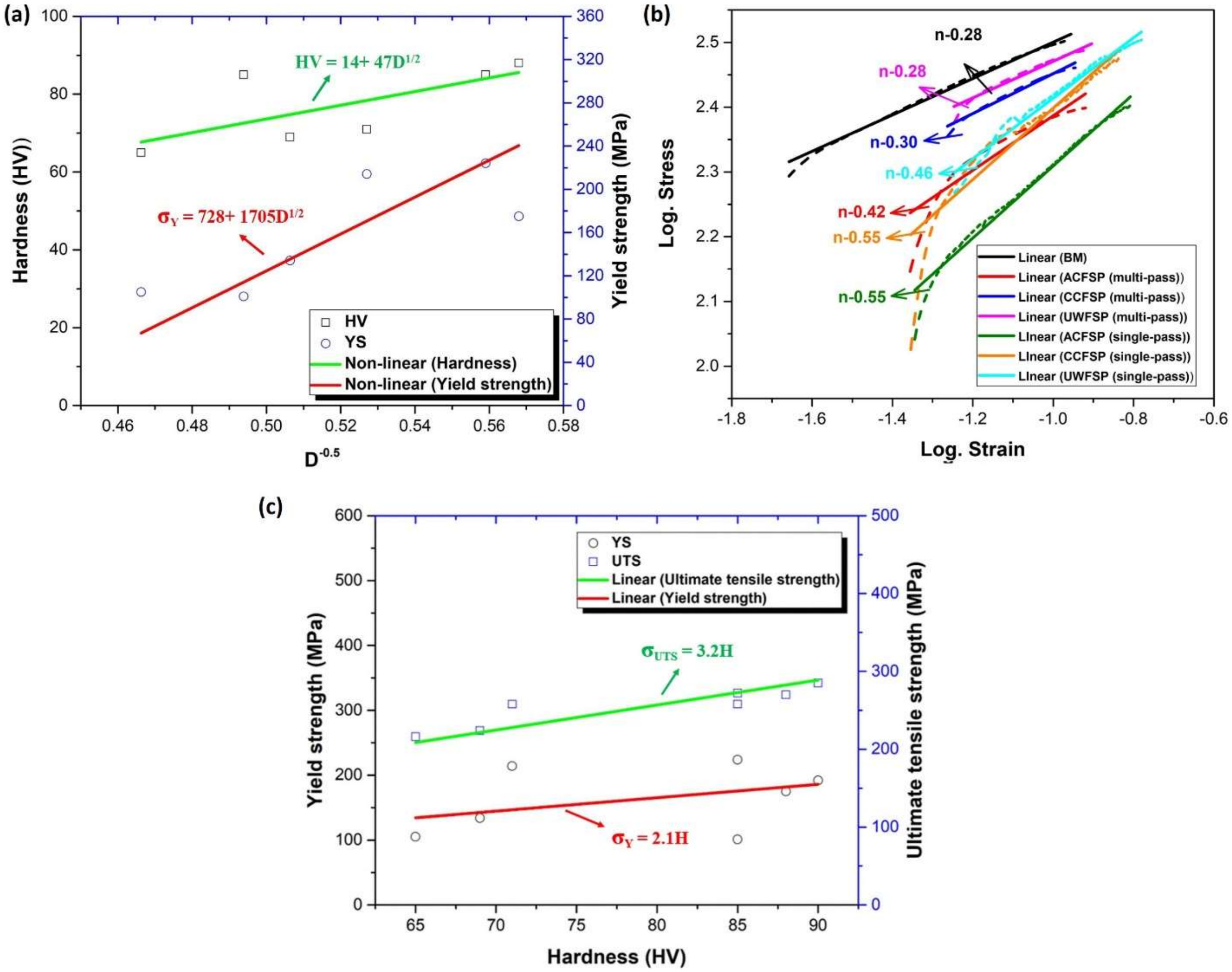

Fig. 4.77. (a) Non-linear curve fitting of variation of hardness and strength in relation to grain size, (b) Extraction of n values using linear curve fitting, and (c) Extraction of the relation between hardness and strength using linear curve fitting.

A similar analysis was conducted on reinforced composites fabricated by FSP. The authors took the data of Jain et al., (2019). They fabricated the AA5083-SiC/CNT composites through FSP, and statistical data of those composites such as grain size, hardness, and tensile strength were summarized in Table 4.31. Using Table 4.31 data, the authors established a relationship between hardness and strength (YS and UTS) using Eq. (4.11 and 4.12) as shown in Fig. 4.78. From Fig. 4.78, it was observed that the established correlations seem unrealistic for reinforced composites fabricated by FSP. The experimental values did not fit well with formulated equations and gave a proportionality constant of 2.4 for σ_Y vs. H relation and 3.1 for σ_{UTS} vs. H relation. Compared to the σ_Y vs. H case, the experimental data deviated in a wide range for the σ_{UTS} vs. H case. It is well known that the hardness and strength composites rely heavily on type, size, and quantity reinforcing agent rather than the grain size of the matrix. While measuring hardness across the SZ of composites fabricated by FSP, the hardness is not uniform and varied drastically due to the presence of reinforcing agents; likewise, the reinforcing agents also alter the tensile strength of composites, resulting in the scattering of experimental data. Hence, it was concluded that it is not possible to establish a relationship between hardness and strength for composites fabricated by FSP due to surface heterogeneity and agglomeration of reinforcing agents.

Table 4.31 Statistical data of AA5083-CNT/SiC composites [Jain et al., (2019)].

Sample condition	**Grain size (µm)**	**Mechanical properties**		
		Hardness (HV)	**YS (MPa)**	**UTS (MPa)**
AA5083-BM	40.0	79.2	138	298
FSPed AA5083	5.8	94.0	210	306
AA5083-SiC	5.2	124.5	320	335
AA5083-SiC/CNT	6.0	112.5	301	361
AA5083-CNT	6.3	107.5	281	316

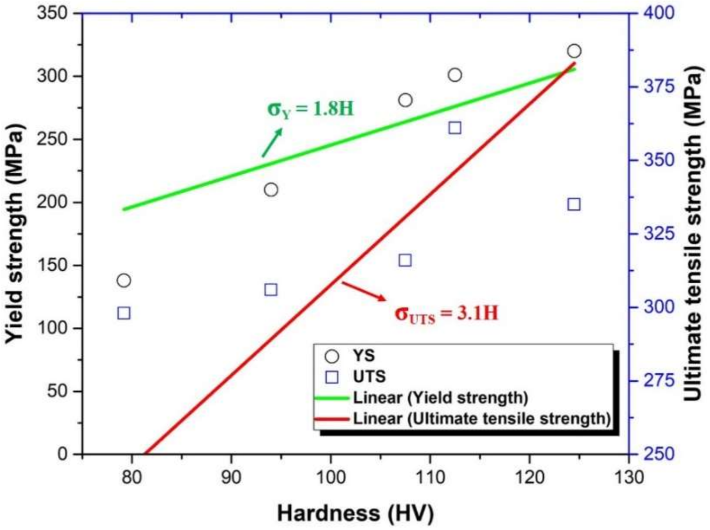

Fig. 4.78. Relation between hardness and strength by linear fitting.

The authors also summarized the friction stir modified and reinforced aluminium alloy data reported in the literature studies to validate the equations. The data gathered from the literature was in terms of hardness, yield strength, and ultimate tensile strength is documented in Table 4.32. The related constants between hardness and strengths were measured and reported for the data reported in Table 4.32. From it was identified that, for friction stir processed alloys, the experimental data was in agreement with Eq. (4.11 and 4.12). On the other hand, the trends of composites fabricated by FSP seemed more complicated and led to the unrealistic estimation of constants between hardness and strength. Finally, it was concluded that it is possible to establish a linear relationship between hardness and strength of friction stir processed aluminium alloys due to the formation of a homogeneous fine-grained structure.

Table 4.32 Establishing correlations for data reported in literature sources of friction stir processed aluminium alloys.

FSP condition	FSP variants	HV	YS (MPa)	UTS (MPa)	YS/HV ratio	UTS/HV ratio	Fitting
friction stir processed AA5005	490 rpm, Tool-I	43	82	129	1.8	3.0	Good
	970 rpm, Tool-I	39	75	122			
	1200 rpm, Tool-I	39	68	123			
	490 rpm, Tool-II	45	103	135			

[Abrahams et al., (2019)]	970 rpm, Tool-II	40	70	118			
	1200 rpm, Tool-II	39	60	119			
Carbon fiber (CF) reinforced AA5052 composites [Cao et al., (2018)]	Base metal	69	176	239	1.5	2.7	Not good
	FSP-AA5052	56	86	234			
	1000-50 (CF)	101	142	253			
	1000-75 (CF)	109	151	283			
	1000-100 (CF)	110	136	261			
Boron carbide reinforced AA5083 composites [Yuvaraj et al., (2015)]	Base metal	82	-	310	-	2.8	Not good
	FSP-AA5083	107	-	331			
	Micro-B_4C-Pass I	112	-	246			
	Micro-B_4C-Pass II	116	-	323			
	Nano-B_4C-Pass I	119	-	334			
	Nano-B_4C-Pass II	124	-	360			

CHAPTER 5

CONCLUSIONS AND FUTURE SCOPE

5.1 Conclusions

The influence of different cooling media (such as air, dry ice, and water) on microstructure, texture evolution, mechanical, corrosion, wear, and fatigue behavior of single-pass and multi-pass overlapping friction stir processed AA2014 and AA6061 was investigated in six objectives.

This chapter summarizes the major conclusions extracted from each objective of the research work

5.1.1 Selection of process parameters and tool geometry during friction stir processing of AA2014 and AA6061 alloys

Trail experiments were successfully carried out, and the following conclusions were drawn.

1. The defect-free structure with better mechanical properties was obtained for the sample processed at 1100 rpm-30 mm/min and 800 rpm-40 mm/min conditions for AA2014 and AA6061. These were preferred as optimized process parameters for conducting FSP with different cooling media.
2. Major defects were formed for the samples processed at high traverse speeds (i.e., 35 mm/min in AA2014 and 50 mm/min in AA6061), whereas minor defects were formed for the samples processed at low rotational speeds (i.e., 1000 rpm in AA2014 and 700 rpm in AA6061) due to insufficient stirring action.
3. Three sharp edges of triangle pin profiles resulted in insufficient plastic flow and leading to poor mechanical properties than other tools.
4. Of all tool geometries, the samples processed with square pin profile for AA2014 and hexagonal pin profile for AA6061 yielded better mechanical properties, and these were selected as optimized tool geometry for conduction of overlapping FSP in different cooling media.

5.1.2 Influence of cooling media in achieving grain refinement of AA2014 alloy using friction stir processing

Grain refinement was successfully achieved in AA2014 via FSP with different cooling media, and the following conclusions were obtained.

1. FSP resulted in the formation of equiaxed fine grains in SZ. Moreover, the incorporation of a cooling medium in UWFSP resulted in forming a UFG structure (900 nm). FSP also caused variation of grain refinement from top to bottom of SZ due to thermal exposure. The fraction of LABs was decreased after FSP in the SZ due to dynamic recovery and continuous DRX.
2. After FSP, the precipitates were fragmented into fine precipitates and distributed in the matrix. Al_2Cu particles were identified as major precipitates in AA2014 by XRD analysis, and these play a vital role in the corrosion process.
3. Within FSP, the highest strength and hardness were achieved in the UWFSP sample. The fine precipitates present in the UWFSP sample can impede grain boundary sliding and improve hardness and strength.
4. Weight-loss test results revealed that the corrosion resistance was significantly improved after FSP due to the formation of homogeneous microstructure and elimination of defects. Within FSP, the sample processed in underwater has good corrosion resistance due to homogeneous fine-grained structure, and the precipitates are randomly distributed in the grain boundary.
5. Tafel polarization test results revealed that the BM was more prone to corrosion attack than FSP samples due to the presence of more precipitate-free area, inhomogeneous microstructure, and large potential difference between coarse precipitates and Al matrix.

5.1.3 Effect of microstructure and precipitate formation on mechanical and corrosion behavior of friction stir processed AA6061 alloy using different cooling media

In the present research, the effect of various cooling media on microstructure, mechanical characteristics, and corrosion behavior was studied, and the following conclusions have been drawn.

1. FSP led to the development of recrystallized fine grains in the SZ of AA6061 alloy. It was identified that various mechanisms, such as dynamic recovery, recrystallization were involved in achieving grain refinement in AA6061 alloy.
2. The cooling media also contributed to additional grain refinement, in addition to various grain refinement mechanisms. The sample that was processed in the water had a very fine-grained structure among FSP samples.
3. Three types of precipitates, needle-shaped Fe-based precipitates, round-shaped Si-based precipitates, and very fine round-shaped Si-based precipitates along the grain boundaries, were identified in BM and SZ of AA6061. These precipitates were exercised a significant impact on mechanical properties and corrosion behavior.
4. The hardness and strength were decreased, while the ductility was improved by thermal softening in FSP samples compared with BM. Within FSP, the water-cooled FSP sample achieved high strength.
5. OPC**,** Tafel polarization and weight-loss tests showed that, due to uniform fine-grained microstructure and discontinuous fine precipitates, the corrosion rate after FSP decreased significantly, and a very fine-grained structure was present in the water-cooled FSP sample resulted in better corrosion resistance than other FSP samples.

5.1.4 Fabrication of large-area stir zone in AA2014 alloy via overlapping friction stir processing using different cooling media

A large-area fine-grained structure was successfully prepared in AA2014 with overlapping FSP, and the following conclusions were drawn from the results.

1. FSP resulted in the development of equiaxed fine grains with the presence of HABS in SZ caused by DRV and C-DRX. The grains in the bottom regions are more refined than those in the upper regions due to AGG caused by thermal variation in SZ.
2. The SZ of first-pass FSP is characterized by strong Brass-{110}<112> component and A{110}<111> component. Further conduction overlapping FSP from second to fifth pass FSP resulted in a change of texture components with varied intensities due to the increased heat input.
3. EDS analysis confirmed Al_2Cu precipitates as primary precipitates in AA2014, and after FSP, these were fragmented into fine precipitates and uniformly distributed throughout the

matrix. These precipitates greatly affected the mechanical and corrosion behavior in BM and FSP samples.

4. Kocks-mecking plot showed that the work-hardening rate of BM is more than the FSP samples, while strain hardening behavior showed that the FSP sample has a more elastic nature than BM.
5. Corrosion tests showed that the corrosion resistance in the FSP sample was significantly improved due to the homogenization of the processed region, less potential variation between precipitates and matrix, less precipitate free area, and uniform distribution of fine precipitates, respectively.
6. Compared to the coarse-grained structure in BM, the fine-grained structure in the FSP samples shows the high resistance to wear due to the high fraction of grain boundary area. On the other hand, the wear rate is high at initial distances, reached a steady state at certain sliding distances, and the further increase in sliding distance resulted in a gradual decrease of wear rate.
7. The fatigue life improved significantly after FSP. Fracture features of fatigue samples revealed the dominance of ridges and plateaus in the initial stage of crack propagation. On the other hand, the presence of dimple and striations in stable crack propagation revealed the mix-mode fracture.

5.1.5 Effect of cooling-assisted overlapping friction stir processing on microstructure, texture evolution, mechanical properties, corrosion, wear, and fatigue behavior of AA6061 alloy

The large-area SZ was successfully prepared on AA6061 alloy using, and the following conclusions were made.

1. After FSP, fine equiaxed α-aluminium grains were produced in large-area SZ. It was also found that overlapping FSP did not significantly affect the grain size variation in the SZ, and the grain size is uniform over the large-area SZ.
2. Two typical types of second-phase particles were identified in the PM and FSP sample of AA6061 alloy; iron-based phase and silicon-based phase.

3. A considerable drop in hardness and strength occurred after FSP due to thermal softening, precipitate dissolution, and reduction in dislocation density. An improvement in elongation of the FSP sample was due to the strain homogeneity in large-area SZ.
4. The corrosion tests revealed that the corrosion resistance after FSP improved due to the formation of homogeneous fine-grained microstructure and discontinuous precipitates. And, the inhomogeneous microstructure and coarse precipitates present in parent metal resulted in less corrosion resistance.
5. The wear rate was significantly decreased after FSP. On the other hand, the difference in wear rate between BM and FSP decreased with an increase in wear load.
6. Fatigue results revealed that the grain refinement and fine precipitates developed in FSP retarded the FCG rate and resulted in high fatigue life than BM. Fatigue striation marks are witnessed in stable FCG regions, while dimples and striations are seen in the rapid crack propagation region.

5.1.6 Establishing a novel relation between local and bulk mechanical strength of friction stir processed aluminium alloys

The present section aimed to find a novel constant between local and bulk strength of experimental investigation together with data reported in the literature studies of friction stir processed aluminium alloys. During the process of finding, the following conclusions were drawn.

1. FSP led to the development of recrystallized fine grains with high angle boundaries in SZ. The provision of cooling media with multi-pass FSP resulted in better grain refinement, which in turn improved strength and hardness as per the Hall-Petch equation.
2. The experimental data fitted well with formulated equations due to the formation of homogeneous SZ. Accordingly, a novel relation of $\sigma_Y = 1.9H$ and $\sigma_{UTS} = 2.7H$ was established between hardness and strength.
3. Finally, the analysis of experimental investigations and literature data revealed that it is not possible to establish a relation between hardness and strength of friction stir processed reinforced composites, primarily due to structural inhomogeneity caused by type, size, and volume of reinforcing agents.

5.2 Scope for future research work

1. The influence of different cooling media and overlapping method on preparing bulk surface composites using friction stir processing may be investigated.
2. The present investigation is beneficial for practical application. So, the overlapping method can be employed to produce large-area processing zone and surface composites in other materials such as copper, magnesium, steel, titanium, and high entropy alloys.
3. Analysis of temperature distribution in each pass of overlapping stir zone and other zones, namely thermo-mechanically affected zone and heat-affected zone.
4. Computational modeling of material flow using different cooling media and overlapping method may be investigated.
5. The other properties like damping, thermal conductivity, creep behavior of large-area stir zone can be explored.
6. The influence of post-welding heat treatment on the production of large-area stir zone can be investigated.

REFERENCES

Abioye, T.E., Zuhailawati, H., Anasyida, A.S., Yahaya, S.A., Dhindaw, B.K., 2019. Investigation of the microstructure, mechanical and wear properties of AA6061-T6 friction stir weldments with different particulate reinforcements addition. J. Mater. Res. Technol. 8, 3917–3928. https://doi.org/10.1016/j.jmrt.2019.06.055

Abrahams, R., Mikhail, J., Fasihi, P., 2019. Effect of friction stir process parameters on the mechanical properties of 5005-H34 and 7075-T651 aluminium alloys. Mater. Sci. Eng. A 751, 363–373. https://doi.org/10.1016/j.msea.2019.02.065

Ahmad Shah, L.H., Midawi, A.R.H., Walbridge, S., Gerlich, A., 2020. Influence of tool eccentricity on the material flow and microstructural properties of AA6061 aluminium alloy friction stir welds. J. Alloys Compd. 826, 1–11. https://doi.org/10.1016/j.jallcom.2020.154219

Ahmed, M.M.Z., Wynne, B.P., El-Sayed Seleman, M.M., Rainforth, W.M., 2016. A comparison of crystallographic texture and grain structure development in aluminium generated by friction stir welding and high strain torsion. Mater. Des. 103, 259–267. https://doi.org/10.1016/j.matdes.2016.04.056

Al-Fadhalah, K.J., Almazrouee, A.I., Aloraier, A.S., 2014a. Microstructure and mechanical properties of multi-pass friction stir processed aluminium alloy 6063. Mater. Des. 53, 550–560. https://doi.org/10.1016/j.matdes.2013.07.062

Alavi Nia, A., Omidvar, H., Nourbakhsh, S.H., 2014a. Effects of an overlapping multi-pass friction stir process and rapid cooling on the mechanical properties and microstructure of AZ31 magnesium alloy. Mater. Des. 58, 298–304. https://doi.org/10.1016/j.matdes.2014.01.069

Alishavandi, M., Razmjoo Khollari, M.A., Ebadi, M., Alishavandi, S., Kokabi, A.H., 2020a. Corrosion-wear behavior of AA1050/mischmetal oxides surface nanocomposite fabricated by friction stir processing. J. Alloys Compd. 832, 153964. https://doi.org/10.1016/j.jallcom.2020.153964

Anderson-Wedge, K., Avery, D.Z., Daniewicz, S.R., Sowards, J.W., Allison, P.G., Jordon, J.B., Amaro, R.L., 2021a. Characterization of the fatigue behavior of additive friction stirdeposition AA2219. Int. J. Fatigue 142, 105951. https://doi.org/10.1016/j.ijfatigue.2020.105951

Anderson-Wedge, K., Stubblefield, G., Zhu, N., Long, B., Daniewicz, S.R., Allison, P., Sowards, J., Rodriguez, O., Amaro, R., 2021b. Characterization of the evolution of 2219-T87 aluminium as a function of the friction stir welding process. Int. J. Fatigue 142, 105954. https://doi.org/10.1016/j.ijfatigue.2020.105954

ASTM E8, 2010. ASTM E8/E8M standard test methods for tension testing of metallic materials 1. Annu. B. ASTM Stand. 4 1–27. https://doi.org/10.1520/E0008

Bahrami, A., Miroux, A., Sietsma, J., 2012. An age-hardening model for Al-Mg-Si alloys considering needle-shaped precipitates. Metall. Mater. Trans. A Phys. Metall. Mater. Sci. 43, 4445–4453. https://doi.org/10.1007/s11661-012-1211-8

Balakrishnan, M., Dinaharan, I., Palanivel, R., Sathiskumar, R., 2019a. Effect of friction stir processing on microstructure and tensile behavior of AA6061/Al3Fe cast aluminium matrix composites. J. Alloys Compd. 785, 531–541. https://doi.org/10.1016/j.jallcom.2019.01.211

Balakrishnan, M., Dinaharan, I., Palanivel, R., Sathiskumar, R., 2019b. Influence of friction stir processing on microstructure and tensile behavior of AA6061/Al 3 Zr cast aluminium matrix composites. J. Manuf. Process. 38, 148–157. https://doi.org/10.1016/j.jmapro.2018.12.039

Barati, M., Abbasi, M., Abedini, M., 2019. The effects of friction stir processing and friction stir vibration processing on mechanical, wear and corrosion characteristics of Al6061/SiO2 surface composite. J. Manuf. Process. 45, 491–497. https://doi.org/10.1016/j.jmapro.2019.07.034

Beden, S.M., Abdullah, S., Ariffin, A.K., 2009. Review of fatigue crack propagation models for metallic components, European Journal of Scientific Research.

Besel, Y., Besel, M., Dietrich, E., Wischek, J., Alfaro Mercado, U., Kakiuchi, T., Uematsu, Y., 2019. Heterogeneous local straining behavior under monotonic and cyclic loadings in a friction stir welded aluminium alloy. Int. J. Fatigue 125, 138–148. https://doi.org/10.1016/j.ijfatigue.2019.03.037

Biro, A.L., Chenelle, B.F., Lados, D.A., 2012. Processing, microstructure, and residual stress effects on strength and fatigue crack growth properties in friction stir welding: A review. Metall. Mater. Trans. B Process Metall. Mater. Process. Sci. 43, 1622–1637. https://doi.org/10.1007/s11663-012-9716-5

Bishop, C.A., Rate, C., Method, E., n.d. acteristics Process Diagnostics and Coating Char- Weight-Loss Method.

Bocchi, S., Cabrini, M., D'Urso, G., Giardini, C., Lorenzi, S., Pastore, T., 2020. Stress enhanced intergranular corrosion of friction stir welded AA2024-T3. Eng. Fail. Anal. https://doi.org/10.1016/j.engfailanal.2020.104483

Cao, X., Shi, Q., Liu, D., Feng, Z., Liu, Q., Chen, G., 2018. Fabrication of in situ carbon fiber/aluminium composites via friction stir processing: Evaluation of microstructural, mechanical and tribological behaviors. Compos. Part B Eng. 139, 97–105. https://doi.org/10.1016/j.compositesb.2017.12.001

Cao, Y., Ni, S., Liao, X., Song, M., Zhu, Y., 2018. Materials Science & Engineering R Structural evolutions of metallic materials processed by severe plastic deformation 133, 1–59.

Charit, I., Mishra, R.S., 2018. Effect of friction stir processed microstructure on tensile properties of an Al-Zn-Mg-Sc alloy upon subsequent aging heat treatment. J. Mater. Sci. Technol. 34, 214–218. https://doi.org/10.1016/j.jmst.2017.10.021

Charit, I., Mishra, R.S., 2005. Low temperature superplasticity in a friction-stir-processed ultrafine grained Al-Zn-Mg-Sc alloy. Acta Mater. 53, 4211–4223. https://doi.org/10.1016/j.actamat.2005.05.021

Charit, I., Mishra, R.S., 2003. High strain rate superplasticity in a commercial 2024 Al alloy via friction stir processing. Mater. Sci. Eng. A 359, 290–296. https://doi.org/10.1016/S0921-5093(03)00367-8

Chauhan, K., Satyanarayana, M.V.N.V., Kumar, A., 2020. Effect of Tool Geometry and Heat Treatment on Friction Stir Processing of AA6061. Lect. Notes Mech. Eng. 947–953. https://doi.org/10.1007/978-981-15-1201-8_101

Chen, Y., Ding, H., Li, J., Cai, Z., Zhao, J., Yang, W., 2016. Influence of multi-pass friction stir processing on the microstructure and mechanical properties of Al-5083 alloy. Mater. Sci.

Eng. A 650, 281–289. https://doi.org/10.1016/j.msea.2015.10.057

Chen, Y., Ding, H., Li, J.Z., Zhao, J.W., Fu, M.J., Li, X.H., 2015. Effect of welding heat input and post-welded heat treatment on hardness of stir zone for friction stir-welded 2024-T3 aluminium alloy. Trans. Nonferrous Met. Soc. China (English Ed. 25, 2524–2532. https://doi.org/10.1016/S1003-6326(15)63871-7

CHEN, Y., DING, H., MALOPHEYEV, S., KAIBYSHEV, R., CAI, Z. hui, YANG, W. jing, 2017. Influence of multi-pass friction stir processing on microstructure and mechanical properties of 7B04-O Al alloy. Trans. Nonferrous Met. Soc. China (English Ed. 27, 789–796. https://doi.org/10.1016/S1003-6326(17)60090-6

Chhangani, S., Masa, S.K., Mathew, R.T., Prasad, M.J.N.V., Sujata, M., 2020. Microstructural evolution in Al–Mg–Sc alloy (AA5024): Effect of thermal treatment, compression deformation and friction stir welding. Mater. Sci. Eng. A 772. https://doi.org/10.1016/j.msea.2019.138790

Cho, J.H., Han, S.H., Lee, C.G., 2016. Cooling effect on microstructure and mechanical properties during friction stir welding of Al-Mg-Si aluminium alloys. Mater. Lett. 180, 157–161. https://doi.org/10.1016/j.matlet.2016.05.157

Corrosion-wear behavior of AA1050_mischmetal oxides surface nanocomposite fabricated by friction stir processing _ Elsevier Enhanced Reader.pdf, n.d.

D'Urso, G., Giardini, C., Lorenzi, S., Cabrini, M., Pastore, T., 2017. The influence of process parameters on mechanical properties and corrosion behaviour of friction stir welded aluminium joints. Procedia Eng. 207, 591–596. https://doi.org/10.1016/j.proeng.2017.10.1026

D'Urso, G., Giardini, C., Lorenzi, S., Pastore, T., 2014. Fatigue crack growth in the welding nugget of FSW joints of a 6060 aluminium alloy. J. Mater. Process. Technol. https://doi.org/10.1016/j.jmatprotec.2014.01.013

Dai, Q., Liang, Z., Chen, G., Meng, L., Shi, Q., 2013. Explore the mechanism of high fatigue crack propagation rate in fine microstructure of friction stir welded aluminium alloy. Mater. Sci. Eng. A. https://doi.org/10.1016/j.msea.2013.05.057

Davis, J.R., 2001. Aluminium and Aluminium Alloys 351–416. https://doi.org/10.1361/autb2001p351

Deng, C., Wang, H., Gong, B., Li, X., Lei, Z., 2016. Effects of microstructural heterogeneity on very high cycle fatigue properties of 7050-T7451 aluminium alloy friction stir butt welds. Int. J. Fatigue. https://doi.org/10.1016/j.ijfatigue.2015.10.001

Deore, H.A., Mishra, J., Rao, A.G., Mehtani, H., Hiwarkar, V.D., 2019. Effect of filler material and post process ageing treatment on microstructure, mechanical properties and wear behaviour of friction stir processed AA 7075 surface composites. Surf. Coatings Technol. 374, 52–64. https://doi.org/10.1016/j.surfcoat.2019.05.048

Devaraju, A., Kishan, V., 2018. Influence of Cryogenic cooling (Liquid Nitrogen) on Microstructure and Mechanical properties of Friction stir welded 2014-T6 Aluminium alloy. Mater. Today Proc. 5, 1585–1590. https://doi.org/10.1016/j.matpr.2017.11.250

Dhal, A., Panigrahi, S.K., Shunmugam, M.S., 2015. Precipitation phenomena, thermal stability and grain growth kinetics in an ultra-fine grained Al 2014 alloy after annealing treatment. J. Alloys Compd. 649, 229–238. https://doi.org/10.1016/j.jallcom.2015.07.098

Donatus, U., Viveiros, B.V.G. de, Alencar, M.C. de, Ferreira, R.O., Milagre, M.X., Costa, I., 2018. Correlation between corrosion resistance, anodic hydrogen evolution and microhardness in friction stir weldment of AA2198 alloy. Mater. Charact. 144, 99–112. https://doi.org/10.1016/j.matchar.2018.07.004

Du, D., Fu, R., Li, Y., Jing, L., Wang, J., Ren, Y., Yang, K., 2015. Modification of the Hall-Petch equation for friction-stir-processing microstructures of high-nitrogen steel. Mater. Sci. Eng. A 640, 190–194. https://doi.org/10.1016/j.msea.2015.05.069

Ebrahimi, M., Par, M.A., 2019. Twenty-year uninterrupted endeavor of friction stir processing by focusing on copper and its alloys 781, 1074–1090.

Edalati, K., Horita, Z., 2016. Materials Science & Engineering A Review article A review on high-pressure torsion (HPT) from 1935 to 1988 652, 325–352.

El-Rayes, M.M., El-Danaf, E.A., 2012. The influence of multi-pass friction stir processing on the microstructural and mechanical properties of Aluminium Alloy 6082. J. Mater. Process.

Technol. 212, 1157–1168. https://doi.org/10.1016/j.jmatprotec.2011.12.017

Elangovan, K., Balasubramanian, V., 2007. Influences of pin profile and rotational speed of the tool on the formation of friction stir processing zone in AA2219 aluminium alloy. Mater. Sci. Eng. A 459, 7–18. https://doi.org/10.1016/j.msea.2006.12.124

Entringer, J., Meisnar, M., Reimann, M., Blawert, C., Zheludkevich, M., dos Santos, J.F., 2019. The effect of grain boundary precipitates on stress corrosion cracking in a bobbin tool friction stir welded Al-Cu-Li alloy. Mater. Lett. X 2, 100014. https://doi.org/10.1016/j.mlblux.2019.100014

Esmaeili, S., Lloyd, D.J., Jin, H., 2011. A thermomechanical process for grain refinement in precipitation hardening AA6xxx aluminium alloys. Mater. Lett. 65, 1028–1030. https://doi.org/10.1016/j.matlet.2010.12.035

Fadaeifard, F., Matori, K.A., Abd Aziz, S., Zolkarnain, L., Abdul Rahim, M.A.Z. Bin, 2017. Effect of the welding speed on the macrostructure, microstructure and mechanical properties of AA6061-T6 friction stir butt welds. Metals (Basel). 7. https://doi.org/10.3390/met7020048

Fee, T., 2020. Electronic slot booking slip Confirmed Booking Slip for Driving License Test . Electronic slot booking slip 9–11.

Felix Xavier Muthu, M., Jayabalan, V., 2016. Effect of pin profile and process parameters on microstructure and mechanical properties of friction stir welded Al-Cu joints. Trans. Nonferrous Met. Soc. China (English Ed. 26, 984–993. https://doi.org/10.1016/S1003-6326(16)64195-X

Figueiredo, R.B., Langdon, T.G., 2012. Fabricating Ultra À ne-Grained Materials through the Application of Severe Plastic Deformation : a Review of Developments in Brazil.

Fonda, R.W., Bingert, J.F., 2007. Texture variations in an aluminium friction stir weld. Scr. Mater. 57, 1052–1055. https://doi.org/10.1016/j.scriptamat.2007.06.068

Fujita, M., Kuki, K., 2016. An evaluation of mechanical properties with the hardness of building steel structural members for reuse by NDT. Metals (Basel). 6. https://doi.org/10.3390/met6100247

Gandra, J., Miranda, R.M., Vilaça, P., 2011. Effect of overlapping direction in multipass friction stir processing. Mater. Sci. Eng. A 528, 5592–5599. https://doi.org/10.1016/j.msea.2011.03.105

Gangil, N., Noor, A., Maheshwari, S., 2017. Aluminium based in-situ composite fabrication through friction stir processing : A review 715.

Ghalehbandi, S.M., Malaki, M., 2019. applied sciences Accumulative Roll Bonding — A Review.

Ghanbari, D., Kasiri Asgarani, M., Amini, K., Gharavi, F., 2017. Influence of heat treatment on mechanical properties and microstructure of the Al2024/SiC composite produced by multi–pass friction stir processing. Meas. J. Int. Meas. Confed. 104, 151–158. https://doi.org/10.1016/j.measurement.2017.03.024

Gharavi, F., Matori, K.A., Yunus, R., Othman, N.K., 2014. Corrosion behavior of friction stir welded lap joints of AA6061-T6 aluminium alloy. Mater. Res. 17, 672–681. https://doi.org/10.1590/S1516-14392014005000053

GHARAVI, F., MATORI, K.A., YUNUS, R., OTHMAN, N.K., FADAEIFARD, F., 2016. Corrosion evaluation of friction stir welded lap joints of AA6061-T6 aluminium alloy. Trans. Nonferrous Met. Soc. China (English Ed. 26, 684–696. https://doi.org/10.1016/S1003-6326(16)64159-6

Ghetiya, N.D., Patel, K.M., 2017. Welding speed effect on joint properties in air and immersed friction stir welding of AA2014. Proc. Inst. Mech. Eng. Part B J. Eng. Manuf. 231, 897–909. https://doi.org/10.1177/0954405417690555

Ghetiya, N.D., Patel, K.M., 2015. Prediction of tensile strength and microstructure characterization of immersed friction stir welding of aluminium alloy AA2014-T4. Indian J. Eng. Mater. Sci. 22, 133–140.

Godasu, A.K., Kumar, A., Mula, S., 2020. Influence of cryocooling on friction stir processing of Al-5083 alloy. Mater. Manuf. Process. 35, 202–213. https://doi.org/10.1080/10426914.2019.1697442

Han, B., Xu, Z., 2008. Grain refinement under multi-axial forging in Fe – 32 % Ni alloy 457, 279–285. https://doi.org/10.1016/j.jallcom.2007.03.067

Heidarzadeh, A., Mironov, S., Kaibyshev, R., Çam, G., Simar, A., Gerlich, A., Khodabakhshi, F., Mostafaei, A., Field, D.P., Robson, J.D., Deschamps, A., Withers, P.J., 2020. Friction stir welding/processing of metals and alloys: A comprehensive review on microstructural evolution. Prog. Mater. Sci. 100752. https://doi.org/10.1016/j.pmatsci.2020.100752

Heidarzadeh, A., Mironov, S., Kaibyshev, R., Çam, G., Simar, A., Gerlich, A., Withers, J., 2021. Progress in Materials Science Friction stir welding / processing of metals and alloys : A comprehensive review on microstructural evolution 117.

Heirani, F., Abbasi, A., Ardestani, M., 2017. Effects of processing parameters on microstructure and mechanical behaviors of underwater friction stir welding of Al5083 alloy. J. Manuf. Process. 25, 77–84. https://doi.org/10.1016/j.jmapro.2016.11.002

Hou, Y.F., Liu, C.Y., Zhang, B., Wei, L.L., Dai, H.T., Ma, Z.Y., 2020. Mechanical properties and corrosion resistance of the fine grain structure of Al–Zn–Mg–Sc alloys fabricated by friction stir processing and post-heat treatment. Mater. Sci. Eng. A 785. https://doi.org/10.1016/j.msea.2020.139393

Hu, W., Ma, Z., Ji, S., Qi, S., Chen, M., Jiang, W., 2020. Improving the mechanical property of dissimilar Al/Mg hybrid friction stir welding joint by PIO-ANN. J. Mater. Sci. Technol. 53, 41–52. https://doi.org/10.1016/j.jmst.2020.01.069

Huang, G., Hou, W., Li, J., Shen, Y., 2018. Development of surface composite based on Al-Cu system by friction stir processing: Evaluation of microstructure, formation mechanism and wear behavior. Surf. Coatings Technol. 344, 30–42. https://doi.org/10.1016/j.surfcoat.2018.03.005

Huang, H., Jiang, M., Wei, L., Liu, C., Liu, S., 2021. Materials Characterization Microstructural and mechanical behavior of Al-Mg-Mn-Sc-Zr alloy subjected to multi-axial forging at room temperature 171, 1–7.

Imam, M., Racherla, V., Biswas, K., 2014. Effect of post-weld natural aging on mechanical and microstructural properties of friction stir welded 6063-T4 aluminium alloy. Mater. Des. 64, 675–686. https://doi.org/10.1016/j.matdes.2014.08.037

Jain, V.K.S., Yazar, K.U., Muthukumaran, S., 2019. Development and characterization of Al5083-

CNTs/SiC composites via friction stir processing. J. Alloys Compd. 798, 82–92. https://doi.org/10.1016/j.jallcom.2019.05.232

Jata, K. V., Sankaran, K.K., Ruschau, J.J., 2000. Friction-stir welding effects on microstructure and fatigue of aluminium alloy 7050-T7451. Metall. Mater. Trans. A Phys. Metall. Mater. Sci. 31, 2181–2192. https://doi.org/10.1007/s11661-000-0136-9

Jian, H., Luo, J., Tang, X., Li, X., Yan, C., 2017a. Influence of microstructure on fatigue crack propagation behaviors of an aluminium alloy: Role of sheet thickness. Eng. Fract. Mech. https://doi.org/10.1016/j.engfracmech.2017.05.038

Jiang, H.J., Liu, C.Y., Zhang, B., Xue, P., Ma, Z.Y., Luo, K., Ma, M.Z., Liu, R.P., 2017. Simultaneously improving mechanical properties and damping capacity of Al-Mg-Si alloy through friction stir processing. Mater. Charact. 131, 425–430. https://doi.org/10.1016/j.matchar.2017.07.037

Johannes, L.B., Mishra, R.S., 2007. Multiple passes of friction stir processing for the creation of superplastic 7075 aluminium. Mater. Sci. Eng. A 464, 255–260. https://doi.org/10.1016/j.msea.2007.01.141

Kadaganchi, R., Gankidi, M.R., Gokhale, H., 2015. Optimization of process parameters of aluminium alloy AA 2014-T6 friction stir welds by response surface methodology. Def. Technol. 11, 209–219. https://doi.org/10.1016/j.dt.2015.03.003

Kalinenko, A., Kim, K., Vysotskiy, I., Zuiko, I., Malopheyev, S., Mironov, S., Kaibyshev, R., 2020. Microstructure-strength relationship in friction-stir welded 6061-T6 aluminium alloy. Mater. Sci. Eng. A 793, 139858. https://doi.org/10.1016/j.msea.2020.139858

Kalita, S.J., 2011. Microstructure and corrosion properties of diode laser melted friction stir weld of aluminium alloy 2024 T351. Appl. Surf. Sci. 257, 3985–3997. https://doi.org/10.1016/j.apsusc.2010.11.163

Kapoor, R., Sarkar, A., Behera, A.N., Sunil, S., 2020. Materials Science & Engineering A Multi-axial forging of Nb-1wt .% Zr : Effect of annealing on microstructure and mechanical properties 772.

Khodabakhshi, F., Gerlich, A.P., 2020. On the correlation between indentation hardness and tensile strength in friction stir processed materials. Mater. Sci. Eng. A 789, 55–58. https://doi.org/10.1016/j.msea.2020.139682

Khodabakhshi, F., Gerlich, A.P., Simchi, A., Kokabi, A.H., 2015. Materials Science & Engineering A Cryogenic friction-stir processing of ultra fi ne-grained Al – Mg – TiO 2 nanocomposites 620, 471–482.

Khodabakhshi, F., Nosko, M., Gerlich, A.P., 2018a. Effects of graphene nano-platelets (GNPs) on the microstructural characteristics and textural development of an Al-Mg alloy during friction-stir processing. Surf. Coatings Technol. 335, 288–305. https://doi.org/10.1016/j.surfcoat.2017.12.045

Krishnan, K., 2019. Ac ce pte d M us pt. J. Phys. D Appl. Phys in press, 0–31.

Kumar, H., Prasad, R., Kumar, P., Tewari, S.P., Singh, J.K., 2020. Mechanical and tribological characterization of industrial wastes reinforced aluminium alloy composites fabricated via friction stir processing. J. Alloys Compd. 831. https://doi.org/10.1016/j.jallcom.2020.154832

Kumar, N., Mishra, R.S., Huskamp, C.S., Sankaran, K.K., 2011. Microstructure and mechanical behavior of friction stir processed ultrafine grained Al-Mg-Sc alloy. Mater. Sci. Eng. A 528, 5883–5887. https://doi.org/10.1016/j.msea.2011.03.109

Kumar, S., Srivastava, A.K., Singh, R.K., 2020. Fabrication of AA7075 hybrid green metal matrix composites by friction stir processing technique. Ann. Chim. Sci. des Mater. 44, 295–300. https://doi.org/10.18280/acsm.440409

Kwesi Nutor, R., 2017. Using the Hollomon Model to Predict Strain-Hardening in Metals. Am. J. Mater. Synth. Process. 2, 1. https://doi.org/10.11648/j.ajmsp.20170201.11

Kwon, Y.J., Shigematsu, I., Saito, N., 2003. Production of ultra-fine grained aluminium alloy using friction stir process. Mater. Trans. 44, 1343–1350. https://doi.org/10.2320/matertrans.44.1343

Langdon, T.G., 2016. A comparison of repetitive corrugation and straightening and high-pressure torsion using an Al-Mg-Sc alloy 5, 353–359.

Lee, S.J., Shin, S.E., Ushioda, K., Fujii, H., 2019. Microstructure, mechanical properties, and damping capacity in stir zone after friction stir welding of Fe–17Mn damping alloy. J. Alloys Compd. 803, 1155–1167. https://doi.org/10.1016/j.jallcom.2019.06.367

Li, S., Beyerlein, I.J., Bourke, M.A.M., 2005. Texture formation during equal channel angular extrusion of fcc and bcc materials: Comparison with simple shear. Mater. Sci. Eng. A 394, 66–77. https://doi.org/10.1016/j.msea.2004.11.032

Li, S., Zhang, Y., Qi, L., Kang, Y., 2018. Effect of single tensile overload on fatigue crack growth behavior in DP780 dual phase steel. Int. J. Fatigue 106, 49–55. https://doi.org/10.1016/j.ijfatigue.2017.09.018

Links, R.E., 2016. Ministry of Skill Development and Entrepreneurship 2–3.

Liu, C.Y., Jiang, H.J., Zhang, B., Ma, Z.Y., 2018a. High damping capacity of Al alloys produced by friction stir processing. Mater. Charact. 136, 382–387. https://doi.org/10.1016/j.matchar.2018.01.009

Liu, C.Y., Qu, B., Xue, P., Ma, Z.Y., Luo, K., Ma, M.Z., Liu, R.P., 2018b. Fabrication of large-bulk ultrafine grained 6061 aluminium alloy by rolling and low-heat-input friction stir welding. J. Mater. Sci. Technol. 34, 112–118. https://doi.org/10.1016/j.jmst.2017.02.008

Liu, C.Y., Zhang, B., Ma, Z.Y., Jiang, H.J., Zhou, W.B., 2019. Effect of Sc addition, friction stir processing, and T6 treatment on the damping and mechanical properties of 7055 Al alloy. J. Alloys Compd. 772, 775–781. https://doi.org/10.1016/j.jallcom.2018.09.109

Liu, C.Y., Zhang, B., Ma, Z.Y., Teng, G.B., Wei, L.L., Zhou, W.B., Zhang, X.Y., 2018c. Effects of pre-aging and minor Sc addition on the microstructure and mechanical properties of friction stir processed 7055 Al alloy. Vacuum 149, 106–113. https://doi.org/10.1016/j.vacuum.2017.12.030

Liu, H., Chen, Y., Yao, Z., Luo, F., 2020. Effect of tool offset on the microstructure and properties of AA6061/AZ31B friction stir welding joints. Metals (Basel). 10. https://doi.org/10.3390/met10040546

Liu, Q., Ma, Q. xian, Chen, G. qiang, Cao, X., Zhang, S., Pan, J. luan, Zhang, G., Shi, Q. yu, 2018. Enhanced corrosion resistance of AZ91 magnesium alloy through refinement and homogenization of surface microstructure by friction stir processing. Corros. Sci. 138, 284–

296. https://doi.org/10.1016/j.corsci.2018.04.028

Lu, W., Shi, Y., Li, X., Lei, Y., 2013. Correlation between tensile strength and hardness of electron beam welded TC4-DT joints. J. Mater. Eng. Perform. 22, 1694–1700. https://doi.org/10.1007/s11665-012-0469-8

Mara, N.A., Beyerlein, I.J., 2015. Interface-dominant multilayers fabricated by severe plastic deformation : Stability under extreme conditions 19, 265–276.

McLean, D., Gurland, J., 1963. The Mechanical Properties of Metals. J. Appl. Mech. 30, 479–479. https://doi.org/10.1115/1.3636604

McNelley, T.R., Swaminathan, S., Su, J.Q., 2008. Recrystallization mechanisms during friction stir welding/processing of aluminium alloys. Scr. Mater. 58, 349–354. https://doi.org/10.1016/j.scriptamat.2007.09.064

Mehta, K.M., Badheka, V.J., 2019. Wear behavior of boron-carbide reinforced aluminium surface composites fabricated by Friction Stir Processing. Wear 426–427, 975–980. https://doi.org/10.1016/j.wear.2019.01.041

MENG, Q., LIU, Y., KANG, J., FU, R. dong, GUO, X. yan, LI, Y. jun, 2019. Effect of precipitate evolution on corrosion behavior of friction stir welded joints of AA2060-T8 alloy. Trans. Nonferrous Met. Soc. China (English Ed. 29, 701–709. https://doi.org/10.1016/S1003-6326(19)64980-0

Milagre, M.X., Donatus, U., Mogili, N. V., Silva, R.M.P., de Viveiros, B.V.G., Pereira, V.F., Antunes, R.A., Machado, C.S.C., Araujo, J.V.S., Costa, I., 2020. Galvanic and asymmetry effects on the local electrochemical behavior of the 2098-T351 alloy welded by friction stir welding. J. Mater. Sci. Technol. 45, 162–175. https://doi.org/10.1016/j.jmst.2019.11.016

Mishra, R.S., Ma, Z.Y., 2005. Friction stir welding and processing 50, 1–78. https://doi.org/10.1016/j.mser.2005.07.001

Moradi, M.M., Jamshidi Aval, H., Jamaati, R., Amirkhanlou, S., Ji, S., 2019. Effect of SiC nanoparticles on the microstructure and texture of friction stir welded AA2024/AA6061. Mater. Charact. 152, 169–179. https://doi.org/10.1016/j.matchar.2019.04.020

Moradi, M.M., Jamshidi Aval, H., Jamaati, R., Amirkhanlou, S., Ji, S., 2018. Microstructure and texture evolution of friction stir welded dissimilar aluminium alloys: AA2024 and AA6061. J. Manuf. Process. 32, 1–10. https://doi.org/10.1016/j.jmapro.2018.01.016

Mosayebi, M., Zarei-Hanzaki, A., Abedi, H.R., Jamili, A.M., Ghaderi, A., Barnett, M., 2020. Development of a novel RE-texture component in a Mg-Y-RE/SiCp magnesium composite through friction stir processing. Mater. Lett. 260, 126899. https://doi.org/10.1016/j.matlet.2019.126899

Nadammal, N., Kailas, S. V., Szpunar, J., Suwas, S., 2018. Development of microstructure and texture during single and multiple pass friction stir processing of a strain hardenable aluminium alloy. Mater. Charact. 140, 134–146. https://doi.org/10.1016/j.matchar.2018.03.044

Nandan, R, Debroy, T., Bhadeshia, H.K.D.H., 2008. Recent advances in friction-stir welding – Process , weldment structure and properties 53, 980–1023. https://doi.org/10.1016/j.pmatsci.2008.05.001

Nascimento, F., Santos, T., Vilaça, P., Miranda, R.M., Quintino, L., 2009. Microstructural modification and ductility enhancement of surfaces modified by FSP in aluminium alloys. Mater. Sci. Eng. A 506, 16–22. https://doi.org/10.1016/j.msea.2009.01.008

Navaser, M., Atapour, M., 2017. Effect of Friction Stir Processing on Pitting Corrosion and Intergranular Attack of 7075 Aluminium Alloy. J. Mater. Sci. Technol. 33, 155–165. https://doi.org/10.1016/j.jmst.2016.07.008

Ni, D.R., Wang, J.J., Ma, Z.Y., 2016. Shape Memory Effect, Thermal Expansion and Damping Property of Friction Stir Processed NiTip/Al Composite. J. Mater. Sci. Technol. 32, 162–166. https://doi.org/10.1016/j.jmst.2015.12.013

Orłowska, M., Brynk, T., Hütter, A., Goliński, J., Enzinger, N., Olejnik, L., Lewandowska, M., 2020. Similar and dissimilar welds of ultrafine grained aluminium obtained by friction stir welding. Mater. Sci. Eng. A 777. https://doi.org/10.1016/j.msea.2020.139076

Pabandi, H.K., Jashnani, H.R., Paidar, M., 2018. Effect of precipitation hardening heat treatment on mechanical and microstructure features of dissimilar friction stir welded AA2024-T6 and

AA6061-T6 alloys. J. Manuf. Process. 31, 214–220. https://doi.org/10.1016/j.jmapro.2017.11.019

Padhy, G.K., Wu, C.S., Gao, S., 2018. Friction stir based welding and processing technologies - processes, parameters, microstructures and applications: A review. J. Mater. Sci. Technol. 34, 1–38. https://doi.org/10.1016/j.jmst.2017.11.029

Paglia, C.S., Buchheit, R.G., 2008. A look in the corrosion of aluminium alloy friction stir welds. Scr. Mater. 58, 383–387. https://doi.org/10.1016/j.scriptamat.2007.10.043

Pavlina, E.J., Van Tyne, C.J., 2008. Correlation of Yield strength and Tensile strength with hardness for steels. J. Mater. Eng. Perform. 17, 888–893. https://doi.org/10.1007/s11665-008-9225-5

PII_ S0079-6425(99)00007-9 _ Elsevier Enhanced Reader.pdf, n.d.

Pradeep, S., Pancholi, V., 2013. Effect of microstructural inhomogeneity on superplastic behaviour of multipass friction stir processed aluminium alloy. Mater. Sci. Eng. A. https://doi.org/10.1016/j.msea.2012.10.050

Qin, H. long, Zhang, H., Sun, D. tong, Zhuang, Q. yu, 2015. Corrosion behavior of the friction-stir-welded joints of 2A14-T6 aluminium alloy. Int. J. Miner. Metall. Mater. 22, 627–638. https://doi.org/10.1007/s12613-015-1116-9

Rajamanickam, N., Balusamy, V., Madhusudhanna Reddy, G., Natarajan, K., 2009. Effect of process parameters on thermal history and mechanical properties of friction stir welds. Mater. Des. 30, 2726–2731. https://doi.org/10.1016/j.matdes.2008.09.035

Rajendrana, C., Srinivasan, K., Balasubramanian, V., Balaji, H., Selvaraj, P., 2017. Identifying Combination of Friction Stir Welding Parameters to Maximize Strength of Lap Joints of AA2014-T6 Aluminium Alloy. Arch. Mech. Technol. Mater. 37, 6–21. https://doi.org/10.1515/amtm-2017-0002

Ramesh, K.N., Pradeep, S., Pancholi, V., 2012. Multipass friction-stir processing and its effect on mechanical properties of aluminium alloy 5086. Metall. Mater. Trans. A Phys. Metall. Mater. Sci. 43, 4311–4319. https://doi.org/10.1007/s11661-012-1232-3

Ramesh, N.R., Kumar, V.S.S., 2020. Experimental erosion-corrosion analysis of friction stir welding of AA 5083 and AA 6061 for sub-sea applications. Appl. Ocean Res. https://doi.org/10.1016/j.apor.2020.102121

Ramesh, S., Nayaka, H.S., Gopi, K.R., 2018. ScienceDirect Influence of Multi Axial Forging (MAF) on Microstructure and Mechanical Properties of Cu-Ti Alloy 5, 25534–25540.

Re, N., Ocheri, C., Jc, O., Ps, N., 2019. Empirical relationship between hardness and tensile strength for medium carbon steel quenched in different media journal of material sciences & engineering. J. Mater. Sci. Eng. 8.

Rouzbehani, R., Kokabi, A.H., Sabet, H., Paidar, M., Ojo, O.O., 2018. Metallurgical and mechanical properties of underwater friction stir welds of Al7075 aluminium alloy. J. Mater. Process. Technol. 262, 239–256. https://doi.org/10.1016/j.jmatprotec.2018.06.033

Sadasivan, N., Balasubramanian, M., Rameshbapu, B.R., 2020. A comprehensive review on equal channel angular pressing of bulk metal and sheet metal process methodology and its varied applications 59, 698–726.

Sahu, P.K., Singh, S., Chen, G., Yijun, L., Zhang, S., Shi, Q., 2020. Wear behavior of the friction stir alloyed AZ31 Mg at different volume fractions of Al particles reinforcement and its enhanced quality attributes. Tribol. Int. 146. https://doi.org/10.1016/j.triboint.2020.106268

Saito, Y., Utsunomiya, H., Tsuji, N., Sakai, T., 1999. Novel Ultra-High Str. Acta Mater. 47.

Sarkari Khorrami, M., Saito, N., Miyashita, Y., 2019a. Texture and strain-induced abnormal grain growth in cryogenic friction stir processing of severely deformed aluminium alloy. Mater. Charact. 151, 378–389. https://doi.org/10.1016/j.matchar.2019.03.010

Sarkari Khorrami, M., Saito, N., Miyashita, Y., 2019b. Texture and strain-induced abnormal grain growth in cryogenic friction stir processing of severely deformed aluminium alloy. Mater. Charact. 151, 378–389. https://doi.org/10.1016/j.matchar.2019.03.010

Sarkari Khorrami, M., Saito, N., Miyashita, Y., Kondo, M., 2019c. Texture variations and mechanical properties of aluminium during severe plastic deformation and friction stir processing with SiC nanoparticles. Mater. Sci. Eng. A 744, 349–364. https://doi.org/10.1016/j.msea.2018.12.031

Sato, Y.S., Takauchi, H., Park, S.H.C., Kokawa, H., 2005. Characteristics of the kissing-bond in friction stir welded Al alloy 1050. Mater. Sci. Eng. A 405, 333–338. https://doi.org/10.1016/j.msea.2005.06.008

Sato, Y.S., Urata, M., Kokawa, H., Ikeda, K., 2003. Hall-Petch relationship in friction stir welds of equal channel angular-pressed aluminium alloys. Mater. Sci. Eng. A 354, 298–305. https://doi.org/10.1016/S0921-5093(03)00008-X

Satyanarayana, M.V.N.., Reddy, P., Kumar, A., 2020. Preparation of bulk-area stir zone in aluminium 6061 alloy via cryogenic friction stir processing. Mater. Today Proc. 1–4. https://doi.org/10.1016/j.matpr.2020.05.730

Satyanarayana, M.V.N.V., Adepu, K., Chauhan, K., 2020. Effect of Overlapping Friction Stir Processing on Microstructure, Mechanical Properties and Corrosion Behavior of AA6061 Alloy. Met. Mater. Int. https://doi.org/10.1007/s12540-020-00757-y

Satyanarayana, M.V.N.V., Kumar, A., 2020. Influence of cooling media in achieving grain refinement of AA2014 alloy using friction stir processing. Proc. Inst. Mech. Eng. Part C J. Mech. Eng. Sci. 234, 4520–4534. https://doi.org/10.1177/0954406220922858

Satyanarayana, M.V.N.V., Kumar, A., 2019. Effect of heat treatment on AA2014 alloy processed through multi-pass friction stir processing. J. Phys. Conf. Ser. 1240. https://doi.org/10.1088/1742-6596/1240/1/012077

Satyanarayana, M.V.N. V, Kumar, A., 2021. Effect of microstructure and precipitate formation on mechanical and corrosion behavior of friction stir processed AA6061 alloy using different cooling media. https://doi.org/10.1177/14644207211005790

Sha, G., Yao, L., Liao, X., Ringer, S.P., Duan, Z.C., Langdon, T.G., 2011. Segregation of solute elements at grain boundaries in an ultrafine grained Al-Zn-Mg-Cu alloy. Ultramicroscopy 111, 500–505. https://doi.org/10.1016/j.ultramic.2010.11.013

Shamanian, M., Mohammadnezhad, M., Szpunar, J., 2014. Texture analysis of a friction stir welded ultrafine grained Al-Al 2O3 composite produced by accumulative roll-bonding. J. Alloys Compd. 615, 651–656. https://doi.org/10.1016/j.jallcom.2014.07.029

Sharma, C., Dwivedi, D.K., Kumar, P., 2012. Influence of in-process cooling on tensile behaviour of friction stir welded joints of AA7039. Mater. Sci. Eng. A 556, 479–487. https://doi.org/10.1016/j.msea.2012.07.016

Shukla, S., Komarasamy, M., Mishra, R.S., 2018. Grain size dependence of fatigue properties of friction stir processed ultrafine-grained Al-5024 alloy. Int. J. Fatigue 109, 1–9. https://doi.org/10.1016/j.ijfatigue.2017.12.007

Shyam Kumar, C.N., Bauri, R., Yadav, D., 2016. Wear properties of 5083 Al-W surface composite fabricated by friction stir processing. Tribol. Int. 101, 284–290. https://doi.org/10.1016/j.triboint.2016.04.033

Singh, R.K.R., Prasad, R., Pandey, S., Sharma, S.K., 2019. Effect of cooling environment and welding speed on fatigue properties of friction stir welded Al-Mg-Cr alloy. Int. J. Fatigue 127, 551–563. https://doi.org/10.1016/j.ijfatigue.2019.06.043

Singh, R.K.R., Sharma, C., Dwivedi, D.K., Mehta, N.K., Kumar, P., 2011. The microstructure and mechanical properties of friction stir welded Al-Zn-Mg alloy in as welded and heat treated conditions. Mater. Des. 32, 682–687. https://doi.org/10.1016/j.matdes.2010.08.001

Singh, S., Pal, K., 2019. Effect of texture evolution on mechanical and damping properties of SiC/ZnAl 2 O 4 /Al composite through friction stir processing. J. Mater. Res. Technol. 8, 222–232. https://doi.org/10.1016/j.jmrt.2017.07.006

Sinhmar, S., Dwivedi, D.K., 2020. Mechanical behavior of FSW joint welded by a novel designed stationary shoulder tool. J. Mater. Process. Technol. 277, 116482. https://doi.org/10.1016/j.jmatprotec.2019.116482

Sinhmar, S., Dwivedi, D.K., 2019. Effect of weld thermal cycle on metallurgical and corrosion behavior of friction stir weld joint of AA2014 aluminium alloy. J. Manuf. Process. 37, 305–320. https://doi.org/10.1016/j.jmapro.2018.12.001

Sinhmar, S., Dwivedi, D.K., 2018. A study on corrosion behavior of friction stir welded and tungsten inert gas welded AA2014 aluminium alloy. Corros. Sci. 133, 25–35. https://doi.org/10.1016/j.corsci.2018.01.012

Sinhmar, S., Dwivedi, D.K., 2017. Enhancement of mechanical properties and corrosion resistance of friction stir welded joint of AA2014 using water cooling. Mater. Sci. Eng. A 684, 413–

422. https://doi.org/10.1016/j.msea.2016.12.087

Sivanesh Prabhu, M., Elaya Perumal, A., Arulvel, S., Franklin Issac, R., 2019. Friction and wear measurements of friction stir processed aluminium alloy 6082/CaCO3 composite. Meas. J. Int. Meas. Confed. 142, 10–20. https://doi.org/10.1016/j.measurement.2019.04.061

Su, J.Q., Nelson, T.W., McNelley, T.R., Mishra, R.S., 2011. Development of nanocrystalline structure in Cu during friction stir processing (FSP). Mater. Sci. Eng. A 528, 5458–5464. https://doi.org/10.1016/j.msea.2011.03.043

Su, Y., Asadi, H., Nikraz, H., 2020. Comparison of varied specimen geometry for simplified VECD test with pulse-rest period, International Journal of Pavement Research and Technology. https://doi.org/10.1007/s42947-020-0181-2

Suhuddin, U.F.H.R., Mironov, S., Sato, Y.S., Kokawa, H., 2010. Grain structure and texture evolution during friction stir welding of thin 6016 aluminium alloy sheets. Mater. Sci. Eng. A 527, 1962–1969. https://doi.org/10.1016/j.msea.2009.11.029

Sun, Y., Morisada, Y., Fujii, H., Tsuji, N., 2018. Ultrafine grained structure and improved mechanical properties of low temperature friction stir spot welded 6061-T6 Al alloys. Mater. Charact. 135, 124–133. https://doi.org/10.1016/j.matchar.2017.11.033

Tan, Y.B., Wang, X.M., Ma, M., Zhang, J.X., Liu, W.C., Fu, R.D., Xiang, S., 2017. A study on microstructure and mechanical properties of AA 3003 aluminium alloy joints by underwater friction stir welding. Mater. Charact. 127, 41–52. https://doi.org/10.1016/j.matchar.2017.01.039

Venkateswara Reddy, K., Bheekya Naik, R., Rao, G.R., Madhusudhan Reddy, G., Arockia Kumar, R., 2020. Microstructure and damping capacity of AA6061/graphite surface composites produced through friction stir processing. Compos. Commun. 20, 100352. https://doi.org/10.1016/j.coco.2020.04.018

Venkateswarlu, G., Devaraju, D., Davidson, M.J., Kotiveerachari, B., Tagore, G.R.N., 2013a. Effect of overlapping ratio on mechanical properties and formability of friction stir processed Mg AZ31B alloy. Mater. Des. 45, 480–486. https://doi.org/10.1016/j.matdes.2012.08.031

Vinogradov, A., Estrin, Y., 2018. Progress in Materials Science Analytical and numerical approaches to modelling severe plastic deformation 95, 172–242.

Vysotskiy, I., Malopheyev, S., Rahimi, S., Mironov, S., Kaibyshev, R., 2019. Unusual fatigue behavior of friction-stir welded Al–Mg–Si alloy. Mater. Sci. Eng. A 760, 277–286. https://doi.org/10.1016/j.msea.2019.06.005

Wang, Q., Zhao, Y., Yan, K., Lu, S., 2015. Corrosion behavior of spray formed 7055 aluminium alloy joint welded by underwater friction stir welding. Mater. Des. 68, 97–103. https://doi.org/10.1016/j.matdes.2014.12.019

Węglowski, M.S., 2018. Friction stir processing – State of the art. Arch. Civ. Mech. Eng. 18, 114–129. https://doi.org/10.1016/j.acme.2017.06.002

Wu, C., Hou, Q., Luo, M., Zan, X., Zhu, Y., Li, P., Xu, Q., Cheng, G., Luo, N., 2019. Preparation of ultra fi ne-grained / nanostructured tungsten materials : An overview 779, 926–941.

XU, W. feng, MA, J., WANG, M., LU, H. jian, LUO, Y. xuan, 2020. Effect of cooling conditions on corrosion resistance of friction stir welded 2219-T62 aluminium alloy thick plate joint. Trans. Nonferrous Met. Soc. China (English Ed. 30, 1491–1499. https://doi.org/10.1016/S1003-6326(20)65313-4

Xu, W., Liu, J., 2009. Microstructure and pitting corrosion of friction stir welded joints in 2219-O aluminium alloy thick plate. Corros. Sci. 51, 2743–2751. https://doi.org/10.1016/j.corsci.2009.07.004

Xu, W., Liu, J., Luan, G., Dong, C., 2009. Microstructure and mechanical properties of friction stir welded joints in 2219-T6 aluminium alloy. Mater. Des. 30, 3460–3467. https://doi.org/10.1016/j.matdes.2009.03.018

Xue, P., Wang, B.B., Chen, F.F., Wang, W.G., Xiao, B.L., Ma, Z.Y., 2016. Microstructure and mechanical properties of friction stir processed Cu with an ideal ultrafine-grained structure. Mater. Charact. 121, 187–194. https://doi.org/10.1016/j.matchar.2016.10.009

Xue, P., Xiao, B.L., Ma, Z.Y., 2013. Achieving Large-area Bulk Ultrafine Grained Cu via Submerged Multiple-pass Friction Stir Processing. J. Mater. Sci. Technol. 29, 1111–1115. https://doi.org/10.1016/j.jmst.2013.09.021

Yazdipour, A., Shafiei M, A., Dehghani, K., 2009. Modeling the microstructural evolution and effect of cooling rate on the nanograins formed during the friction stir processing of Al5083. Mater. Sci. Eng. A 527, 192–197. https://doi.org/10.1016/j.msea.2009.08.040

Yu, Y., Wang, P., Pei, X., Dong, P., Fang, H., 2020. Fatigue resistance characterization of frictions stir welds between complex aluminium extrusions: An experimental and finite element study. Int. J. Fatigue 141, 105861. https://doi.org/10.1016/j.ijfatigue.2020.105861

Yuvaraj, N., Aravindan, S., Vipin, 2015. Fabrication of Al5083/B4C surface composite by friction stir processing and its tribological characterization. J. Mater. Res. Technol. 4, 398–410. https://doi.org/10.1016/j.jmrt.2015.02.006

Zhang, C., Cao, Y., Huang, G., Zeng, Q., Zhu, Y., Huang, X., Li, N., Liu, Q., 2020. Influence of tool rotational speed on local microstructure, mechanical and corrosion behavior of dissimilar AA2024/7075 joints fabricated by friction stir welding. J. Manuf. Process. 49, 214–226. https://doi.org/10.1016/j.jmapro.2019.11.031

Zhang, H., Zhao, X., Liu, Y., 2021. Effect of high frequency impacting and rolling on fatigue crack growth of 2A12 aluminium alloy welded joint. Int. J. Fatigue. https://doi.org/10.1016/j.ijfatigue.2021.106172

Zhang, L., Zhong, H., Li, S., Zhao, H., Chen, J., Qi, L., 2020. Microstructure, mechanical properties and fatigue crack growth behavior of friction stir welded joint of 6061-T6 aluminium alloy. Int. J. Fatigue 135, 105556. https://doi.org/10.1016/j.ijfatigue.2020.105556

Zhang, P., Li, S.X., Zhang, Z.F., 2011. General relationship between strength and hardness. Mater. Sci. Eng. A 529, 62–73. https://doi.org/10.1016/j.msea.2011.08.061

Zhang, W., Ding, H., Cai, M., Yang, W., Li, J., 2018. Ultra-grain refinement and enhanced low-temperature superplasticity in a friction stir-processed Ti-6Al-4V alloy. Mater. Sci. Eng. A 727, 90–96. https://doi.org/10.1016/j.msea.2018.03.009

Zhang, W., Tan, L., Ni, D., Chen, J., Zhao, Y.C., Liu, L., Shuai, C., Yang, K., Atrens, A., Zhao, M.C., 2019. Effect of grain refinement and crystallographic texture produced by friction stir processing on the biodegradation behavior of a Mg-Nd-Zn alloy. J. Mater. Sci. Technol. 35, 777–783. https://doi.org/10.1016/j.jmst.2018.11.025

Zhang, Z., Xiao, B.L., Ma, Z.Y., 2014. Influence of water cooling on microstructure and mechanical properties of friction stir welded 2014Al-T6 joints. Mater. Sci. Eng. A 614, 6–15. https://doi.org/10.1016/j.msea.2014.06.093

Zhang, Z.Y., Yang, R., Li, Y., Chen, G., Zhao, Y.T., Liu, M.P., 2018. Microstructural evolution and mechanical properties of friction stir processed ZrB2/6061Al nanocomposites. J. Alloys Compd. 762, 312–318. https://doi.org/10.1016/j.jallcom.2018.05.216

Zhao, H., Pan, Q., Qin, Q., Wu, Y., Su, X., 2019a. Effect of the processing parameters of friction stir processing on the microstructure and mechanical properties of 6063 aluminium alloy. Mater. Sci. Eng. A 751, 70–79. https://doi.org/10.1016/j.msea.2019.02.064

Zhao, Y., Wang, Q., Chen, H., Yan, K., 2014. Microstructure and mechanical properties of spray formed 7055 aluminium alloy by underwater friction stir welding. Mater. Des. 56, 725–730. https://doi.org/10.1016/j.matdes.2013.11.071

Zhao, Y.H., Lin, S.B., Wu, L., Qu, F.X., 2005. The influence of pin geometry on bonding and mechanical properties in friction stir weld 2014 Al alloy. Mater. Lett. 59, 2948–2952. https://doi.org/10.1016/j.matlet.2005.04.048

Zhilyaev, A.P., Langdon, T.G., 2008. Progress in Materials Science Using high-pressure torsion for metal processing : Fundamentals and applications 53, 893–979. https://doi.org/10.1016/j.pmatsci.2008.03.002

Zhu, M.L., Xuan, F.Z., 2010. Correlation between microstructure, hardness and strength in HAZ of dissimilar welds of rotor steels. Mater. Sci. Eng. A 527, 4035–4042. https://doi.org/10.1016/j.msea.2010.03.066

PUBLICATIONS:

Publications (Accepted/Published)

1. MVNV Satyanarayana, Kumar Adepu, Microstructure evolution, mechanical and corrosion behavior of AA2014 alloy processed through cryogenic friction stir processing, *Advanced Engineering Materials* (**SCI, IF-3.862**).
2. MVNV Satyanarayana, Kumar Adepu, Karan Chauhan, Effect of overlapping friction stir processing on microstructure, mechanical properties and corrosion behavior of AA6061 alloy, *Metals and Materials International* (**SCI, IF-3.642)**.
3. MVNV Satyanarayana, Sowmya B, Adepu Kumar, Towards finding an actual fatigue behavior of friction stir processed AA2014 alloy, *Materials Letters* (**SCI, IF-3.423**).
4. MVNV Satyanarayana, Kumar Adepu, Kranthi Kumar, Towards finding a novel constant between local and bulk strength of friction stir processed aluminium alloys, *Journal of Materials: Design and Applications* (**SCI, IF-2.311**).
5. MVNV Satyanarayana, Adepu Kumar, Shivraman Tapliyal, Effect of microstructure and precipitate formation on mechanical and corrosion behavior of friction stir processed AA6061 using different cooling media, *Journal of Materials: Design and Applications* (**SCI, IF-2.311**).
6. MVNV Satyanarayana, Adepu Kumar, Influence of cooling media in achieving grain refinement of AA2014 alloy using friction stir processing, Journal of Mechanical Engineering Sciences, 234 (22) 4524-4530. **(SCI, IF-1.762).**

Publications (Comments received/Under review)

7. MVNV Satyanarayana, Kumar Adepu, Microstructure, texture and mechanical behavior of friction stir processed AA2014 alloy, *Metallurgical Materials Transactions A* (**SCI, IF-2.556, Major comments received and submitted**).
8. MVNV Satyanarayana, Sowmya Bathula, Adepu Kumar, Effect of external cooling on fatigue crack growth behavior of friction stir processed AA6061 alloy, *Materials Characterization* (**SCI, IF- 4.342 Under review**).